

APPENDIX II

DETAILS OF RISK ANALYSIS OF ROUTINE, INCIDENT-FREE TRANSPORTATION

TABLE OF CONTENTS

List of Figures.....	247
List of Tables.....	247
II.1 Introduction.....	249
II.2 The RADTRAN Model of Routine Transportation.....	249
II.2.1 Description of the RADTRAN program.....	249
II.2.2 The RADTRAN Software.....	253
II.3 RADTRAN Input Parameters.....	254
II.3.1 Vehicle-specific Input Parameters.....	254
II.3.2 Route-Specific Input Parameters.....	255
II.3.3. Other parameters.....	256
II.4. Routes.....	257
II.5 Results.....	261
II.5.1 Maximally exposed resident in-transit dose.....	262
II.5.2 Unit risk: rail routes.....	262
II.5.3 Unit risk: truck routes.....	263
II.5.4 Doses along selected routes.....	264
II.5.4.1 Collective doses to receptors along the route.....	264
II.5.4.2 Doses to occupants of vehicles sharing the route.....	275
II.5.4.3 Doses from stopped vehicles.....	282
II.5.4.4 Occupational Doses.....	286
II.6 Interpretation of Collective Dose.....	286

List of Figures

Figure II- 1. RADTRAN model of the vehicle in routine, incident-free transportation	250
Figure II-2. Diagram of a truck route as modeled in RADTRAN.	252
Figure II-3. Diagram of truck stop model.....	253
Figure II-4. RADCAT vehicle screen.....	254
Figure II-5. WebTRAGIS map of truck routes from INL.	260

List of Tables

Table II-1. Vehicle-specific parameters.....	255
Table II-2. Route parameters for unit risk calculation (USDOT 2004a, b)	256
Table II-3. Parameter values in the RADTRAN 6 analysis.....	257
Table II-4. Specific routes modeled.....	258
Table II-5. Population multipliers.....	259
Table II-6 Maximum individual doses.....	262
Table II-7. Average doses to various receptors, rail routes.	263
Table II-8. Average doses to various receptors, truck routes.	263
Table II-9. Collective doses (person- μ Sv) from rail transportation; shipment origin INL.....	265
Table II-11. Collective doses (person-Sv) rail transportation; shipment origin Kewaunee	267
Table II-12. Collective doses (person-Sv) from rail transportation; shipment origin Maine Yankee -- continued.....	269
Table II-13. Collective doses (person-Sv) from truck transportation (Truck-DU); shipment origin Maine Yankee.....	270
Table II-13. Collective doses (person-Sv) from truck transportation (Truck-DU); shipment origin Maine Yankee -- continued	271
Table II-14 Collective doses (person-Sv) from truck transportation (Truck-DU); shipment origin Indian Point.....	272
Table II-15. Collective doses (person- μ Sv) from truck transportation (Truck-DU); shipment origin INL	273
Table II-16. Collective doses (person- μ Sv) from truck transportation (Truck-DU); shipment origin Kewaunee.	274
Table II-17. Collective doses (person-Sv) to occupants of trains sharing the route.	276
Table II-18. States comprising the ten EPA regions.....	276
Table II-19. Collective doses (person-Sv) from truck transportation (Truck-DU); shipment origin Maine Yankee.....	278
Table II-19. Collective doses (person-Sv) from truck transportation (Truck-DU); shipment origin Maine Yankee -- continued	279
Table II-20. Collective doses (person-Sv) from truck transportation (Truck-DU); shipment origin Indian Point.	280
Table II-21. Collective doses (person-Sv) from truck transportation (Truck-DU); shipment origin INL	281
Table II-22. Collective doses (person-Sv) from truck transportation (Truck-DU); shipment origin Kewaunee.	282
Table II-23. Example of rail stops on the Maine Yankee-to-Hanford rail route	283
Table II-23. Doses at rail stops on the Maine Yankee-to-Hanford rail route	284

Table II-24 Collective doses to residents near truck stops285
Table II-25 summarizes the occupational doses.286
Table II-25. Occupational doses per shipment from routine incident-free transportation.....286

APPENDIX II

DETAILS OF RISK ANALYSIS OF ROUTINE, INCIDENT-FREE TRANSPORTATION

II.1 Introduction

NUREG-0170 (NRC, 1977) documented estimates of the radiological consequences and risks associated with the shipment by truck, train, plane, or barge of about 25 different radioactive materials, including power reactor spent fuel. The estimates were calculated using Version 1 of the RADTRAN code (Taylor and Daniel, 1977), which was developed for NRC by Sandia National Laboratories specifically to support the conduct of the NUREG-0170 study. RADTRAN Version 6, integrated with the input file generator RADCAT, (Neuhauser, et al., 2000¹; Weiner, et al., 2009) is the computational tool used in this study.

The basic risk assessment method employed in the RADTRAN code is widely accepted. Changes to the code are tracked by a software quality assurance plan that is consistent with American National Standards Institute guidelines. The incident-free module of an earlier version of RADTRAN, RADTRAN 5.25, was validated by measurement (Steinman, et al, 2002); this module is the same in RADTRAN 6.0, the version used in the current study. Verification and validation of RADTRAN 6.0 are documented in Dennis, et al (2008).

II.2 RADTRAN Model of Routine Transportation

II.2.1 Description of the RADTRAN program

RADTRAN calculates the radiological consequences and risks associated with the shipment of a specific radioactive material in a specific package along a specific route. Shipments that take place without the occurrence of accidents are routine, incident free shipments, and the radiation doses to various receptors are called "incident-free doses." Since the probability of routine, incident-free shipment is essentially equal to one², RADTRAN calculates a dose rather than a risk for such shipments. RADTRAN calculates a dose or dose risk from a scenario; the scenario is either routine transportation or a transportation accident. An analyst who wishes to estimate that an accident will take place at a particular point along the route can combine the collective incident free dose to the location of the accident with the collective dose risk from the accident, if desired. This is rarely done. The usual practice is to calculate incident free doses along the chosen routes, and assume that an accident could occur on any segment of that route.

The dose from a routine shipment is based on the external dose from the part of the vehicle carrying the radioactive cargo, referred to as the "vehicle" in this discussion of RADTRAN. Doses to

¹ Neuhauser, et al (2000) is the technical manual for RADTRAN 5, and is cited because the basic equations for the incident-free analyses in RADTRAN 6 are the same as those in RADTRAN 5 and the technical manual for RADTRAN 6 is not yet available.

² The probability of an incident or accident transportation depends on the trip length and would be about 10^{-3} , for a cross-country trip, the probability of routine transportation on such a trip is 1-0.001, or 0.999, or essentially one. For a shorter trip the probability of routine transportation is even closer to one.

receptors from the external radiation from the vehicle depend on the distance between the receptor and the radioactive cargo being transported and the exposure time, the length of time the receptor is exposed to external emissions from the radioactive cargo.

The radioactive inventory of the cargo determines the amount of shielding needed to achieve a particular external dose rate. The resulting external dose rate then becomes the virtual source for doses to receptors from routine, incident-free transportation. The doses in routine transportation therefore depend only on the external dose rate from the cargo.

RADTRAN models the vehicle as a spherical radiation source traveling along the route. The source strength is the transport index (TI), which is one percent of the dose rate in mSv/hour³ at 1 m from the cask. The TI is treated as an isotropically radiating virtual source at the center of the sphere, as shown in Figure II-1.

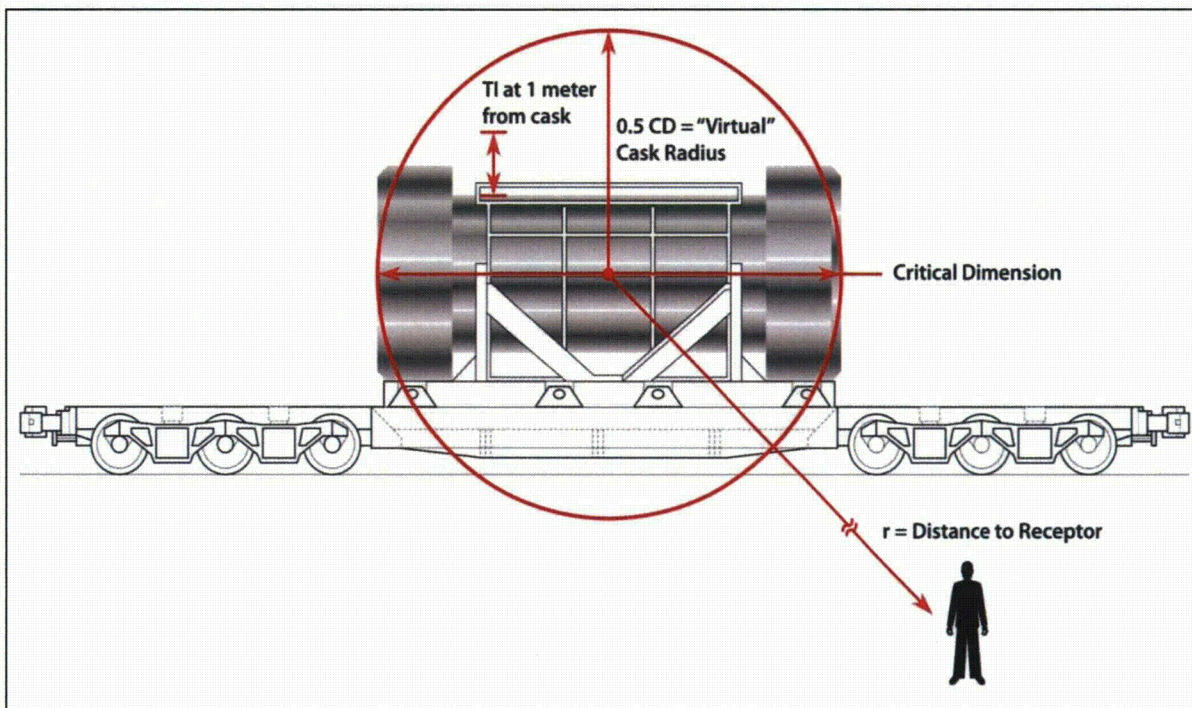


Figure II- 1. RADTRAN model of the vehicle in routine, incident-free transportation

When the distance to the receptor r is much larger than the largest dimension of the cask, RADTRAN models the dose to the receptor as proportional to $1/r^2$. When the distance to the receptor r is similar to or less than the largest dimension of the cask, as for crew or first responders, RADTRAN models the dose to the receptor as proportional to $1/r$. The TIs for the Rail-Lead and the Rail-Steel casks, were calculated from the dose rates at 2 meters as reported in the Safety Analysis Reports of these casks (Holtec International, 2004, NAC international, 2004) and are shown in Table II-1.

³ One mSv = 100 mrem. Thus, 1% of the dose rate in mSv at one meter from the package is equivalent to the dose rate in mrem per hr.

The basic equation for calculating incident-free doses to a population along a transportation route is Equation II-1:

$$(II-1) \quad D(x) = \frac{Qk_0DR_v}{V} \int_{-\infty}^{\infty} \int_{x_{min}}^{x_{max}} \left\{ \frac{(\exp(-\mu r))(B(r))}{r\sqrt{r^2 - x^2}} \right\} dx dr$$

where x is the distance between the receptor and the source, perpendicular to the route

Q includes factors that correct for unit differences

k_0 is the package shape factor

DR_v is the vehicle external dose rate: the TI

V is the vehicle speed

μ is the radiation attenuation factor

B is the radiation buildup factor

r is the distance between the receptor and the source along the route

Details of the application of this and similar equations may be found in Neuhauser et al, (2000).

External radiation from casks carrying used nuclear fuel includes both gamma and neutron radiation. For calculating doses from gamma radiation, RADTRAN uses Equation II-2,

$$(II-2) \quad (e^{-\mu r}) * B(r) = 1$$

for conservatism. For calculating doses from neutron radiation, RADTRAN uses Equation II-3

$$(II-3) \quad (e^{-\mu r}) * B(r) = (e^{-\mu r}) * (1 + a_1r + a_2r^2 + a_3 r^3 + a_4r^4)$$

where the coefficients are characteristics of the material. The default coefficients in RADTRAN are those for the neutron flux at the surface of a lead-shielded spent fuel shipping cask (Neuhauser et al, 2000, page 34).

Collective (population) doses are calculated by integrating over a 770-meter-wide strip along the route where the population resides (the x integration in Equation II-1) and then integrating along the route from minus to plus infinity ($-\infty$ to ∞)⁴ (the r integration in Equation II-1). This is illustrated for a truck route in Figure II-2. The x integration limits in Figure II-2 are not to scale: x_{min} is usually 30 m and x_{max} is usually 800 m. Integration of x to distances greater than 800 meters results in risks not significantly different from integration to 800 m, since the decrease in dose with distance is exponential.

⁴ A dose from ionizing radiation is proportional to $1/r^2$. There is no threshold for such a dose, so there is no cutoff point to the integration along the route in the direction that the cask travels.

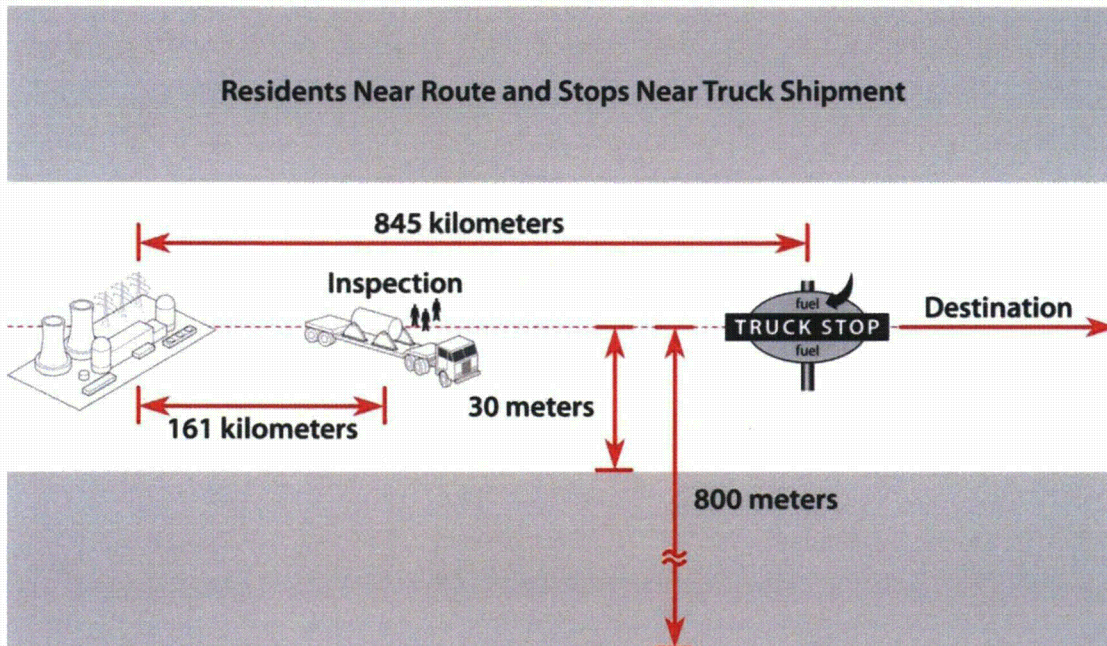


Figure II-2. Diagram of a truck route as modeled in RADTRAN; 845 km is the average distance a very large truck travels on half of its fuel capacity. The 161 km (100 miles) is the distance between spent fuel shipment inspections estimated for shipments to a geologic repository (DOE, 2002, Appendix J, Table J-17).

Variants of Equation II-1 are used to calculate doses to members of the public at stops, to vehicle crew members and other workers, to occupants of vehicles that share the route with the vehicle carrying the radioactive cargo, and to any other receptor identified. Figure II-3 is a diagram of the model used to calculate doses at truck stops. The inner circle defines the area occupied by people who are between the spent fuel truck and the building, and who are not shielded from the truck's external radiation. The dimensions of this circle and the average number of people who occupy it, along with the method used to determine these, are found in Griego et al (1996).

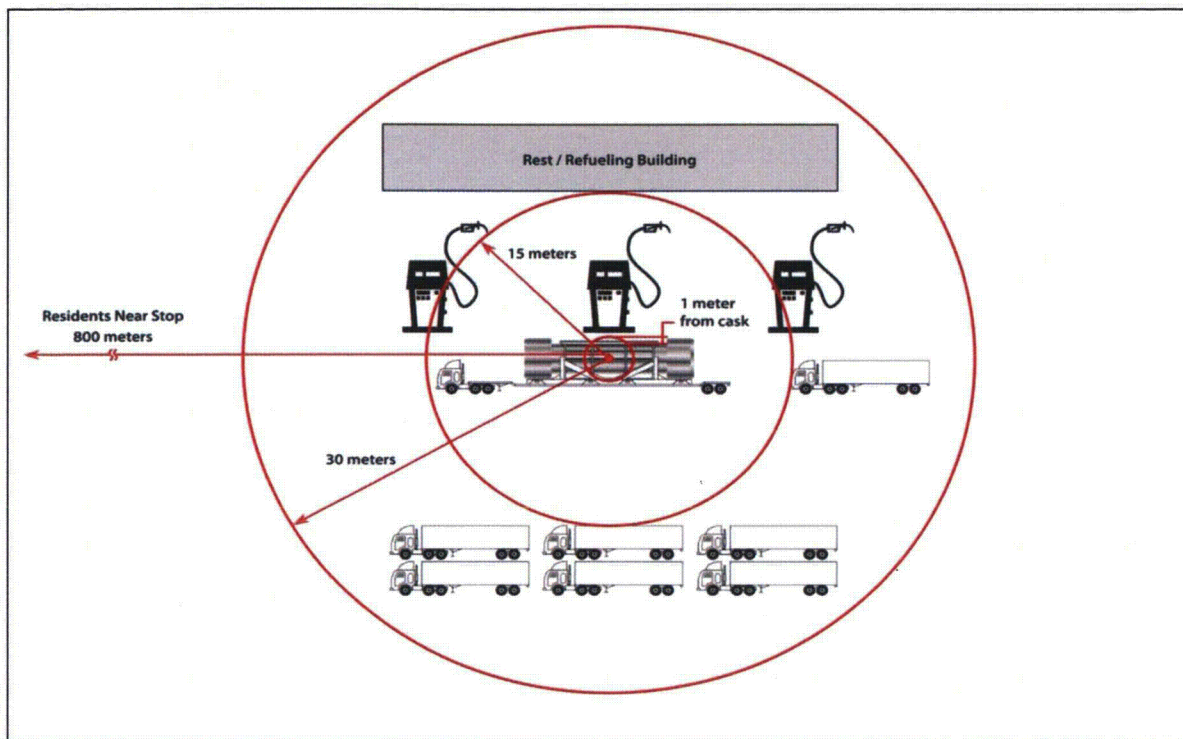


Figure II-3. Diagram of truck stop model from which radiation doses to members of the public are calculated. People at the stop occupy the 14-meter-wide annular space between the truck carrying the cask and the rest stop building. Residents of the area are modeled as occupying an annulus of inner radius 30 m from the cask and outer radius 800 m. from the cask.

II.2.2 RADTRAN Software

This section is a brief description of the RADTRAN software program. A full description of the software and how to use it may be found in the RADCAT User Guide (Weiner, et al, 2009).

The equations that RADTRAN uses, variants of Equation II-1, are programmed in FORTRAN 95. RADTRAN reads in:

- an input text file that contains the input parameters as defined by the RADTRAN user,
- a text file that contains an internal library of 148 radionuclides with their associated dose conversion factors and half-lives,
- a binary file that contains the societal ingestion doses for one curie of each radionuclide in the internal radionuclide library,
- dilution factors and isopleths areas for several weather patterns.

Only the first of these is used in calculating doses from incident-free transportation; the other three are used in the accident analysis and will be discussed in Appendix V.

The input text file can be written directly using a text editor, or can be constructed using the input file generator RADCAT. RADCAT, programmed in XML and running under Java Webstart, provides a series of screens that guide the user in entering values for RADTRAN input parameters. Figure II-4 shows a RADCAT screen.

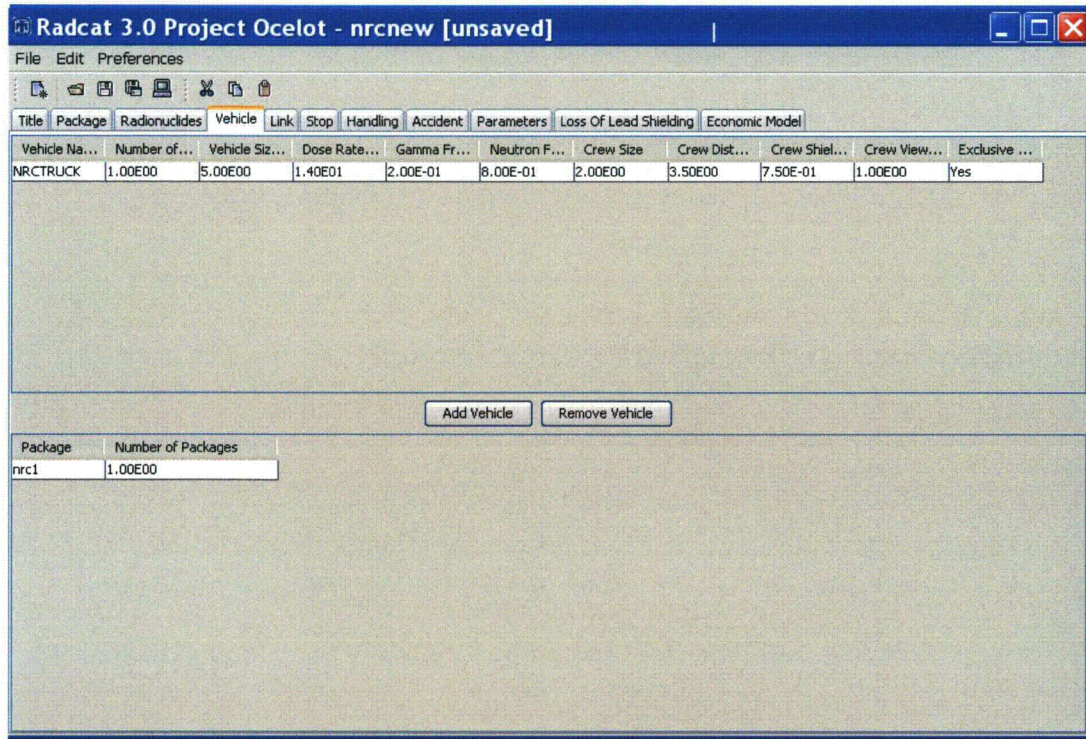


Figure II-4. RADCAT vehicle screen.

RADTRAN output is a text file that can be saved as text or as a spreadsheet.

II.3 RADTRAN Input Parameters

The following sections provide some details of the input parameters used in the RADTRAN analysis performed for this risk analysis.

II.3.1 Vehicle-specific Input Parameters

RADTRAN does not allow for the offset of the package from the trailer edge, so the physical dimensions of the package are considered the physical dimensions of the vehicle. Table II-1 shows the vehicle-specific input parameters to RADTRAN and shows the parameter values used in this analysis. The Rail-Steel is modeled transporting canistered fuel; the Rail- Lead is modeled transporting uncanistered fuel. The Truck-DU is a truck cask. In this analysis, the Truck-DU is assumed to be transported by truck; the Rail- Lead and the Rail- Steel, by rail.

Table II-1. Vehicle-specific parameters (Holtec International, 2004; General Atomics, 1998; NAC International, 2004;

	Truck-DU	Rail-Steel-Lead	Rail-Steel
Transportation mode	highway	rail	Rail
Longest vehicle dimension)	5.94 m	4.90m	5.08 m
Diameter of surface facing crew ("crew view")	2.29 m	2.5 m	3.2 m
Distance from end of cargo to crew cab	3.5 m	150 m minimum	150 m minimum
TI	14	14.02	10.34
Gamma fraction	0.77	0.89	0.90
Neutron fraction	0.23	0.11	0.10
Number of packages per vehicle	1 per truck	1 per railcar	1 per railcar
Number of crew	2	3	3
Exclusive use?^a	yes	NA	NA
Dedicated rail^b	NA	Yes	Yes
17 x 17 PWR assemblies	4	26	24

^aAn exclusive use vehicle is used for only one type of cargo

^bA dedicated train takes a single type of freight from origin to destination.

II.3.2 Route-Specific Input Parameters

Route-specific input parameters are shown in Table II-2 for a single cask in one shipment traveling one kilometer past a population of one person per km². This is called a unit risk calculation. The input parameters are common to the sixteen specific routes analyzed. The vehicle density for rail assumes that only one car of a freight train carries a spent fuel cask.

Table II-2. Route parameters for unit risk calculation (USDOT 2004a, b)

Parameter	Interstate Highway	Freight Rail
Vehicle speed (U.S. average kph)		
Rural	108	40.4
Suburban	102	40.4
Urban	97	24
Vehicle density (U.S. average vehicles/hr)		
Rural	1119	17 ^a
Suburban	2464	17
Urban	5384	17
Persons per vehicle	1.5	2
Farm fraction	0.5	0.5
Stops		
Minimum distance from nearby residents (m)	30	200
Maximum distance from nearby residents (m)	800	800
Stop time for classification (hours)	NA	27
Stop time in transit for railroad change (hours)	NA	0.5
Stop time for truck inspections (hours)	0.75	NA
Stop time at truck stops (hours)	0.83	NA
Average number of people sharing the stop	6.9 ^b	NA
Minimum distance to people sharing the stop (m)	1 ^b	NA
Maximum distance to people sharing the stop (m)	15 ^b	NA
Truck stop worker distance from cask (m)	15	NA
Truck stop worker shielding factor	0.018	NA
Truck crew shielding factor (no regulatory limit)^c	0.377	NA
Escort distance from cask (m)	4	16

^aRailcars per hr ^bGriego et al, 1996. ^c From crew doses with and without the regulatory limit.

II.3.3. Other parameters

RADTRAN includes a set of parameters whose values are not generally known by the user and which have been used routinely in transportation risk assessments. RADTRAN contains default values for these parameters, but all default values can be changed by the user. Table II-3 lists the parameter values used in the incident-free analysis.

Table II-3. Parameter values in the RADTRAN 6 analysis

Parameter	Value
Shielding factor for residents (fraction of energy impacting the receptor): R= rural, S=suburban, U=urban	R=1.0
	S=0.87
	U=0.018
Fraction of outside air in urban buildings	0.25
Fraction of urban population on sidewalk	0.48
Fraction of urban population in buildings	0.52
Ratio of non-residents to residents in urban areas	6
Distance from in-transit shipment for maximum exposure in m. (RMEI exposure)	30
Vehicle speed for maximum exposure in km/hr. (RMEI exposure)	24
Distance from in-transit shipment to nearest resident in rural and suburban areas, m	30
Distance from in-transit shipment to nearest resident in urban areas, m	27
Population bandwidth m	800
Distance between vehicles (trains), m	3.0
Minimum number of rail classification stops	1

Additional input parameters are rural, suburban, and urban route lengths and population densities, characteristics of stops along a route and the TI of the package.

II.4. Routes

This study analyzes both the unit (per-km) doses from a single shipment on rural, suburban, and urban route segments and doses to receptors from a single shipment on 16 representative routes, chosen to represent a range of route lengths and a variety of populations. The actual truck and rail routes were selected for a number of reasons, which are discussed in Chapter 2, Section 2.3.2. The combination of four origins and four destinations represent a variety of route lengths and population densities and both private and government facilities, a large number of states, and includes origins and destinations that were included in the analyses of NUREG/CR-6672 (Sprung, et al, 2000).

Power reactor spent fuel (SNF) and high-level radioactive waste (HLW) are currently stored at 77 locations in the U.S. (67 nuclear generating plants, five storage facilities at sites of decommissioned nuclear plants, and five DOE defense facilities). The origin sites (Table II-4) include two nuclear generating plants (Indian Point and Kewaunee) a storage site (Maine Yankee) and a National Laboratory (Idaho National Laboratory). The destination sites include the two proposed repository sites not characterized (Deaf Smith County, TX and Hanford, WA) (DOE, 1986), the site of the proposed Private Fuel Storage facility (Skull Valley, UT), and a National Laboratory site (Oak Ridge, TN). The routes modeled are shown in Table II-4. Both truck and rail versions of each route are analyzed.

Table II-4. Specific routes modeled

Origin	Destination
Maine Yankee site, ME	Hanford, WA
	Deaf Smith County, TX
	Skull Valley, UT
	Oak Ridge, TN
Kewaunee NP, WI	Hanford, WA
	Deaf Smith County, TX
	Skull Valley, UT
	Oak Ridge, TN
Indian Point NP, NY	Hanford, WA
	Deaf Smith County, TX
	Skull Valley, UT
	Oak Ridge, TN
Idaho National Lab, ID	Hanford, WA
	Deaf Smith County, TX
	Skull Valley, UT
	Oak Ridge, TN

Route segments and population densities are provided by WebTRAGIS (Johnson and Michelhaugh (2003)). WebTRAGIS uses census data from the 2000 census. Updated population data to 2006 were provided in the 2008 Statistical Abstract (U.S. Census Bureau 2008). Table 13 of U.S. Census Bureau (2008) shows the percent increase in population for each of the 50 states of the United States, as well as for the U. S. as a whole, and Table 21 shows the percent increase in population for the 50 largest metropolitan areas in the U.S. Data from these two tables were combined to give population multipliers for states along routes for which the collective dose and the population increase were significant enough to make a correction.

The population multipliers used are shown in Table II-5. “Significant” was taken to mean that the population difference was more than 1% (i.e., multipliers larger than 0.99 but smaller than 1.01 were not considered significant). The state-specific multiplier was applied to rural and suburban routes through the state, and the multiplier for the largest metropolitan area in that state was applied to the urban routes.

Table II-5. Population multipliers

State	Rural, Suburban, Urban Designation	Population Multiplier	State	Rural, Suburban, Urban Designation	Population Multiplier
Arizona	Rural, Suburban	1.202	Nevada	Rural, Suburban	1.249
	Urban	1.242		Urban	1.292
Arkansas	Rural, Suburban	1.051	New Mexico	Rural, Suburban	1.075
	Urban	1.051		Urban	1.075
California	Rural, Suburban	1.076	Oklahoma	Rural, Suburban	1.037
	Urban	1.15		Urban	1.07
Colorado	Rural, Suburban	1.105	Pennsylvania	Rural, Suburban	1.013
	Urban	1.105		Urban	1.025
Georgia	Rural, Suburban	1.144	Oregon	Rural, Suburban	1.082
	Urban	1.21		Urban	1.109
Idaho	Rural, Suburban	1.133	Tennessee	Rural, Suburban	1.061
	Urban	1.133		Urban	1.109
Illinois	Rural, Suburban	1.033	Texas	Rural, Suburban	1.127
	Urban	0.959		Urban	1.175
Maryland	Rural, Suburban	1.037	Utah	Rural, Suburban	1.142
	Urban	1.041		Urban	1.102
Missouri	Rural, Suburban	1.044	Virginia	Rural, Suburban	1.08
	Urban	1.044		Urban	1.103

Parameters like population density and route segment lengths, that are specific to each route, were developed using WebTRAGIS. Figures II-5 through II-8 are maps showing the 16 highway and 16 rail routes in Table II-4.

Maine Yankee NP Routes

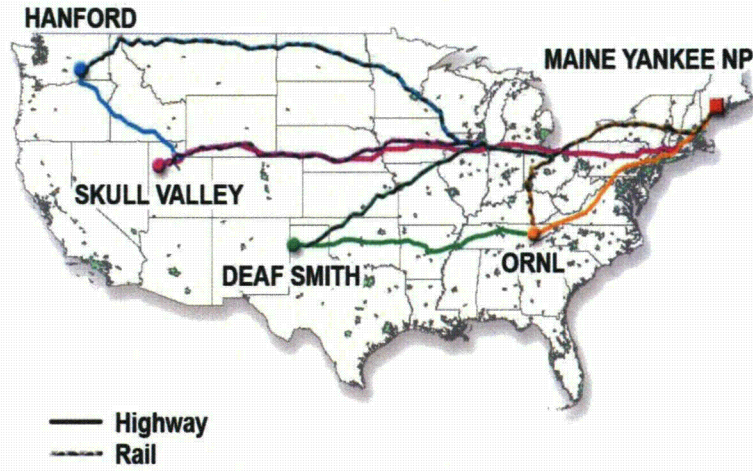


Figure II-5. Highway and rail routes from Maine Yankee Nuclear Plant site .

Kewanee NP Routes

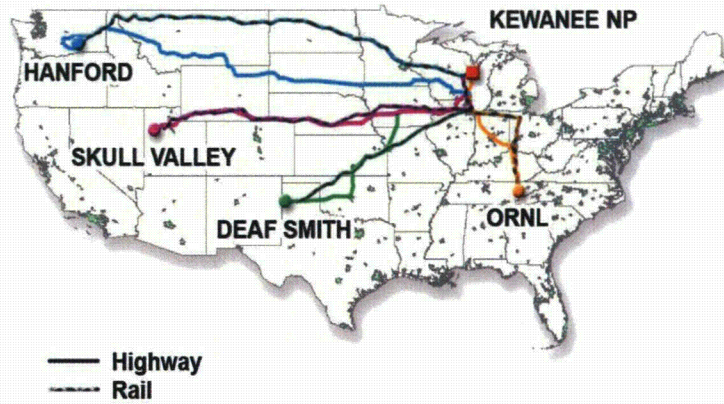


Figure II-6. Highway and rail routes from Kewanee Nuclear Plant

Indian Point NP Routes

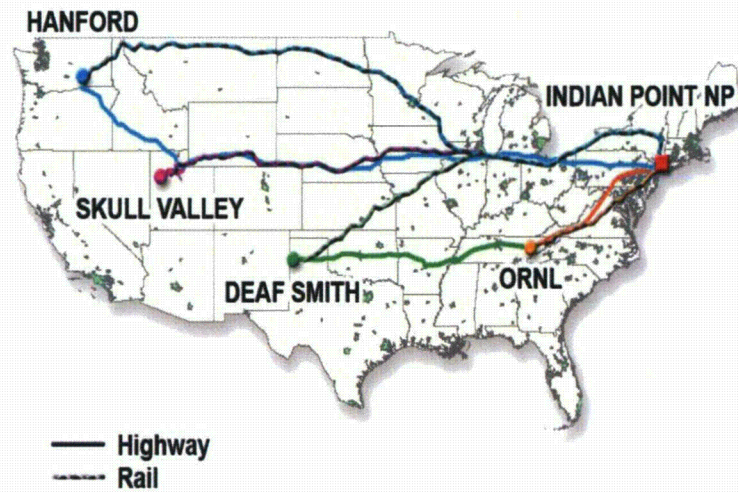


Figure II-7. Highway and rail routes from Indian Point Nuclear Plant

Idaho National Laboratory Routes

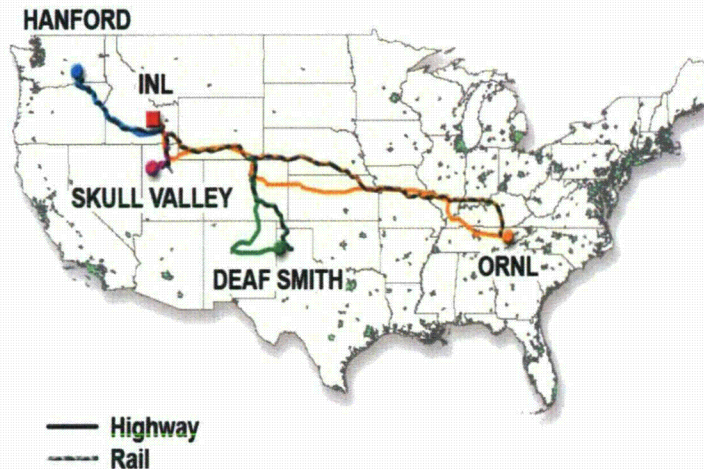


Figure II-8. Highway and rail routes from Idaho National Laboratory

II.5 Results

All results presented here are for a single shipment (one cask).

II.5.1 Maximally exposed resident in-transit dose

The largest dose from a moving vehicle to an individual member of the public is sustained when that individual is 30 meters (a conservative estimate of the interstate right-of-way) from the moving vehicle, and the vehicle is moving at the slowest speed it would be likely to maintain. This speed is 24 kph (16 mph) for both rail and truck. Table II-6 shows the maximum individual dose, in Sv, for each package. These doses are directly proportional to the external dose rate (TI) of each package. For comparison, a single dental x-ray delivers a dose of 4×10^{-5} Sv (Stabin, 2009), about 7000 times the doses shown in Table II-6.

Table II-6 Maximum individual doses.

Package	Dose in Sv
Rail- Lead (rail)	5.7×10^{-9}
Rail-Steel (rail)	4.3×10^{-9}
Truck-DU (truck)	6.7×10^{-9}

II.5.2 Unit risk: rail routes

The doses to railyard workers along the route, to residents and others along the route, and to occupants of vehicles that share the route from a single shipment (one rail cask) traveling one km past a population density of one person/km² are shown in Table II-7. The public occupants of trains sharing the route do not include crew. The dose units are person-Sv. The doses are calculated assuming one cask on a train, because railcar-km is the unit usually used to describe freight rail transport. The data in this table may be used to calculate collective doses along routes as follows:

- Multiply the railyard crew dose by the kilometers of each type of route traveled. This is a conservatively calculated dose that assumes that the total dose that the railyard crew receives during stops along the route is the product of 1.8 percent of the classification yard dose and the total route length. The classification yard occupational collective dose (Wooden, 1986), assuming a 30-hour classification stop, is integrated into RADTRAN. The RADTRAN output dose was adjusted to reflect the 27-hour stop (DOT, 2004b).
- The area along the route occupied by the population is the product of the kilometers traveled and 1.6, since the strip on each side of the route is 0.8 km (800 m) wide. Therefore, multiply the “population along route” dose by this area and the appropriate population density (obtained from a routing code like WebTRAGIS).

Table II-7. Average individual doses (“unit risks”) to various receptors, rail routes. The units of the average dose to the residents near the yard, Sv-km²/hour, reflect the output of the RADTRAN stop model, which incorporates the area occupied.

Cask and route type	Resident along route, Sv	Resident near yard Sv-km ² /hour	Occupants of vehicles sharing the route person-Sv
Rail- Lead rural	7.3E-10	3.5E-07	6.5E-09
Rail- Lead suburban	6.3E-10	3.5E-07	6.5E-09
Rail- urban	2.2E-10	3.5E-07	9.1E-08
Rail- Steel rural	5.6E-10	2.7E-07	4.9E-09
Rail- Steel suburban	4.8E-10	2.7E-07	4.9E-09
Rail- Steel urban	1.7E-11	2.7E-07	1.4E-08

II.5.3 Unit risk: truck routes

The collective doses to truck crew, residents and others along the route, and to occupants of vehicles that share the route from a single shipment (one truck cask) traveling one kilometer past a population density of one person/km² are shown in Table II-8. Rural, suburban, and urban doses to residents living near stops are calculated by multiplying the appropriate stop dose (truck stops are not typically located in urban areas) by the appropriate population density (obtained from a routing code like WebTRAGIS). The number of stops on each route segment is calculated by dividing the length of the route segment by 845 km (average distance between refueling stops for a large semi-detached trailer truck (DOE, 2002, Appendix J). The area of the band occupied by the population along the route is equal to the kilometers traveled multiplied by, e.g., 1.6 for a band width of 800 m on each side of the route the same as for rail routes described above.

Table II-8. Average individual dose (“unit risk”) to various receptors, truck routes.

	Resident near stops Sv-km ² /hour	Resident along route Sv	Occupants of vehicles sharing route
Truck-DU rural	3.26E-06	3.1E-10	1.2E-07
Truck-DU suburban	2.84E-06	2.7E-10	2.7E-07
Truck-DU urban	N/A	5.2E-12	6.0E-07
Truck-DU urban rush hour	N/A	1.2E-12	5.5E-07
6.9 people sharing stop (person-rem)	2.3E-04	N/A	N/A

II.5.4 Doses along selected routes.

Doses to receptors along the routes shown in Table II-5 are presented below.

II.5.4.1 Collective doses to receptors along the route

Using route data from Web TRAGIS, collective doses from incident-free transportation were calculated. For rural and suburban route segments, collective doses calculated were doses sustained by the resident population. Non-resident populations were included with residents as receptors along the urban segments of the routes. Tables II-9 to II-12 show collective doses along rail routes and Tables II-13 to II-116, along highway routes. Blank cells in the tables indicate that no route miles or population was present in those cells.

Table II-9. Collective doses to residents along the route (person-Sv) from rail transportation; shipment origin INL Route totals are in Chapter 2. ^a

DESTINATION AND ROUTE	Rail-Lead			Rail-Steel		
	Rural	Suburban	Urban	Rural	Suburban	Urban
ORNL						
Colorado	2.1E-07	9.3E-07		1.6E-07	7.1E-07	
Idaho	2.8E-06	1.2E-05	5.5E-06	2.1E-06	9.3E-06	4.2E-07
Illinois	2.8E-06	2.7E-05	7.2E-06	2.8E-06	2.7E-05	5.5E-07
Indiana	2.7E-06	1.3E-05	2.9E-06	2.1E-06	1.0E-05	2.2E-07
Kansas	2.0E-06	1.1E-05	2.5E-06	1.6E-06	8.1E-06	1.9E-07
Kentucky	4.2E-06	3.4E-05	1.4E-05	3.2E-06	2.6E-05	1.0E-06
Missouri	3.8E-06	3.6E-05	1.8E-05	2.9E-06	2.7E-05	1.4E-06
Nebraska	5.6E-06	2.0E-05	5.6E-06	4.3E-06	1.5E-05	4.2E-07
Tennessee	2.0E-06	1.3E-05	6.7E-07	1.5E-06	9.6E-06	5.1E-08
Wyoming	2.3E-06	1.4E-05	3.3E-06	1.7E-06	1.1E-05	2.5E-07
DEAF SMITH						
Colorado	5.2E-06	6.6E-05	3.0E-05	2.7E-05	5.1E-05	2.1E-06
Idaho	2.8E-06	1.2E-05	6.0E-06	5.5E-06	9.3E-06	4.2E-07
Oklahoma	1.7E-07	2.9E-07		1.3E-07	2.2E-07	
Texas	6.5E-07	5.4E-06	9.4E-07	5.0E-07	4.1E-06	7.1E-08
Wyoming	1.8E-06	9.6E-06	2.4E-06	2.4E-06	7.3E-06	1.8E-07
HANFORD						
Idaho	6.0E-06	2.6E-05	9.6E-06	9.6E-06	4.0E-06	7.3E-07
Oregon	2.3E-06	1.5E-05	3.5E-06	3.5E-06	1.5E-06	2.7E-07
Washington	1.9E-07	7.0E-06	4.2E-06	4.2E-06	1.2E-07	3.2E-07
SKULL VALLEY						
Idaho	2.3E-06	1.0E-05	5.3E-06	5.3E-06	1.5E-06	4.1E-07
Utah	2.6E-06	3.0E-05	1.8E-05	1.8E-05	2.3E-05	1.4E-06

^aAn empty cell indicates that there was no population on the route segment.

Table II-10. Collective doses to residents along the route (person-Sv), rail transportation, shipment origin Indian Point Route totals are in Chapter 2.

DESTINATION	Rail- Lead			Rail- Steel		
	Rural	Suburban	Urban	Rural	Suburban	Urban
ORNL						
Delaware	2.0E-08	1.2E-05	1.3E-05	1.5E-08	8.9E-06	1.0E-06
Washington DC	5.1E-09	1.4E-06	7.3E-06	3.9E-09	1.1E-06	5.5E-07
Maryland	1.1E-06	3.6E-05	3.2E-05	8.4E-07	2.7E-05	2.4E-06
New Jersey	6.5E-07	1.9E-05	2.2E-05	4.9E-07	1.5E-05	1.7E-06
New York	4.9E-08	2.6E-06	5.4E-05	3.7E-08	2.0E-06	4.1E-06
Pennsylvania	7.9E-08	1.4E-05	5.1E-05	6.0E-08	1.0E-05	3.9E-06
Tennessee	3.6E-06	4.9E-05	1.0E-05	2.7E-06	3.7E-05	8.0E-07
Virginia	6.5E-06	9.4E-05	3.9E-05	5.0E-06	7.2E-05	2.7E-06
DEAF SMITH						
Illinois	2.4E-06	4.3E-05	3.9E-05	1.8E-06	3.3E-05	2.9E-06
Indiana	3.3E-06	1.8E-05	8.6E-06	2.5E-06	1.4E-05	6.6E-07
Iowa	4.7E-07	1.0E-06	5.0E-07	3.6E-07	7.6E-07	3.8E-08
Kansas	3.2E-06	2.9E-05	1.3E-05	2.5E-06	2.2E-05	9.6E-07
Missouri	1.9E-06	1.1E-05	3.8E-06	1.5E-06	8.6E-06	2.9E-07
New York	8.7E-06	9.8E-05	7.9E-05	6.6E-06	7.4E-05	6.0E-06
Ohio	3.9E-06	5.1E-05	3.7E-05	3.0E-06	3.9E-05	2.8E-06
Oklahoma	7.2E-07	6.4E-06	8.3E-07	5.5E-07	4.9E-06	6.3E-08
Pennsylvania	6.6E-07	1.5E-05	7.8E-06	5.0E-07	4.4E-07	4.0E-07
Texas	1.2E-06	8.2E-06	2.0E-06	8.9E-07	6.2E-06	1.5E-07
HANFORD						
Idaho	1.6E-06	1.1E-05	1.5E-06	1.2E-06	1.0E-06	2.9E-07
Illinois	2.1E-06	3.2E-05	3.7E-05	1.6E-06	1.4E-06	8.6E-07
Indiana	3.4E-06	1.8E-05	8.6E-06	2.9E-06	2.2E-06	4.8E-07
Minnesota	5.1E-06	4.7E-05	1.9E-05	3.9E-06	3.4E-06	1.3E-06
Montana	0.0E+00	2.1E-05	2.2E-06	0.0E+00	0.0E+00	5.6E-07
New York	8.7E-06	9.8E-05	7.9E-05	6.6E-06	7.4E-05	6.0E-06
North Dakota	1.6E-06	1.3E-05	4.1E-06	1.2E-06	1.1E-06	3.5E-07
Ohio	3.9E-06	5.1E-05	3.7E-05	3.0E-06	3.9E-05	2.8E-06
Pennsylvania	6.6E-07	1.5E-05	7.8E-06	5.0E-07	4.4E-07	4.0E-07
Washington	1.8E-06	2.2E-05	1.0E-05	1.4E-06	1.2E-06	5.7E-07
Wisconsin	2.7E-06	1.3E-05	6.0E-06	2.0E-06	1.8E-06	3.5E-07
SKULL VALLEY						
Colorado	2.1E-07	9.3E-07	0.0E+00	1.6E-07	7.1E-07	0.0E+00
Illinois	2.1E-06	3.3E-05	4.3E-05	1.6E-06	2.5E-05	3.3E-06
Indiana	3.3E-06	1.8E-05	8.6E-06	2.5E-06	1.4E-05	6.6E-07
Iowa	6.4E-06	2.9E-05	5.5E-06	6.4E-06	2.9E-05	6.0E-06
Nebraska	6.7E-06	3.2E-05	9.9E-06	5.1E-06	2.4E-05	7.5E-07
New York	8.7E-06	9.8E-05	7.9E-05	6.6E-06	7.4E-05	6.0E-06
Ohio	3.9E-06	5.1E-05	3.7E-05	3.0E-06	3.9E-05	2.8E-06
Pennsylvania	6.6E-07	1.5E-05	7.8E-06	5.0E-07	4.4E-07	4.0E-07
Utah	2.0E-06	2.9E-05	1.8E-05	1.6E-06	1.4E-06	7.4E-07
Wyoming	2.2E-06	1.5E-05	3.7E-06	1.6E-06	1.4E-06	4.0E-07

Table II-11. Collective doses to residents along the route (person-Sv) rail transportation; shipment origin Kewaunee. ^aRoute totals are in Chapter 2.

DESTINATION AND ROUTES	Rail-Lead			Rail-Steel		
	Rural	Suburban	Urban	Rural	Suburban	Urban
ORNL						
Illinois	3.8E-07	3.3E-05	4.0E-05	2.9E-07	2.5E-05	3.0E-06
Indiana	3.3E-06	1.8E-05	8.6E-06	2.5E-06	1.4E-05	6.6E-07
Kentucky	5.1E-06	2.6E-05	1.1E-05	3.9E-06	2.0E-05	8.6E-07
Ohio	3.5E-06	4.8E-05	2.3E-05	2.6E-06	3.6E-05	1.7E-06
Tennessee	1.2E-06	7.9E-06	6.5E-07	9.0E-07	6.1E-06	5.0E-08
Wisconsin	3.1E-06	4.0E-05	2.4E-05	6.0E-08	1.0E-05	1.8E-06
DEAF SMITH						
Illinois	2.6E-06	5.6E-05	4.8E-05	2.0E-06	4.3E-05	3.7E-06
Iowa	4.7E-07	1.0E-06	5.0E-07	3.6E-07	7.6E-07	3.8E-08
Kansas	3.2E-06	2.9E-05	1.3E-05	2.5E-06	2.2E-05	9.6E-07
Missouri	1.9E-06	1.1E-05	4.5E-06	1.5E-06	8.6E-06	2.9E-07
Oklahoma	6.7E-07	6.0E-06	7.3E-07	5.1E-07	4.6E-06	5.6E-08
Texas	1.2E-06	8.2E-06	2.0E-06	8.9E-07	6.2E-06	1.5E-07
Wisconsin	3.1E-06	4.0E-05	2.4E-05	6.0E-08	1.0E-05	1.8E-06
HANFORD						
Idaho	1.4E-06	1.1E-05	1.5E-06	1.2E-06	1.0E-06	1.2E-07
Minnesota	5.3E-06	4.8E-05	1.5E-05	4.0E-06	3.5E-06	1.1E-06
Montana	0.0E+00	2.1E-05	2.2E-06	0.0E+00	1.6E-05	1.7E-07
North Dakota	1.6E-06	1.3E-05	4.1E-06	1.2E-06	1.1E-06	3.5E-07
Washington	1.8E-06	2.2E-05	1.0E-05	1.4E-06	1.2E-06	7.9E-07
Wisconsin	5.7E-06	3.5E-05	1.4E-05	4.3E-06	3.8E-06	1.1E-06
SKULL VALLEY						
Colorado	2.1E-07	9.3E-07		1.6E-07	7.1E-07	
Illinois	2.3E-06	4.3E-05	4.4E-05	1.7E-06	3.3E-05	3.4E-06
Iowa	6.4E-06	2.9E-05	5.5E-06	4.9E-06	2.2E-05	4.2E-07
Nebraska	6.7E-06	3.2E-05	9.9E-06	5.1E-06	2.4E-05	7.5E-07
Utah	2.0E-06	2.9E-05	1.8E-05	1.6E-06	1.4E-06	1.4E-06
Wisconsin	3.1E-06	4.0E-05	2.4E-05	6.0E-08	1.0E-05	1.8E-06
Wyoming	2.2E-06	1.5E-05	3.7E-06	1.6E-06	1.4E-06	2.8E-07

^a An empty cell indicates that there was no population on the route segment.

**Table II-12. Collective doses to residents along the route (person-Sv) rail shipment origin
Maine Yankee. ^aRoute totals are in Chapter 2.**

DESTINATION AND ROUTES	Rail-Lead			Rail-Steel		
	Rural	Suburban	Urban	Rural	Suburban	Urban
ORNL						
Kentucky	5.1E-06	2.6E-05	1.1E-05	3.9E-06	2.0E-05	8.6E-07
Maine	1.5E-06	2.5E-05	9.9E-06	1.1E-06	1.9E-05	7.5E-07
Massachusetts	2.1E-06	4.6E-05	2.8E-05	1.6E-06	3.5E-05	2.2E-06
New Hampshire	6.1E-07	1.2E-05	4.0E-06	4.6E-07	9.2E-06	3.1E-07
New York	7.7E-06	8.3E-05	2.9E-05	5.9E-06	6.3E-05	2.2E-06
Ohio	5.7E-06	7.8E-05	5.2E-05	4.4E-06	6.0E-05	3.9E-06
Pennsylvania	6.7E-07	1.5E-05	8.1E-06	5.1E-07	1.1E-05	6.2E-07
Tennessee	1.2E-06	7.9E-06	6.5E-07	9.0E-07	6.1E-06	5.0E-08
Vermont	1.1E-07	8.3E-07		8.1E-08	6.3E-07	
DEAF SMITH						
Illinois	2.4E-06	4.3E-05	3.9E-05	1.8E-06	3.3E-05	2.9E-06
Indiana	3.3E-06	1.8E-05	8.6E-06	2.5E-06	1.4E-05	6.6E-07
Iowa	4.7E-07	1.0E-06	5.0E-07	3.6E-07	7.6E-07	3.8E-08
Kansas	3.2E-06	2.9E-05	1.3E-05	2.5E-06	2.2E-05	9.6E-07
Maine	1.5E-06	2.5E-05	9.9E-06	1.1E-06	1.9E-05	7.5E-07
Massachusetts	2.1E-06	4.6E-05	2.8E-05	1.6E-06	3.5E-05	2.2E-06
Missouri	1.9E-06	1.1E-05	3.8E-06	1.5E-06	8.6E-06	2.9E-07
New Hampshire	6.1E-07	1.2E-05	4.0E-06	4.6E-07	9.2E-06	3.1E-07
New York	7.7E-06	8.3E-05	2.9E-05	5.9E-06	6.3E-05	2.2E-06
Ohio	3.9E-06	5.1E-05	3.7E-05	3.0E-06	3.9E-05	2.8E-06
Oklahoma	6.9E-07	6.2E-06	7.8E-07	5.3E-07	4.7E-06	5.9E-08
Pennsylvania	6.6E-07	1.5E-05	7.8E-06	5.0E-07	1.1E-05	5.9E-07
Texas	1.2E-06	8.2E-06	2.0E-06	8.9E-07	6.2E-06	1.5E-07
Vermont	1.1E-07	8.3E-07		8.1E-08	6.3E-07	

^aAn empty cell indicates that there was no population on the route segment.

Table II-12. Collective doses to residents along the route (person-Sv) from rail transportation; shipment origin Maine Yankee – continued ^aRoute totals are in Chapter 2.

DESTINATION	Rail Lead			Rail Steel		
	Rural	Suburban	Urban	Rural	Suburban	Urban
HANFORD						
Idaho	1.6E-06	1.1E-05	1.5E-06	1.2E-06	8.2E-06	1.2E-07
Illinois	2.2E-06	3.3E-05	3.5E-05	1.7E-06	2.5E-05	2.7E-06
Indiana	3.3E-06	1.8E-05	8.6E-06	2.5E-06	1.4E-05	6.6E-07
Maine	1.5E-06	2.5E-05	9.9E-06	1.1E-06	1.9E-05	7.5E-07
Massachusetts	2.1E-06	4.6E-05	2.8E-05	1.6E-06	3.5E-05	2.2E-06
Minnesota	5.1E-06	4.7E-05	1.9E-05	3.9E-06	3.6E-05	1.4E-06
Montana	3.5E-06	2.1E-05	2.2E-06	2.7E-06	1.6E-05	1.7E-07
New Hampshire	6.1E-07	1.2E-05	4.0E-06	4.6E-07	9.2E-06	3.1E-07
New York	7.7E-06	8.3E-05	3.5E-05	5.9E-06	6.3E-05	2.2E-06
North Dakota	1.6E-06	1.3E-05	4.1E-06	1.2E-06	1.0E-05	3.2E-07
Ohio	3.9E-06	5.1E-05	3.7E-05	3.0E-06	3.9E-05	2.8E-06
Pennsylvania	6.6E-07	1.5E-05	7.8E-06	5.0E-07	1.1E-05	5.9E-07
Vermont	1.1E-07	8.3E-07		8.1E-08	6.3E-07	
Washington	1.8E-06	2.2E-05	1.0E-05	1.4E-06	1.2E-06	5.7E-07
Wisconsin	2.7E-06	1.3E-05	6.0E-06	2.0E-06	1.0E-05	4.6E-07
SKULL VALLEY						
Colorado	1.0E-06	4.3E-05	2.0E-05	7.8E-07	3.2E-05	1.5E-06
Illinois	3.2E-06	2.6E-05	8.2E-06	2.4E-06	1.9E-05	6.0E-07
Indiana	3.2E-06	2.7E-05	7.8E-06	2.4E-06	2.1E-05	5.9E-07
Iowa	7.2E-06	2.6E-05		5.5E-06	2.0E-05	
Maine	1.5E-06	2.6E-05		1.2E-06	2.0E-05	
Massachusetts	1.0E-06	4.5E-05		7.9E-07	3.4E-05	
Nebraska	7.6E-06	2.1E-05	5.9E-06	5.8E-06	1.6E-05	4.5E-07
New Hampshire	1.8E-07	5.9E-06	7.8E-07	1.4E-07	4.5E-06	5.9E-08
New York	7.7E-06	8.3E-05	2.9E-05	5.9E-06	6.3E-05	2.2E-06
Ohio	3.9E-06	5.1E-05	3.7E-05	3.0E-06	3.9E-05	2.8E-06
Pennsylvania	7.8E-07	1.8E-05	9.5E-06	6.0E-07	1.3E-05	7.2E-07
Utah	2.0E-06	2.9E-05	1.8E-05	1.6E-06	1.4E-06	1.4E-06
Vermont	1.1E-07	8.3E-07		8.1E-08	6.3E-07	
Wyoming	2.2E-06	1.5E-05	3.7E-06	1.6E-06	1.4E-06	2.8E-07

^a An empty cell indicates that there was no population on the route segment.

Table II-13. Collective doses to residents along the route (person-Sv) from truck transportation (Truck-DU); shipment origin Maine Yankee Route totals are in Chapter 2.

DESTINATION	ROUTES	Rural	Suburban	Urban	Urban/Rush Hour
ORNL	Connecticut	4.5E-07	2.4E-05	9.0E-07	2.0E-08
	Maine	6.3E-07	1.2E-05	1.1E-07	2.4E-09
	Maryland	5.4E-08	2.1E-06	2.1E-08	4.8E-10
	Massachusetts	4.3E-07	1.9E-05	3.2E-07	7.1E-09
	New Hampshire	7.6E-08	2.4E-06	1.2E-08	2.6E-10
	New Jersey	2.9E-07	1.0E-05	4.9E-07	1.1E-08
	New York	3.4E-09	2.6E-06	4.9E-07	1.1E-08
	Pennsylvania	1.8E-06	2.1E-05	2.6E-07	5.7E-09
	Tennessee	1.2E-06	1.5E-05	1.3E-07	2.8E-09
	Virginia	2.8E-06	3.1E-05	2.0E-07	4.5E-09
	West Virginia	1.8E-07	4.2E-06	1.2E-08	2.6E-10
DEAF SMITH	Connecticut	4.6E-07	2.4E-05	9.1E-07	2.0E-08
	Maine	6.4E-07	1.1E-05	5.9E-08	1.3E-09
	Maryland	5.4E-08	2.1E-06	2.2E-08	4.8E-10
	Massachusetts	4.3E-07	1.9E-05	3.2E-07	7.1E-09
	New Hampshire	7.6E-08	2.4E-06	1.2E-08	2.6E-10
	New Jersey	3.9E-07	1.4E-05	2.8E-07	6.2E-09
	New York	3.8E-08	6.8E-06	3.2E-07	7.1E-09
	Oklahoma	2.6E-06	1.3E-05	1.8E-07	3.9E-09
	Pennsylvania	1.5E-06	1.7E-05	2.1E-07	4.7E-09
	Tennessee	4.7E-06	4.0E-05	6.3E-07	1.4E-08
	Texas	6.3E-07	3.6E-06	1.5E-07	3.4E-09
	Virginia	2.7E-06	3.0E-05	2.0E-07	4.4E-09
	West Virginia	1.8E-07	4.2E-06	1.2E-08	2.6E-10

Table II-13. Collective doses to residents along the route (person-Sv) from truck transportation (Truck-DU); shipment origin Maine Yankee -- continued. Route totals are in Chapter 2.

	ROUTES	Rural	Suburban	Urban	Urban Rush Hour
HANFORD	Connecticut	4.3E-07	1.8E-05	4.8E-07	1.1E-08
	Idaho	2.2E-06	1.1E-05	1.5E-07	3.4E-09
	Illinois	1.3E-06	1.0E-05	1.9E-07	4.3E-09
	Indiana	1.3E-06	1.1E-05	1.8E-07	4.1E-09
	Iowa	3.0E-06	1.1E-05	9.3E-08	2.1E-09
	Maine	6.4E-07	1.1E-05	5.9E-08	1.3E-09
	Massachusetts	4.5E-07	2.0E-05	3.3E-07	7.4E-09
	Nebraska	3.2E-06	8.6E-06	1.4E-07	3.1E-09
	New Hampshire	7.6E-08	2.4E-06	1.2E-08	2.6E-10
	New York	4.4E-07	9.1E-06	8.0E-08	1.8E-09
	Ohio	2.0E-06	2.0E-05	2.7E-07	6.1E-09
	Oregon	1.3E-06	4.6E-06	4.2E-08	9.4E-10
	Pennsylvania	3.2E-06	1.8E-05	1.3E-07	2.9E-09
	Utah	1.0E-06	6.4E-06	2.9E-08	6.5E-10
	Washington	1.4E-07	1.3E-06	8.0E-08	1.8E-09
Wyoming	1.5E-06	5.7E-06	5.6E-08	1.2E-09	
SKULL VALLEY	Connecticut	4.3E-07	1.8E-05	4.8E-07	1.1E-08
	Illinois	1.3E-06	1.0E-05	1.9E-07	4.3E-09
	Indiana	1.3E-06	1.1E-05	1.8E-07	4.1E-09
	Iowa	3.0E-06	1.1E-05	9.3E-08	2.1E-09
	Maine	6.4E-07	1.1E-05	5.9E-08	1.3E-09
	Massachusetts	4.3E-07	1.9E-05	3.2E-07	7.1E-09
	Nebraska	3.2E-06	8.6E-06	1.4E-07	3.1E-09
	New Hampshire	7.6E-08	2.4E-06	1.2E-08	2.6E-10
	New York	4.4E-07	9.1E-06	8.0E-08	1.8E-09
	Ohio	2.0E-06	2.0E-05	2.7E-07	6.1E-09
	Pennsylvania	3.2E-06	1.8E-05	1.3E-07	2.9E-09
	Utah	8.2E-07	7.4E-06	3.3E-07	7.3E-09
	Wyoming	1.5E-06	5.7E-06	5.6E-08	1.2E-09

Table II-14 Collective doses to residents along the route (person-Sv) from truck transportation (Truck-DU); shipment origin Indian Point. Route totals are in Chapter 2.

DESTINATION	ROUTES	Rural	Suburban	Urban	Urban/Rush Hour
ORNL	Maryland	5.4E-08	2.1E-06	2.2E-08	4.6E-10
	New Jersey	3.9E-07	1.4E-05	2.8E-07	6.2E-09
	New York	7.5E-08	7.0E-06	3.5E-07	7.8E-09
	Pennsylvania	1.5E-06	1.7E-05	2.1E-07	4.6E-09
	Tennessee	1.3E-06	1.6E-05	1.1E-07	2.1E-09
	Virginia	2.7E-06	3.0E-05	2.0E-07	4.4E-09
	West Virginia	1.8E-07	4.2E-06	1.2E-08	2.6E-10
DEAF SMITH	Arkansas	2.3E-06	1.6E-05	1.6E-07	3.5E-09
	Maryland	5.4E-08	2.1E-06	2.1E-08	4.8E-10
	New Jersey	3.9E-07	1.4E-05	2.8E-07	6.2E-09
	New York	7.5E-08	7.0E-06	3.5E-07	7.8E-09
	Oklahoma	2.7E-06	1.4E-05	1.9E-07	3.6E-09
	Pennsylvania	1.5E-06	1.7E-05	2.1E-07	4.6E-09
	Texas	6.3E-07	3.6E-06	1.5E-07	2.9E-09
	Virginia	2.7E-06	3.0E-05	2.0E-07	4.4E-09
	West Virginia	1.8E-07	4.2E-06	1.2E-08	2.6E-10
HANFORD	Idaho	2.2E-06	1.1E-05	1.5E-07	3.0E-09
	Illinois	1.3E-06	1.0E-05	2.0E-07	4.5E-09
	Indiana	1.4E-06	1.1E-05	1.8E-07	4.1E-09
	Iowa	3.0E-06	1.1E-05	9.3E-08	2.1E-09
	Nebraska	3.2E-06	8.6E-06	1.4E-07	3.1E-09
	New Jersey	4.2E-07	1.1E-05	2.3E-07	5.0E-09
	New York	7.5E-08	7.0E-06	3.5E-07	7.8E-09
	Ohio	2.0E-06	2.0E-05	2.7E-07	6.1E-09
	Oregon	1.4E-06	5.1E-06	4.2E-08	9.4E-10
	Pennsylvania	2.9E-06	1.4E-05	5.9E-08	1.3E-09
	Utah	1.0E-06	6.4E-06	2.9E-08	6.5E-10
	Washington	1.4E-07	1.3E-06	8.0E-08	1.8E-09
	Wyoming	1.5E-06	5.7E-06	5.6E-08	1.2E-09
SKULL VALLEY	Illinois	1.3E-06	1.0E-05	1.9E-07	4.3E-09
	Indiana	1.3E-06	1.1E-05	1.8E-07	4.1E-09
	Iowa	3.0E-06	1.1E-05	9.3E-08	2.1E-09
	Nebraska	3.2E-06	8.6E-06	1.4E-07	3.1E-09
	New Jersey	4.2E-07	1.1E-05	2.3E-07	5.0E-09
	New York	7.5E-08	7.0E-06	3.5E-07	7.8E-09
	Ohio	2.0E-06	2.0E-05	2.7E-07	6.1E-09
	Pennsylvania	2.9E-06	1.4E-05	5.9E-08	1.3E-09
	Utah	8.2E-07	7.4E-06	3.3E-07	7.3E-09
Wyoming	1.5E-06	5.7E-06	5.6E-08	1.2E-09	

Table II-15. Collective doses to residents along the route (person-Sv) from truck transportation (Truck-DU); shipment origin INL. ^aRoute totals are in Chapter 2.

DESTINATION	ROUTES	Rural	Suburban	Urban	Urban Rush Hour
ORNL	Colorado	1.7E-06	7.4E-06	2.2E-07	4.9E-09
	Idaho	1.0E-06	4.3E-06	3.9E-08	7.7E-10
	Illinois	1.4E-06	9.7E-06	3.1E-08	7.2E-10
	Kansas	2.6E-06	1.1E-05	1.8E-07	4.0E-09
	Kentucky	9.2E-07	3.7E-06	2.9E-09	6.6E-11
	Missouri	1.9E-06	2.4E-05	5.0E-07	1.1E-08
	Tennessee	2.2E-06	1.4E-05	1.8E-07	4.1E-09
	Utah	1.1E-06	6.7E-06	2.9E-08	6.5E-10
	Wyoming	1.3E-06	4.0E-06	3.9E-08	8.8E-10
DEAF SMITH	Colorado	2.0E-06	2.5E-05	7.1E-07	1.6E-08
	Idaho	1.0E-06	4.3E-06	3.9E-08	8.7E-10
	New Mexico	1.9E-06	8.9E-06	3.0E-07	6.6E-09
	Texas	8.4E-08	1.5E-07		
	Utah	9.6E-07	6.1E-06	2.8E-08	5.9E-10
	Wyoming	1.3E-06	4.1E-06	4.1E-08	8.8E-10
HANFORD	Idaho	2.7E-06	1.4E-05	1.8E-07	4.0E-09
	Oregon	1.3E-06	4.7E-06	4.0E-08	9.0E-10
	Washington	1.4E-07	1.3E-06	8.0E-08	1.8E-09
SKULL VALLEY	Idaho	1.0E-06	4.3E-06	3.9E-08	8.7E-10
	Utah	9.6E-07	1.2E-05	3.9E-07	8.6E-09

^s An empty cell indicates that there was no population on the route segment.

Table II-16. Collective doses to residents along the route (person-Sv) from truck transportation (Truck-DU); shipment origin Kewaunee. Route totals are in Chapter 2.

DESTINATION	ROUTES	Rural	Suburban	Urban	Urban-Rush Hour
ORNL	Illinois	3.4E-07	1.6E-05	5.7E-07	1.3E-08
	Indiana	2.1E-06	1.9E-05	3.2E-07	7.2E-09
	Kentucky	1.9E-06	1.7E-05	2.1E-07	4.6E-09
	Ohio	9.5E-08	1.3E-06	1.7E-08	3.9E-10
	Tennessee	5.8E-07	9.9E-06	1.3E-07	2.5E-09
	Wisconsin	1.6E-06	1.2E-05	5.6E-07	1.2E-08
DEAF SMITH	Illinois	1.2E-06	5.2E-06	2.0E-08	4.6E-10
	Iowa	2.3E-06	1.2E-05	1.0E-07	2.2E-09
	Kansas	1.7E-06	1.1E-05	2.6E-07	5.7E-09
	Missouri	1.0E-06	9.7E-06	1.0E-07	1.8E-09
	Oklahoma	1.7E-06	9.6E-06	1.5E-07	3.3E-09
	Texas	6.3E-07	3.6E-06	1.0E-07	2.9E-09
	Wisconsin	2.0E-06	1.2E-05	4.4E-07	9.8E-09
HANFORD	Idaho	3.3E-07	6.6E-06	9.5E-08	1.9E-09
	Minnesota	2.7E-06	4.4E-06	2.1E-08	4.6E-10
	Montana	3.3E-06	1.3E-05	1.6E-07	3.5E-09
	South Dakota	2.3E-06	6.2E-06	4.9E-08	1.1E-09
	Washington	1.6E-06	1.5E-05	3.3E-07	7.3E-09
	Wisconsin	3.3E-06	1.8E-05	4.3E-07	9.6E-09
	Wyoming	8.9E-07	2.6E-06	3.5E-08	7.8E-10
SKULL VALLEY	Illinois	1.2E-06	5.2E-06	2.0E-08	4.6E-10
	Iowa	3.0E-06	1.1E-05	9.3E-08	2.1E-09
	Nebraska	3.2E-06	8.6E-06	1.4E-07	3.1E-09
	Utah	8.2E-07	7.4E-06	3.3E-07	6.6E-09
	Wisconsin	2.0E-06	1.2E-05	4.4E-07	9.8E-09
	Wyoming	1.5E-06	5.7E-06	5.6E-08	1.2E-09

Collective dose is best used in comparing the risks of routine transportation along different routes because the collective dose reflects differences in populations transited. All collective doses modeled are of the order of 10^{-5} person-Sv or less. The tables show that, in general, urban residents sustain a larger dose from rail transportation than from truck transportation on the same state route, even though urban population densities are similar; e.g., for the Maine urban segment of the Maine Yankee-to-ORNL route,

- the truck route urban population density is 2706 persons/km² and the collective dose is 1×10^{-7} person-Sv
- the rail route urban population density is 2527 persons/km², but the collective dose is 9.9×10^{-6} person-Sv from the Rail- Lead cask is almost 100 times larger than the dose from the Truck-DU cask, even though the external dose rates from the two casks are nearly the same.

Doses from rail transportation through urban areas are larger than those from truck transportation because train transportation was designed, and train tracks were laid, to go from city center to city center. Trucks carrying spent fuel, on the other hand, are required to use the interstate highway system, and to use bypasses around cities where such bypasses exist. In the example presented, the truck traverses 5 km of urban route while the train traverses 13 urban km. In addition, the average urban train speed is 24 km/hour (15mph) while the average urban truck speed is 102 km/hour (63.4 mph). A truck carrying a cask through an urban area at about four times the speed of a train carrying a similar cask will deliver $\frac{1}{4}$ the dose of the rail cask.

Suburban collective doses from truck casks are on the average 50 to 100 times urban collective doses because of two factors: shielding in urban areas is about 50 times as effective as shielding in suburban areas, and the total population transited in suburban areas is between 1.5 and 2 times the total population transited in urban areas. Urban route lengths are usually about 10 percent as long as suburban route lengths.

II.5.4.2 Doses to occupants of vehicles sharing the route

Rail

The dose to occupants of trains other than the train carrying the radioactive cargo is provided in Table II-17. The vehicle occupancies used to calculate the table, one person on rural and suburban segments, and five people on urban segments, have been used historically in RADTRAN since 1988. These do not include train crew. The occupancy is consistent with the following considerations:

- Freight trains carry a crew of three, but all but one or two of the 60 to 120 cars on a freight train are unoccupied.
- Urban track carries almost all passenger rail traffic.
- Dose is calculated for one cask on a train, and rail statistics are per railcar, not per train.

The net dose to occupants of other trains depends on train speed and the external dose rate from the spent fuel cask. Train speeds are available only for the entire U.S., not for each state. Therefore, the doses to occupants of trains that share the route with either a loaded Rail-Lead cask or a loaded Rail-Steel cask are shown in Table II-17 for rural, suburban, and urban segments of each entire route.

Table II-17. Collective doses (person-Sv) to occupants of trains sharing the route.

SHIPMENT ORIGIN	SHIPMENT DESTINATION	Rail-Lead Cask			Rail-Steel Cask		
		Rural	Suburban	Urban	Rural	Suburban	Urban
MAINE YANKEE	ORNL	2.8E-05	2.6E-05	2.1E-05	2.1E-05	2.0E-05	1.7E-05
	DEAF SMITH	5.4E-05	1.9E-05	2.7E-05	4.1E-05	1.4E-05	2.2E-05
	HANFORD	8.0E-05	2.3E-05	2.9E-05	6.1E-05	1.8E-05	2.4E-05
	SKULL VALLEY	6.9E-05	2.6E-05	2.3E-05	5.2E-05	2.0E-05	1.9E-05
KEWAUNEE	ORNL	1.9E-05	9.9E-06	1.6E-05	1.5E-05	7.5E-06	1.3E-05
	DEAF SMITH	3.4E-05	7.4E-06	1.4E-05	2.5E-05	5.6E-06	1.2E-05
	HANFORD	3.5E-05	9.5E-06	7.8E-06	2.7E-05	7.2E-06	6.4E-06
	SKULL VALLEY	5.0E-05	1.1E-05	1.6E-05	3.8E-05	8.4E-06	1.3E-05
INDIAN POINT	ORNL	1.3E-05	1.1E-05	2.7E-05	9.8E-06	8.7E-06	2.2E-05
	DEAF SMITH	5.1E-05	1.5E-05	2.6E-05	3.9E-05	1.2E-05	2.2E-05
	HANFORD	6.1E-05	2.0E-05	2.9E-05	4.6E-05	1.5E-05	2.4E-05
	SKULL VALLEY	6.2E-05	1.9E-05	5.3E-06	4.7E-05	1.4E-05	4.0E-06
INL	ORNL	6.5E-05	1.0E-05	9.6E-06	4.9E-05	7.6E-06	7.9E-06
	DEAF SMITH	3.9E-05	4.6E-06	5.2E-06	2.9E-05	3.5E-06	4.3E-06
	HANFORD	2.2E-05	2.5E-06	2.6E-06	1.6E-05	1.9E-06	2.1E-06
	SKULL VALLEY	7.8E-06	2.1E-06	3.3E-06	5.9E-06	1.6E-06	2.7E-06

Truck

Vehicle density data for large semi-detached trailer trucks traveling U.S. interstates and primary highways is available and well qualified. Every state records traffic counts on major (and most minor) highways, and publishes these routinely. Average vehicle density data from each of the 10 EPA regions was used (Weiner et al., 2009, Appendix D). The EPA regions were used because they include all of the “lower 48” U.S. states (Alaska and Hawaii are included in EPA Region 10 but are not considered in this risk assessment). Table II-18 shows the 10 EPA regions.

Table II-18. States comprising the ten EPA regions

Region	States Included in Region
1	Connecticut, Massachusetts, Maine, New Hampshire, Rhode Island, Vermont
2	New Jersey, New York
3	Delaware, Maryland, Pennsylvania, Virginia, West Virginia
4	Alabama, Florida, Georgia, Kentucky, Mississippi, North Carolina, South Carolina, Tennessee
5	Illinois, Indiana, Michigan, Minnesota, Ohio, Wisconsin
6	Arkansas, Louisiana, New Mexico, Oklahoma, Texas
7	Iowa, Kansas, Missouri, Nebraska
8	Colorado, Montana, North Dakota, South Dakota, Utah, Wyoming
9	Arizona, California, Nevada
10	Idaho, Oregon, Washington

The calculation of doses to occupants sharing the highway route with the radioactive materials truck is complex in that vehicles traveling in both directions are considered (the equations that describe this calculation are Equations 28 and 34 of Neuhauser et al, 2000).

The dose received by people in a vehicle traveling in the opposite direction from the cask is

$$(II-4) \quad \int \frac{K \cdot DR_v \cdot N \cdot PPV \cdot L}{V \cdot x \cdot r^2} dx$$

Where K is a proportionality constant, DR_v is the vehicle dose rate, N is the vehicles per hour, PPV is the persons per vehicle, L is the distance the shipment travels, V is the vehicle speed, x is the distance between the lanes occupied by the vehicle, r is the distance to the receptor, and the integral is essentially the same as in Equation II-1. The equation for the dose received by people in a vehicle traveling in the same direction as the cask is the same as Equation II-4, except that the x term is missing from the integration.

Figure II-6 is the diagram accompanying these equations and shows the parameters used in the calculation. Parameter values are in Table II-1.

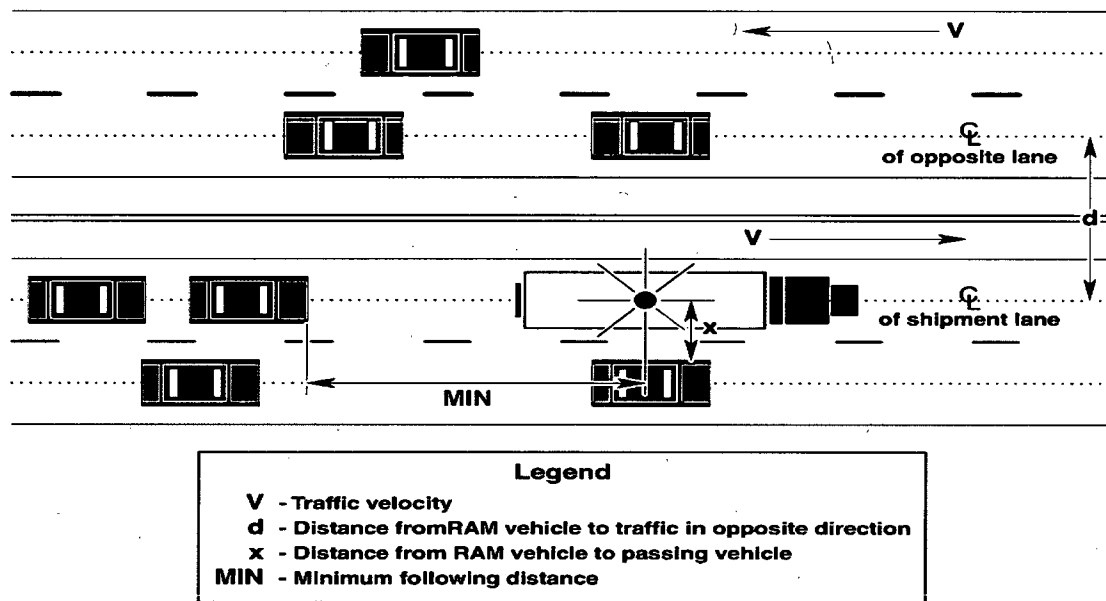


Figure II-9. Parameters for calculating doses to occupants of highway vehicles sharing the route with the radioactive shipment (From Figure 3-2 of Neuhauser, et al, 2000).

Tables II-19 to II-22 show the doses to individuals in vehicles sharing the highway route with the truck carrying a loaded Truck-DU cask.

Table II-19. Collective doses to persons sharing the route (person-Sv) from truck transportation (Truck-DU); shipment origin Maine Yankee.

DESTINATION	ROUTES	Rural	Suburban	Urban	Urban Rush Hour
ORNL	Connecticut	1.9E-06	9.1E-06	9.1E-06	8.5E-07
	Maine	2.9E-06	6.7E-06	1.1E-06	1.0E-07
	Maryland	1.3E-06	4.9E-06	9.0E-07	8.3E-08
	Massachusetts	1.7E-06	8.7E-06	3.4E-06	3.2E-07
	New Hampshire	3.7E-07	1.4E-06	1.9E-07	1.8E-08
	New Jersey	5.1E-06	1.2E-05	9.2E-06	8.5E-07
	New York	1.8E-07	2.1E-06	1.3E-05	1.2E-06
	Pennsylvania	3.0E-05	4.8E-05	7.0E-06	6.5E-07
	Tennessee	1.7E-05	3.2E-05	4.2E-06	3.9E-07
	Virginia	6.4E-05	9.3E-05	6.2E-06	5.7E-07
	West Virginia	2.8E-06	1.2E-05	4.5E-07	4.1E-08
DEAF SMITH	Connecticut	3.1E-05	2.1E-05	2.8E-06	2.6E-07
	Maine	2.0E-06	9.2E-06	9.2E-06	8.5E-07
	Maryland	2.9E-06	6.8E-06	7.3E-07	6.8E-08
	Massachusetts	1.3E-06	4.9E-06	9.0E-07	8.3E-08
	New Hampshire	4.2E-06	2.9E-05	8.7E-06	8.0E-06
	New Jersey	9.5E-07	4.8E-06	4.8E-07	4.4E-07
	New York	4.5E-06	1.6E-05	6.6E-06	6.1E-07
	Oklahoma	7.5E-07	6.8E-06	6.9E-06	6.4E-07
	Pennsylvania	4.2E-05	1.6E-05	2.8E-06	2.6E-07
	Tennessee	3.0E-05	4.8E-05	7.0E-06	6.5E-07
	Texas	7.8E-05	8.6E-05	2.0E-05	1.8E-06
	Virginia	2.2E-05	3.1E-06	2.4E-06	2.2E-07
	West Virginia	6.4E-05	9.3E-05	6.2E-06	5.7E-07

Table II-19. Collective doses to persons sharing the route (person-Sv) from truck transportation (Truck-DU); shipment origin Maine Yankee -- continued.

DESTINATION	ROUTES	Rural	Suburban	Urban	Urban Rush Hour
HANFORD	Connecticut	1.7E-06	8.0E-06	5.1E-06	4.7E-07
	Idaho	4.4E-05	2.3E-05	4.6E-06	4.2E-07
	Illinois	2.4E-05	2.0E-05	5.0E-06	4.6E-07
	Indiana	1.8E-05	2.6E-05	4.6E-06	4.3E-07
	Iowa	4.0E-05	1.7E-05	1.4E-06	1.3E-07
	Maine	2.9E-06	6.8E-06	7.3E-07	6.8E-08
	Massachusetts	1.7E-06	8.7E-06	3.4E-06	3.2E-07
	Nebraska	6.7E-05	1.3E-05	1.9E-06	1.8E-07
	New Hampshire	3.7E-07	1.4E-06	1.9E-07	1.8E-08
	New York	2.5E-06	4.6E-06	1.1E-06	9.9E-08
	Ohio	8.7E-05	6.9E-05	4.0E-06	3.7E-07
	Oregon	3.7E-05	9.5E-06	1.4E-06	1.3E-07
	Pennsylvania	8.7E-05	6.9E-05	4.0E-06	3.7E-07
	Utah	1.6E-05	1.1E-05	6.2E-07	5.7E-08
	Washington	7.6E-06	2.1E-06	2.6E-06	2.4E-07
Wyoming	7.5E-05	1.0E-05	2.1E-06	2.0E-07	
SKULL VALLEY	Connecticut	1.7E-06	8.0E-06	5.1E-06	4.7E-07
	Illinois	2.4E-05	2.0E-05	5.0E-06	4.6E-07
	Indiana	1.8E-05	2.6E-05	4.6E-06	4.3E-07
	Iowa	4.0E-05	1.7E-05	1.4E-06	1.3E-07
	Maine	2.9E-06	6.8E-06	7.3E-07	6.8E-08
	Massachusetts	1.7E-06	8.7E-06	3.4E-06	3.2E-07
	Nebraska	6.7E-05	1.3E-05	1.9E-06	1.8E-07
	New Hampshire	9.5E-07	4.8E-06	4.8E-07	4.4E-07
	New York	5.8E-06	1.3E-05	2.1E-06	1.9E-07
	Ohio	8.7E-05	6.9E-05	4.0E-06	3.7E-07
	Pennsylvania	8.7E-05	6.9E-05	4.0E-06	3.7E-07
	Utah	1.8E-05	8.1E-06	6.1E-06	5.6E-07
Wyoming	7.5E-05	1.0E-05	2.1E-06	2.0E-07	

Table II-20. Collective doses to persons sharing the route (person-Sv) from truck transportation (Truck-DU); shipment origin Indian Point.

DESTINATION	ROUTES	Rural	Suburban	Urban	Urban/Rush Hour
ORNL	Maryland	1.3E-06	4.9E-06	9.0E-07	8.3E-08
	New Jersey	4.5E-06	1.6E-05	6.6E-06	6.1E-07
	New York	1.3E-06	6.5E-06	7.6E-06	7.0E-07
	Pennsylvania	3.0E-05	4.8E-05	7.0E-06	6.5E-07
	Tennessee	1.7E-05	3.4E-05	3.8E-06	3.5E-07
	Virginia	6.4E-05	9.3E-05	6.2E-06	5.7E-07
	West Virginia	6.4E-05	1.2E-05	4.5E-07	4.1E-08
DEAF SMITH	Arkansas	3.1E-05	2.1E-05	2.8E-06	2.6E-07
	Maryland	1.3E-06	4.9E-06	9.0E-07	8.3E-08
	New Jersey	4.5E-06	1.6E-05	6.6E-06	6.1E-07
	New York	1.3E-06	6.5E-06	7.6E-06	7.0E-07
	Oklahoma	4.2E-05	1.6E-05	2.8E-06	2.6E-07
	Pennsylvania	3.0E-05	4.8E-05	7.0E-06	6.5E-07
	Texas	7.8E-05	8.6E-05	2.0E-05	1.8E-06
	Virginia	2.2E-05	3.1E-06	2.4E-06	2.2E-07
	West Virginia	6.4E-05	9.3E-05	6.2E-06	5.7E-07
HANFORD	Idaho	2.8E-06	1.2E-05	4.5E-07	4.1E-08
	Illinois	4.4E-05	2.3E-05	4.6E-06	4.2E-07
	Indiana	2.4E-05	2.0E-05	5.0E-06	4.6E-07
	Iowa	1.8E-05	2.6E-05	4.6E-06	4.3E-07
	Nebraska	4.0E-05	1.7E-05	1.4E-06	1.3E-07
	New Jersey	6.7E-05	1.3E-05	1.9E-06	1.8E-07
	New York	4.8E-06	1.3E-05	5.6E-06	5.2E-07
	Ohio	1.3E-06	6.5E-06	7.6E-06	7.0E-07
	Oregon	1.5E-06	7.6E-06	8.1E-06	7.4E-07
	Pennsylvania	3.7E-05	9.5E-06	1.4E-06	1.3E-07
	Utah	8.0E-05	5.7E-05	2.2E-06	2.0E-07
	Washington	1.6E-05	1.1E-05	6.2E-07	5.7E-08
	Wyoming	7.6E-06	2.1E-06	2.6E-06	2.4E-07
SKULL VALLEY	Illinois	7.5E-05	1.0E-05	2.1E-06	2.0E-07
	Indiana	2.4E-05	2.0E-05	5.0E-06	4.6E-07
	Iowa	1.8E-05	2.6E-05	4.6E-06	4.3E-07
	Nebraska	4.0E-05	1.7E-05	1.4E-06	1.3E-07
	New Jersey	6.7E-05	1.3E-05	1.9E-06	1.8E-07
	New York	5.6E-06	1.5E-05	5.9E-06	5.5E-07
	Ohio	1.5E-06	7.6E-06	8.1E-06	7.4E-07
	Pennsylvania	2.8E-05	4.1E-05	7.3E-06	6.7E-07
	Utah	8.0E-05	5.7E-05	2.2E-06	2.0E-07
Wyoming	1.7E-05	8.1E-06	6.1E-06	5.6E-07	

Table II-21. Collective doses to persons sharing the route (person-Sv) from truck transportation (Truck-DU); shipment origin INL^a

DESTINATION	ROUTES	Rural	Suburban	Urban	Urban Rush Hour
ORNL	Colorado	3.1E-05	1.1E-05	4.0E-06	3.7E-07
	Idaho	2.2E-05	8.0E-06	1.3E-06	1.2E-07
	Illinois	2.5E-05	2.4E-05	1.1E-06	1.0E-07
	Kansas	6.2E-05	1.4E-05	2.7E-06	2.5E-07
	Kentucky	1.8E-05	1.1E-05	1.2E-07	1.2E-08
	Missouri	2.5E-05	2.3E-05	7.2E-06	6.7E-07
	Tennessee	3.3E-05	3.5E-05	5.2E-06	4.8E-07
	Utah	1.3E-05	1.1E-05	6.2E-07	5.7E-08
	Wyoming	7.0E-05	7.6E-06	1.5E-06	1.4E-07
DEAF SMITH	Colorado	3.9E-05	3.6E-05	1.9E-05	1.8E-05
	Idaho	2.2E-05	8.0E-06	1.3E-06	1.2E-07
	New Mexico	6.4E-05	9.8E-06	4.8E-06	4.4E-07
	Texas	7.7E-06	1.7E-07		
	Utah	1.3E-05	1.1E-05	6.2E-07	5.7E-08
	Wyoming	7.0E-05	7.6E-06	1.5E-06	1.4E-07
HANFORD	Idaho	5.5E-05	6.3E-05	5.4E-06	5.0E-07
	Oregon	3.7E-05	2.0E-05	1.4E-06	1.31E-07
	Washington	7.6E-06	2.1E-06	2.6E-06	2.4E-07
SKULL VALLEY	Idaho	2.2E-05	8.0E-06	1.3E-06	1.2E-07
	Utah	1.5E-05	1.5E-05	7.2E-06	6.6E-07

^aAn empty cell indicates that there was no population on the route segment.

Table II-22. Collective doses to persons sharing the route (person-Sv) from truck transportation (Truck-DU); shipment origin Kewaunee.

DESTINATION	ROUTES	Rural	Suburban	Urban	Urban
ORNL	Illinois	3.7E-06	2.0E-05	1.4E-05	1.3E-06
	Indiana	3.3E-05	3.8E-05	8.3E-06	7.7E-07
	Kentucky	2.7E-05	4.3E-05	7.2E-06	6.7E-07
	Ohio	1.4E-06	2.5E-06	5.4E-07	5.0E-08
	Tennessee	1.1E-05	1.8E-05	4.4E-06	4.1E-07
	Wisconsin	2.0E-05	2.1E-05	1.3E-05	1.2E-06
DEAF SMITH	Illinois	2.0E-05	1.2E-05	5.9E-07	5.4E-08
	Iowa	3.2E-05	1.6E-05	1.6E-06	1.4E-07
	Kansas	2.9E-05	1.2E-05	3.5E-06	3.2E-07
	Missouri	1.4E-05	1.1E-05	1.3E-06	1.2E-07
	Oklahoma	3.4E-05	1.1E-05	2.8E-06	2.6E-07
	Texas	2.2E-05	3.1E-06	2.4E-06	2.2E-07
	Wisconsin	2.5E-05	2.3E-05	9.8E-06	9.0E-07
HANFORD	Idaho	9.3E-06	1.1E-05	3.0E-06	2.8E-07
	Minnesota	5.2E-05	1.3E-05	5.4E-07	5.0E-08
	Montana	9.6E-05	3.0E-05	5.4E-06	5.0E-07
	South Dakota	5.3E-05	1.2E-05	1.0E-06	9.5E-08
	Washington	4.6E-05	3.0E-05	1.1E-05	1.0E-06
	Wisconsin	4.6E-05	4.0E-05	9.9E-06	9.2E-07
	Wyoming	4.0E-05	4.1E-06	1.4E-06	1.3E-07
SKULL VALLEY	Illinois	2.0E-05	1.2E-05	5.9E-07	5.4E-08
	Iowa	4.0E-05	1.7E-05	1.4E-06	1.3E-07
	Nebraska	6.7E-05	1.3E-05	1.9E-06	1.8E-07
	Utah	2.4E-05	1.0E-05	8.8E-06	8.1E-06
	Wisconsin	2.5E-05	2.3E-05	9.8E-06	9.0E-07
	Wyoming	7.5E-05	1.0E-05	2.1E-06	2.0E-07

II.5.4.3 Doses from stopped vehicles

Rail

Trains are stopped in classification yards at the origin and destination of the trip. The usual length of these classification stops is 27 hours. The collective dose to the railyard workers at these classification stops from the radioactive cargo is calculated internally by RADTRAN and is based on calculations of Wooden (1986) which authors of this document have verified. This "classification yard dose" for the two rail casks studied is:

- For the Rail- Lead: 1.5×10^{-5} person-Sv
- For the Rail- Steel: 1.1×10^{-5} person-Sv

- These collective doses include doses to the train crew while the train is in the yard.

The collective dose to people living near a classification yard is calculated by multiplying the average dose from the rail cask to an individual living near a classification yard, as shown in Table II-7, by the population density between 200 and 800 meters from the rail yard. The population density is obtained from WebTRAGIS, and the integration from 200 to 800 meters (Table II-2) is performed by RADTRAN.

Most train stops along any route are shown in the WebTRAGIS output for that route. The stops on the rail route from Maine Yankee to Hanford are shown in Table II-23 as an example.

Table II-23. Example of rail stops on the Maine Yankee-to-Hanford rail route

Stop	Reason	Route type ^a and State	Time (hours)
1	Railroad transfer (short line to ST)	Suburban, ME	4.0
2	Railroad transfer (ST to CSXT)	Rural, NY	4.0
3	Railroad transfer (CSXT to IMB)	Suburban, IL	4.0
4	Railroad transfer (IMB to BNSF)	Suburban, IL	<5 minutes
5	Railroad transfer (BNSF to UP)	Suburban, WA	<5 minutes

^aDetermined by the user from the WebTRAGIS output

Railyard worker collective doses can then be calculated for Stops 1, 2, and 3 in Table II-23. Parameter values are from Table II-23 and the associated text.

Dose: $(4/27) * (1.5 \times 10^{-5}) = 2.2 \times 10^{-6}$ person-Sv for the Rail-Lead cask.

Dose: $(4/27) * (1.1 \times 10^{-5}) = 1.6 \times 10^{-6}$ person-Sv for the Rail-Steel cask.

The factor of 4/27 is in the equation because the classification stop doses are calculated by RADTRAN for activities lasting a total of 27 hours, and the in-transit stops are for only four hours.

The average dose to an individual living 200 to 800 meters from a classification yard, as calculated by RADTRAN, is

- 3.5×10^{-7} Sv from the Rail-Lead cask.
- 2.7×10^{-7} Sv from the Rail-Steel cask.

Collective doses to residents near a yard (a classification yard or railroad stop) are then calculated using Equation II-5 :

$$(II-5) \text{ Dose (person-Sv)} = (\text{Population density}) * (\text{Dose/hr to resident near yard}) * (\text{Stop time})$$

Thus, for a rural population density of 13.2 persons/km² (the average along the Maine Yankee-to-Hanford route) living near Stop 1 in Table II-23,

$$\text{Dose} = (13.2 \text{ persons/km}^2) * (3.5 \times 10^{-7} \text{ Sv-km}^2/\text{hour}) * (4 \text{ hours}) = 1.9 \times 10^{-5} \text{ person-Sv.}$$

Results for the stops are in Table II-24.

Table II-24. Doses at rail stops on the Maine Yankee-to-Hanford rail route

Stop	Route type ^a (and State and State ^a)	Time (hours)	Railyard worker dose (person-Sv)		Residents near stop (person-Sv)	
			Rail-Lead	Rail-Steel	Rail- Lead	Rail-Steel
1	Suburban, ME	4.0	2.16E-06	1.61E-06	3.42E-06	2.59E-06
2	Rural, NY	4.0	2.16E-06	1.61E-06	9.15E-07	6.94E-07
3	Suburban, IL	2.0	1.08E-06	8.05E-07	1.24E-05	9.37E-06

^aDetermined by the user from the WebTRAGIS output

Truck

Doses at truck stops are calculated differently from doses at rail stops. There are two types of receptors at a truck stop, in addition to the truck crew: residents who live near the stop and people who share the stop with the refueling truck (no members of the public share rail stops with the train carrying the cask). Griego, et al (1996) conducted some time and motion studies at a number of truck stops. They found that, while a large semi-detached trailer was refueling, the average number of people at the stop between the gas pumps and the nearest building was 6.9, the average distance from the fuel pump to the nearest building was 15 meters, and the longest refueling time for a large semi was 0.83 hour (50 minutes). With these parameters, the collective dose to the people sharing the stop would be 2.3×10^{-4} person-Sv (Table II-8).

The collective dose to residents near the stop is calculated using Equation II-6 with the data in Table II-8, the population density of the region around the stop, and the stop time.

$$(II-6) \text{ Dose (person-Sv)} = (\text{Population density}) * (\text{Dose/hr to resident near stop}) * (\text{Stop time})$$

Thus, for a rural population density of 15.1 persons/km² (the average along the Maine Yankee-to-Hanford route):

$$\text{Dose} = (15.1 \text{ persons/km}^2) * (3.3 \times 10^{-6} \text{ Sv-km}^2/\text{hour}) * (0.83 \text{ hours}) = 4.1 \times 10^{-5} \text{ person-Sv.}$$

The population density used in the calculation is the density around the truck stop; appropriate residential shielding factors (Table II-3) are used in the calculation. Unlike a train, the truck will stop several times on any truck route to fill the fuel tanks. Very large trucks generally carry two 80-gallon tanks each and stop for fuel when the tanks are half empty. A semi carrying a Truck-DU cask can travel an average of 845 km (DOE, 2002) before needing to refuel. The number of refueling (and rest) stops depends on the length of each type of route segment. The following equations are used in this calculation

$$(II-7) \text{ Route segment length (km)} / (845 \text{ km/stop}) = \text{stops/route segment}$$

$$(II-8) \text{ Dose (person-Sv)} = (\text{population/km}^2) * (\text{dose to resident near stop (Sv-km}^2/\text{hr)}) *$$

(stops/route segment)*(hours/stop)

Table II-25 shows the collective doses to residents near stops for the rural and suburban segments of the 16 routes in Table II-4. Trucks carrying Truck-DU casks of spent fuel are unlikely to stop in urban areas.

Table II-25. Collective doses to residents near truck stops.^{a,b}

Origin	Route	Type	Persons/ km ²	Average number of stops	Person-Sv	
Maine Yankee	ORNL	Rural	19.9	1.73	1.1E-06	
		Suburban	395	2.09	2.3E-05	
	Deaf Smith	Rural	18.6	2.47	1.5E-06	
		Suburban	371	1.6	1.7E-05	
	Hanford	Rural	15.4	4.33	2.2E-06	
		Suburban	325	1.5	1.4E-05	
	Skull Valley	Rural	16.9	3.5	1.9E-06	
		Suburban	332.5	1.3	1.2E-05	
	Kewaunee	ORNL	Rural	19.8	0.81	5.2E-07
			Suburban	386.0	0.59	
Deaf Smith		Rural	13.5	2.0	6.0E-06	
		Suburban	339	0.52	8.6E-07	
Hanford		Rural	10.5	3.4	5.0E-06	
		Suburban	316	0.60	1.2E-06	
Skull Valley		Rural	12.5	2.6	5.4E-06	
		Suburban	324.5	0.44	1.1E-06	
Indian Point		ORNL	Rural	20.5	0.71	4.1E-06
			Suburban	388	0.71	4.7E-07
	Deaf Smith	Rural	17.1	2.3	7.8E-06	
		Suburban	370	1.2	1.3E-06	
	Hanford	Of stops	13.0	4.1	1.3E-06	
		Suburban	338	1.1	1.8E-06	
	Skull Valley	Rural	14.2	3.3	1.1E-05	
		Suburban	351	0.93	1.5E-06	
	INL	ORNL	Rural	12.4	3.1	9.3E-06
			Suburban	304	0.72	1.3E-06
Deaf Smith		Rural	7.8	2.3	6.3E-06	
		Suburban	339	0.35	5.8E-07	
Hanford		Rural	6.5	0.43	3.4E-06	
		Suburban	200	0.57	9.0E-08	
Skull Valley		Rural	10.1	0.42	3.2E-06	
		Suburban	343	0.11	1.4E-07	

^aAn empty cell indicates that there was no population on the route segment.

^bThe number of stops on a route segment is calculated by dividing the kilometers of the route segment by 845 km and may be a fraction.

The rural and suburban population densities in Table II-25 are the averages for the entire route. An analogous calculation can be made for each state traversed. However, in neither case can one determine beforehand exactly where the truck will stop to refuel. A truck stop, which could be in either a rural or a suburban area. In some cases (e.g., INL to Skull Valley) the truck may not stop at all; the total distance from INL to the Skull Valley site is only 466.2 km.

II.5.4.4 Occupational Doses

Occupational doses from routine, incident-free radioactive materials transportation include doses to truck and train crew, railyard workers, inspectors, and escorts. Workers who handle spent fuel containers in storage, loading and unloading casks from vehicles or during intermodal transfer are not addressed in this analysis. Truck refueling stops in the U.S. no longer have attendants who refuel trucks.⁵ Gas station and truck stop workers are in concrete or brick buildings and would be shielded from the radiation with the same shielding as in urban housing (98% shielded, since the shielding factor for urban buildings is 0.018, as shown in Table II-3).

Table II-26 summarizes the occupational doses.

Table II-26. Occupational doses from routine incident-free transportation.

Gask and route type	Train crew: 3 people; person-Sv	Truck crew: 2 people; person-Sv	Escort: Sv/hour	Inspector: Sv/hour per inspection	Truck stop worker: Sv per shipment	Rail classification yard workers: person-Sv
Rail-Lead rural/suburban	5.4E-09	NA	5.8 E-06	NA	NA	1.5E-05
Rail-Lead urban	9.1E-08	NA	5.8 E-06	NA	NA	NA
Rail- Steel rural/suburban	4.1E-09	NA	4.4 E-06	NA	NA	1.1E-05
Rail- Steel urban	6.8E-09	NA	4.4 E-06	NA	NA	NA
TRUCK - DU rural/suburban	NA	3.8E-09	3.2E-09	3.2E-09	2.0E-09	NA
TRUCK - DU urban	NA	3.6E-09	3.2E-09	NA	NA	NA

NA = not applicable.

II.6 Interpretation of Collective Dose

Collective dose is essentially the product of an average radiation dose and the number of people who receive that average dose. Together with the linear non-threshold theory (BEIR VII, 2006, p.16), collective dose provides a method to estimate the number of "health effects," cancer in particular, that will occur in a group of people. The following example – a state suburban segment on a particular route – is typical of all routes in all states; only the specific numbers change.

⁵ The State of Oregon still requires gas station attendants to refuel cars and light duty vehicles, but heavy truck crews do their own refueling.

The following parameters characterize a particular segment of the Maine Yankee-to-Hanford truck route, the suburban segment through Illinois:

- Route segment length: 73 km (from WebTRAGIS output)
- Suburban population density: 324 persons/km² (from WebTRAGIS output)
- Area occupied by population along the route segment: 0.800 km x 2 x 73 km = 116.8 km²
- Total suburban population exposed to the shipment = 37,800 people
- From Table II-13, the collective radiation dose to that population, from routine, incident-free transportation, is 1.0 x 10⁻⁵ person-Sv.
- U.S. background is 0.0036 Sv per year or 4.1 x 10⁻⁷ Sv per hour. At an average speed of 108 kph, the population is exposed for 0.675 hour.

The background dose sustained by each member of this population is 2.8 x 10⁻⁷ Sv for a total collective dose of 0.11 person-Sv. The total collective dose is thus 0.11001 person-Sv with the shipment, and 0.11 person-Sv without the shipment. Estimates of the collective radiation risk from shipments of spent fuel are only meaningful when compared to the collective risk to the particular population when there is no shipment.

II.7 Observations

- Radiation doses from a routine, incident-free shipment of spent nuclear fuel to the maximally exposed individual is negligible: less than 10⁻⁸ Sv.
- Average radiation doses from a routine, incident-free shipment of spent nuclear fuel are less than 10⁻⁹ Sv.
- The largest average dose to a member of the public from a routine, incident-free shipment of spent nuclear fuel could be sustained by a person at a truck stop when the truck carrying the cask is refueling. That dose would be about 10⁻⁵ Sv.
- Collective doses to residents along the route are of the order of 10⁻⁵ person-Sv or less on any rural, suburban, or urban route segment modeled.
- Doses from rail transportation through urban areas are larger than those from truck transportation because train transportation was designed, and train tracks were laid, to go from city center to city center.
- The collective dose from an incident-free shipment of spent nuclear fuel to residents along a route or to occupants of vehicles that share the route is negligible compared to the collective background dose, and cannot be distinguished from background. The collective dose from 100 such shipments would be less than one percent of the collective background dose.

APPENDIX III
DETAILS OF CASK RESPONSE TO IMPACT ACCIDENTS

Table of Contents

APPENDIX III DETAILS OF CASK RESPONSE TO IMPACT ACCIDENTS	288
List of Figures	290
List of Tables	292
APPENDIX III DETAILS OF CASK RESPONSE TO IMPACT ACCIDENTS	293
III.1 Finite Element Analysis of the Rail-Steel Cask.....	293
III.1.1 Problem statement.....	293
III.1.2 Geometric Assumptions and Mesh	293
III.1.3 Material Properties.....	297
III.1.4 Criteria for Element Death.....	301
III.1.5. Analysis Results.....	302
III.1.6 Acknowledgements.....	311
III.2 Finite Element Analysis of the Rail-Lead cask	311
III.2.1 Problem statement.....	311
III.2.2 Geometric Assumptions and Mesh	311
III.2.3 Material Properties.....	315
III.2.4 Criteria for Element Death	320
III.2.5 Analysis Results.....	321
III.2.6 Determination of Lid Gaps	327
III.2.7 Acknowledgements.....	340
III.3 Impacts onto Yielding Targets.....	340
III.3.1 Introduction.....	340
III.3.2 Method	341
III.3.3 Soil Targets	343
III.3.4 Concrete Targets	344
III.3.5 Hard Rock Targets	346
III.3.6 Results for Real Target Calculations	347
III.3.7 Impacts onto Water	347
III.4 Response of Spent Fuel Assemblies	347
III.4.1 Introduction.....	347
III.4.2 Description and Method.....	348
III.4.3 Finite Element Models	350
III.4.3 Discussion and Conclusions	364

List of Figures

Figure III-1. Half-symmetric mesh of Rail-Steel cask.....	294
Figure III-2. Impact limiter mesh.....	295
Figure III-3. Impact limiter mesh with honeycomb removed, showing the internal support structure.....	295
Figure III-4. Mesh of lid closure bolts and impact limiter attachment bolts	296
Figure III-5. Locations and magnitudes of internal gaps in the model	296
Figure III-6. Orientation of cask model for material property definitions.....	297
Figure III-7. Rail-Steel cask end impact at 193 KPH (120 MPH).....	302
Figure III-8. Rail-Steel cask corner impact at 48 KPH (30 MPH)	303
Figure III-9. Rail-Steel cask corner impact at 97 KPH (60 MPH)	303
Figure III-10. Rail-Steel cask corner impact at 145 KPH (90 MPH)	304
Figure III-11. Rail-Steel cask side impact at 193 KPH (120 MPH)	304
Figure III-12. Plastic strain in the interior welded canister of the Rail-Steel cask from the end impact at 48 KPH (30 MPH)	305
Figure III-13. Plastic strain in the interior welded canister of the Rail-Steel cask from the end impact at 97 KPH (60 MPH)	306
Figure III-14. Plastic strain in the interior welded canister of the Rail-Steel cask from the end impact at 145 KPH (90 MPH)	306
Figure III-15. Plastic strain in the interior welded canister of the Rail-Steel cask from the end impact at 193 KPH (120 MPH)	307
Figure III-16. Plastic strain in the interior welded canister of the Rail-Steel cask from the corner impact at 48 KPH (30 MPH)	307
Figure III-17. Plastic strain in the interior welded canister of the Rail-Steel cask from the corner impact at 97 KPH (60 MPH)	308
Figure III-18. Plastic strain in the interior welded canister of the Rail-Steel cask from the corner impact at 145 KPH (90 MPH)	308
Figure III-19. Plastic strain in the interior welded canister of the Rail-Steel cask from the corner impact at 193 KPH (120 MPH)	309
Figure III-20. Plastic strain in the interior welded canister of the Rail-Steel cask from the side impact at 48 KPH (30 MPH)	309
Figure III-21. Plastic strain in the interior welded canister of the Rail-Steel cask from the side impact at 97 KPH (60 MPH)	310
Figure III-22. Plastic strain in the interior welded canister of the Rail-Steel cask from the side impact at 145 KPH (90 MPH)	310
Figure III-23. Plastic strain in the interior welded canister of the Rail-Steel cask from the side impact at 193 KPH (120 MPH)	311
Figure III-24. Half-symmetric mesh of Rail-Lead cask.....	312
Figure III-25. Impact limiter mesh.....	313
Figure III-26. Impact limiter mesh with wood removed.....	313

Figure III-27. Mesh of inner and outer lid closure bolts.....	314
Figure III-28. Orientation of cask model for material property definitions.....	315
Figure III-29. Rail-Lead cask end impact at 48 KPH (30 MPH).....	321
Figure III-30. Rail-Lead cask end impact at 97 KPH (60 MPH).....	322
Figure III-31. Rail-Lead cask end impact at 145 KPH (90 MPH).....	322
Figure III-32. Rail-Lead cask end impact at 193 KPH (120 MPH).....	323
Figure III-33. Rail-Lead cask corner impact at 48 KPH (30 MPH)	323
Figure III-34. Rail-Lead cask corner impact at 97 KPH (60 MPH)	324
Figure III-35. Rail-Lead cask corner impact at 145 KPH (90 MPH)	324
Figure III-36. Rail-Lead cask corner impact at 193 KPH (120 MPH)	325
Figure III-37. Rail-Lead cask side impact at 48 KPH (30 MPH)	325
Figure III-38. Rail-Lead cask side impact at 97 KPH (60 MPH)	326
Figure III-39. Rail-Lead cask side impact at 145 KPH (90 MPH)	326
Figure III-40. Rail-Lead cask side impact at 193 KPH (120 MPH)	327
Figure III-41. Gap opening locations for end impact orientation	327
Figure III-42. Gap opening locations for corner impact orientation.....	328
Figure III-43. Gap opening locations for side impact orientation	328
Figure III-44. Gaps in the inner and outer lids of the Rail-Lead cask from the end impact at 48 KPH (30 MPH)	329
Figure III-45. Gaps in the inner and outer lids of the Rail-Lead cask from the end impact at 97 KPH (60 MPH)	330
Figure III-46. Gaps in the inner and outer lids of the Rail-Lead cask from the end impact at 145 KPH (90 MPH)	331
Figure III-47. Gaps in the inner and outer lids of the Rail-Lead cask from the end impact at 193 KPH (120 MPH)	332
Figure III-48. Gaps in the inner and outer lids of the Rail-Lead cask from the corner impact at 48 KPH (30 MPH)	333
Figure III-49. Gaps in the inner and outer lids of the Rail-Lead cask from the corner impact at 97 KPH (60 MPH)	334
Figure III-50. Gaps in the inner and outer lids of the Rail-Lead cask from the corner impact at 145 KPH (90 MPH)	335
Figure III-51. Gaps in the inner and outer lids of the Rail-Lead cask from the corner impact at 193 KPH (120 MPH)	336
Figure III-52. Gaps in the inner and outer lids of the Rail-Lead cask from the side impact at 48 KPH (30 MPH)	337
Figure III-53. Gaps in the inner and outer lids of the Rail-Lead cask from the side impact at 97 KPH (60 MPH)	338
Figure III-54. Kinetic energy time histories for the Rail-Lead cask from 193 KPH (120 MPH) impact analyses in the end, side, and corner orientations	342
Figure III-55. Force generated by the Rail-Lead cask penetrating hard desert soil.....	344

Figure III-56. Comparison of test force-deflection curves with those derived from the empirical equations.	346
Figure III-57. PWR fuel assembly	348
Figure III-58. Fuel rod schematic drawing	349
Figure III-59. Beam Fuel Assembly finite element model	351
Figure III-60. Cross-section of 17x17 fuel assembly with guide tubes (in blue)	352
Figure III-61. Acceleration curves applied to fuel assembly beam model	353
Figure III-62. Spacer grid 100g analysis plastic strain	354
Figure III-63. Hexahedron test model for solid rod-to-rod contact in Abaqus/Explicit	355
Figure III-64. Test model for beam-to-beam contact in Abaqus/Explicit	355
Figure III-65. Comparison of contact forces between solid rod and beam element rod.....	356
Figure III-66. Comparison of contact forces as a function of impact velocity	356
Figure III-67. Continuum rod finite element model	357
Figure III-68. Kinetic energy for Analysis Case 1	359
Figure III-69. Maximum equivalent plastic strain versus time for four inter-spacer grid locations. The spacer grids are specified by the letters in the legend (cf. Figure III-74).....	360
Figure III-70. Maximum equivalent plastic strain field in cladding for Analysis Case 1	360
Figure III-71. Maximum equivalent plastic strain versus time for three spacer grid locations The spacer grids are specified by the letters in the legend (cf. Figure III-74).....	361
Figure III-72. Schematic showing maximum equivalent plastic strain for spacer grid and inter-spacer-grid locations	361
Figure III-73. Maximum equivalent plastic strain field in cladding for Analysis Case 2	362
Figure III-74. Maximum equivalent plastic strain versus time for four inter-spacer grid locations. The spacer grids are specified by the letters in the legend (cf. Figure III-78).....	363
Figure III-75. Maximum equivalent plastic strain versus time for four spacer grid locations The spacer grids are specified by the letters in the legend (cf. Figure III-78).....	363
Figure III-76. Schematic showing maximum equivalent plastic strain for spacer grid and inter-spacer-grid locations, Analysis Case 2	364

List of Tables

Table III-1. Available areas for leakage from the Rail-Lead cask.....	340
Table III-2. Peak contact force for the Rail-Lead cask impacts onto an unyielding target (bold numbers are for the cases where there may be seal leaks).....	343
Table III-3. Equivalent velocities for Rail-Lead cask impacts onto various targets, KPH.....	347
Table III-4. Properties of fuel assembly	350
Table III-5. Zircaloy-4 material parameters.....	353
Table III-6. Standard Material Properties	358
Table III-7. Load case parameter changes	358
Table III-8. Analysis Case Summary.....	364

APPENDIX III

DETAILS OF CASK RESPONSE TO IMPACT ACCIDENTS

III.1 Finite Element Analysis of the Rail-Steel Cask

III.1.1 Problem statement

Simulate impact of a loaded Rail-Steel cask onto an unyielding surface. Consider impact velocities of 48 kph (30 mph), 97 kph (60 mph), 145 kph (90 mph) and 193 kph (120 mph). Include end, side, and center-of-gravity (cg) over corner impact orientations. Results will be used to assess integrity of the containment boundary and to estimate the extent of any possible breach. Although the deformation and failure of the lid closure bolts is of interest, the ultimate question of containment breach can be determined by assessing the integrity of the inner container. Plastic strains in the stainless steel inner container will be used to predict possible breach of the cask.

III.1.2 Geometric Assumptions and Mesh

A finite element model of the Rail-Steel cask was developed for use with the Sierra Mechanics code Presto. Presto is a nonlinear transient dynamics finite element code developed at Sandia National Laboratories and used extensively for weapons qualification work. The Rail-Steel cask model was developed over several years with many changes along the way to work around limitations in Presto. The model was also required to include the most important geometric features without becoming so large that it couldn't be run on the available computational platforms. The final half-symmetric model consisted of 1.4 million solid hex elements. The drop event lasted approximately 0.5 seconds. The simulation of this drop event required approximately 6-8 days of run time on 256 processors of the Tbird high performance computer at Sandia.

An earlier version of the model used shell elements in areas of thin walled components. The code had difficulty with contact between hexes and embedded shells, and the boundary conditions between the shells and hexes required careful and complicated consideration. Ultimately, the shell elements were replaced by hex elements with 2 or 3 elements through the thickness. Although 2 elements through the thickness is insufficient to correctly predict bending response, these instances were limited to components where bending responses were not considered important. For example, the outer shell of the impact limiters was modeled with 2 hex elements through the thickness. The purpose of this outer layer is to provide constraint to the aluminum honeycomb that comprises the impact limiter. The details of how it bends and folds away from the honeycomb are not important, and not accurate with 2 elements through the thickness. The model details are shown in Figures III-1 to III-4. To allow for internal impacts, gaps were included between the fuel region and the canister and between the canister and the cask interior. Figure III-5 shows the location and magnitude of these gaps.

Closure bolts were modeled with hex elements, with a minimum of 4 elements across the diameter of the bolt, as shown in Figure III-4.

The total weight of the cask was 364,700 lbs. This weight is high due to an incorrect density value for the aluminum honeycomb that was not discovered until after the runs were completed. The over-weight of the impact limiters results in a more severe loading environment because it increases the amount of kinetic energy that must be absorbed, making all results conservative.

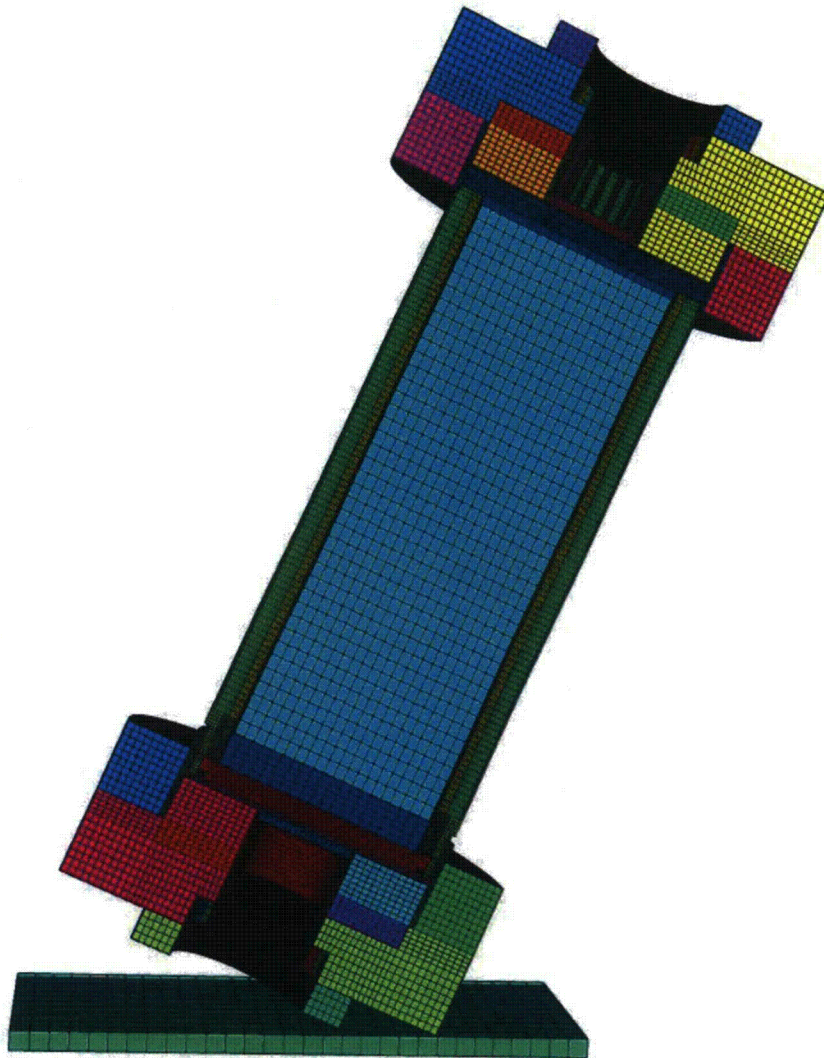


Figure III-1. Half-symmetric mesh of Rail-Steel cask

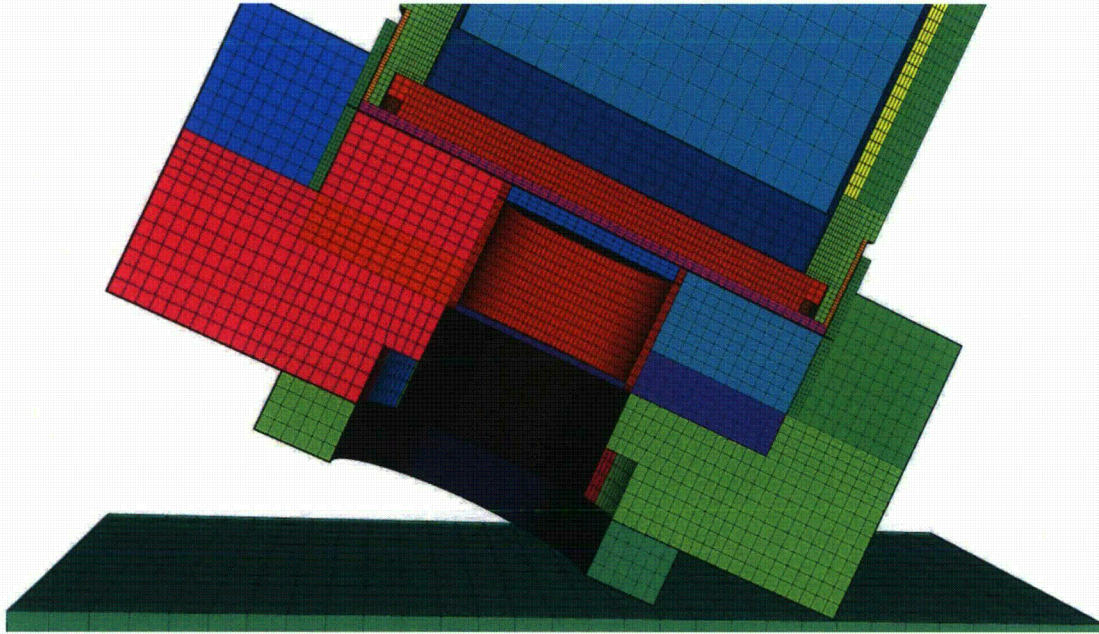


Figure III-2. Impact limiter mesh

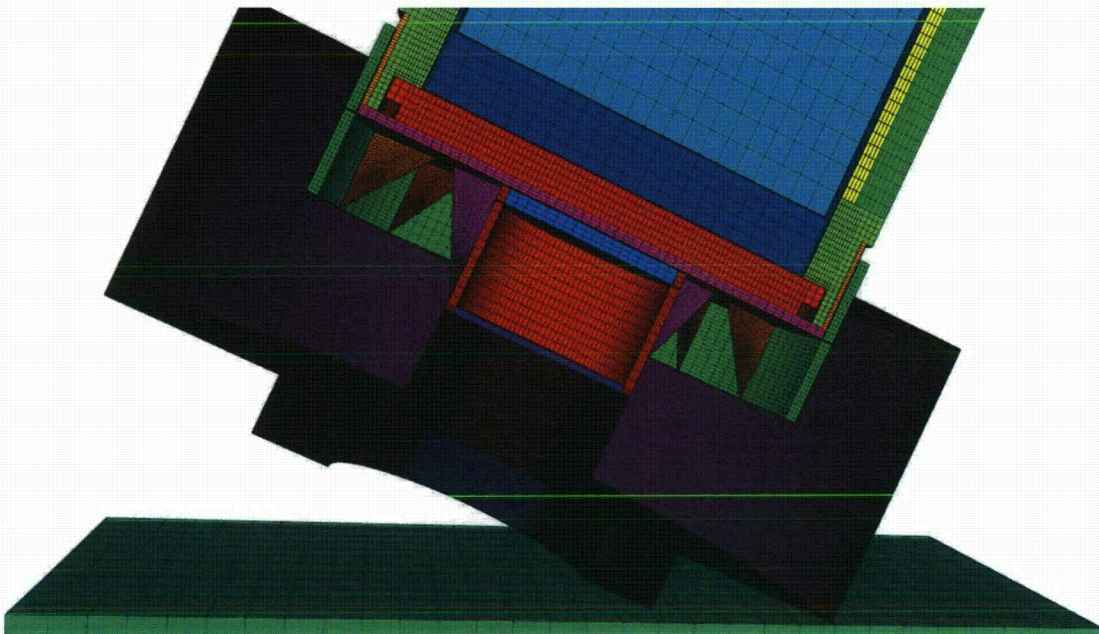


Figure III-3. Impact limiter mesh with honeycomb removed, showing the internal support structure

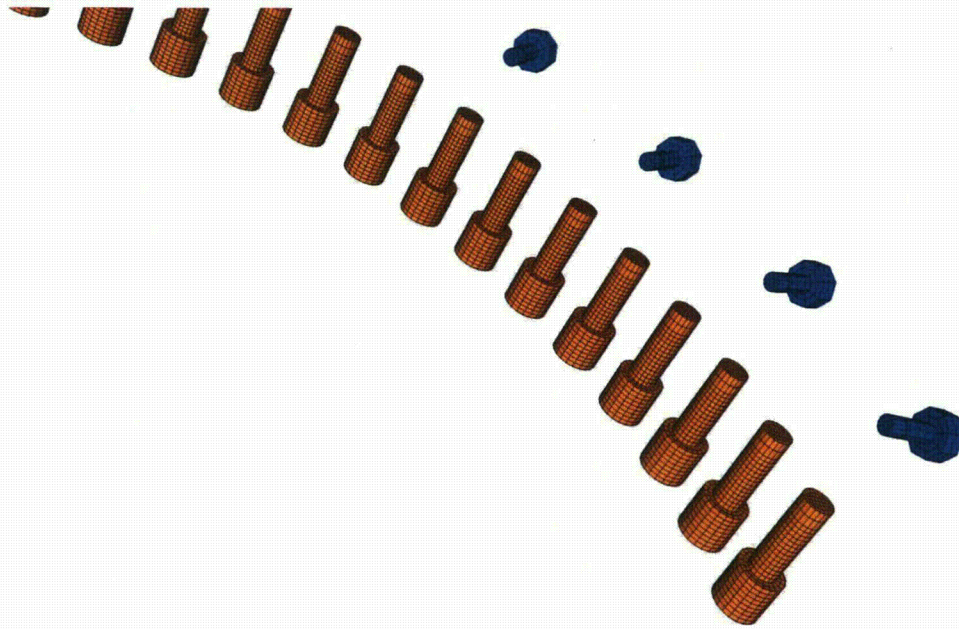


Figure III-4. Mesh of lid closure bolts and impact limiter attachment bolts

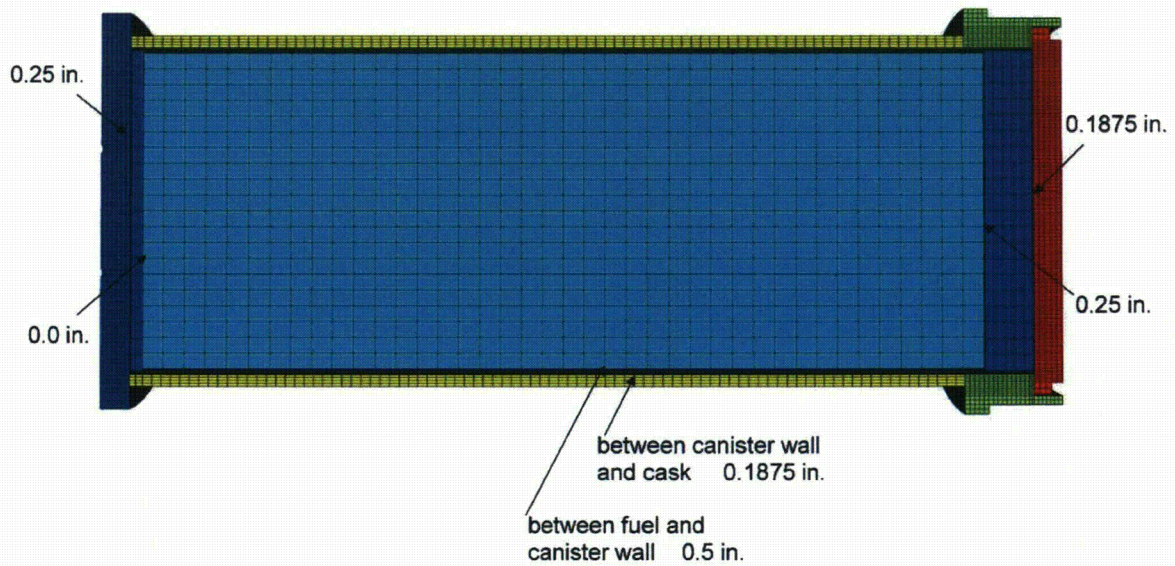


Figure III-5. Locations and magnitudes of internal gaps in the model

The orientation of the model is important to the definition of orthotropic material properties. The cask model is oriented as shown in Figure III-6, and the impact direction is changed for the three impact conditions. For an end drop, the initial velocity is in the +z direction. For a side drop, the

initial velocity is in the $-x$ direction. And for a c.g. over corner drop, the initial velocity is in a $-0.38269x + 0.92388z$ direction.



Figure III-6. Orientation of cask model for material property definitions

III.1.3 Material Properties

The response of the closure bolts was of primary importance in these analyses. The threaded ends of the bolts were modeled as fixed into their mating parts using equivalent nodes. The remainder of the bolt was allowed to slide in its through hole. Bolt failure was predicted by considering the equivalent plastic strain (eqps) required for failure. The value of eqps that constitutes failure was assessed using tensile test data and/or references. Details are given below.

The aluminum honeycomb in the impact limiters was assumed to be equally strong in the axial and radial directions, and weaker in the circumferential direction. Properties were not varied at 15 degree increments as specified by the design. Instead, properties were defined in the global x-y-z directions and aligned with the loading direction at the point of impact. The honeycomb was modeled with an orthotropic crush material model. The model has been used for many years in Presto and in the commercially available FEM code LSDyna. It is known to behave poorly at the transition to a fully compacted state, when the material transitions from a unidirectional compaction to an isotropic compression with Poisson's expansion. For lower impact velocities (30 and 60mph), this was not an issue. However, for the higher impact velocities the model

became unstable at material lock-up. To allow the code to continue running, elements that behaved badly were deleted. Since they had already absorbed the energy of the impact and were now just maintaining volume, their deletion was not considered important to the overall cask response.

Material properties are listed below along with the parameters required by Presto(SIERRA, 2009).

Material sa350lf3

Material SA350-LF3 low alloy steel (Holtec, 2001) used for top lid and cask bottom.

Density = 0.00074 lb-s²/in⁴
Material model ep_power_hard
Youngs Modulus = 28.0e6 psi
Poissons Ratio = 0.27
Yield Stress = 37.0e3 psi
Hardening Constant = 192746.0
Hardening Exponent = 0.748190
Luders Strain = 0.0

Material sa230e

Material SA203-E nickel alloy (Klamerus et al., 1996) used for the overpack outer wall.

Density = 0.00074 lb-s²/in⁴
Material model ep_power_hard
Youngs Modulus = 28.0e6 psi
Poissons Ratio = 0.27
Yield Stress = 40.0e3 psi
Hardening Constant = 192746
Hardening Exponent = 0.748190
Luders Strain = 0.0

Material sa516gr70

Material SA-516 Grade 70 (Klamerus et al., 1996), used for overpack external wall, buttress plates, and impact limiter gusset plates

Density = 0.00074 lb-s²/in⁴
Material model ep_power_hard
Youngs Modulus = 29.0e06 psi
Poissons Ratio = 0.3
Yield Stress = 53.097e3 psi
Hardening Constant = 0.131331E+06
Hardening Exponent = 0.479290
Luders Strain = 0.781E-02

Material testfoam

Material properties taken from typical aluminum honeycomb data as measured at Sandia National Labs (Hinnerichs et al., 2006). Properties used for holtite and impact limiter aluminum cross-ply honeycomb.

Density = 0.0003002 lb-s²/in⁴
Material model orthotropic_crush
 Youngs Modulus = 4e6 psi
 Poissons Ratio = 0.3
 Yield Stress = 40000. psi
 Ex = 5.00e04 psi
 Ey = 5.00e04 psi
 Ez = 5.00e04 psi
 Gxy = 2.50e04 psi
 Gyz = 2.50e04 psi
 Gzx = 2.50e04 psi
 Vmin = 0.70
 Crush xx = 2300_T
 Crush yy = 2300_T
 Crush zz = 2300_L
 Crush xy = 2300_T
 Crush yz = 2300_T
 Crush zx = 2300_T

Function 2300_L

0 1415.384615
0.05 2123.076923
0.1 2300
0.4 2300
0.5 1592.307692
0.6 3737.5
0.7 20000
0.9 20000

Function 2300_T

0 1415.384615
0.05 2123.076923
0.1 2300
0.4 2300
0.5 1592.307692
0.6 3737.5
0.7 20000
0.9 20000

Material internals

Used for cask contents inside of inner container.

Density = 0.00029 lb-s²/in⁴
Material model Orthotropic_Crush
Youngs Modulus = 0.5e6 psi
Poissons Ratio = 0.3
Yield Stress = 20000.0 psi
Ex = 0.5e06 psi
Ey = 0.5e06 psi
Ez = 2.2e06 psi
Gxy = 0.25e06 psi
Gyz = 1.1e06 psi
Gzx = 1.1e06 psi
Vmin = 0.70
Crush xx = 2300_T
Crush yy = 700_W
Crush zz = 2300_L
Crush xy = foam_cross_1
Crush yz = foam_cross_2
Crush zx = foam_cross_1

Function foam_cross_1

0 1000
0.6 1000
0.7 10000
0.8 10000

Function foam_cross_2

0 500
0.6 500
0.7 5000
0.8 5000

Material sb637

Material SB637-N07718 (DOD, 199) used for lid closure bolts.

Density = 0.00074 lb-s²/in⁴
Material model ml_ep_fail
Youngs Modulus = 28.6e6
Poissons Ratio = 0.3
Yield Stress = 160000.
Beta = 1.0
Hardening Function = MLEP_Hardening
Youngs Modulus Function = constant_one
Poissons Ratio Function = constant_one
Yield Stress Function = constant_one
Critical Tearing Parameter = 0.13

Critical Crack Opening Strain = 0.01

Material 304ss

Used for MPC, bottom impact limiter bolts, top impact limiter bolts and shell surrounding impact limiters (Hucek, 1986).

Density = 0.00074 lb-s²/in⁴
Material model ep_power_hard
Youngs Modulus = 53.3e06 psi
Poissons Ratio = 0.3
Yield Stress = 46.246e3 psi
Hardening Constant = 319.05e3
Hardening Exponent = 0.68
Luders Strain = 0.0

III.1.4 Criteria for Element Death

For all attachment bolts, elements failure is defined according to Presto (SIERRA, 2009) convention.

Criterion is element value of eqps > 1.12
Death on inversion = on

To account for instability in the orthotropic crush material model, elements are removed from the mesh if the following condition occurs, stated in the Presto element death convention.

Criterion is element value of solid_angle <= 0.05
Criterion is max nodal value of velocity(1) > 20000
Criterion is max nodal value of velocity(2) > 20000
Criterion is max nodal value of velocity(3) > 20000
Criterion is max nodal value of velocity(1) < -20000
Criterion is max nodal value of velocity(2) < -20000
Criterion is max nodal value of velocity(3) < -20000
Death on inversion = on

The impact limiter gusset plates and aluminum impact limiter honeycomb are in contact within the impact limiter. The honeycomb would likely fail before the gusset plates in an experiment. Due to the homogenized material modeling of the honeycomb and the relatively coarse mesh, the gusset plates are significantly deformed by the honeycomb. The failure of the gusset plates is defined according to Presto convention.

Criterion is element value of timestep < -0.01
Criterion is element value of volume <= 0.0

Death on inversion = on

III.1.5. Analysis Results

The deformed shape of the cask following each impact analysis is presented below.

Time = 0.05280

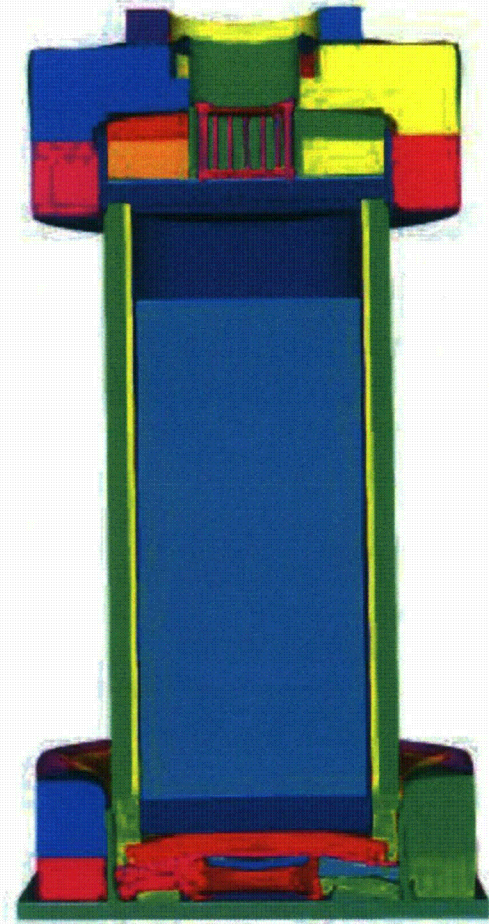


Figure III-7. Rail-Steel cask end impact at 193 KPH (120 MPH)

Time = 0.05680

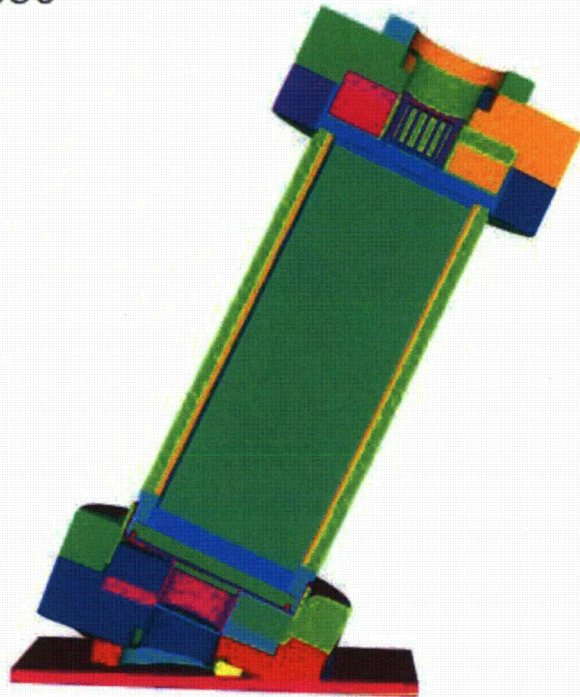


Figure III-8. Rail-Steel cask corner impact at 48 KPH (30 MPH)

Time = 0.06100

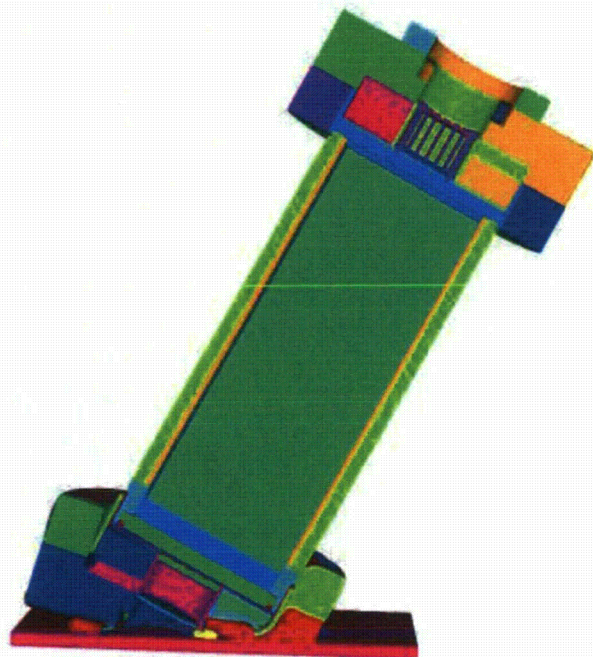


Figure III-9. Rail-Steel cask corner impact at 97 KPH (60 MPH)

Time = 0.04960

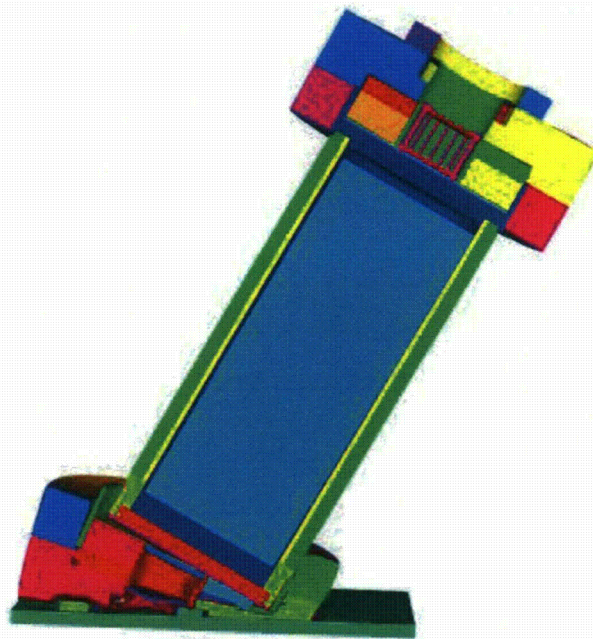


Figure III-10. Rail-Steel cask corner impact at 145 KPH (90 MPH)

Time = 0.03760

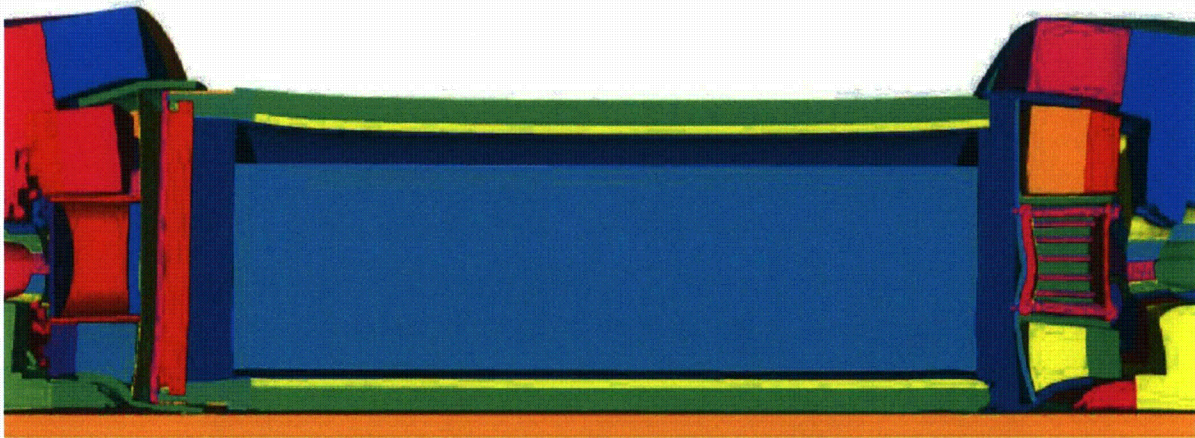


Figure III-11. Rail-Steel cask side impact at 193 KPH (120 MPH)

In the following sections the equivalent plastic strains in the welded inner canister are shown for each analysis case.

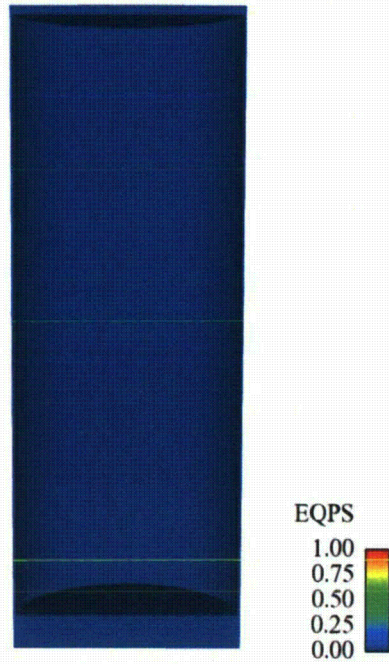


Figure III-12. Plastic strain in the interior welded canister of the Rail-Steel cask from the end impact at 48 KPH (30 MPH)

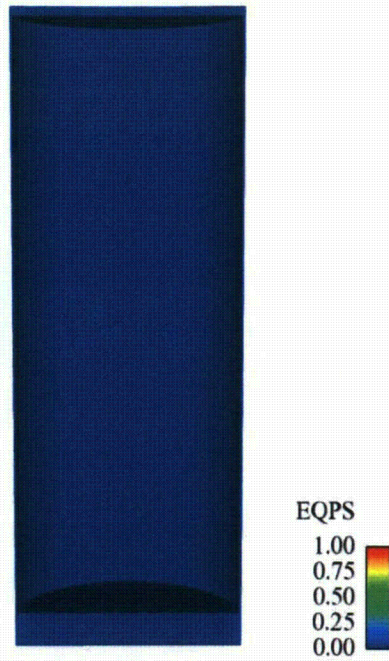


Figure III-13. Plastic strain in the interior welded canister of the Rail-Steel cask from the end impact at 97 KPH (60 MPH)

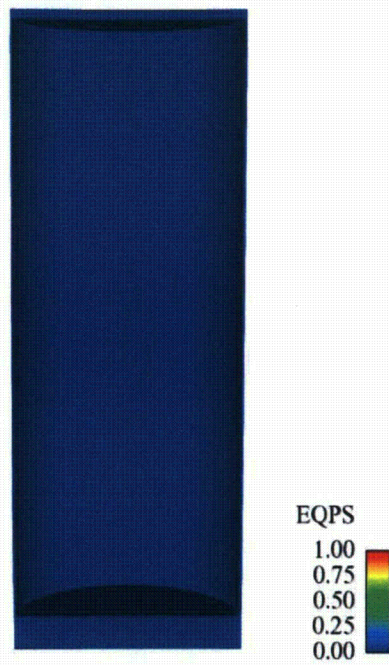


Figure III-14. Plastic strain in the interior welded canister of the Rail-Steel cask from the end impact at 145 KPH (90 MPH)

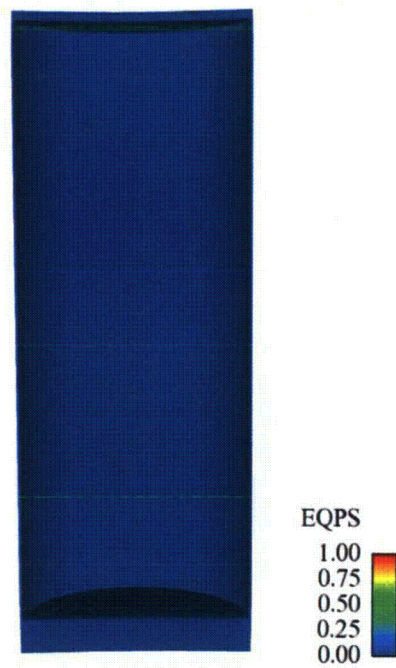


Figure III-15. Plastic strain in the interior welded canister of the Rail-Steel cask from the end impact at 193 KPH (120 MPH)



Figure III-16. Plastic strain in the interior welded canister of the Rail-Steel cask from the corner impact at 48 KPH (30 MPH)



Figure III-17. Plastic strain in the interior welded canister of the Rail-Steel cask from the corner impact at 97 KPH (60 MPH)



Figure III-18. Plastic strain in the interior welded canister of the Rail-Steel cask from the corner impact at 145 KPH (90 MPH)



Figure III-19. Plastic strain in the interior welded canister of the Rail-Steel cask from the corner impact at 193 KPH (120 MPH)



Figure III-20. Plastic strain in the interior welded canister of the Rail-Steel cask from the side impact at 48 KPH (30 MPH)



Figure III-21. Plastic strain in the interior welded canister of the Rail-Steel cask from the side impact at 97 KPH (60 MPH)

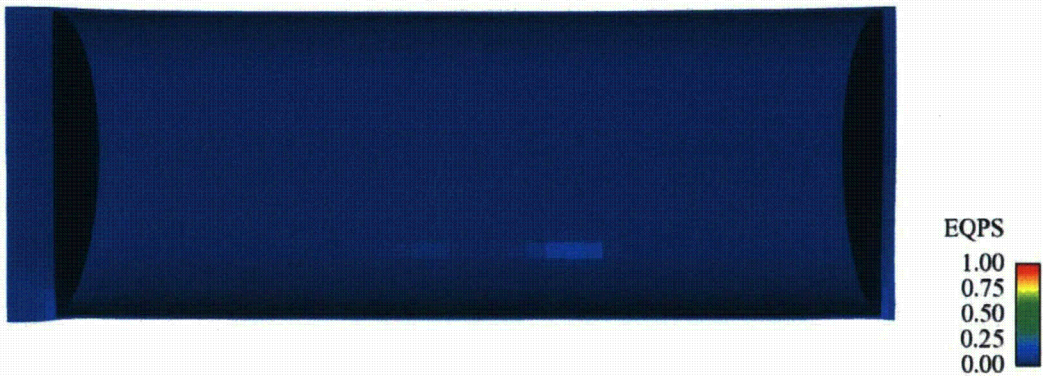


Figure III-22. Plastic strain in the interior welded canister of the Rail-Steel cask from the side impact at 145 KPH (90 MPH)



Figure III-23. Plastic strain in the interior welded canister of the Rail-Steel cask from the side impact at 193 KPH (120 MPH)

III.1.6 Acknowledgements

A number of people at Sandia contributed to the development of this model, including Jeff Smith, Bob Kalan, Lili Akin, and Chris Clutz. Nathan Crane was instrumental in finally getting it to run in Presto.

III.2 Finite Element Analysis of the Rail-Lead cask

III.2.1 Problem statement

Simulate impact of a loaded Rail-Lead cask onto an unyielding surface. Consider impact velocities of 48 kph (30 mph), 97 kph (60 mph), 145 kph (90 mph) and 193 kph (120 mph). Include end, side, and c.g. over corner impact orientations. Results will be used to assess integrity of the containment boundary and to estimate the extent of any possible breach. Estimate the deformation and failure of the lid closure bolts and any resulting gap between the lids and the cask. Also estimate the maximum lead slump distance.

III.2.2 Geometric Assumptions and Mesh

A finite element model of the Rail-Lead cask was developed for use with the Sierra Mechanics code Presto(SIERRA, 2009). Presto is a nonlinear transient dynamics finite element code developed at Sandia National Laboratories and used extensively for weapons qualification work. The finite element model was built primarily of hex elements. Shell elements used for the thin stainless steel skin that wraps around the impact limiters. The final half-symmetric model

consisted of 750000 elements. The drop event lasted approximately 0.5 seconds. The simulation of this drop event required approximately 36-60 hours of run time on 64 processors of the RedSky high performance computer at Sandia.

The model details are shown in Figures III-24 to III-27. Unlike the Rail-Steel cask, the basket in the NAC STC completely fills the internal space of the cask. There is the possibility of gaps between the individual fuel elements and the cask lid, but the probability of each of these fuel elements contacting the lid at the same time is very small, so no gap was included in the model.

Closure bolts were modeled with hex elements, with a minimum of 4 elements across the diameter of the bolt, as shown in Figure III-26.

The total weight of the cask was 247300 lbs.

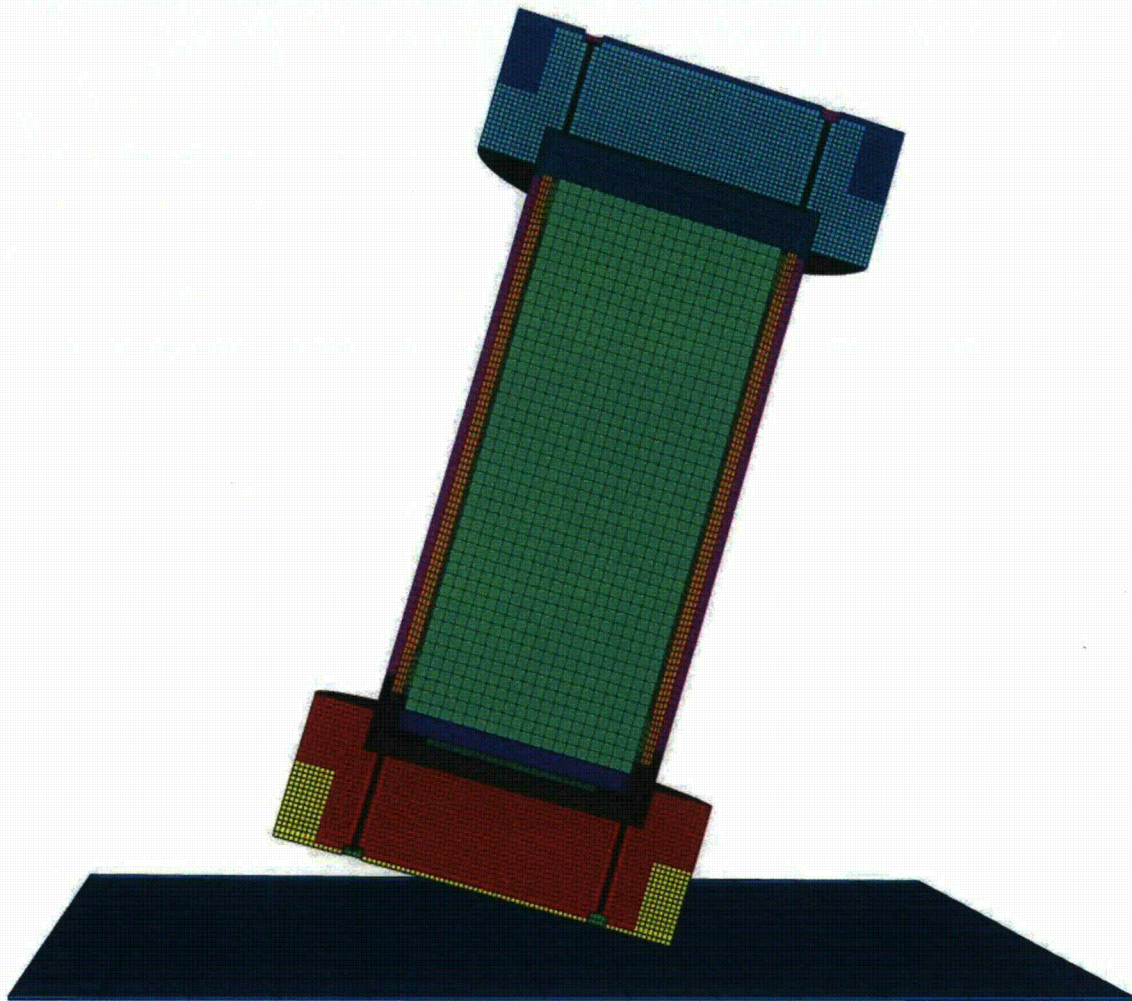


Figure III-24. Half-symmetric mesh of Rail-Lead cask

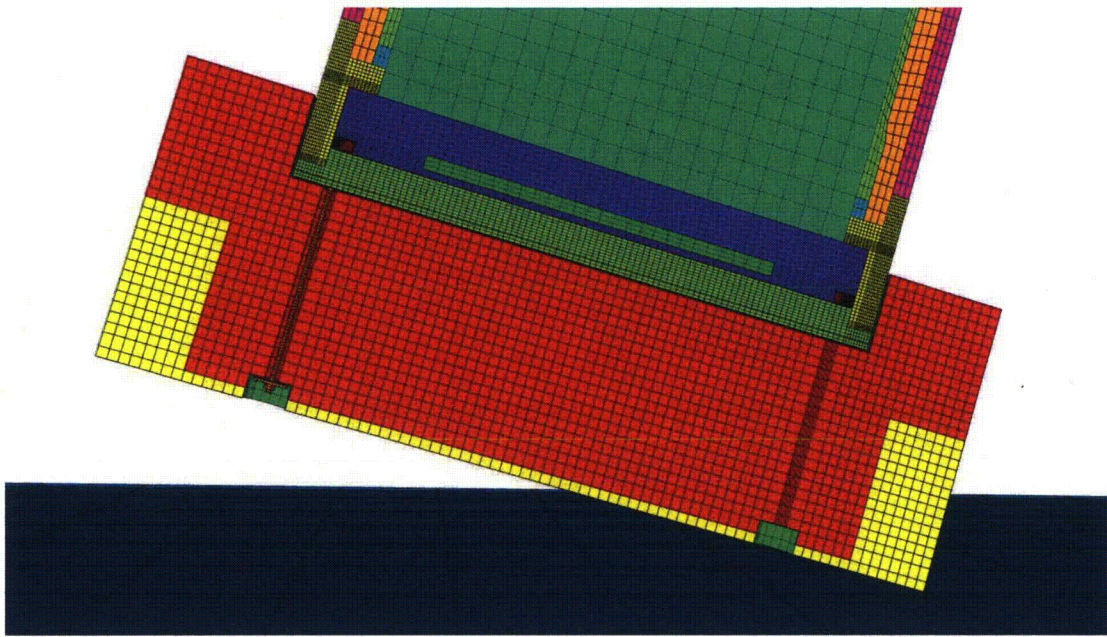


Figure III-25. Impact limiter mesh

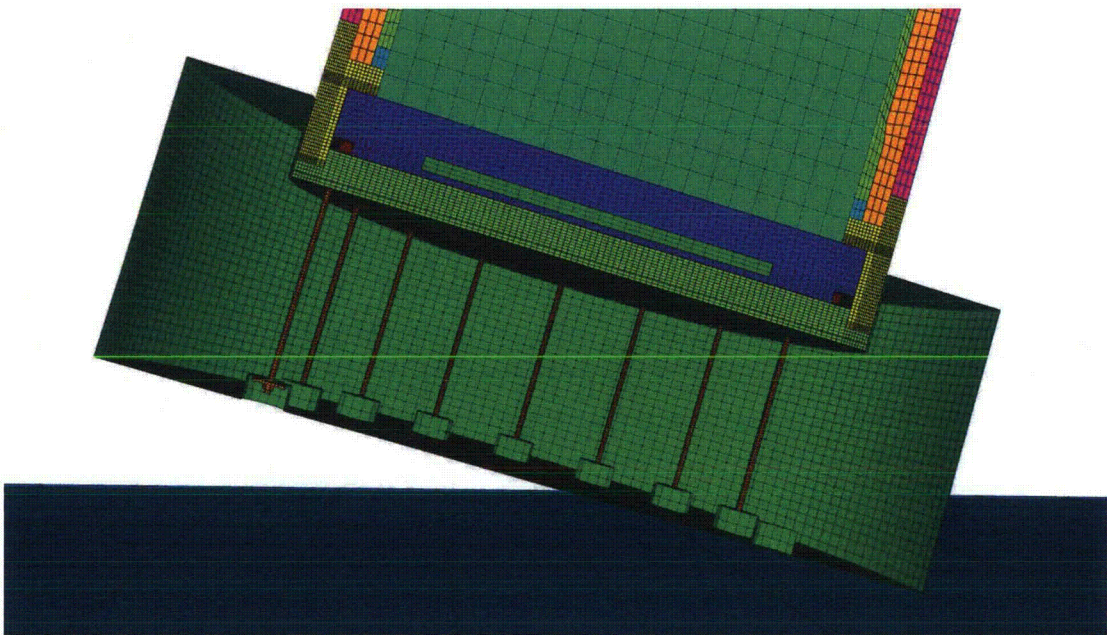


Figure III-26. Impact limiter mesh with wood removed

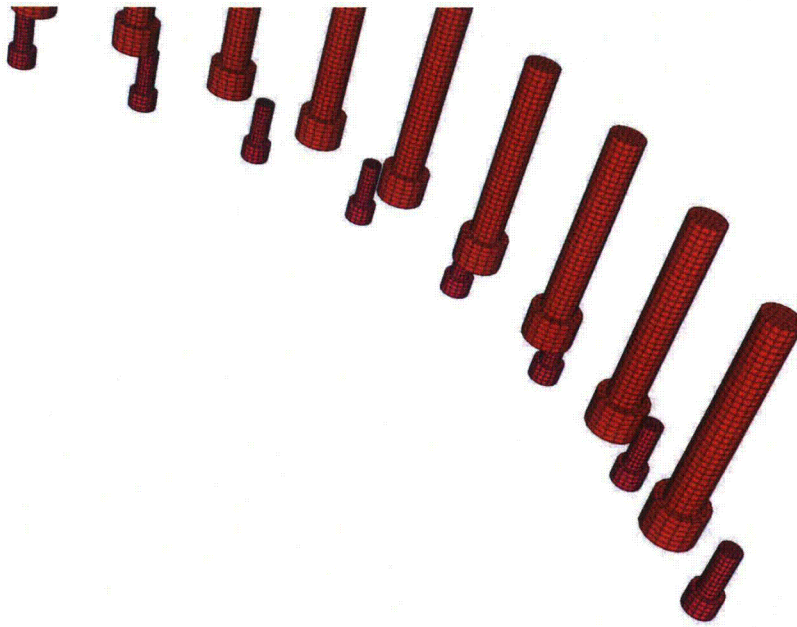


Figure III-27. Mesh of inner and outer lid closure bolts

The orientation of the model is important to the definition of orthotropic material properties. The cask model is oriented as shown in Figure III-27, and the impact direction is changed for the three impact conditions. For an end drop, the initial velocity is in the $-y$ direction. For a side drop, the initial velocity is in the $-x$ direction. And for a c.g. over corner drop, the initial velocity is in a $0.169912x - 0.98546y$ direction.

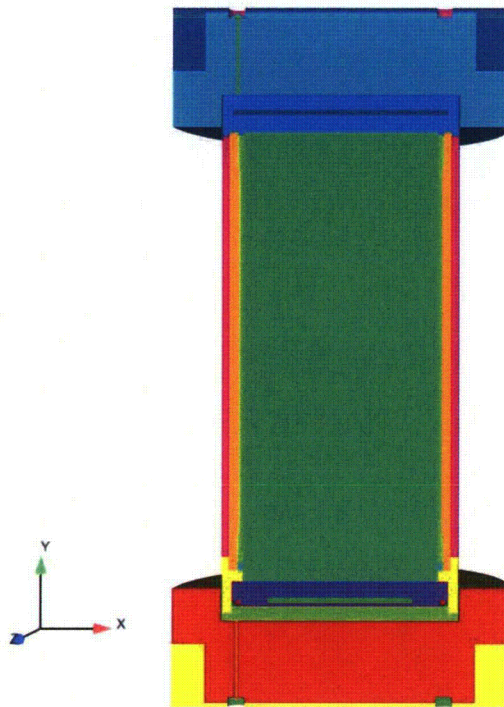


Figure III-28. Orientation of cask model for material property definitions

III.2.3 Material Properties

Material redwood

Used for top and bottom impact limiter

Density = 5.682×10^{-5} lb-s²/in⁴
 Material model orthotropic_crush
 Young's Modulus = 1.5×10^6 psi
 Poisson's Ratio = 0.3
 Yield Stress = 20000 psi
 Vmin=0.9
 Ex = 1.5×10^6 psi
 Ey = 0.3×10^6 psi
 Ez = 1.5×10^6 psi
 Gxy = 0.2×10^6 psi
 Gyz = 0.2×10^6 psi
 Gzx = 0.2×10^6 psi
 Crush xx = redwood_strong
 Crush yy = redwood_weak
 Crush zz = redwood_strong
 Crush xy = redwood_shear
 Crush yz = redwood_shear
 Crush zx = redwood_shear

Function redwood_strong

strain stress (psi)

0. 2000.

0.14 4200.

0.28 5100.

0.42 5430.

0.57 6100.

0.71 10100.

0.80 15000.

0.90 20000.

Function redwood_weak

strain stress (psi)

0. 400.

0.14 986.

0.28 1200.

0.42 1275.

0.57 1432.

0.71 2371.

0.80 3521.

0.90 4690.

Function redwood_shear

strain stress (psi)

0.0 1000.

0.60 1000.

0.70 10000.

0.90 10000.

Material balsa

Used for outer corner of top and bottom impact limiters

Density = $1.5e-5$ lb-s²/in⁴

Material model orthotropic_crush

Young's Modulus = $1.5e6$ psi

Poisson's Ratio = 0.3

Yield Stress = 20000 psi

Vmin = 0.9

Ex = $1.5e6$ psi

Ey = $0.3e6$ psi

Ez = $1.5e6$ psi

Gxy = $0.2e6$ psi

Gyz = $0.2e6$ psi

Gzx = $0.2e6$ psi

Crush xx = balsa_strong

Crush yy = balsa_weak

Crush zz = balsa_strong

Crush xy = balsa_shear

Crush yz = balsa_shear

Crush $\dot{\epsilon}$ = balsa_shear

Function balsa_strong
strain stress (psi)
0. 2000.
0.14 4200.
0.28 5100.
0.42 5430.
0.57 6100.
0.71 10100.
0.80 15000.
0.90 20000.

Function balsa_weak
strain stress (psi)
0. 400.
0.14 986.
0.28 1200.
0.42 1275.
0.57 1432.
0.71 2371.
0.80 3521.
0.90 4690.

Function balsa_shear
strain stress (psi)
0.0 1000.
0.60 1000.
0.70 10000.
0.90 10000.

Material 304_ss

Properties for 304 stainless steel were obtained from tensile tests conducted at Sandia National Labs.

Elastic values match Rail-Lead SAR (NAC, 2004), but complete response curve is used for plasticity.

Used for inner and outer cask wall, shell surrounding impact limiters, and impact limiter attachment bolts.

Density = $7.48e-4$ lb-s²/in⁴
Material model ml_ep_fail
Youngs Modulus = $28.0e6$ psi
Poissons Ratio = 0.27
Yield Stress = $33.0e3$ psi
Beta = 1.0
Youngs Modulus Function = 304_SS_YM
Poissons Ratio Function = 304_SS_PR
Yield stress Function = 304_SS_YS

Hardening Function = 304_SS_H
Critical Tearing Parameter = 7.779
Critical Crack Opening Strain = 0.20

Function 304_SS_H

strain stress (psi)

0.0	0.
0.0395	23.4e3
0.0782	34.9e3
0.1151	45.1e3
0.1509	54.0e3
0.1857	61.7e3
0.2197	68.5e3
0.2527	74.7e3
0.2848	80.5e3
0.3165	86.0e3
0.3470	91.2e3
0.3767	96.4e3
0.4077	101.5e3
0.4378	106.4e3
0.4690	111.4e3
0.5209	119.1e3
0.5797	128.4e3
0.6595	140.6e3
0.7520	156.5e3
0.8639	176.3e3
1.0129	204.2e3
1.2049	242.9e3
1.4476	298.5e3
1.7499	382.8e3
2.1246	519.1e3
2.5960	754.3e3
3.1689	1161.6e3
3.7371	1624.0e3
6.0	3465.5e3

Material filler

Used for internals

Density = $2.92e-4$ lb-s²/in⁴

Material model elastic

Youngs Modulus = 122.0e3 psi

Poissons Ratio = 0.30

Material 17 4 ss

Properties for 17-4 stainless steel were obtained from tensile tests conducted at Sandia National Labs.

Elastic values match Rail-Lead SAR (NAC, 2004), but complete response curve is used for plasticity.

Used for outer lid and outer lid bolts.

Density = $7.48e-4$ lb-s²/in⁴
Material model ml_ep_fail
Youngs Modulus = 28.0e6 psi
Poissons Ratio = 0.28
Yield Stress = 100000. psi
Beta = 1.0
Youngs Modulus Function = 304_SS_YM
Poissons Ratio Function = 304_SS_PR
Yield Stress Function = 304_SS_YS
Hardening Function = 17_4_SS_H
Critical Tearing Parameter = 10.0
Critical Crack Opening Strain = 0.20

Function 17_4_SS_H

strain	stress (psi)
0	100000.0
0.00407825	136477.69
0.00879119	153992.02
0.01402863	161193.41
0.01969711	164727.25
0.02677325	166808.60
0.03772328	168627.66
0.12541256	176332.05
0.24107482	183114.13
0.37338829	196318.29
0.51621765	212319.68
0.67105461	234527.78
0.84082846	261327.83
1.03088417	297249.64
1.24626188	344040.44
1.49347177	408459.72
1.78071924	499087.83
2.13871929	625460.64

Material SB637

Material SB-637 Grade N07718 Nickel Alloy Steel (NAC, 2004) used for inner lid bolts

Density = $7.324e-4$ lb-s²/in⁴
Material model elastic_plastic
Youngs Modulus = 2.9e7 psi
Poissons Ratio = 0.32
Yield Stress = 1.508e5
Hardening Modulus = 5.314e5 psi

Beta = 1.0

Material Pb

Lead (Hoffman and Attaway, 1991), used for mid cask wall

Density = $1.06e-3 \text{ lb-s}^2/\text{in}^4$
Material model elastic_plastic
Youngs Modulus = $2.0e6 \text{ psi}$
Poissons Ratio = 0.3
Yield Stress = $1700. \text{ psi}$
Hardening Modulus = $2000. \text{ psi}$
Beta = 1.

Material ns4fr

Solid synthetic polymer NS-4-FR used for neutron shielding inserts in top and bottom lids

The neutron shielding material was developed by BISCO Products, Inc. and is now supplied by Genden Engineering Services and Construction Company.

NS-4-FR is an epoxy resin that contains boron

Density = $1.571e-4 \text{ lb-s}^2/\text{in}^4$
Material model elastic
Youngs Modulus = $5.61e5$
Poissons Ratio = 0.3

III.2.4 Criteria for Element Death

To account for instability in the orthotropic crush material model, elements are removed from the mesh if the following condition occurs, stated in the Presto (SIERRA, 2009) element death convention.

Criterion is max nodal value of velocity(1) > 20000
Criterion is max nodal value of velocity(2) > 20000
Criterion is max nodal value of velocity(3) > 20000
Criterion is max nodal value of velocity(1) < -20000
Criterion is max nodal value of velocity(2) < -20000
Criterion is max nodal value of velocity(3) < -20000
Death on inversion = on

For the impact limiter attachment bolts, elements failure is defined according to Presto convention. This means that failure occurs when the critical tearing parameter (Wellman and Salzbrenner, 1992) is reached, as defined for 304 stainless steel.

Material criterion = ml_ep_fail

Failure of the outer lid and outer lid bolts was defined according to Presto convention when a maximum value of eqps was reached in 17-4 stainless steel. This value of eqps was established

using an analysis of a tensile test specimen, and defining failure at the true strain that corresponds to the true stress approximately midway between the true stress at maximum load and the final true stress. The conservative value was chosen to compensate for the relatively coarse mesh in the bolt.

Criterion is element value of eqps > 1.5

Failure of the inner lid bolts was defined according to Presto convention when a maximum value of eqps was reached in SB-637 Grade N07718 Nickel Alloy Steel.

Criterion is element value of eqps > 0.1

III.2.5 Analysis Results

The deformed shape of the cask following each impact analysis is presented below.

Time = 0.03480

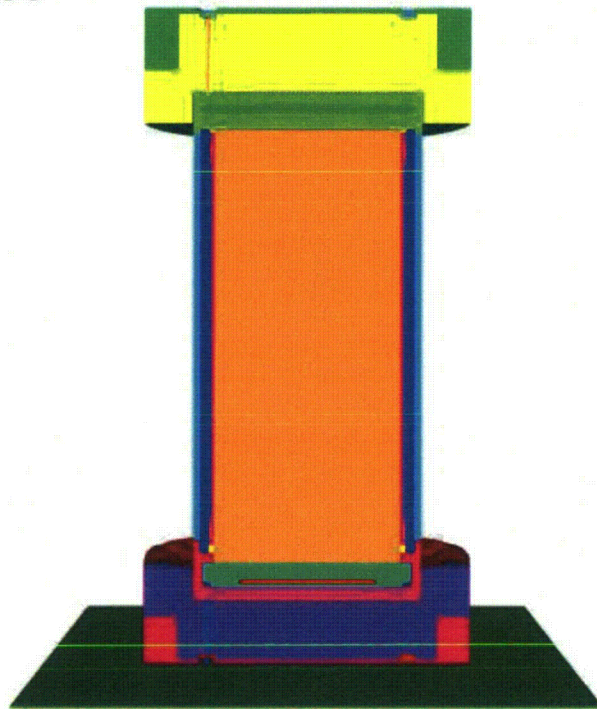


Figure III-29. Rail-Lead cask end impact at 48 KPH (30 MPH)

Time = 0.03480

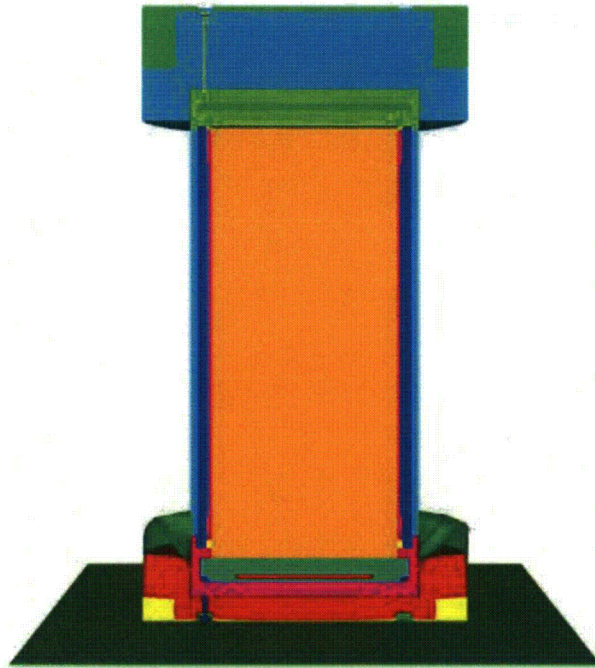


Figure III-30. Rail-Lead cask end impact at 97 KPH (60 MPH)

Time = 0.03480

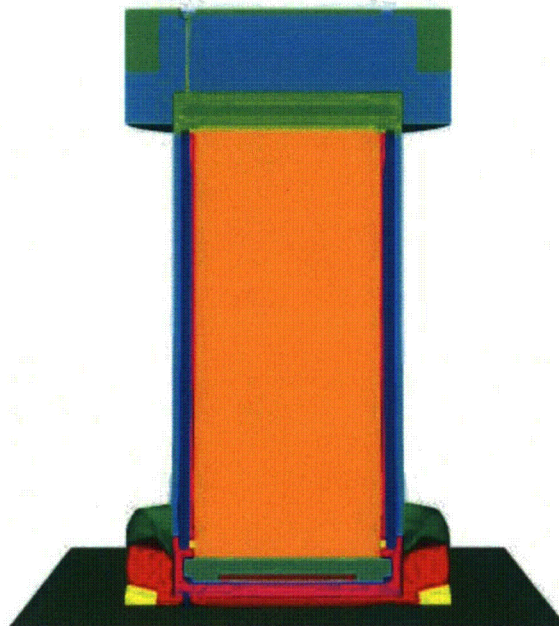


Figure III-31. Rail-Lead cask end impact at 145 KPH (90 MPH)

Time = 0.03480

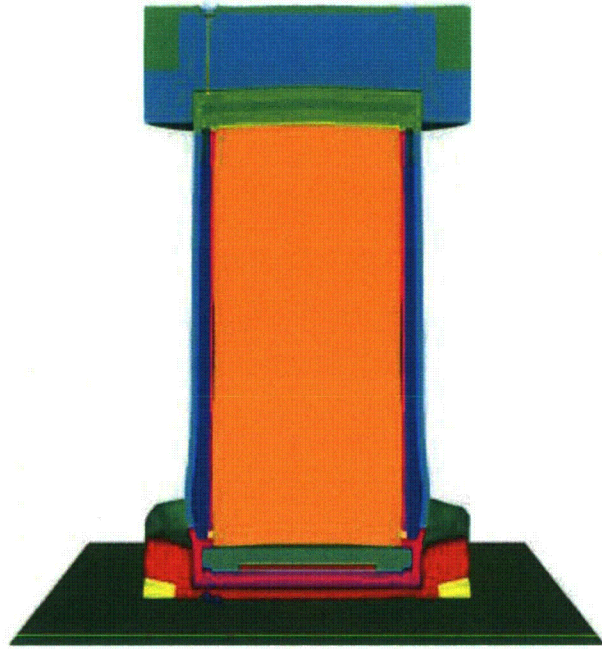


Figure III-32. Rail-Lead cask end impact at 193 KPH (120 MPH)

Time = 0.06420

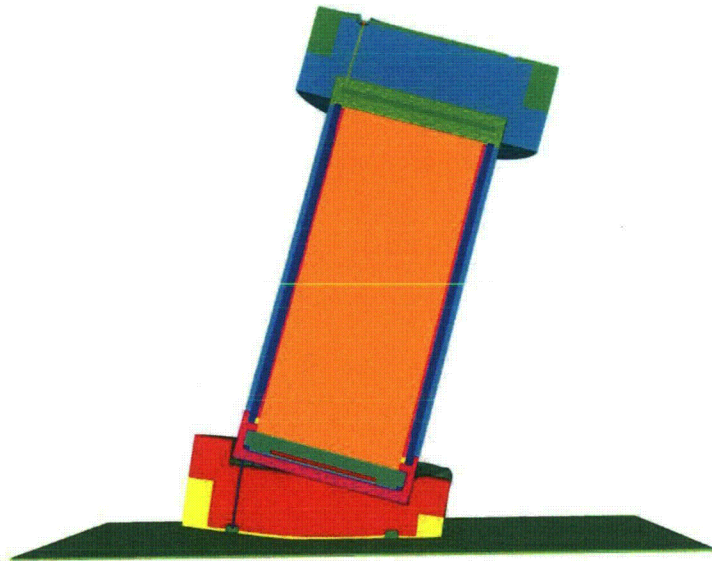


Figure III-33. Rail-Lead cask corner impact at 48 KPH (30 MPH)

Time = 0.05040

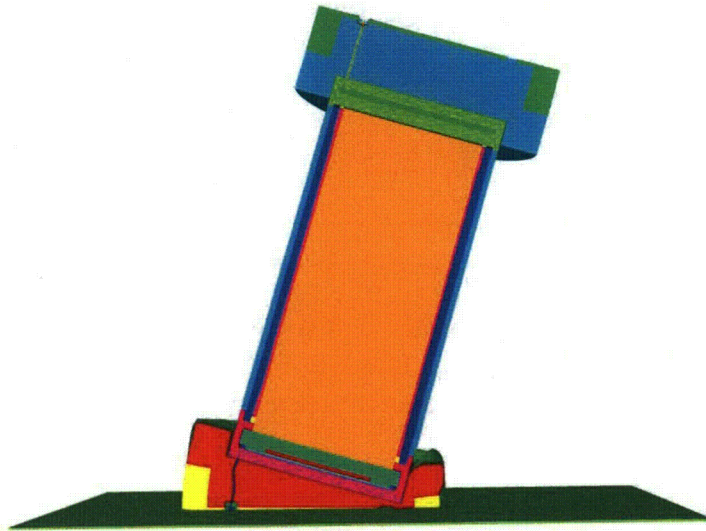


Figure III-34. Rail-Lead cask corner impact at 97 KPH (60 MPH)

Time = 0.03500

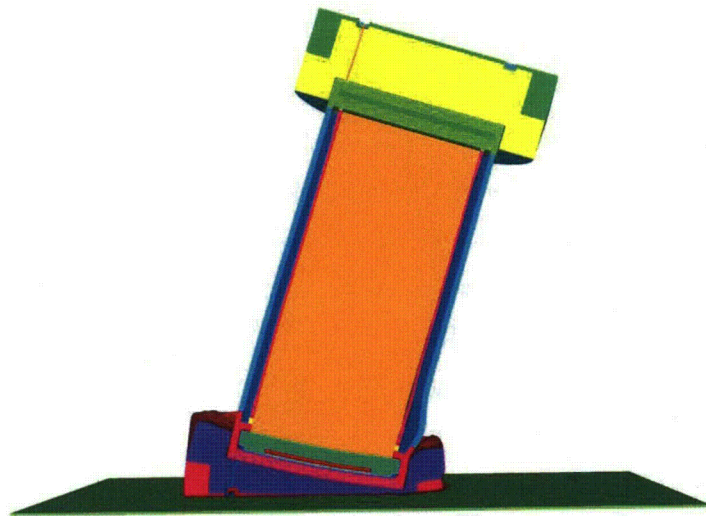


Figure III-35. Rail-Lead cask corner impact at 145 KPH (90 MPH)

Time = 0.03500

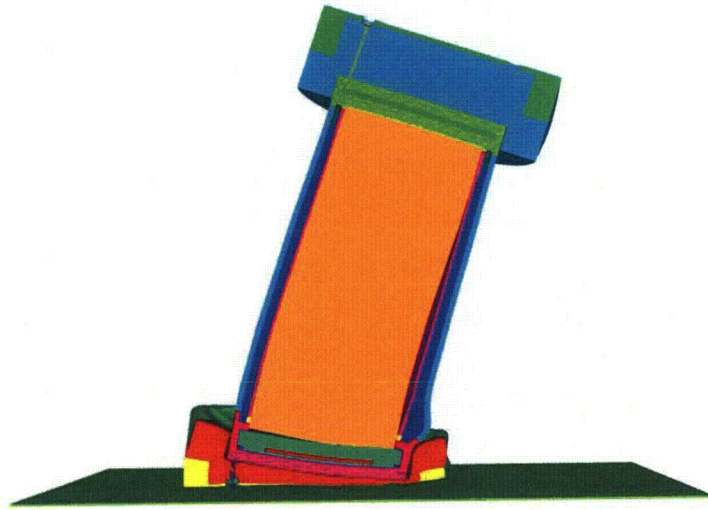


Figure III-36. Rail-Lead cask corner impact at 193 KPH (120 MPH)

Time = 0.03000



Figure III-37. Rail-Lead cask side impact at 48 KPH (30 MPH)

Time = 0.03000

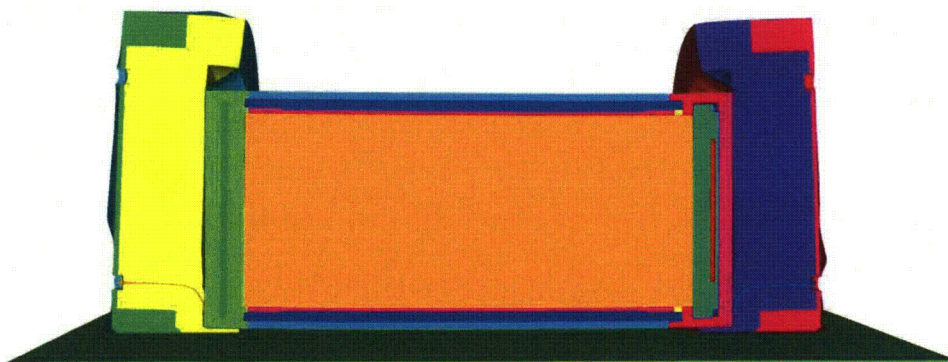


Figure III-38. Rail-Lead cask side impact at 97 KPH (60 MPH)

Time = 0.02400

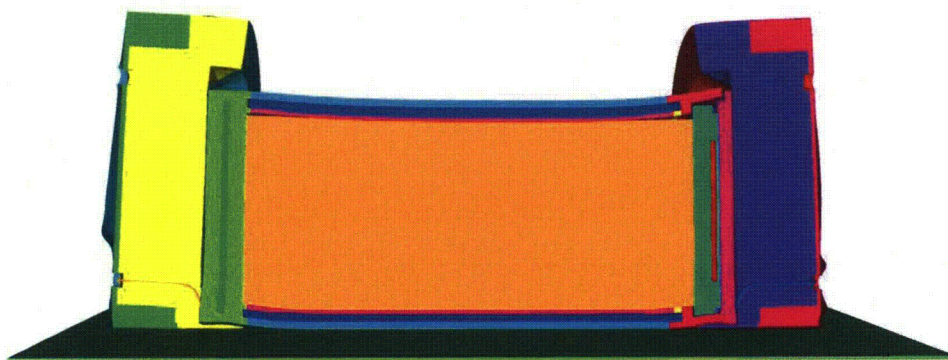


Figure III-39. Rail-Lead cask side impact at 145 KPH (90 MPH)

Time = 0.01800



Figure III-40. Rail-Lead cask side impact at 193 KPH (120 MPH)

III.2.6 Determination of Lid Gaps

Possible gaps between the lids and the cask were extracted from the final drop results. The longitudinal orientation of the cask was along the y-direction, so the difference in y-direction displacement between the lid and the cask gave a measure of the gap. A node on the cask was paired with the nearest node on the lid for this gap calculation. The nodes did not align exactly in the xz plane. Two gap values were calculated for the end drop orientation since the deformations were axisymmetric. For side down and cg over corner orientations, gap values were calculated at 5 equally spaced locations around the half-circumference of the cask, as shown in Figures III-41 to III-43.

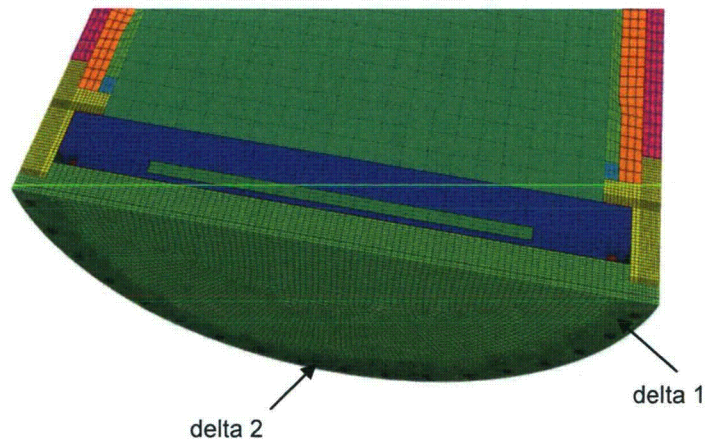


Figure III-41. Gap opening locations for end impact orientation

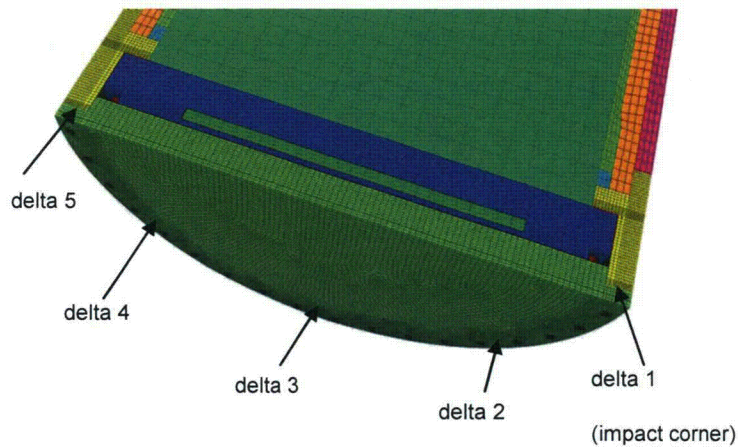


Figure III-42. Gap opening locations for corner impact orientation

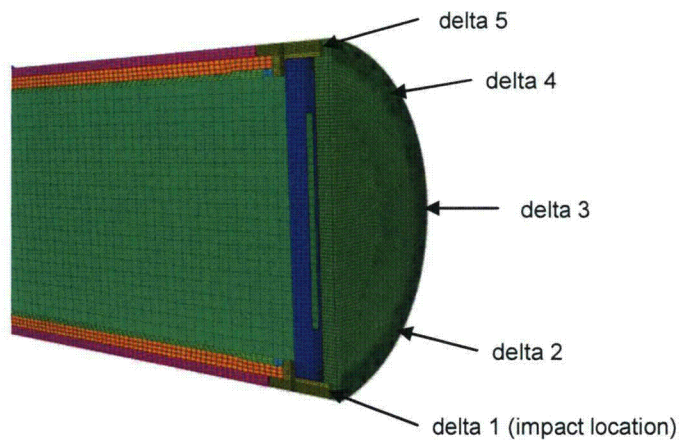


Figure III-43. Gap opening locations for side impact orientation

The next set of figures show plots of the gap sizes as a function of time for the inner and outer lid for each analysis case. All of the gaps calculated are somewhat conservative because the bolts did not include any pre-load. Pre-load decreased the gap size because the bolts do not start to elongate until the pre-load is overcome. As an example, if the 7.1-inch long inner lid bolts are pre-loaded to 50% of their yield strength ($0.5 \times 150.8 = 75.4$ ksi) the elastic elongation is 0.018 inches. This indicates the calculated gap for the inner lid is probably overestimated by this amount.

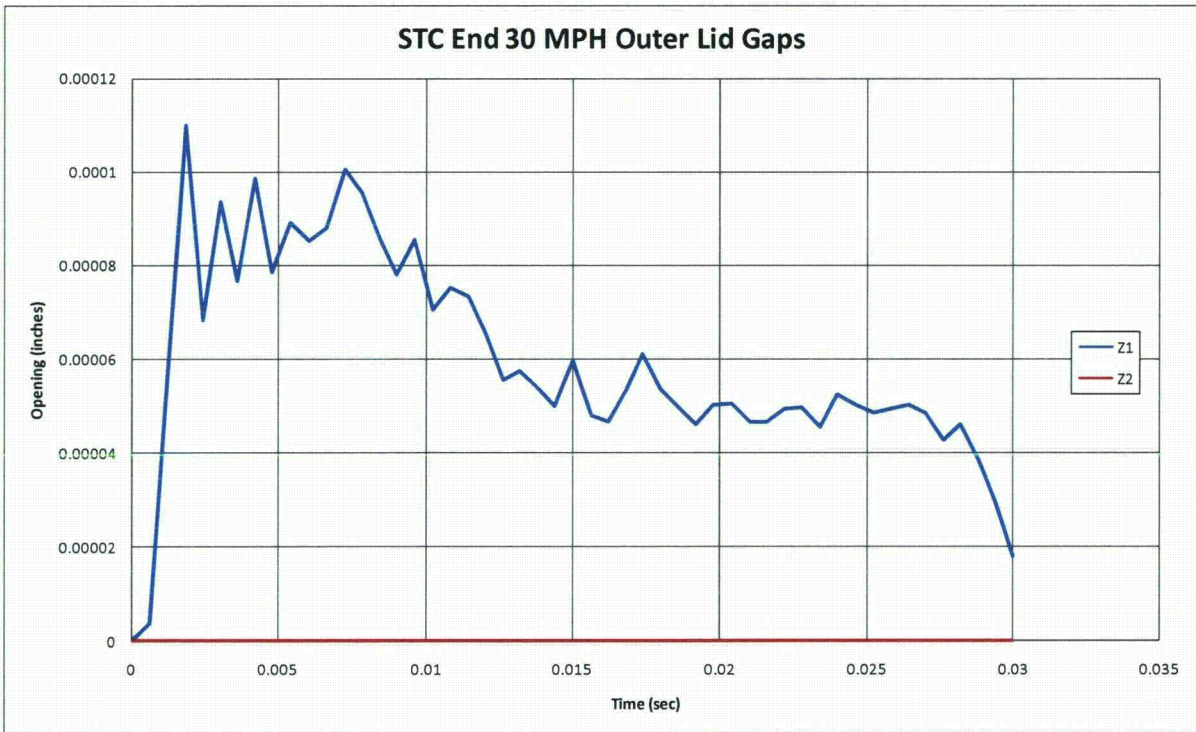


Figure III-44. Gaps in the inner and outer lids of the Rail-Lead cask from the end impact at 48 KPH (30 MPH)

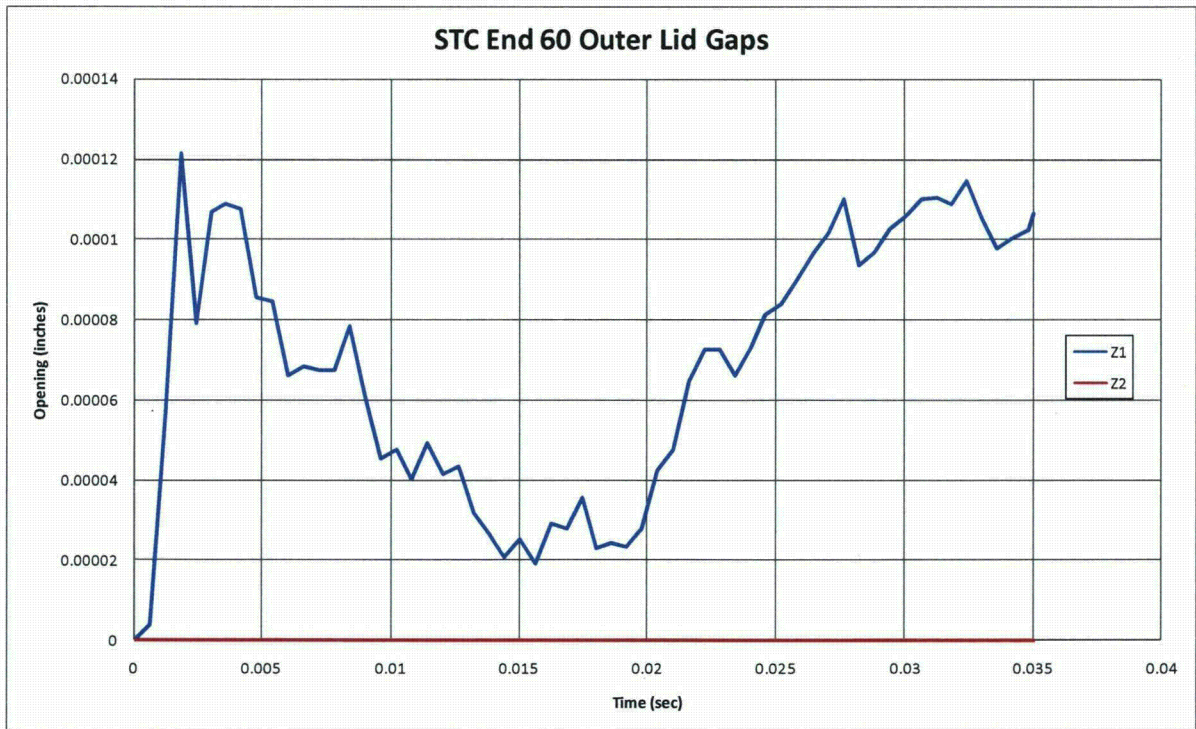
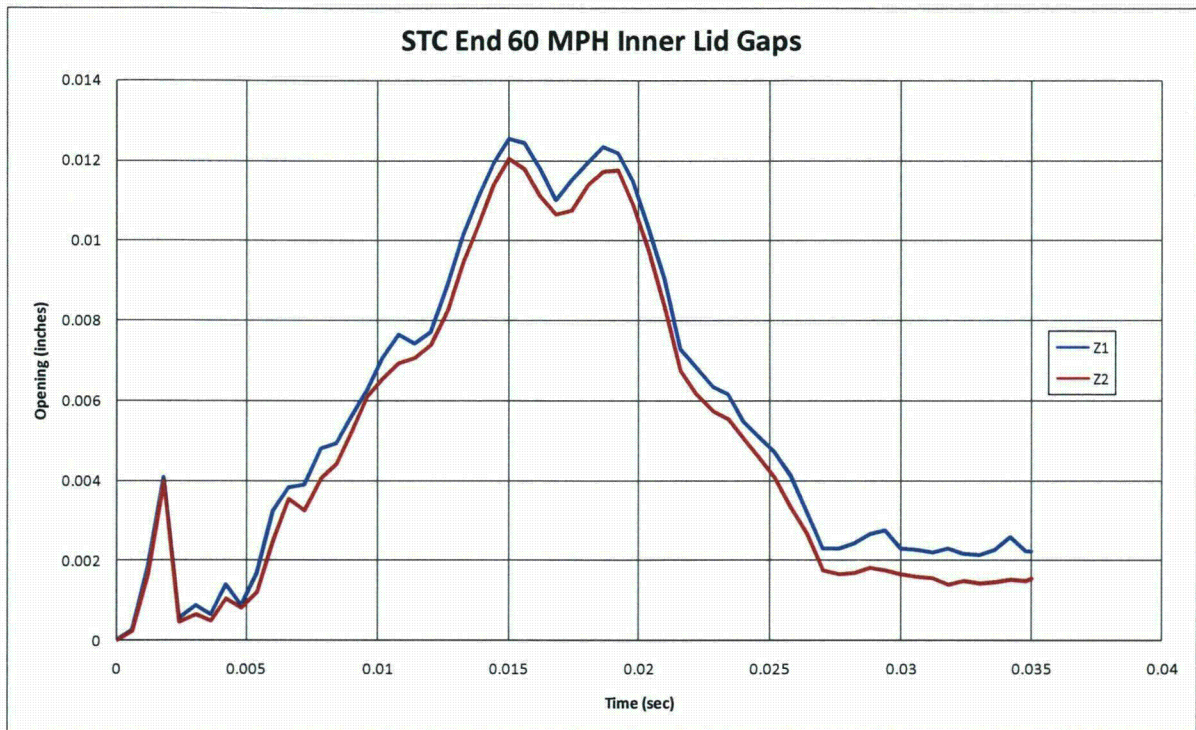


Figure III-45. Gaps in the inner and outer lids of the Rail-Lead cask from the end impact at 97 KPH (60 MPH)



Figure III-46. Gaps in the inner and outer lids of the Rail-Lead cask from the end impact at 145 KPH (90 MPH)

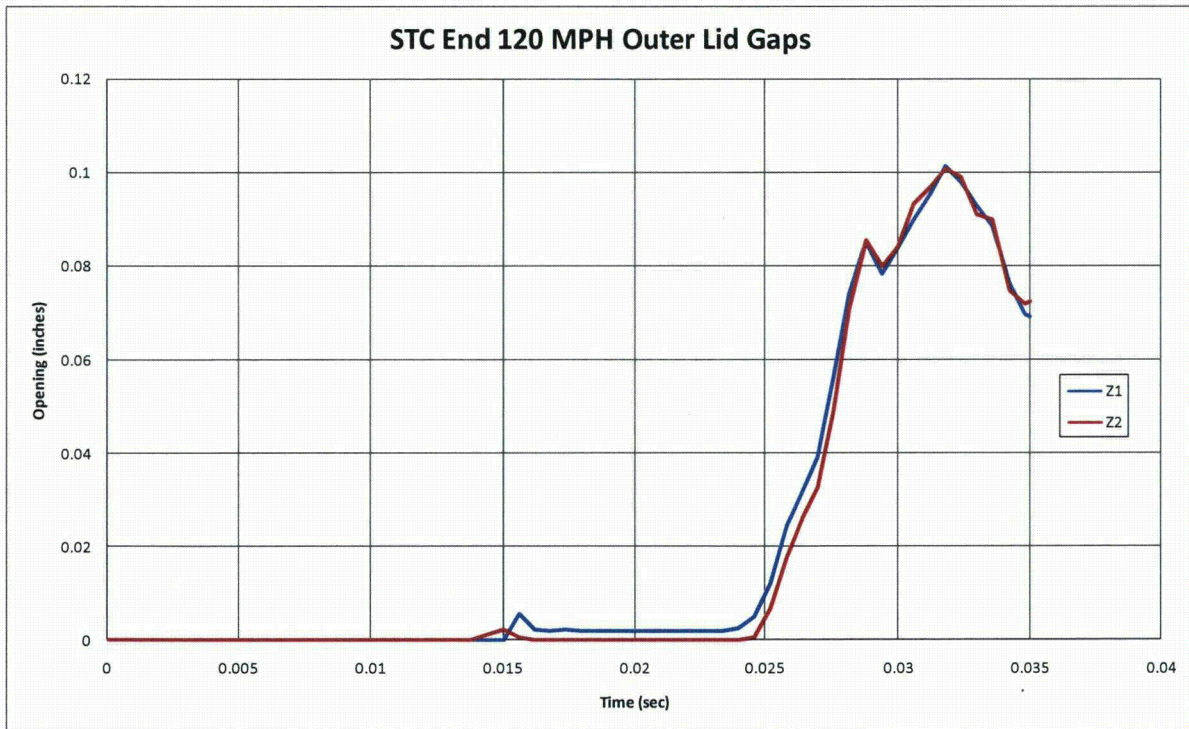


Figure III-47. Gaps in the inner and outer lids of the Rail-Lead cask from the end impact at 193 KPH (120 MPH)

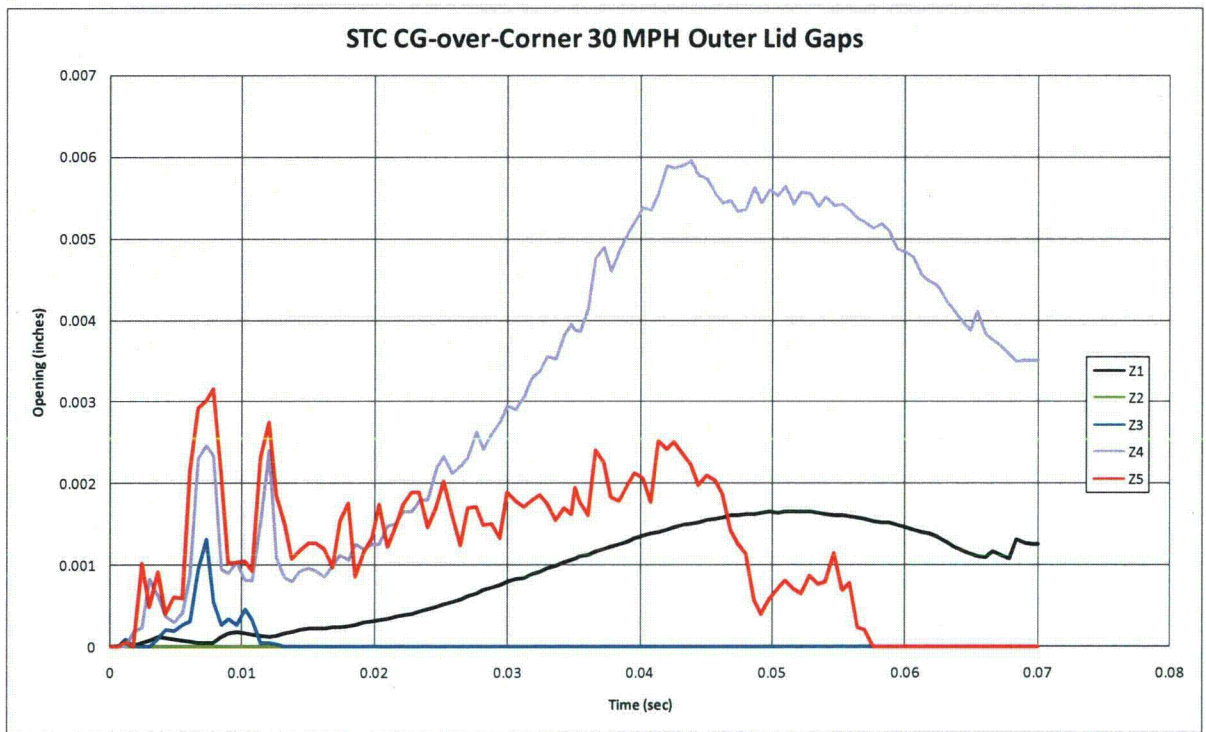
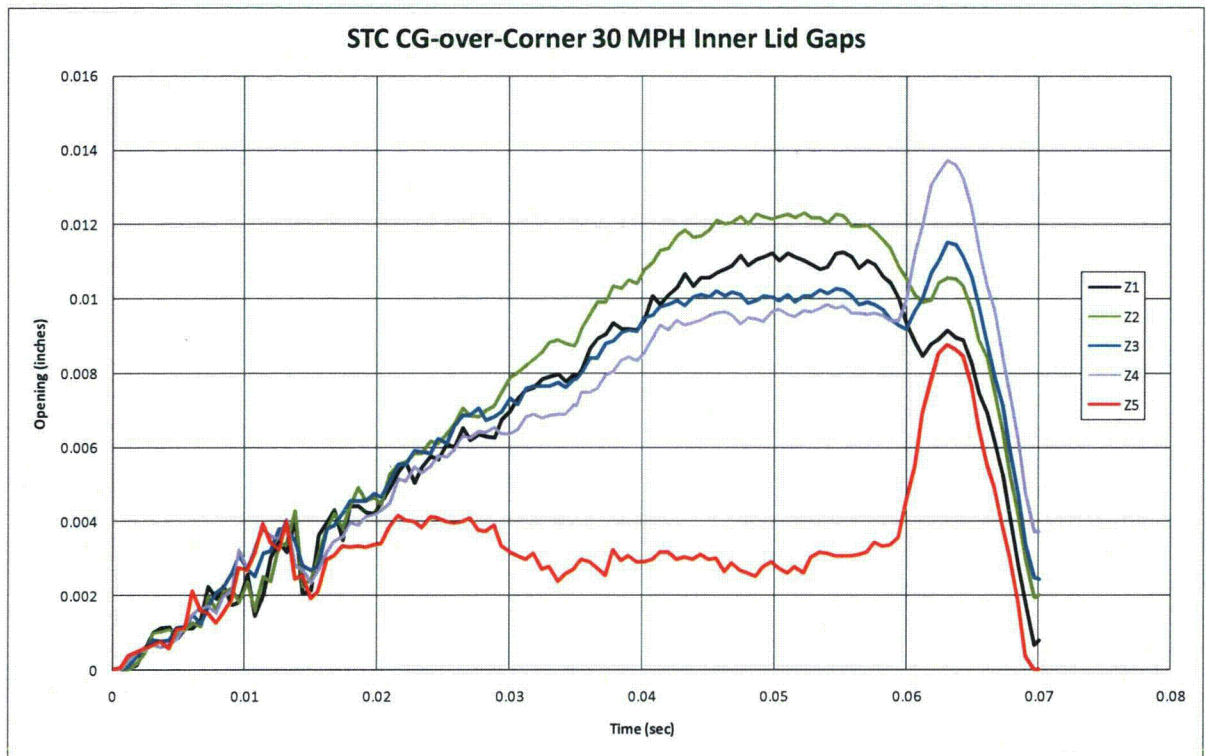


Figure III-48. Gaps in the inner and outer lids of the Rail-Lead cask from the corner impact at 48 KPH (30 MPH)

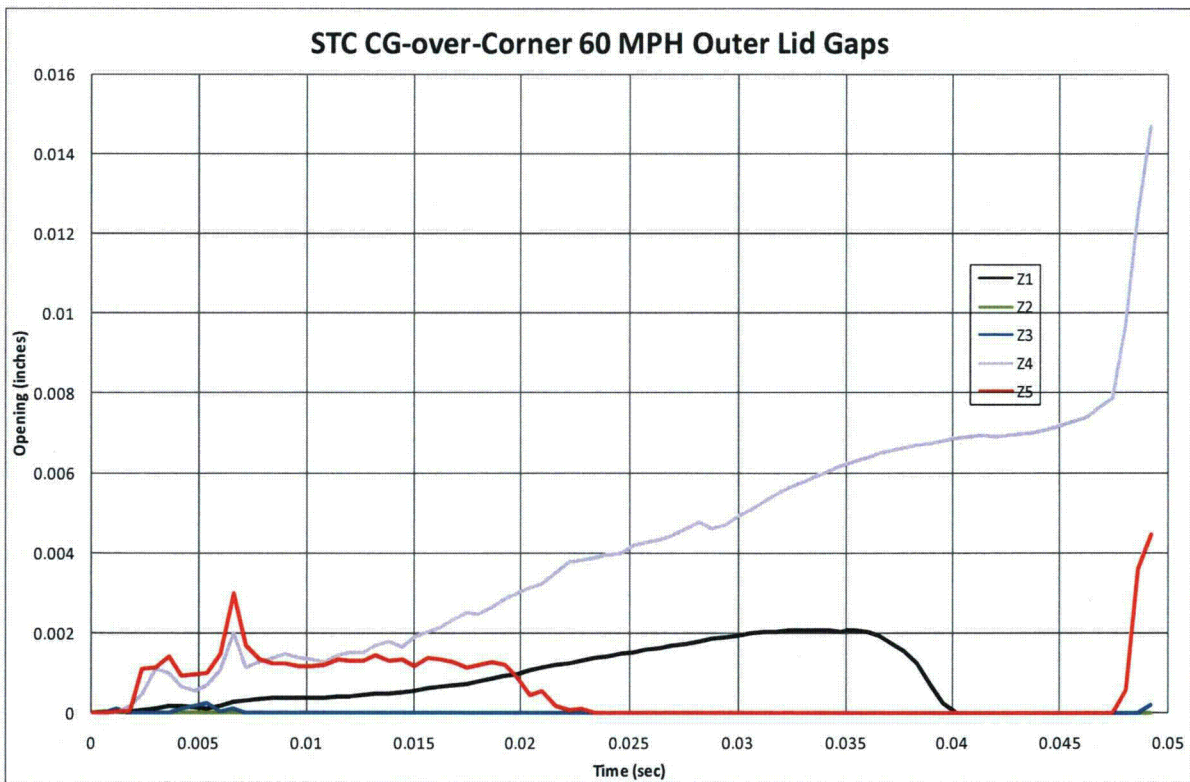
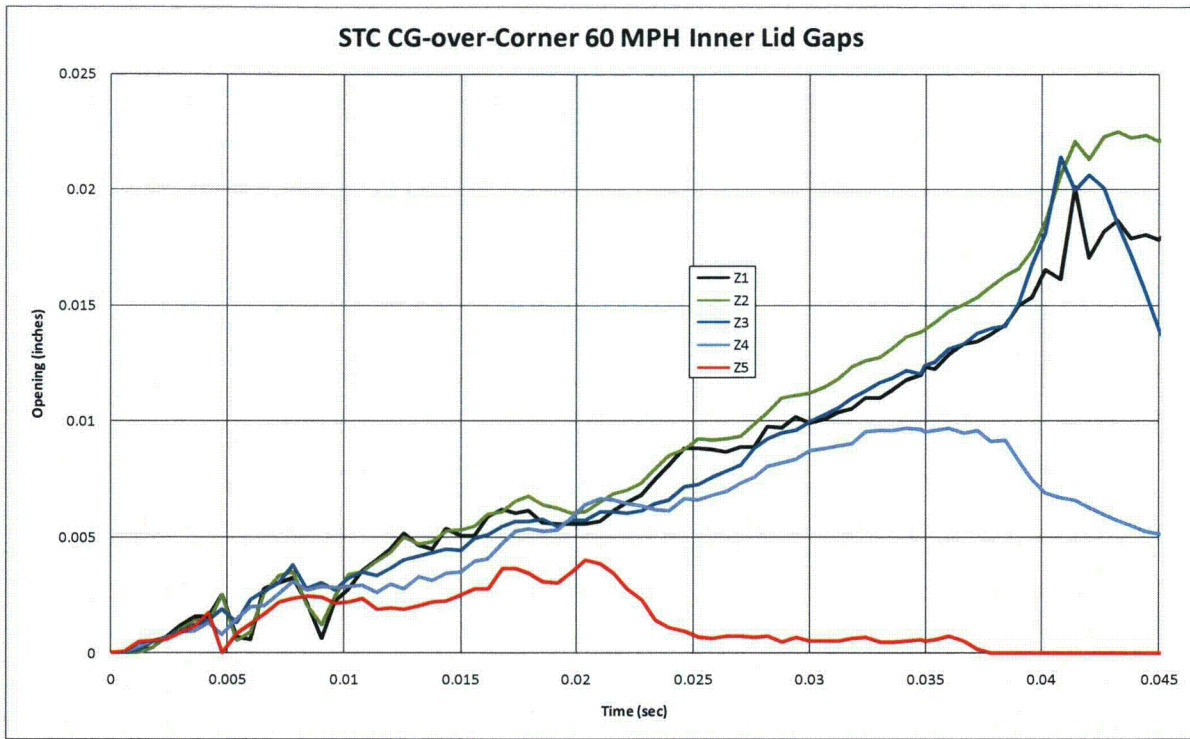


Figure III-49. Gaps in the inner and outer lids of the Rail-Lead cask from the corner impact at 97 KPH (60 MPH)

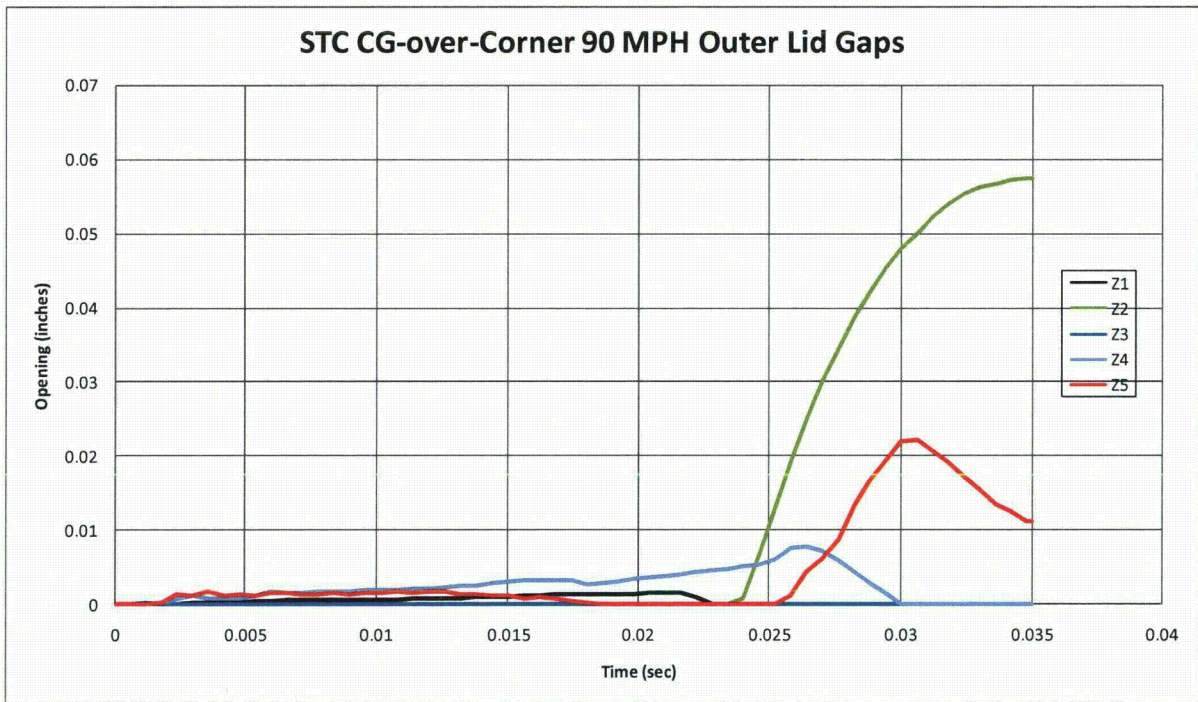
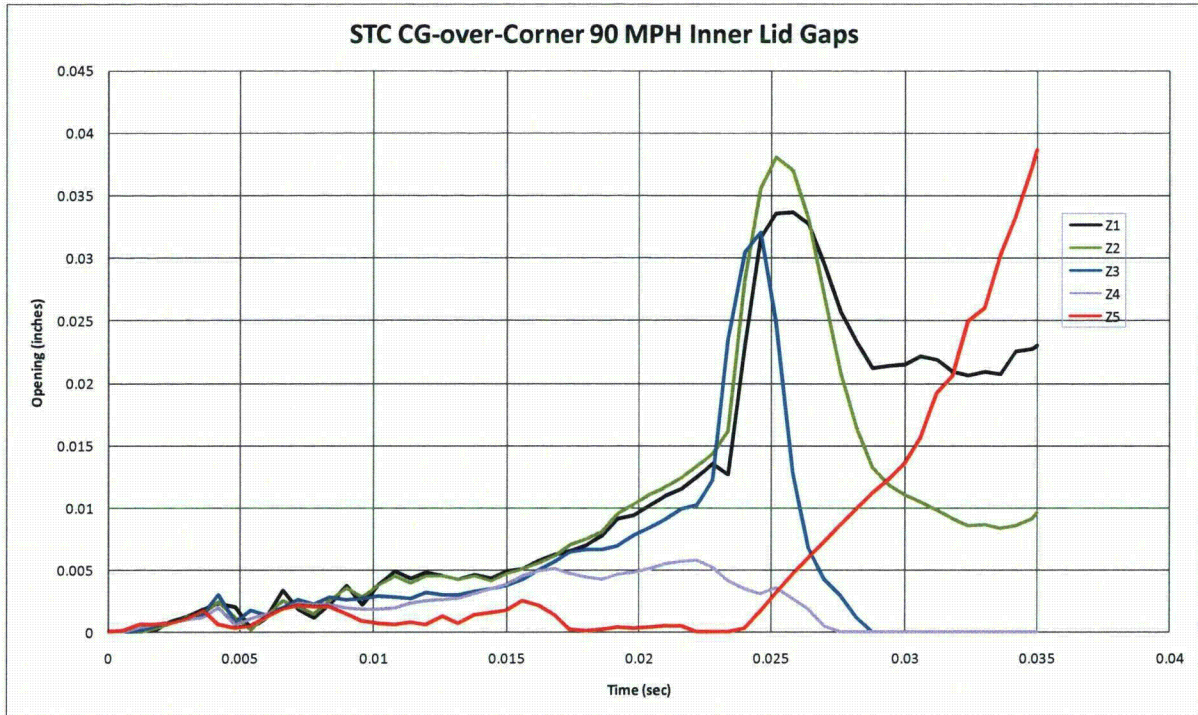


Figure III-50. Gaps in the inner and outer lids of the Rail-Lead cask from the corner impact at 145 KPH (90 MPH)

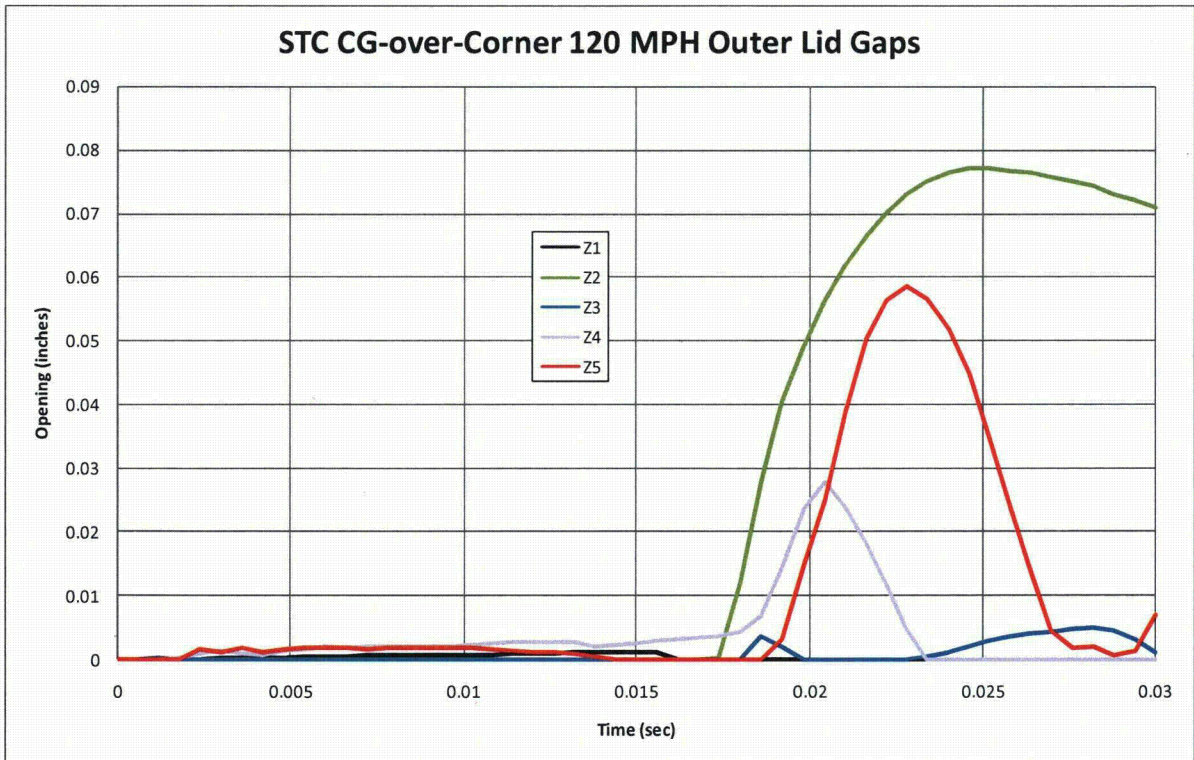
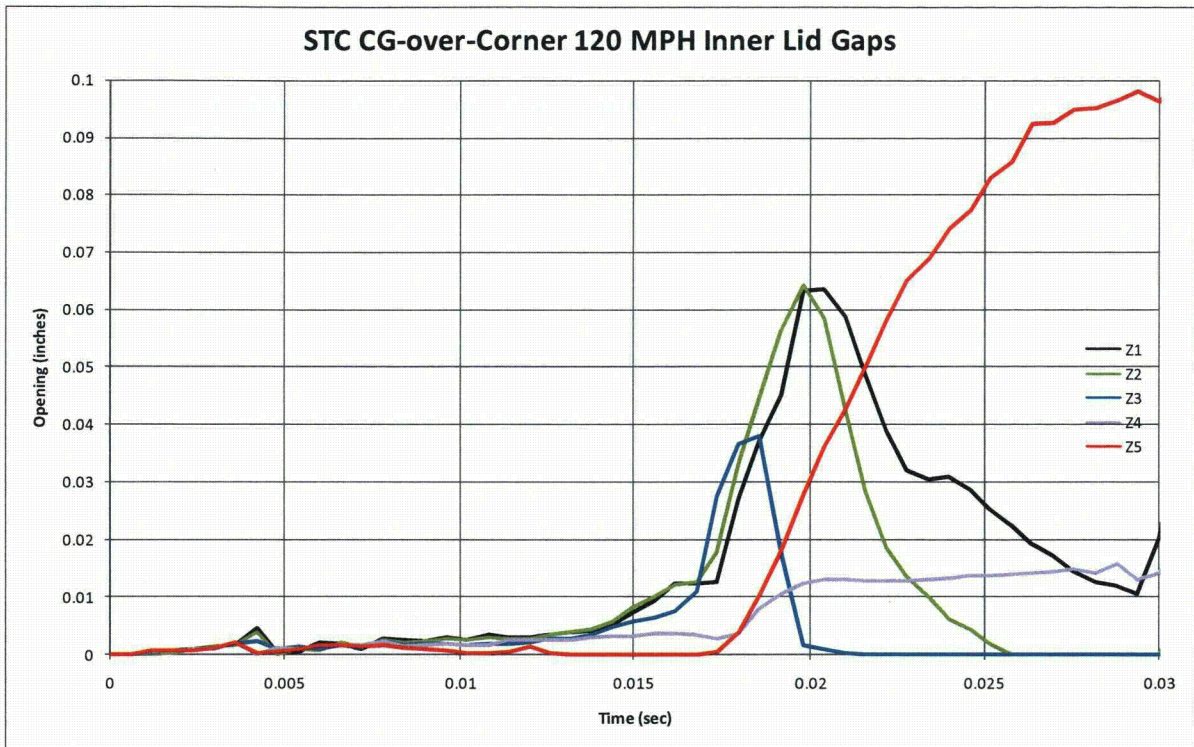


Figure III-51. Gaps in the inner and outer lids of the Rail-Lead cask from the corner impact at 193 KPH (120 MPH)

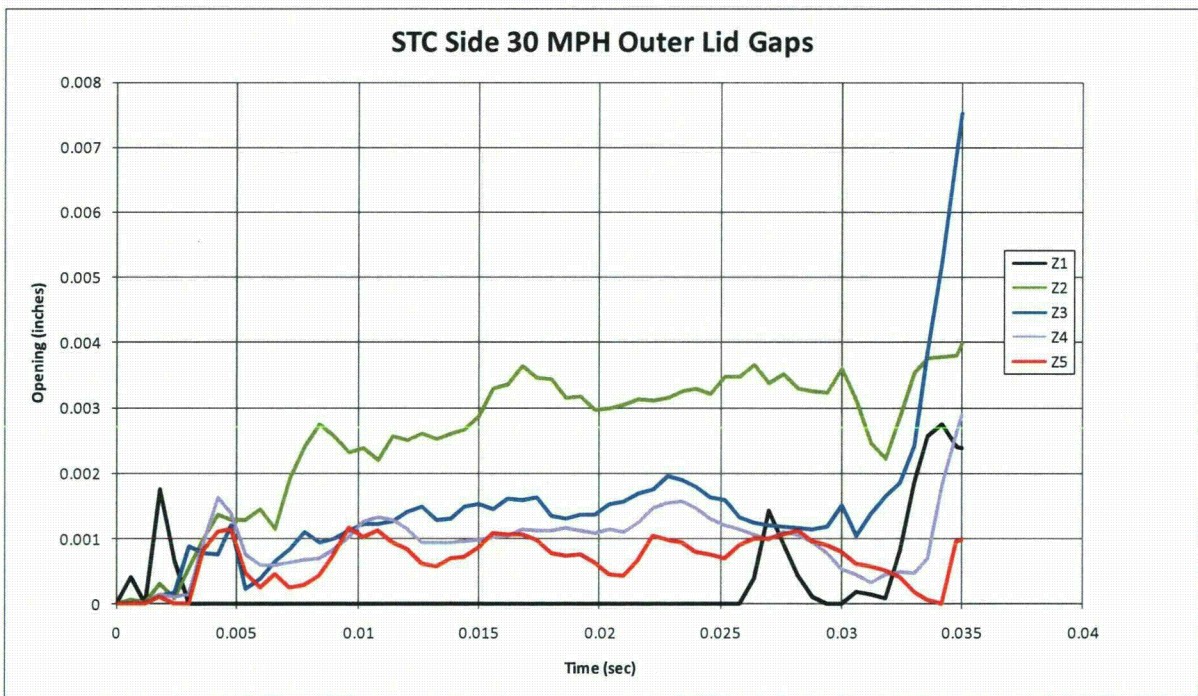


Figure III-52. Gaps in the inner and outer lids of the Rail-Lead cask from the side impact at 48 KPH (30 MPH)

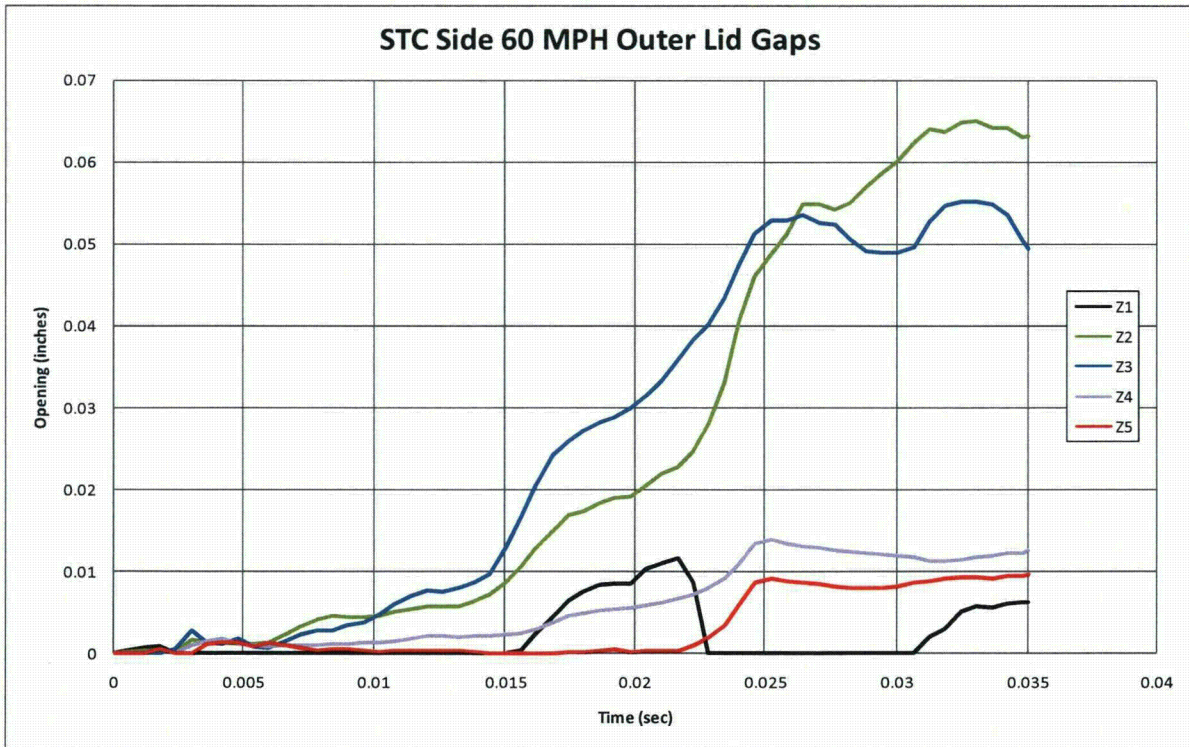
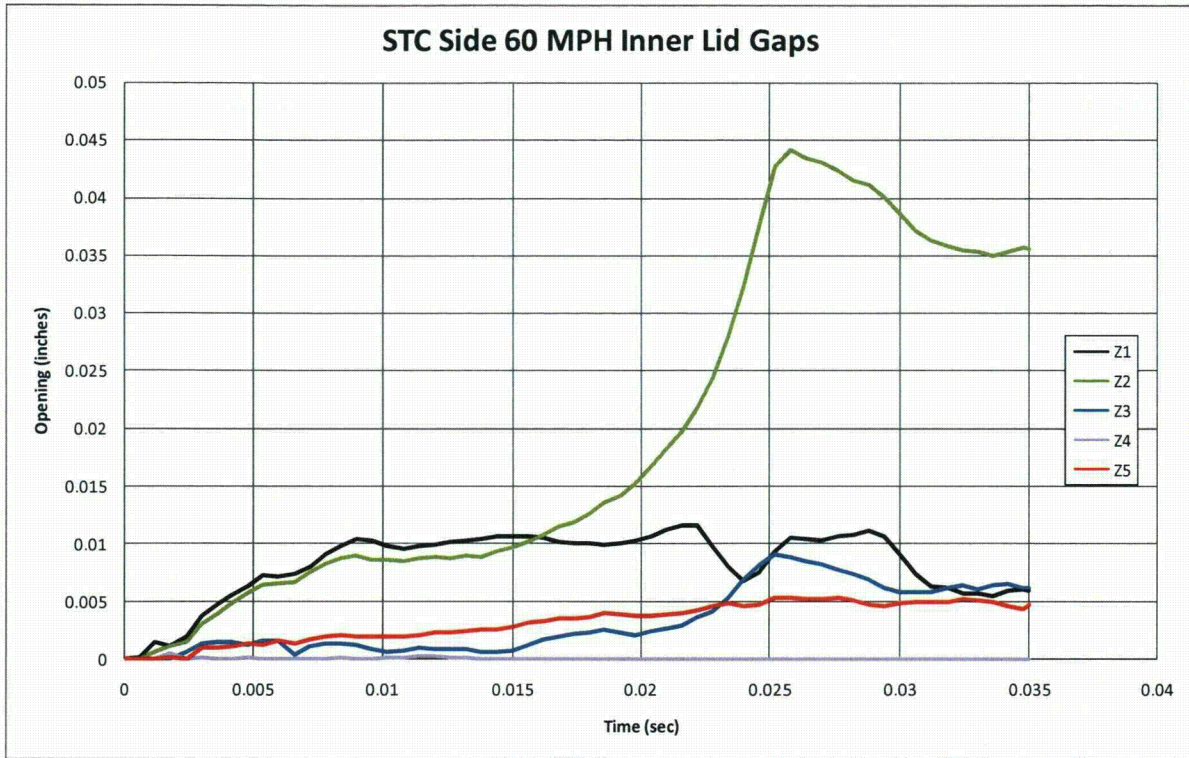


Figure III-53. Gaps in the inner and outer lids of the Rail-Lead cask from the side impact at 97 KPH (60 MPH)

To calculate any leak size based upon the gaps the compliance of the o-rings had to be taken into account. The Rail-Lead cask can be sealed with either elastomeric o-rings or metallic o-rings. Elastomeric o-rings can typically maintain a seal when the opening between the mating surfaces opens by 2.5 mm (0.10 in.), and this number is used as the compliance for the cases with elastomeric o-rings. Metallic o-rings are much less tolerant to gaps, and a value of 0.25 mm (0.010 in.) is used as the compliance for the cases with metallic o-rings. For the end impact analyses the gap size is uniform for the entire circumference of the seal, and the hole size is calculated by subtracting the compliance of the o-ring from the gap and multiplying by the circumference. If either the inner seal or the outer seal has a gap less than the compliance, then there is no leak area. For end impacts the only case where there is any leakage is for the 193 KPH (120 MPH) impact with metallic o-rings.

For the corner and side impacts the amount of gap varies around the circumference of the seal, and a more complicated algorithm is needed to calculate the hole size. As in the end impact, the compliance of the seal is subtracted from the gap and a trapezoidal area between measurement locations is assumed. In the corner impact, none of the gaps is large enough to overcome the compliance of elastomeric o-rings, but there would be some leakage for the 97, 145, and 193 KPH (60, 90, and 120 MPH) impacts. The calculated hole sizes for these three cases are 65, 599, and 1716 mm², respectively. In the side impact at 97 KPH (60 MPH) the gaps are not sufficient to cause a leakage with elastomeric seals, but with metallic seals a hole size of 799 mm² is calculated. In the 145 and 193 KPH (90 and 120 MPH) analyses there are a number of failed bolts and very large openings between the lids and the cask body. In these cases both the elastomeric and metallic seals fail and the resulting hole size is more than 10,000 mm². Table III-1 gives the final gap and hole sizes for each of the analyses.

Table III-1. Available areas for leakage from the Rail-Lead cask

Orientation	Speed (KPH)	Location	Lid Gap (mm)	Seal Type	Hole Size (mm ²)
End	48	Inner	0.226	Metal	none
		Outer	0	Elastomer	none
	97	Inner	0.056	Metal	none
		Outer	0.003	Elastomer	none
	145	Inner	2.311	Metal	none
		Outer	0.047	Elastomer	none
	193	Inner	5.588	Metal	8796
		Outer	1.829	Elastomer	none
Corner	48	Inner	0.094	Metal	none
		Outer	0.089	Elastomer	none
	97	Inner	0.559	Metal	65
		Outer	0.381	Elastomer	none
	145	Inner	0.980	Metal	599
		Outer	1.448	Elastomer	none
	193	Inner	2.464	Metal	1716
		Outer	1.803	Elastomer	none
Side	48	Inner	0.245	Metal	none
		Outer	0.191	Elastomer	none
	97	Inner	0.914	Metal	799
		Outer	1.600	Elastomer	none
	145	Inner	8*	Metal	>10000
		Outer	25*	Elastomer	>10000
	193	Inner	15*	Metal	>10000
		Outer	50*	Elastomer	>10000

III.2.7 Acknowledgements

Jim Bean at Sandia contributed significantly to the development of this model.

III.3 Impacts onto Yielding Targets

III.3.1 Introduction

The finite element results discussed in the previous section are all for impacts onto a rigid target. For this type of impact, the entire kinetic energy of the impact is absorbed by the cask. For finite element analyses a rigid target is easily implemented by enforcing a no displacement boundary condition at the target surface. In real life, the construction of a rigid target is impossible, but it is possible to construct a target that is sufficiently rigid that increasing its rigidity does not increase the amount of damage to the cask. This is because in real impacts there is a sharing of energy absorption between the cask and the target. If the target is much weaker than the cask, the target will absorb most of the energy. If the target is much stronger than the cask, most of the energy will be absorbed by the cask. In this section the partitioning of the drop energy between the four generic casks and several “real-world” targets will be developed in order to obtain impact speeds

onto real surfaces that give the same damage as impacts onto rigid targets. Impacts onto hard desert soil, concrete highways, and hard rock are considered. Impacts onto water surfaces are not explicitly treated, but are discussed. In addition, the probability of puncture of the cask caused by impact against a non-flat surface (or impact by a puncture probe) is developed.

III.3.2 Method

For each finite element calculation for impact onto a rigid target the total kinetic energy of the finite element model is output at 100 time-steps through the analysis. The total kinetic energy is one half of the sum of the mass associated with each node times the velocity of that node squared. Figure III-54 shows kinetic energy time-histories for the steel-lead-steel truck cask for each orientation from the 120-mph impact analyses with pre-crushed impact limiters. From the time-history of kinetic energy, a velocity time history is derived. The rigid-body velocity for each time-step is calculated assuming that all of the kinetic energy of the model is caused by velocity in the direction of the impact. Equation III-1 shows this mathematically.

$$v_t = \sqrt{\frac{2KE_t}{\sum m_i}} \quad (\text{Eq. III-1})$$

where v_t is the velocity at time t , KE_t is the kinetic energy at time t , m_i is the mass associated with node i , and the summation is over all of the nodes in the finite element model.

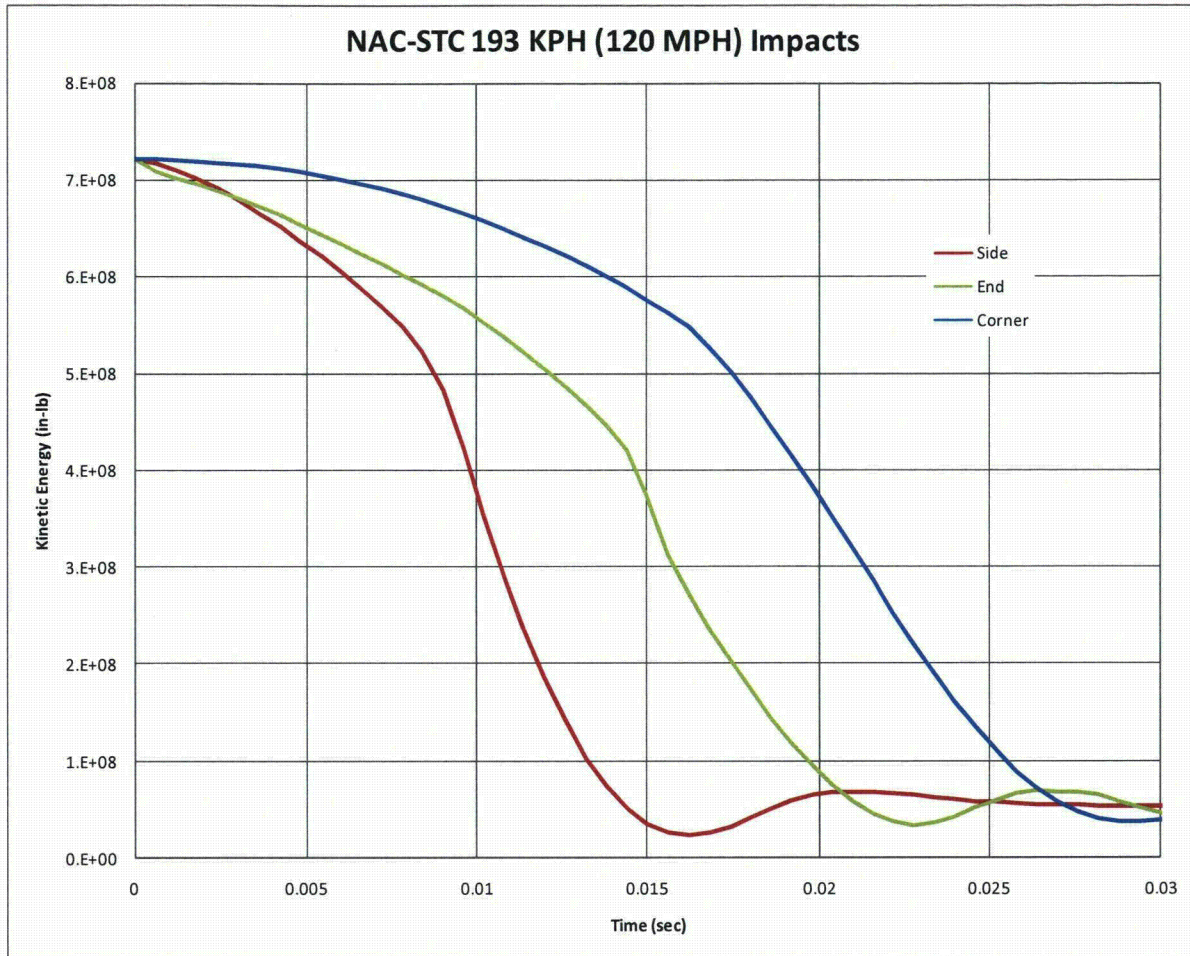


Figure III-54. Kinetic energy time histories for the Rail-Lead cask from 193 KPH (120 MPH) impact analyses in the end, side, and corner orientations

For each analysis the peak contact force is determined. Table III-2 lists these forces. For an impact onto a real target to be as damaging to the cask as the impact onto the rigid target, the target must be able to impart a force equal to this peak force to the cask.

The energy absorbed by the target in developing this force is added to the initial kinetic energy of the cask. This total absorbed energy is used to calculate an equivalent velocity by replacing KE_t in Equation III-1 with the total energy.

Table III-2. Peak contact force for the Rail-Lead cask impacts onto an unyielding target (bold numbers are for the cases where there may be seal leaks)

Orientation	Speed (KPH)	Accel. (G)	Contact Force (Millions of Pounds)	Contact Force (MIN)
End	48	58.5	14.6	65.0
	97	111.6	27.9	123.9
	145	357.6	89.3	397.1
	193	555.5	138.7	616.8
Corner	48	36.8	9.2	40.9
	97	132.2	33.0	146.8
	145	256.7	64.1	285.1
	193	375.7	93.8	417.2
Side	48	76.1	19.0	84.5
	97	178.1	44.5	197.8
	145	411.3	102.7	456.7
	193	601.1	150.0	667.4

III.3.3 Soil Targets

The force that hard desert soil imparts onto a cask following an impact was derived from results of impact tests performed by Gonzales [5-13], Waddoups [5-14], and Bonzon and Schamaun [5-15]. The tests by Gonzales and Waddoups used casks that were comparable to Rail-Lead cask, but much smaller. The tests by Bonzon and Schamaun were with casks that were less stiff than the Rail-Lead cask. This large amount of test data was used to develop an empirical soil target force-deflection equation that is a function of impactor area. Figure III-54 shows the force-deflection curves for impact of the Rail-Lead cask onto a soil target. Corner impacts were assumed to have the same contact area on the soil target as the end impacts, so only two curves are shown. Similar curves were developed for each of the other casks. Comparison of Figure III-55 with the forces in Table III-2 show that many of the impacts will result in very large soil penetrations. This is consistent with the results seen in Waddoups' tests, where casks were dropped 2,000 feet from a helicopter. Penetration depths for these impacts were up to 8 feet, and the equivalent rigid target impact velocity was less than 30 mph. Integration of the force-deflection curve up to the peak contact force determines the amount of energy absorbed by the target.

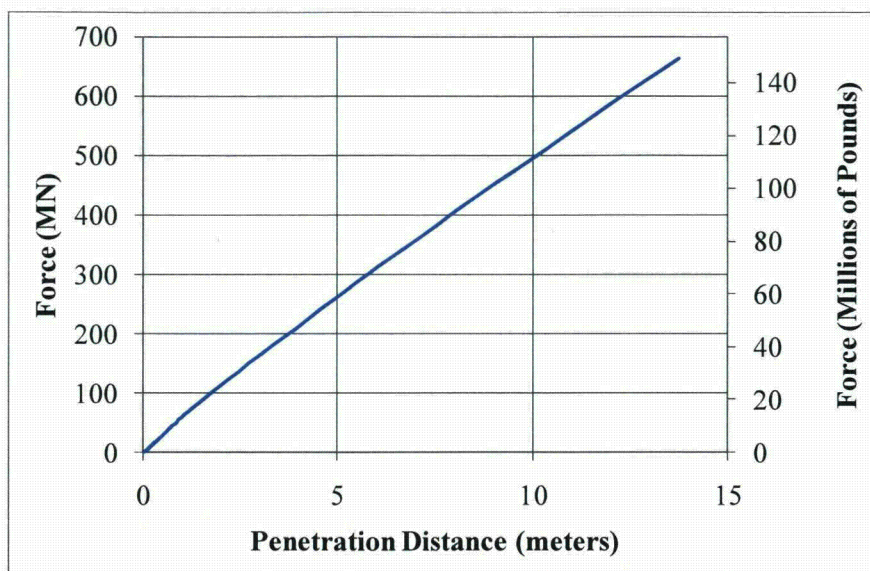


Figure III-55. Force generated by the Rail-Lead cask penetrating hard desert soil

III.3.4 Concrete Targets

The force imparted to a cask by impact onto a concrete target is derived from test results by Gonzales [5-13]. In his series of tests, a cask-like test unit was impacted onto two types of concrete targets, one 12 inches thick and one 18 inches thick, at velocities from 30 to 60 mph. All of the impacts were in an end-on orientation. Based upon the results of these tests and engineering mechanics, an empirical relationship between the force and energy absorbed was derived. For impacts onto concrete slab targets there are two mechanisms that produce large forces onto the cask. The first is the generation of a shear plug in the concrete. The force required to produce this shear plug is linearly related to the impact velocity, the diameter of the impacting body, and the thickness of the concrete. Equation III-2 gives the empirical equation for the force required to produce the shear plug.

$$F_s = C_s v_e d_i t_c \quad (\text{Eq. III-2})$$

where F_s is the force required to produce the shear plug, C_s is an empirical constant (16.84), v_e is the equivalent impact velocity, d_i is the diameter of the impactor, and t_c is the thickness of the concrete slab.

The energy absorbed in producing this shear plug is linearly related to the cask diameter, the square of the impact velocity, and the fourth root of the slab thickness. Equation III-3 gives the empirical equation for the energy required to produce the shear plug.

$$E_s = C_e d_i v_e^2 t_c^{0.25} \quad (\text{Eq. III-3})$$

where E_s is the energy required to produce the shear plug and C_e is an empirical constant (0.00676).

After the shear plug is formed, further resistance to penetration is achieved by the behavior of the subgrade and soil beneath the concrete. This material is being penetrated by the cask and the shear plug. Generally, the shear plug forms with 45-degree slopes on the side. Therefore, the diameter of the soil being penetrated is equal to the cask diameter plus twice the slab thickness. The behavior of the subgrade and soil is assumed to be the same as the hard desert soil used for the soil target impacts. Figure III-56 shows a comparison of the empirical relationship with one of Gonzales' tests. For corner and side impacts an equivalent diameter is calculated to fit with the empirical equations. For each case the diameter is calculated by assuming the shear plug forms when the concrete target has been penetrated two inches. The area of the equivalent diameter is equal to the area of the concrete in contact with the cask when the penetration depth is two inches. To calculate the equivalent velocity for concrete targets the force required to generate the shear plug must be compared to the peak contact force for the impact onto the rigid target. The velocity required to produce this force can be calculated from Equation III-2. The kinetic energy associated with this velocity is absorbed by a combination of producing the shear plug, penetration of the subgrade and soil beneath the concrete, and deformation of the cask. The energy absorbed in producing the shear plug is calculated by Equation III-3, the energy absorbed by the cask is equal to the kinetic energy of the rigid target impact, and the energy absorbed by the subgrade and soil is calculated in a manner similar to that for the soil impact discussed above. If the amount of energy to be absorbed by the soil is sufficiently high, the force in the soil will be higher than the force required to produce the shear plug. In this case, an iterative approach is necessary to derive an equivalent velocity so that the maximum force generated in penetrating the subgrade and soil beneath the concrete is equal to the peak contact force for the rigid target impact.

Gonzales Impacts onto Highway Targets

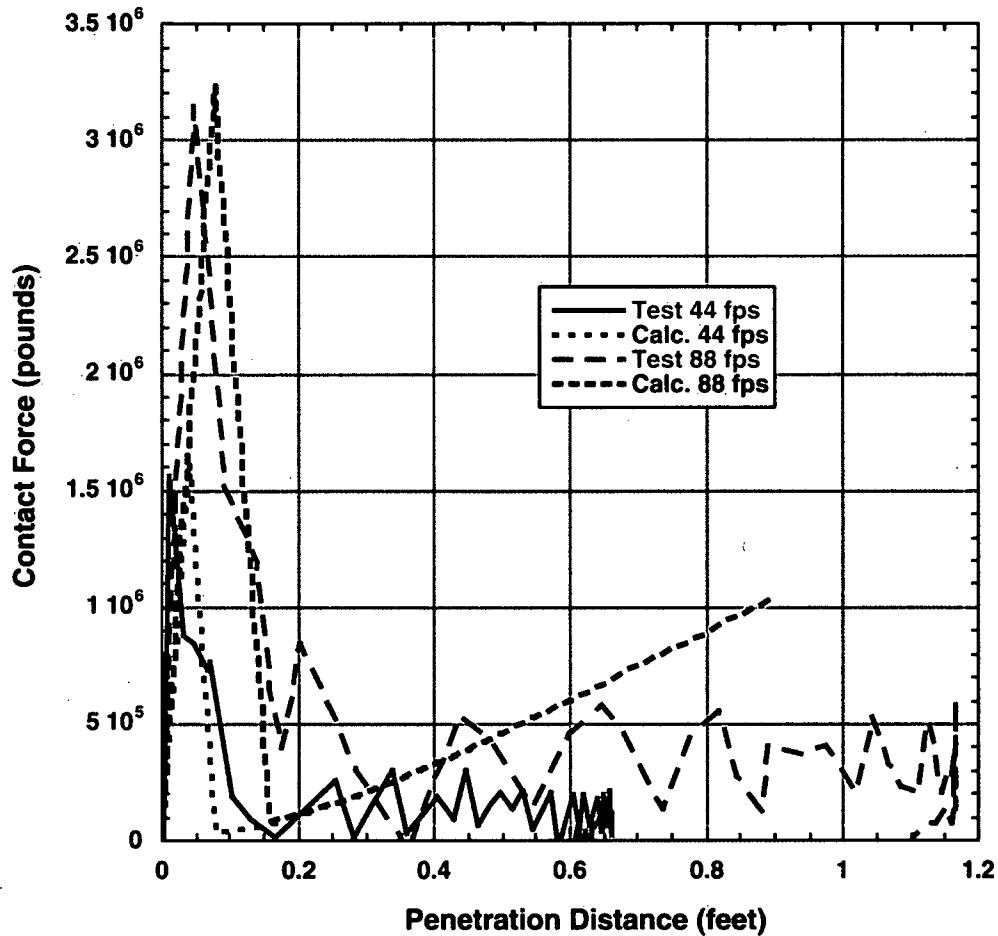


Figure III-56. Comparison of test force-deflection curves with those derived from the empirical equations.

The only orientation of impacts onto concrete targets where test data is available is for end impacts. In this orientation the contact area between the cask and the concrete does not increase with increasing penetration distance. In order to use the empirical relationships developed for end impacts with other impact orientations, an equivalent diameter must be determined. For both the side and corner impacts, the equivalent diameter was calculated to have an area equal to the area of the cask two inches above the contact point. For side impact orientations, this area is a rectangle. For corner impact orientations this area is a truncated parabola.

III.3.5 Hard Rock Targets

For impacts onto hard rock targets the target is assumed to be a semi-infinite half plane. The force and energy absorbed by the target is determined by the volumetric behavior of the rock. For hard rock surfaces this behavior is sufficiently stiff that very little energy is absorbed by the target. For this reason these impacts are treated as rigid target impacts.

III.3.6 Results for Real Target Calculations

Table III-3 gives the results for impacts onto soil and concrete targets.

Table III-3. Equivalent velocities for Rail-Lead cask impacts onto various targets, KPH

Orientation	Rigid	Soil	Concrete
End	48	102	71
	97	205	136
	145	>250	>250
	193	>250	>250
Corner	48	73	70
	97	236	161
	145	>250	>250
	193	>250	>250
Side	48	103	79
	97	246	185
	145	>250	>250
	193	>250	>250

III.3.7 Impacts onto Water

Equivalent velocities for impacts onto water targets for velocities greater than the regulatory impact are assumed to be above the range of possible impact velocities (150 mph). The incompressible nature of water makes perfectly flat impacts quite severe. As the impact velocity increases smaller deviations from the perfectly flat orientation are sufficient to cause the lack of shear strength in water to dominate the response. Because perfectly flat impacts are very improbable, this approach is justified.

III.4 Response of Spent Fuel Assemblies

III.4.1 Introduction

The response of spent power reactor fuel assemblies to impact accidents is not well understood. While this area has been investigated in the past (Sanders et al. 1992), those models tended to be relatively crude and imprecise. In addition, there is a renewed interest on the part of utility companies in shipping higher burnup spent fuel. Therefore, determining a more accurate response of spent fuel assembly to impact loads that may be the result of transportation or handling accidents or malevolent acts is essential. Sandia National Laboratories has performed a series of computational analyses to predict the structural response of a spent nuclear fuel assembly that is subjected to a hypothetical regulatory impact accident, as defined in 10 CFR71.73. This study performs a structural analysis of a typical pressurized water reactor (PWR) fuel assembly using the Abaqus/Explicit finite element analysis code. The configuration of the pellet/cladding interface and the material properties of the pellet have been varied in the model to account for possible variations in actual spent fuel assemblies.

III.4.2 Description and Method

A typical PWR fuel assembly is shown in Figure III-57. The assembly consists of a series of fuel pins, or rods, grouped together in a square array. The fuel rods are held in place by a series of equally spaced grids. Within the array of fuel tubes are a series of guide tubes in which control rods are placed for controlling the fission reaction during operation. The guide tubes are attached to endplates, nozzles or end fittings, which provide rigidity for handling.

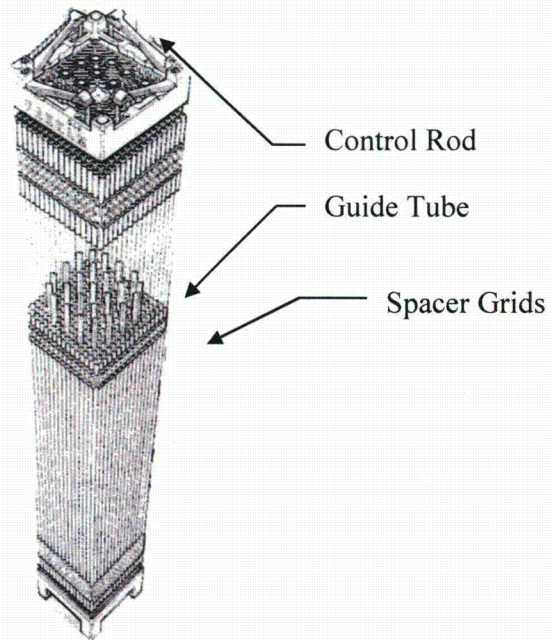
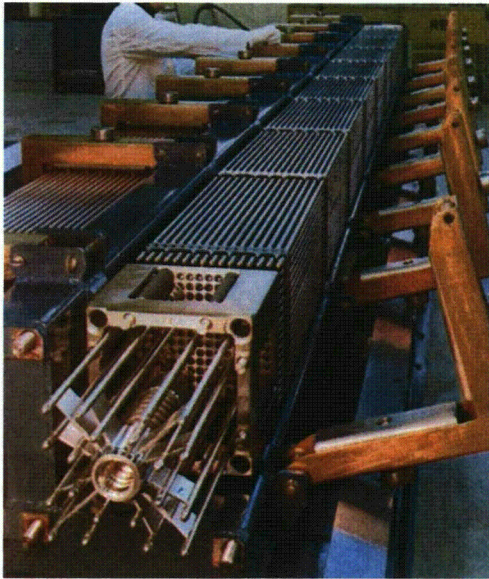


Figure III-57. PWR fuel assembly

An individual fuel rod is shown schematically in Figure . It is constructed by stacking a series of Uranium Dioxide (UO_2) pellets inside a Zirconium tube, placing a spring on the top of the pellet stack and welding on end caps. A plenum is added at the top of the assembly to provide a sufficient volume to collect released fission gases.

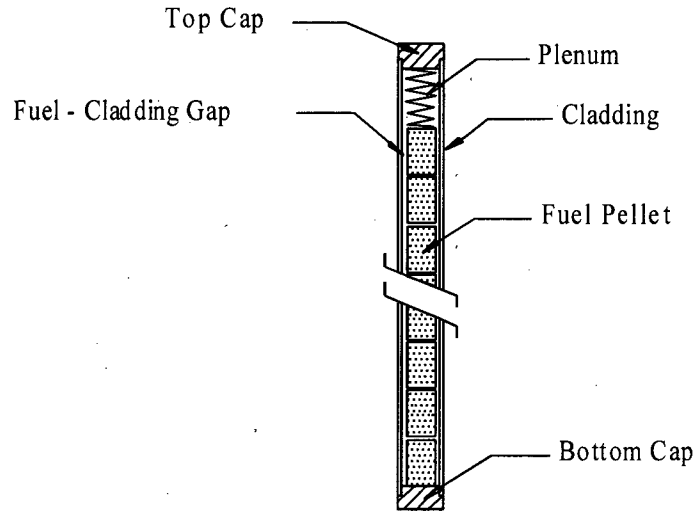


Figure III-58. Fuel rod schematic drawing

The working environment of a reactor is extremely harsh. The fuel rods are subjected to neutron radiation, large thermal gradients, large stress due to external water pressure and large local stress from contact between the pellet and the cladding. Upon the first power cycle, the uranium pellet cracks into pie shaped pieces due to the large radial temperature gradients across the pellet. Over a short period of time (months), the pellets shrink as fine porosity in the fuel is removed by radiation densifications. The cladding slowly creeps down onto the pellet due to its high operating temperature and the external pressure of the coolant. The pellet also begins to expand due to fission product swelling. Over a period of 1-2 years the initial gap between the fuel rod and the pellet is eliminated. However, the contact between the cladding and the fuel pellet is not necessarily circular and uniform. This leads to local increases in the cladding stress. In addition, zirconium is one of the few elements that react with both oxygen and hydrogen. This can lead to a reaction between the ZrO_2 layers on the inner cladding surface and the fuel pellet to form a bonding interface of $(U,Zr)O_2$ between the fuel pellet and the cladding. In essence, bonding the pellet to the cladding wall. In addition, hydride precipitants can also form in the Zircaloy cladding wall.

Upon the removal from the reactor, the state of the spent fuel assembly at any future time depends on the spent fuel's environmental history as well as its condition upon removal from the reactor. The internal gas pressure in a fuel rod having been removed from the reactor now provides tensile hoop and axial stresses on the cladding. This stress along with changes in cladding temperature may allow hydrogen to precipitate out and possibly reform along the circumferential directions (direction of highest stress). Plastic creep in the cladding may cause a gap to develop between the cladding and the fuel pellet and the development of void spaces in the crack pellets. The current material conditions and stress state of any particular rod at the time of an accident is complex and unknown. Therefore, the current material properties and geometric

configuration will be varied over a small range to attempt to account for the actual unknown material and geometric variations.

Table III-4 lists the material properties and nominal dimensions of a 17x17 PWR fuel assembly. Due to the large number of rods and the large ratio between the fuel assembly length and the fuel rod diameter, modeling a complete assembly using the finite element method is challenging. To build the entire model using continuum and structural shell elements with a high enough resolution in each fuel rod would produce a model with so many degrees of freedom as to be computationally intractable. Therefore, the current analysis will be broken down into three steps. In the first step, the entire assembly will be modeled using structural beam and shell elements. Then in the second step, the loads from the highest loaded rod in the full assembly model will be transferred to a single rod model constructed of continuum and structural shell elements. This model will provide the detailed stress field necessary to determine the integrity of the fuel rod. Due to the severe nature of the reactor environments there are significant material and geometric changes in the fuel rods. Very little if any test data is available for the Zircaloy-4 material under high irradiation conditions, therefore as a third step, a series of parametric analyses were conducted with the continuum model to determine the sensitivity of the model to changes in the rod geometry and the pellet and cladding material properties.

Table III-4. Properties of fuel assembly

Assembly Type 17 x 17	
Cladding Material	Zircaloy-4
Assembly Cross-section (in)	8.43-8.54
Number of Fuel Rods per Assembly	264
Fuel Rod OD (in)	0.374 to 0.379
Minimum Cladding Thickness	0.023
Pellet Diameter (in)	0.3225 to 0.3232
Maximum Active Fuel Length (in)	144

III.4.3 Finite Element Models

Two major models have been developed in this analysis. The first of these is the beam fuel assembly model which is a structural model consisting of beam and shell elements. This model is used to determine the overall response of the fuel assembly. Using data from this model a

detailed continuum model of a single rod is developed to determine a more detailed response of the most highly loaded rod. Several parametric analyses are conducted with the latter model to determine the effect of variations of rod material properties and geometry. In addition to these models, several smaller models have been developed to aid in the overall analysis. Initial models were developed to test the capabilities of the finite element codes. Small models were also developed when problems arose in the analyses. All of these models along with the final rod analysis are discussed in the following section.

Fuel Assembly Finite Element Model

Using the latest version of the Abaqus/Explicit finite element code, a complete fuel assembly model (shown in Figure III-59) was constructed and analyzed. It incorporates 3D beam elements for the fuel pins and control rods, and shell elements for the spacer grid assemblies and the support plates representing the basket walls. The endplates are modeled as solid plates using hexahedron elements so that the support rod beam elements can be attached. The model contains 265 fuel pins and 24 tie rods. There are a total of 129,440 elements, with 41,616 beam elements. There are 144 beam elements along the length of each fuel rod and support rod. The location of the guide tubes in the cross-section of the fuel assembly is presented in Figure III-60.

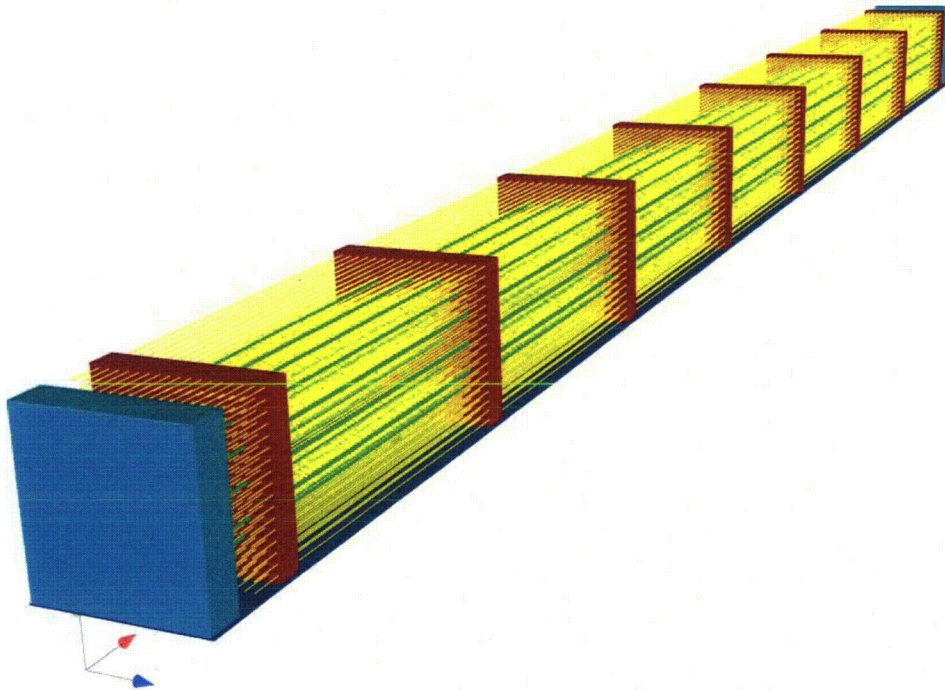


Figure III-59. Beam Fuel Assembly finite element model

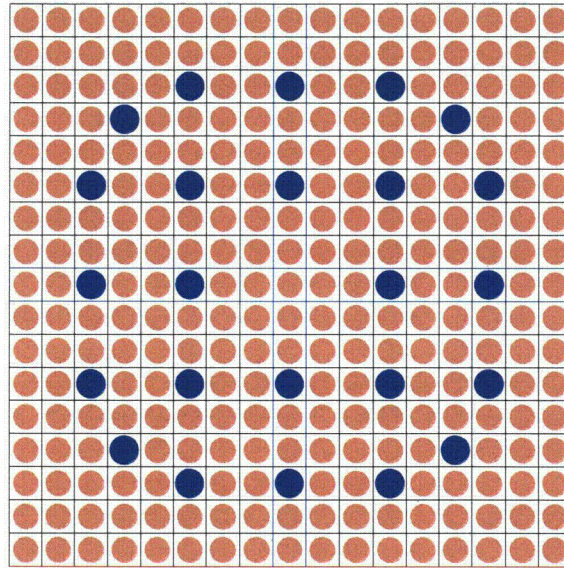


Figure III-60. Cross-section of 17x17 fuel assembly with guide tubes (in blue)

The fuel assembly model was loaded using acceleration curves developed from experimental data of a side impact drop test. The full-scale data for the analysis was calculated from the $\frac{1}{4}$ scale test data. A plot of the full-scale data is presented in Figure III-61. An additional curve was generated from the full-scale data to yield a maximum acceleration of 100 g's, while maintaining the same total impulse. The fuel rods are given an initial velocity of 528 in/sec, which corresponds to a 9-meter drop test. The acceleration is applied to the lower plate, which represents the side of the fuel basket.

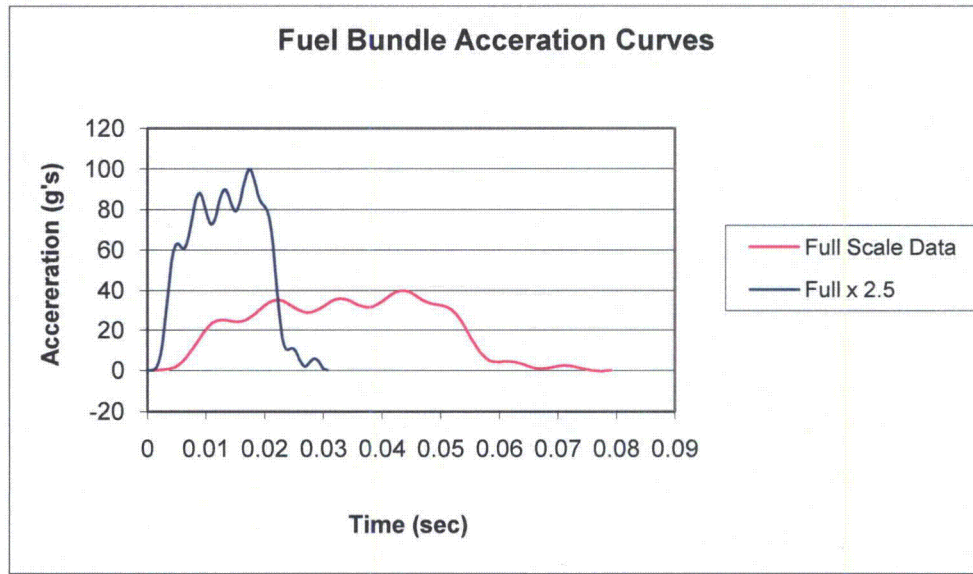


Figure III-61. Acceleration curves applied to fuel assembly beam model

The fuel rod material is modeled as unirradiated Zircaloy-4, using a power law hardening constitutive model fit to test data from the literature, Pierron et al. [5] The calculated material parameters are shown in Table III-5. These material properties are used for the fuel pins, the ties rods, and the support grid. In this analysis, the fuel pins and tie rods are modeled as solid beams with a circular cross-section.

Table III-5. Zircaloy-4 material parameters

Elastic Modulus	13.0 E3 ksi
Yield Stress	65 ksi
Luder Strain	0.00
Hardening Constant	103.5 ksi
Hardening Exponent	0.845

Fuel Assembly Model Results

For the lower acceleration curve given in Figure III-61, which represents a rail cask, there is no plastic deformation in the fuel rods or the spacer grids. The entire model remains elastic. For the analysis with the higher acceleration curve, there is no plastic deformation in the fuel rods and some plastic deformation in the spacer grids. Figure III-62 shows the most highly strained spacer grid. The lower three sections of the spacer grid buckle and a maximum plastic strain of 28% is calculated.

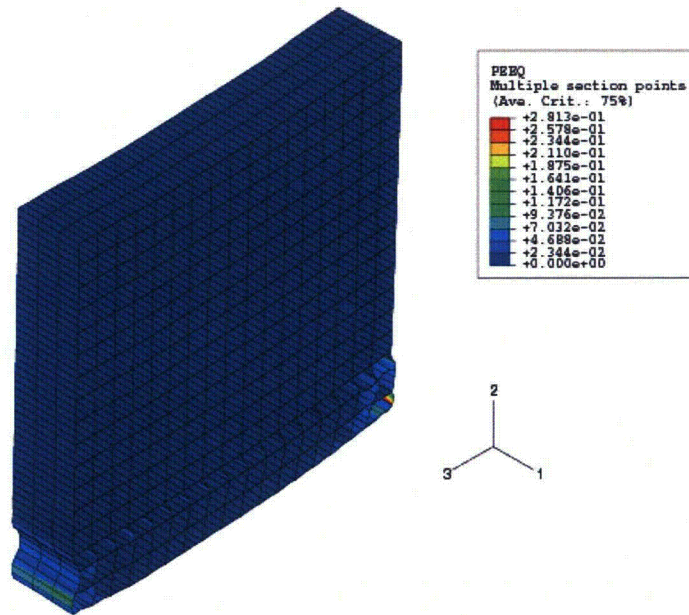


Figure III-62. Spacer grid 100g analysis plastic strain

The contact forces from the beam fuel assembly model will be used as input to a single rod continuum model. Since these forces occur over very short durations during the analysis, it was necessary to obtain data points at each time step in the fuel assembly model. Therefore, contact forces at a total of 20,349 time steps were obtained from the fuel assembly analysis.

Beam Element Versus Solid Element Contact

In processing the contact forces from the beam fuel assembly model, it was observed that the forces calculated during beam-to-beam contact were very large and acted over very short durations. They were much larger than the forces calculated in the model for the beam-to-shell contact. To investigate this difference in the magnitude and duration of the contact forces, two additional models were developed. The first, shown in Figure III-63, is a model of two impacting rods modeled with hexahedron elements. The second, shown in Figure III-64, is a model of two impacting rods modeled using beam elements. Since the beam elements in the beam fuel assembly model remain elastic, these models were evaluated for impact using elastic material properties.

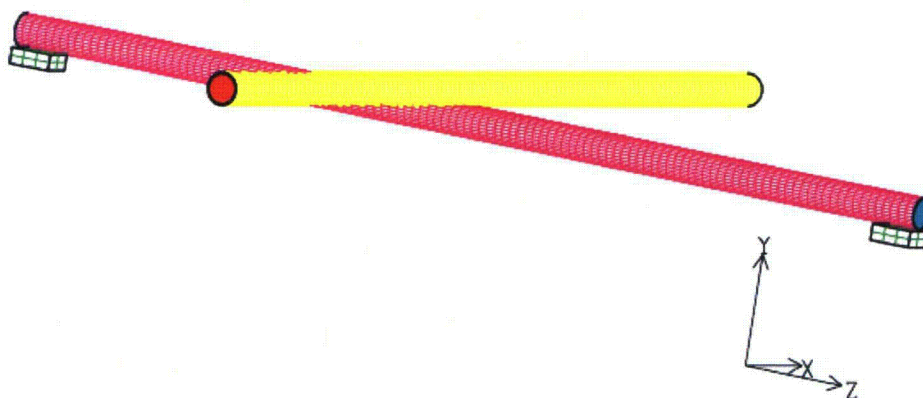


Figure III-63. Hexahedron test model for solid rod-to-rod contact in Abaqus/Explicit

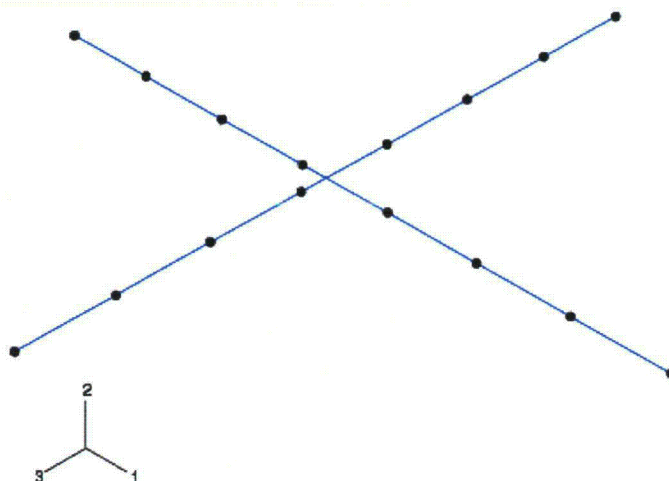


Figure III-64. Test model for beam-to-beam contact in Abaqus/Explicit

The results from the two finite element rod models are shown in Figure III-65 and Figure III-66. For the same mass, impact velocity and cross-sectional geometry, the two models generate two different sets of contact forces. As shown in Figure III-65, the beam element impact forces are much larger and shorter in duration than those generated from the hex rod model. The magnitudes of the forces differ by about a factor of five. An additional check was made comparing the hexahedron Abaqus/Explicit model to a similar model run in the Sandia code PRONTO3D. Both codes generated similar contact and reaction forces. Continued evaluation of the two models generated the curves shown in Figure III-66. For the velocity range of interest there is a good linear fit for each curve. Therefore, in transferring the loads between the beam fuel assembly model and the continuum beam model the magnitude of the forces were scaled in accordance with the curves in Figure 66. The length of each beam element impulse was increased to keep the integral of the curve the same. That is, the total impulse was maintained to conserve the change in momentum.

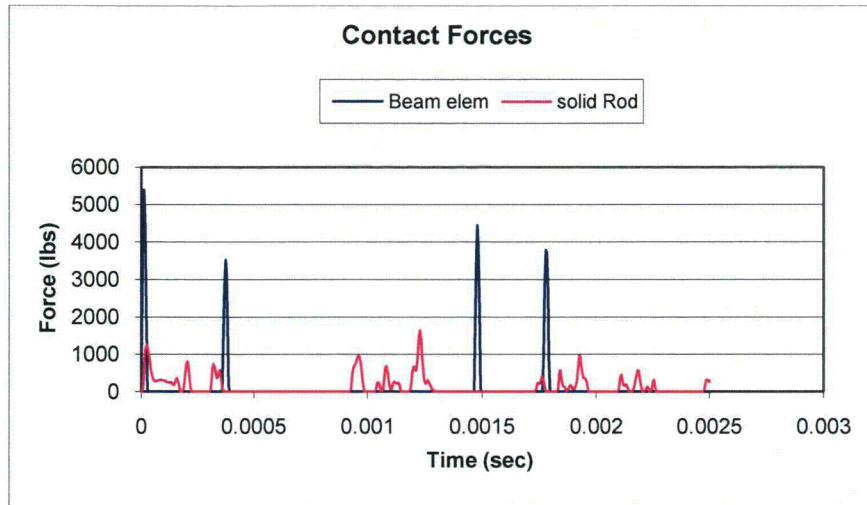


Figure III-65. Comparison of contact forces between solid rod and beam element rod

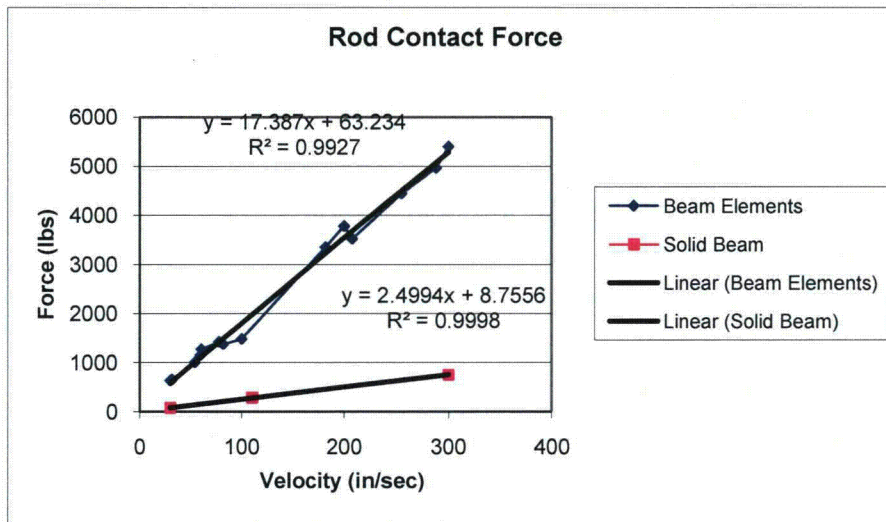


Figure III-66. Comparison of contact forces as a function of impact velocity

Continuum Rod Model

A continuum model was constructed using shell and hexahedral elements. The mesh is shown in Figure , with a blowup of the end region showing the mesh density. The magenta colored regions represent the locations of the spacer grids. There is a plane of symmetry along the longitudinal axis of the beam. The symmetric model contains 162,000 elements, with 139,000 hexahedron

elements used to model the UO_2 core and 23,000 shell elements used to model the Zircaloy-4 cladding. The hexahedron core has 16 elements across the diameter and there are 16 shell elements around the semicircular arc of the cladding.

The contact forces obtained from the beam fuel assembly model for the 100g loading are applied to a set of shell nodes running along the top and bottom of the symmetry plane. There are 1,446 nodes along each surface. Positive contact forces are applied to the bottom set of nodes and negative forces are applied to the upper nodes. As noted in the previous section the forces from the beam fuel assembly model that result from beam-to-beam contact are scaled according to the curves in Figure III-66 and the duration of the load is then increased to conserve the change in momentum. In the region of the spacer grid where there is beam-to-shell contact, the loads are not scaled. The new load curves are then interpolated from the element nodes in the beam fuel assembly model to a larger number of element nodes in the continuum model. The rod model is given the same initial velocity as the beam fuel assembly model, 528 in/sec.

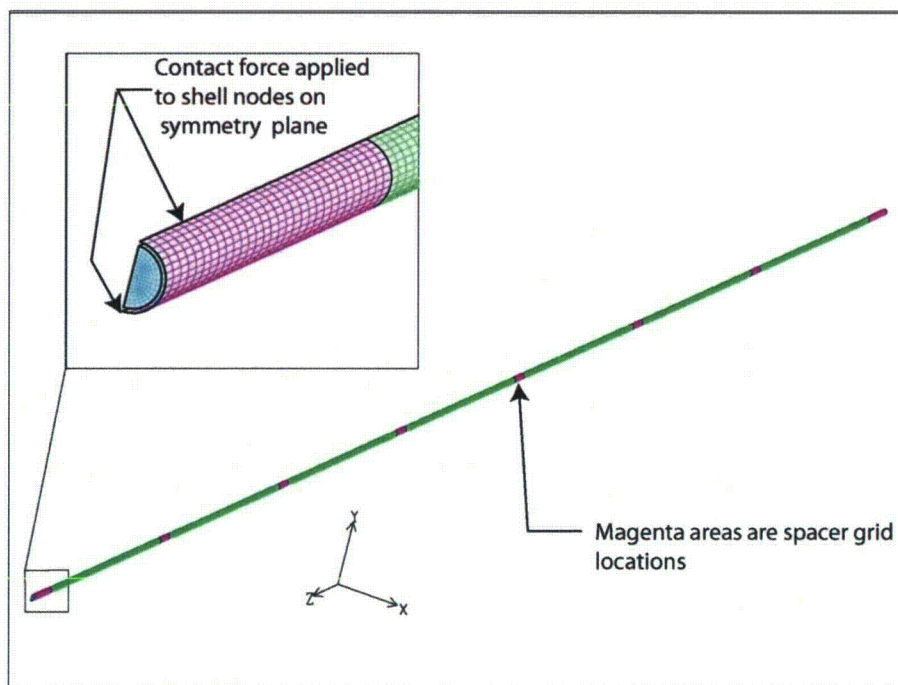


Figure III-67. Continuum rod finite element model

The rod materials are also modeled using a power-law hardening model. The parameters are presented in Table III-6. The model was run for two different load cases as shown in Table III-7. In the first case, the outside diameter of the UO_2 core and the inside diameter of the cladding are the same, the Zircaloy-4 material is modeled as unirradiated fuel and the UO_2 is also assumed to be pristine. In the second load case, the cladding material is assumed unirradiated, while the

modulus of the UO₂ is decreased by an order of magnitude to simulate a softer, crumbled material, which has been irradiated. The results from both of these analyses are presented in the following section.

Table III-6. Standard Material Properties

	Zircaloy	Uranium Oxide
Elastic Modulus	13.0 E3 ksi	28.0 E3 ksi
Yield Stress	65 ksi	21.6 ksi
Luder Strain	0.00	0.00
Hardening Constant	103.5 ksi	103.5 ksi
Hardening Exponent	0.845	0.845

Table III-7. Load case parameter changes

Load Case parameters			
Case	Cladding Yield Strength (psi)	UO ₂ Modulus (psi)	Cladding Gap (inches)
Case 1	65,250	28 x 10 ⁶	None
Case 2	65,250	28 x 10 ⁵	None

Continuum Rod Results

Analysis Case 1

The first analysis case models unirradiated Zircaloy-4 material with no gap between the UO₂ rod and the cladding. The resulting kinetic energy plot for this analysis case is presented in Figure III-68. Almost all of the kinetic energy is lost from the rod; this indicates that the load impulse applied in the continuum model matches the impulse generated in the beam fuel assembly model. There is a large decrease in the kinetic energy at approximate 5.2 msec. This corresponds to the large loads applied to the rod due to beam-beam contact forces at locations between the spacer grids. These impacts are illustrated in Figure III-69, which show the maximum equivalent plastic strain (EQPS) in the rod cladding as a function of time for three inter-grid locations. A maximum plastic strain of 1.5% is observed between spacer grid locations G and H. A detailed contour plot of this region is presented in Figure III-70.

The plastic strain in the rods at several spacer grid locations is presented in Figure III-71. These strains are approximately an order of magnitude smaller than inter-grid strains. This indicates that the spacer grids contact is much softer than beam-to-beam contact.

Figure III-72 shows the distribution of plastic strains along the length of the rod. The peak equivalent plastic strains are at the inter-rod locations between spacer grids G and H and between grids D and E. Strain at most of spacer grid locations along the rod remain elastic. The maximum plastic strain in the rod at a spacer grid is 0.06% at spacer grid C.

A close examination of the strain distribution in Figure III-74 shows that they are not symmetric about the center of the beam, although the initial beam fuel assembly finite element model and its loading were symmetric. This artifact is a result of the beam contact algorithm in Abaqus. As shown in Figure III-65, the impulses calculated for beam-to-beam contact are only a few microseconds long or roughly equal to three analysis time increments. Since the resolution of the impulse and the analysis time step are of the same order of magnitude, any accumulative numerical error on the position of the beam element nodes may result in a change in the time of contact and therefore the magnitude of the contact force and the subsequent position and velocity of the nodes. This results in a slight asymmetry in the calculated beam forces in the beam fuel assembly model. These forces are subsequently applied to the continuum model and result is the asymmetry of the strain fields shown in Figure III-72.

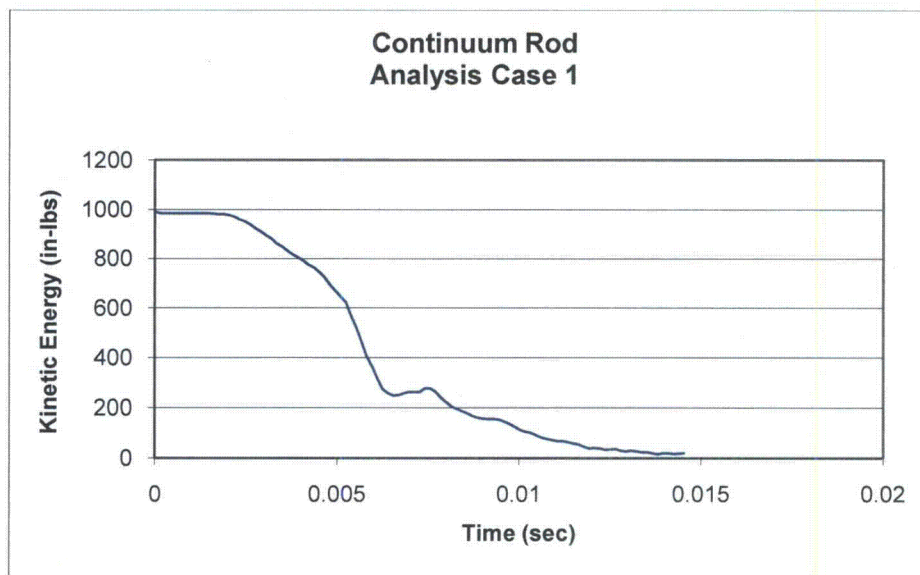


Figure III-68. Kinetic energy for Analysis Case 1

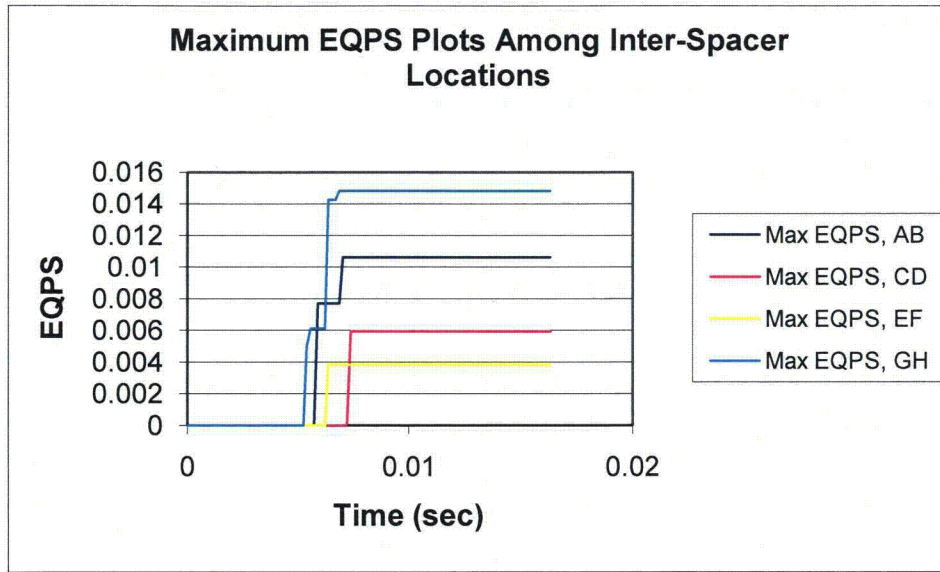


Figure III-69. Maximum equivalent plastic strain versus time for four inter-spacer grid locations. The spacer grids are specified by the letters in the legend (cf. Figure III-74)

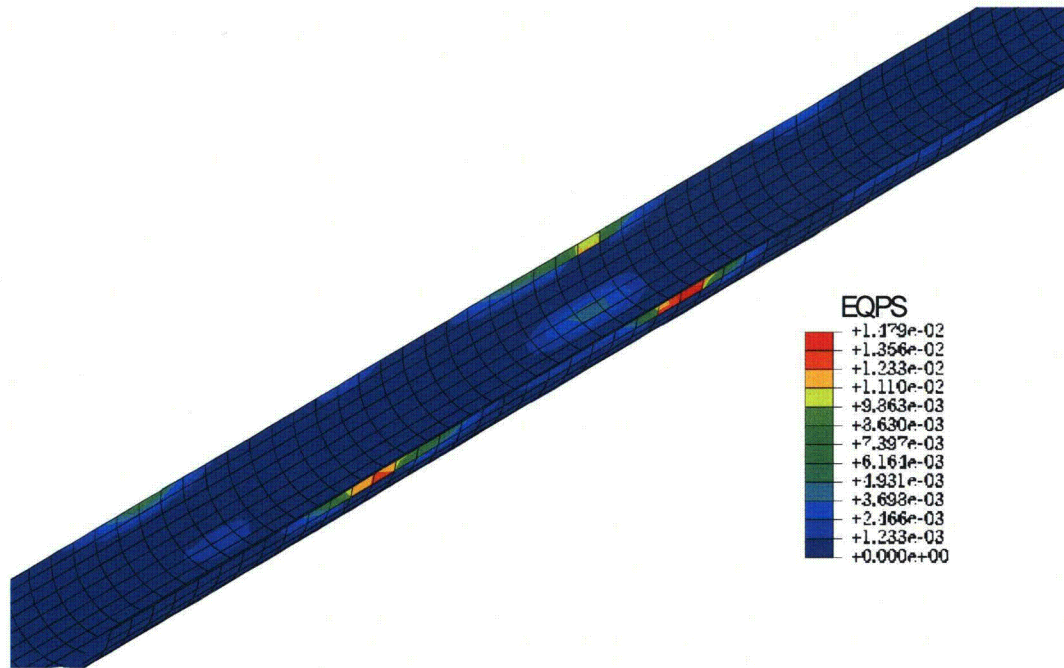


Figure III-70. Maximum equivalent plastic strain field in cladding for Analysis Case 1

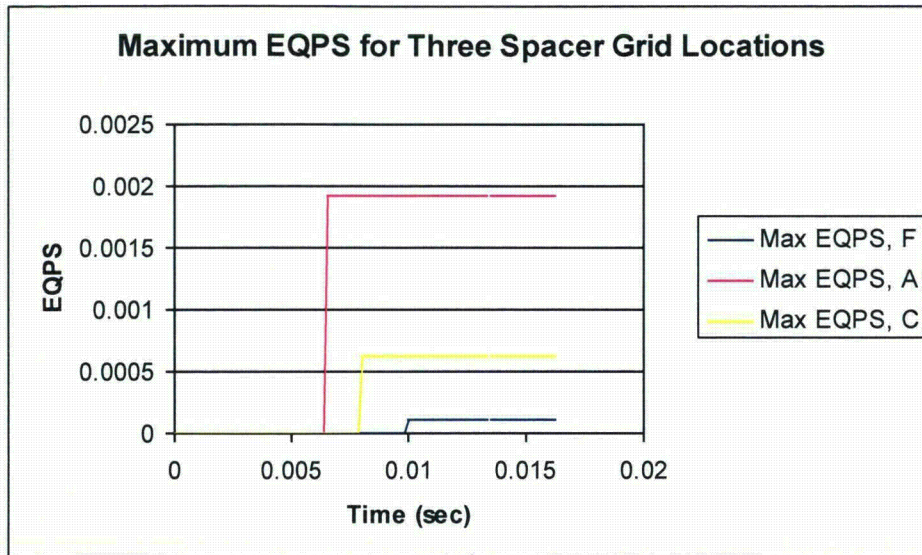


Figure III-71. Maximum equivalent plastic strain versus time for three spacer grid locations. The spacer grids are specified by the letters in the legend (cf. Figure III-74).

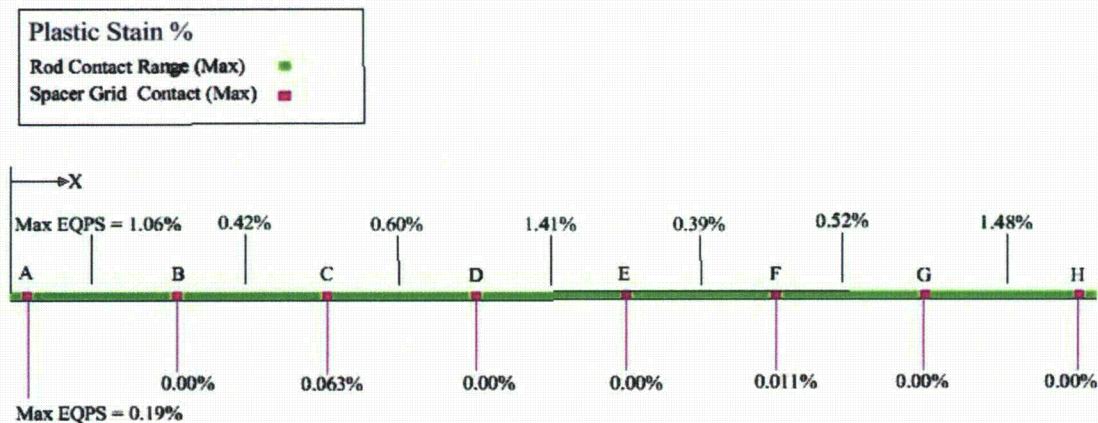


Figure III-72. Schematic showing maximum equivalent plastic strain for spacer grid and inter-spacer-grid locations.

Analysis Case 2

For the second analysis case, the Zircaloy material properties remain the same, but the modulus of the UO_2 is decreased by an order of magnitude to provide a probable overestimation of the softness in the post-reactor UO_2 . This softness is engendered by the large cracks that develop in the fuel pellets during its in-core lifetime. The largest plastic strains for this configuration are about one-third higher than those in the previous case of an unirradiated (pristine) UO_2 core. The

maximum EQPS is reached between spacer grids A and B and has a value of 1.98%. A contour plot of this region is presented in Figure III-73, which shows an axial region about 2 inches long with strain between 1% and 2%. The maximum EQPS at four inter-spacer locations as a function of time is shown in Figure III-74 and the maximum EQPS for four spacer grid locations is shown in Figure III-75. These curve are similar in shape to those in Analysis Case 1 where large strains occur at 5.2 msec. For this configuration there are plastic strains in the rod at all but one of the spacer grid locations and the maximum value of plastic strain for a spacer grid location is 0.67% at spacer grid C. A distribution of plastic strain over the entire rod is presented in Figure III-76.

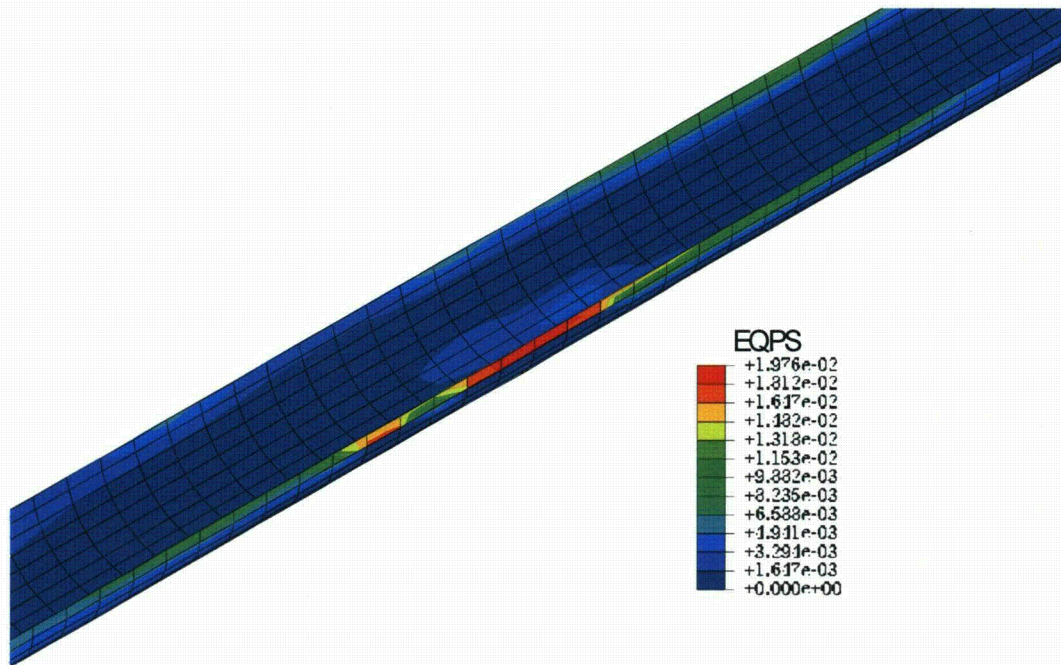


Figure III-73. Maximum equivalent plastic strain field in cladding for Analysis Case 2

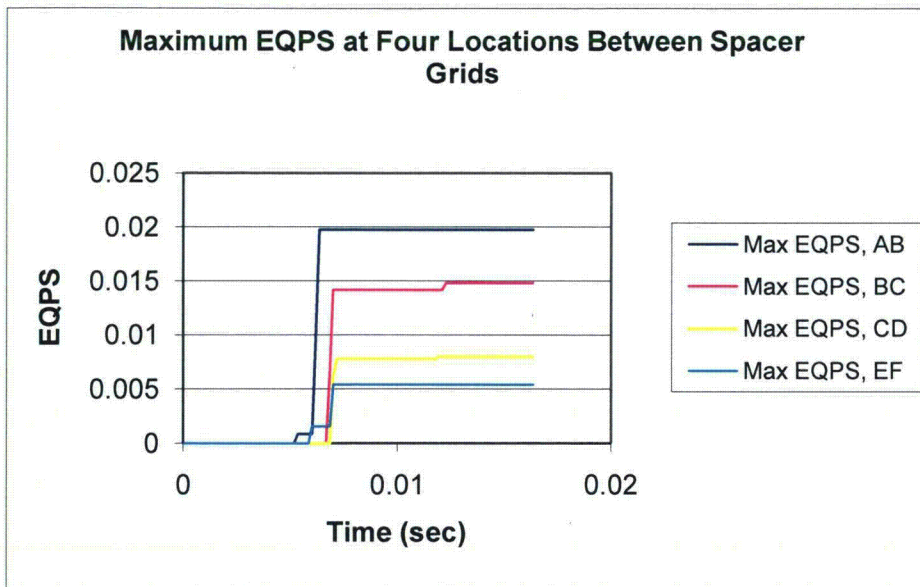


Figure III-74. Maximum equivalent plastic strain versus time for four inter-spacer grid locations. The spacer grids are specified by the letters in the legend (cf. Figure III-78)

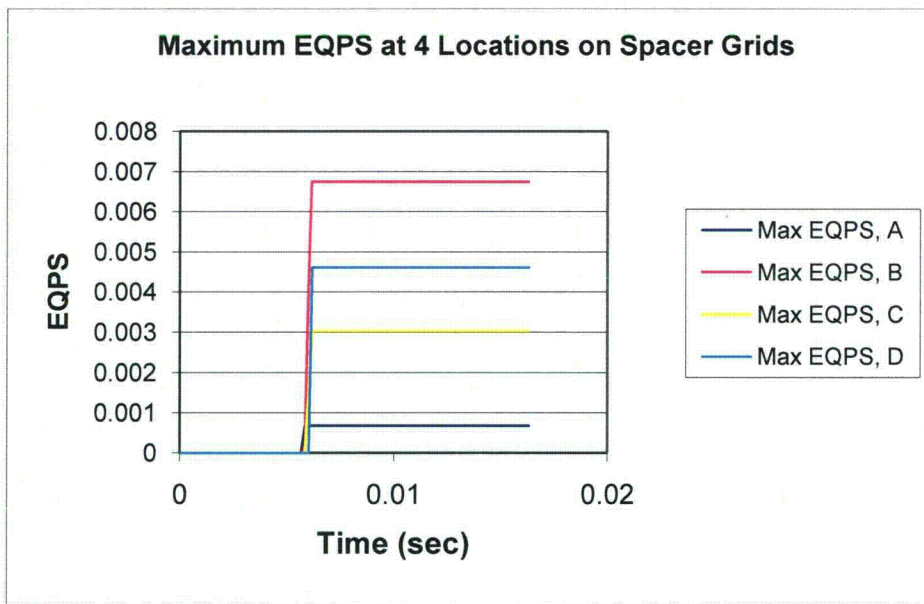


Figure III-75. Maximum equivalent plastic strain versus time for four spacer grid locations. The spacer grids are specified by the letters in the legend (cf. Figure III-78)

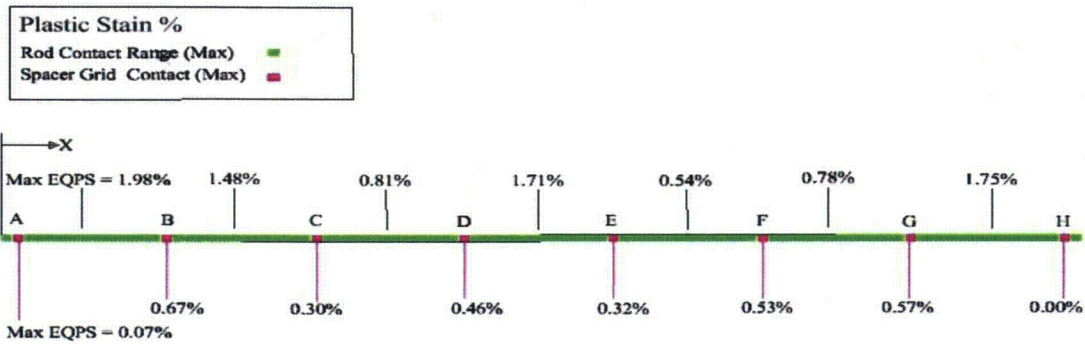


Figure III-76. Schematic showing maximum equivalent plastic strain for spacer grid and inter-spacer-grid locations, Analysis Case 2

III.4.3 Discussion and Conclusions

In this study explicit dynamic finite element analyses of a pressurized water reactor fuel assembly were conducted using two separate finite element models. The first model consisted of structural beam and shell elements and was used to determine the overall response of the complete fuel assembly to a regulatory side impact. Loading data from this analysis was applied to a continuum model of a single fuel pin to determine the localized stress and strain fields. It was observed that during impact the largest loads on the rods were generated from beam-to-beam contact.

Due to the lack of experimental data and the variability in properties of stored spent fuel rods, a series of analyses were conducted with variations in the stiffness of the UO₂ core material. A summary of the parameters used in each analysis and the maximum plastic strain calculated in the cladding wall is presented in Table III-8. From Table III-8 it can be concluded that an order of magnitude change in the stiffness of the pellet material results in a 30% increase in the maximum plastic strain in the rod. The materials in this study were modeled as isotropic and homogenous using an elastic plastic power-law hardening model. It is not clear that this approximation accurately models the response of the UO₂ pellets. It is more likely that the initial response would not be a steep linear response as modeled, but would be nonlinear, with a soft initial reaction that would increase in stiffness as the pellet is squeezed. Any attempt to estimate the nonlinear response of the pellet at this point would be pure conjecture.

Table III-8. Analysis Case Summary

Case	Cladding Yield Strength (psi)	UO ₂ Modulus (psi)	Cladding Gap (inches)	Max EQPS (%)
Case 1	65,250	28 x 10 ⁶	None	1.5
Case 2	65,250	28 x 10 ⁵	None	1.96

APPENDIX IV
DETAILS OF CASK RESPONSE TO FIRE ACCIDENTS

Table of Contents

APPENDIX IV DETAILS OF CASK RESPONSE TO FIRE ACCIDENTS	365
APPENDIX IV DETAILS OF CASK RESPONSE TO FIRE ACCIDENTS.....	370
IV.1 Introduction.....	370
IV.2 CAFE Finite Volume Domain and Boundary Conditions	371
IV.2.1 Geometric Consideration	373
IV.2.2 Rail-Steel Cask Thermal Behavior and Model Assumptions	381
IV.2.3 Rail-Steel Cask Materials and Thermal Properties	383
IV.2.4 Rail-Steel Cask, Finite Element Model and Boundary Conditions.....	391
IV.2.5 Rail-Steel Cask Thermal Analysis Results	393
IV.3 Rail Cask with Lead Shielding.....	393
IV.3.1 Geometry Considerations.....	404
IV.3.2 Rail-Lead Cask Thermal Behavior and Model Assumptions	407
IV.3.3 Rail-Lead Cask Materials and Thermal Properties	409
IV.3.4 Rail-Lead Cask Finite Element Model.....	413
IV.3.5 Rail-Lead Cask Thermal Analysis Results.....	425
IV.4 Truck Cask with Depleted Uranium	425
IV.4.1 Geometric Considerations	425
IV.5 Truck Cask with Depleted Uranium	425
IV.5.1 Geometric Considerations	425
IV.5.2 Truck-DU Thermal Behavior and Model Assumptions.....	427
IV.5.3 Truck Lead Materials and Thermal Properties.....	428
IV.5.4 Truck-DU P-Thermal Finite Element Model.....	429
IV.5.5 Truck-DU Cask Thermal Analysis Results.....	432
IV.6 CAFE Benchmark	432
IV.6.1 Large Calorimeter Test and Benchmark Results.....	434
IV.6.2 Small Calorimeter Test and Benchmark Results	437
IV.6.3 Summary of Benchmark Results.....	437
IV.7 Summary	438

List of Figures

Figure IV-1. CAFE three-dimensional domain: (a) CAFE regulatory fire, (b) cask on ground and at the center of the pool, (c) cask on the ground and 3m (10ft) from the edge of the pool, (d) cask on the ground and 18.3m (60ft) from the edge of the pool.	372
Figure IV-2. Rail-Steel cask transportation system	374
Figure IV-3. Rail-Steel cask: (a) assembly of MPC and overpack, and (b) cask with limiters (Holtec 2004).	374
Figure IV-4. Rail-Steel cask overpack: (a) cross-sectional view through the center of the cask, (b) cross-sectional view through the mid-plane of the overpack (Holtec 2004).	375
Figure IV-5. Rail-Steel cask MPC: (a) cross-sectional view through the axis of the cask, (b) cross-sectional through the midplane of the overpack (Holtec 2004).	377
Figure IV-6. Fuel assembly (Holtec 2004) (a) and fuel rod (b).	379
Figure IV-7. Fuel-basket region (left) and equivalent fuel-basket region (right). (Holtec 2004).	380
Figure IV-8. Rail-Steel cask upper (a) and lower (b) impact limiters (Holtec 2004).	380
Figure IV-9. Rail-Steel cask finite element mesh (model is symmetric, only half shown).	392
Figure IV-10. Rail-Steel Cask Regulatory Uniform Heating Results (P-Thermal)	394
Figure IV-11. Rail-Steel Cask CAFE regulatory fire.	396
Figure IV-12. Rail-Steel Cask CAFE fire with cask on ground and at the pool center.	398
Figure IV-13. Rail-Steel Cask CAFE fire with cask on ground 3.0m (10ft) from the edge of the pool.	400
Figure IV-14. Rail-Steel Cask CAFE fire with cask on ground 18.3m (60ft) from the edge of the pool.	402
Figure IV-15. Rail-Lead cask components with the direct loaded fuel basket shown to the right (NAC International, 2004).	405
Figure IV-16. Cross-section view of the Rail-Lead cask with the directly loaded fuel basket. .	405
Figure IV-17. Axial burn up profile for the directly loaded fuel basket (NAC International, 2004).	407
Figure IV-18. Three-dimension, quarter section of the directly loaded basket. The helium material is not shown.	408
Figure IV-19. The Rail-Lead cask mesh (mesh is symmetric, only half shown).	414
Figure IV-20. Rail-Lead cask Regulatory Uniform Heating Results.	415
Figure IV-21. Rail-Lead Cask CAFE Regulatory Fire	417
Figure IV-22. Rail-Lead cask on ground at the pool center.	419
Figure IV-23. Rail-Lead cask on ground 3.0m (10ft) from the edge of the pool.	421
Figure IV-24. Rail-Lead cask on ground 18.3m (60ft) from the edge of the pool.	423
Figure IV-25. Components of Truck-DU cask (General Atomics 1993).	426
Figure IV-26. Truck-DU cask mesh	431
Figure IV-27. CAFE three-dimensional domain with Truck-DU cask on ground.	432
Figure IV-28. Truck-DU cask on ground at the pool center.	433
Figure IV-29. Large calorimeter fire test: (a) test setup and (b) fire fully engulfing the calorimeter.	435
Figure IV-30. Side view (looking from the north) of calorimeter and test setup. Note: the calorimeter is centered with the pool. This drawing is not to scale.	435

Figure IV-31. CAFE benchmark results using fully engulfed large calorimeter: (a) temperatures average along the 0, 90, 180, and 270 degree side looking at the calorimeter from the negative z-direction, and (b) temperatures averaged over each ring starting from Ring 1 located on the positive side of the z-axis..... 436

Figure IV-32. CAFE benchmark results using a small calorimeter 1.5m (4.9ft) from the edge of the fire. 437

List of Tables

Table IV-1. Axial burn up profile in the active fuel region of the Rail-Steel cask.....	381
Table IV-2. Thermal conductivities for the Rail-Steel cask materials.....	384
Table IV-3. Specific heat for the Rail-Steel cask materials.....	385
Table IV-4. Densities for the Rail-Steel cask materials.....	386
Table IV-5. Emissivity for some of the Rail-Steel cask materials and paints.	386
Table IV-6. Effective thermal conductivity for the fuel-basket region.	388
Table IV-7. Effective thermal conductivity of the aluminum heat conduction elements.	389
Table IV-8. Effective thermal conductivity of the intermediate shells in the in-plane directions.	390
Table IV-9. Effective conductivity of the neutron shield region.	390
Table IV-10. Thermal conductivities for the Rail-Lead cask materials.....	410
Table IV-11. Specific heat for the Rail-Lead cask materials.....	410
Table IV-12. Densities for the Rail-Lead cask materials.....	411
Table IV-13. Emissivity for some of the Rail-Lead cask materials.....	411
Table IV-14. Effective thermal properties of the directly loaded fuel basket.	413
Table IV-15. Effective thermal conductivities for the neutron shield region of the Rail-Lead cask.	414
Table IV-16. Axial burn up profile in the active fuel region of the Truck-DU cask	428
Table IV-17. Thermal conductivities for the Truck-DU cask materials.....	429
Table IV-18. Volumetric Specific heat for the Truck-DU cask materials.....	430
Table IV-19. Effective thermal conductivities for the Truck-DU cask materials.....	430
Table IV-20. Effective volumetric specific heat for the Truck-DU cask materials.....	431

APPENDIX IV

DETAILS OF CASK RESPONSE TO FIRE ACCIDENTS

IV.1 Introduction

A thermal analysis of Rail-Steel, Rail-Lead, and Truck-DU cask types is performed to obtain the thermal response of these casks to the hypothetical fire scenarios described in Chapter 4. The approach used to model these casks is similar to the ones used in the HI-STAR 100 and NAC-STC Safety Analysis Reports (SARs) (Holtec International, 2004, NAC International, 2004) and in the GA-4 Final Design Report (FDR) (General Atomics, 1993), a combination of thermal resistor network analysis, and two- and three-dimensional finite element modeling. The thermal resistor network method is used to obtain effective thermal properties for several regions of the casks. These homogenized regions are then added to the finite element model with equivalent effective properties. This process eliminated some of the geometric redundancies and/or discretization complexities inherent in the models, while at the same time keeping the essential thermal response of the casks.

For the Rail-Steel and Truck-DU casks, results reported in the Rail-Steel cask SAR (Holtec International, 2004) and in the Truck-DU cask FDR (General Atomic, 1993), respectively, are used, but modified where necessary to reflect the current study. The approach used to model the Rail-Lead cask is similar to the approach used in the Rail-Lead cask SAR (NAC International, 2004). The only exception is in how the contents of the cask are modeled. In the Rail-Lead cask SAR, the fuel-basket region and the rest of the overpack are modeled explicitly using a three-dimensional, quarter-section of the cask to obtain a steady-state solution. The maximum temperature difference between the center of the fuel-basket region and the inner wall of the overpack obtained in the steady-state solution is then used to calculate the fuel-basket cladding temperature for the regulatory uniform heating flux (see 10CFR71.73), which did not include a fuel-basket region.

In this study, a three-dimensional, quarter section of the fuel basket is used to obtain effective thermal properties for the Rail-Lead cask, fuel basket. The fuel-basket region is replaced in the full-scale, three-dimensional, finite element model using effective properties for the homogenized basket region. With the exception of the fuel basket region, results in the Rail-Lead cask SAR are used to obtain the thermal response of this cask; with minor changes to reflect the current study. Results taken from the Rail-Steel and the -Lead cask SARs and from the Truck-DU cask FDR are checked where possible using formulas taken directly from these reports or using formulas derived from independent analysis.

Some boundary conditions and material properties are slightly different from those used in the Rail-Steel and Rail-Lead cask SARs, and in the Truck-DU cask FDR. The intent of this thermal analysis is to determine the temperature of critical components during and after a hypothetical fire accident using material properties and boundary conditions that closely resemble the conditions in a real fire accident. Since realistic boundary conditions are sometimes difficult to implement using available data and/or current analysis tools, some simplifications had to be made. For example, the insulation material used in the neutron shields of both casks is assumed to decompose completely when its operational temperature limit is reached. In such cases,

conservative assumptions are made to maximize heat input to the casks, as is done in both SARs cited above. In the case of material properties, those presented in the SARs are preferred, followed by those in standard thermal textbooks and journals. For some materials, properties are available but only over a limited temperature range. In such cases, the value available at the highest temperature is used throughout the rest of the temperature range.

As mentioned in Chapter 4, MSC PATRAN-Thermal (P-Thermal) (MSC, 2008) is the finite element heat transfer code used to solve the internal thermal response of the and Rail-Lead casks in the regulatory uniform heating scenario. This scenario effectively simulates fire conditions using a spatially uniform radiation flux over the external surfaces of the casks as established in 10 CFR 71.73. CAFE (Container Analysis Fire Environment) is the computational fluid dynamics (CFD) code used to generate the fire environment for the CAFE regulatory and CAFE non-regulatory scenarios described in Chapter 4. For these scenarios, CAFE and P-Thermal are coupled together to obtain the thermal response of the Rail-Steel and Rail-Lead casks. CAFE generates more realistic fire conditions on the external surfaces of the casks, as opposed to spatially uniform heating conditions. P-Thermal uses CAFE-predicted, external conditions to calculate the internal thermal response of the casks.

Three hypothetical fire accident scenarios different from the regulatory configuration are analyzed for the rail casks and one hypothetical fire accident scenario, the worst case in the rail cask analysis, is analyzed for the truck cask as described in Chapter 4. These scenarios represent the hypothetical case in which the fuel pool and the cask are separated by one rail car width or one rail car length.

In the following sections, the geometry, material properties, and boundary conditions used to model the Rail-Steel, Rail-Lead, and Truck-DU casks are described, and results that supplement discussions in Chapter 4 are shown. The three-dimensional domain and the boundary conditions used in the CAFE runs are described first, followed by the geometry and boundary conditions used in the Rail-Steel and Rail-Lead, P-thermal, finite element, cask models. Finally, results from two CAFE benchmark runs are presented.

IV.2 CAFE Finite Volume Domain and Boundary Conditions

CAFE (Suo-Antilla et al., 2005) uses the finite volume approach with orthogonal Cartesian discretization to solve: (1) the three momentum equations for predicting the velocity and momentum field, (2) the mass continuity equation, (3) the energy equation for predicting the temperature field, (4) the equation of state, (5) a number of scalar transport equations for tracking the flow of species, and (2) two transport equations to solve thermal radiation within and external to the fire. CAFE uses a variable density PISO (Pressure-Implicit Split-Operator) algorithm to obtain a velocity field which satisfies both the momentum and continuity equations. CAFE has a number of turbulence models, but for this study a large eddy simulation formulation is used. Thermal radiation transport within and near the fires is split into two types: diffusive radiation inside the flame zone and clear air radiation outside the flame zone. Diffusive thermal radiation transport is modeled with the Rosseland approximation. Clear air radiation outside the flame zone is modeled using view factor methods.

CAFE is coupled to P-Thermal through a set of user subroutines that are responsible for passing temperature and thermal heat flux data between both codes. CAFE uses a specialized scheme to

map the temperature and heat fluxes to the exterior surfaces of the finite element model (Suon-Antilla et al., 2005). MSC PATRAN is the front end code employed to generate the material database, the finite element discretization, and the boundary conditions used by P-Thermal. It is through a special boundary condition, setup in PATRAN, that CAFE and P-Thermal are able to exchange data.

Figure IV-1 illustrates the domain configurations used in the CAFE fire scenarios discussed in Chapter 4. Figure IV-1(a) shows the computational fluid dynamics domain used for the CAFE regulatory run, and Figure IV-1(b) through Figure IV-1(d) show the domain for the CAFE non-regulatory runs. As explained in Chapter 4, all non-regulatory CAFE runs were determined based

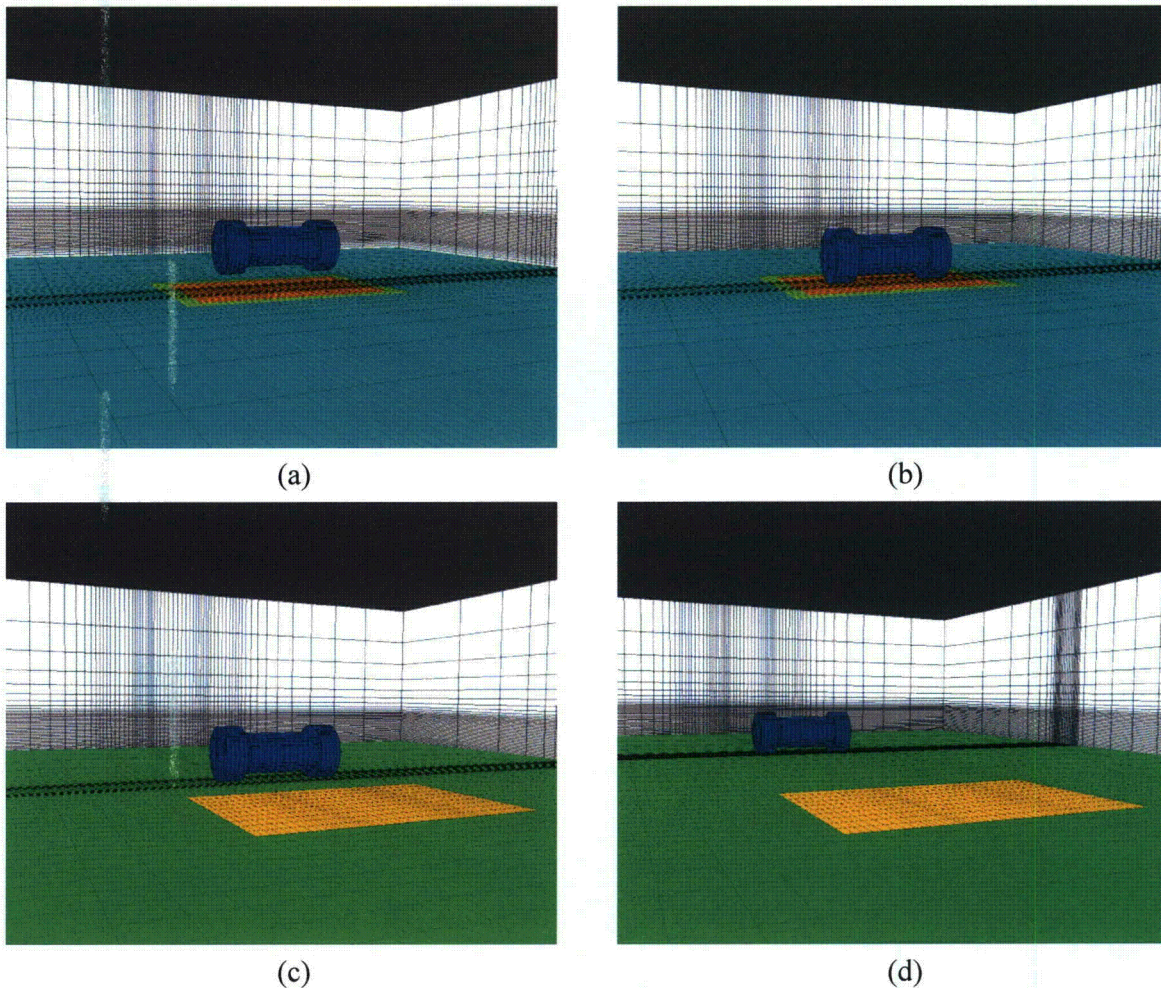


Figure IV-1. CAFE three-dimensional domain: (a) CAFE regulatory fire, (b) cask on ground and at the center of the pool, (c) cask on the ground and 3m (10ft) from the edge of the pool, (d) cask on the ground and 18.3m (60ft) from the edge of the pool.

on the severity and frequency of occurrence of the scenario. A square pool is used to assure the specifications from 10CFR71.73 are met in the case of regulatory fires. For consistency the pool remained a square in all other cases. The pool area is 9.25x13.80m (30.35x45.28ft) in the Rail-Steel cask configurations, and 9.14x12.42m (29.99x40.75ft) in the Rail-Lead cask configurations. These pool areas corresponded to a fully-loaded rail tank car burning over a period of 3 hours, the maximum burn time based on 113.6m³ (30,000 gallons) of fuel. The pool area is 8.3x12m (27.2x39.3ft) in the Truck-DU cask configuration. These pool area corresponded to a fully-loaded, fuel tanker-truck burning over a period of 1 hours, the maximum burn time based on 34.1m³ (9000 gallons) of fuel. Only the scenario depicted in Figure IV-1(b), the most severe fire scenario in the analysis of the rail casks, was analyzed for the Truck-DU. The pool edges remained 3m (9.8ft) away from the surface of the cask in all cask runs.

An appropriate domain size is determined from del Valle et. al. (2007) and from del Valle (2009), in which thermal analyses were conducted with CAFE using a calorimeter the size of a rail cask. In these studies, results of CAFE runs are compared to experiments and showed good agreement. In the current study, the ground dimensions varied between cases since a larger domain is required for the cask offset cases, but are at least 25x15x25m (82x49x82ft), about the size of the domain used in del Valle et. al. (2007) and del Valle (2009). A mesh refinement study is conducted to assess the sensitivity of the cask external temperatures to mesh size and to determine an appropriate mesh size. Based on this study, a mesh with approximately 90,000 finite volumes was deemed acceptable for this study for both casks. As observed in Figure IV-1, the mesh is finer in the region near the pool. All CAFE scenarios used calm wind conditions; the velocity at the boundaries and inside the domain are originally set to zero, but are allowed to float as the fire develops. The Rail-Steel Cask

The Rail-Steel cask is designed for transportation of a variety of nuclear spent fuel assemblies and is intended to fit horizontally on a rail car bed (see Figure IV-2). Therefore, the Rail-Steel cask system is assumed to be in the horizontal position in all CAFE runs (see Figure IV-1), as it would be after derailment if the flatbed rail car overturns or if the cask detached from a rail car after an accident. Only the thermally relevant components of the Rail-Steel cask are considered in this thermal analysis. As stated in the introduction, some results reported in the Rail-Steel cask SAR (Holtec International, 2004) are used in this analysis. Values taken from this report are checked where possible to assess validity of assumptions and to verify results.

IV.2.1 Geometric Consideration

The Rail-Steel cask consists of an overpack, a multipurpose canister (MPC), and two impact limiters; these components fit together as shown in Figure IV-3. The MPC stores the nuclear spent fuel material, and is sealed tight to prevent the contents from leaking into the overpack inner cavity. The MPC is the first containment barrier in the Rail-Steel cask. The overpack is designed to attenuate both the heat, and the neutron and gamma rays generated inside the MPC. The overpack is also sealed tight to prevent the contents from a breached canister from further leaking into the external environment; thus, the overpack forms the second containment barrier in the Rail-Steel cask. During transportation, the overpack ends are fitted with impact limiters that, besides absorbing most of the impact energy during an impact, add an additional thermal insulation layer to the extreme ends of the overpack when intact.

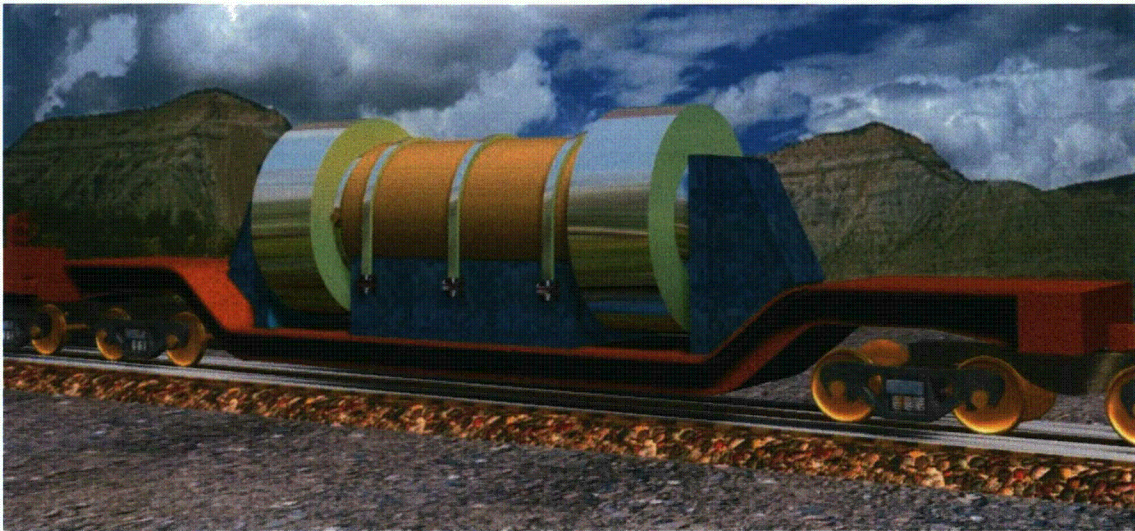


Figure IV-2. Rail-Steel cask transportation system

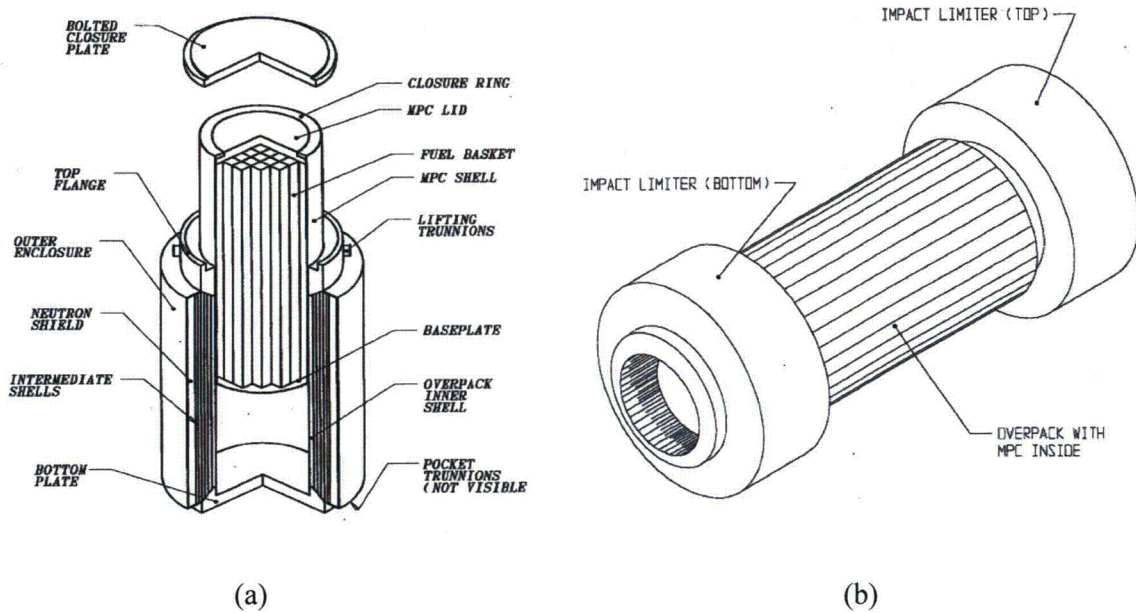


Figure IV-3. Rail-Steel cask: (a) assembly of MPC and overpack, and (b) cask with limiters (Holtec 2004).

IV.2.1.1 The Overpack

The Rail-Steel overpack is a multilayered cylindrical vessel approximately 2.11m (83.3in) in diameter and 5.16m (203.1in) in length. The inner cavity of the overpack is approximately 1.75m (64.7in) in diameter and 4.85m (191.1in) in length. The inner cavity is formed by (1) welding a thick wall cylinder, called the inner shell, to a metal base cup at the bottom and to a large diameter flange at the top, and (2) bolting a closure plate onto the flange as shown in Figure IV-4. Five thin wall cylinders, tightly fitted to one another and to the inner shell, form the next structural layer of the overpack, strengthening the overpack against puncture or penetration. These cylinders are jointly referred to as the intermediate shells and act as the gamma shield. Channels welded to the outermost intermediate shell extend radially outward and delimit the last layer of the overpack. These channels act as fins enhancing conduction to the periphery of the overpack. Plates welded between the ends of each successive channel complete the outer enclosure shell of the overpack. The cavities formed between the channel walls, and between the outermost intermediate shell and the outer enclosure plates are filled with a neutron shield material which provides thermal insulation in addition to neutron attenuation. The outermost intermediate shell, the neutron shield region, and the outer enclosure shell effectively extend the diameter of the overpack an additional 32.3cm (12.7in) beyond the perimeter of the flange and the metal base cup.

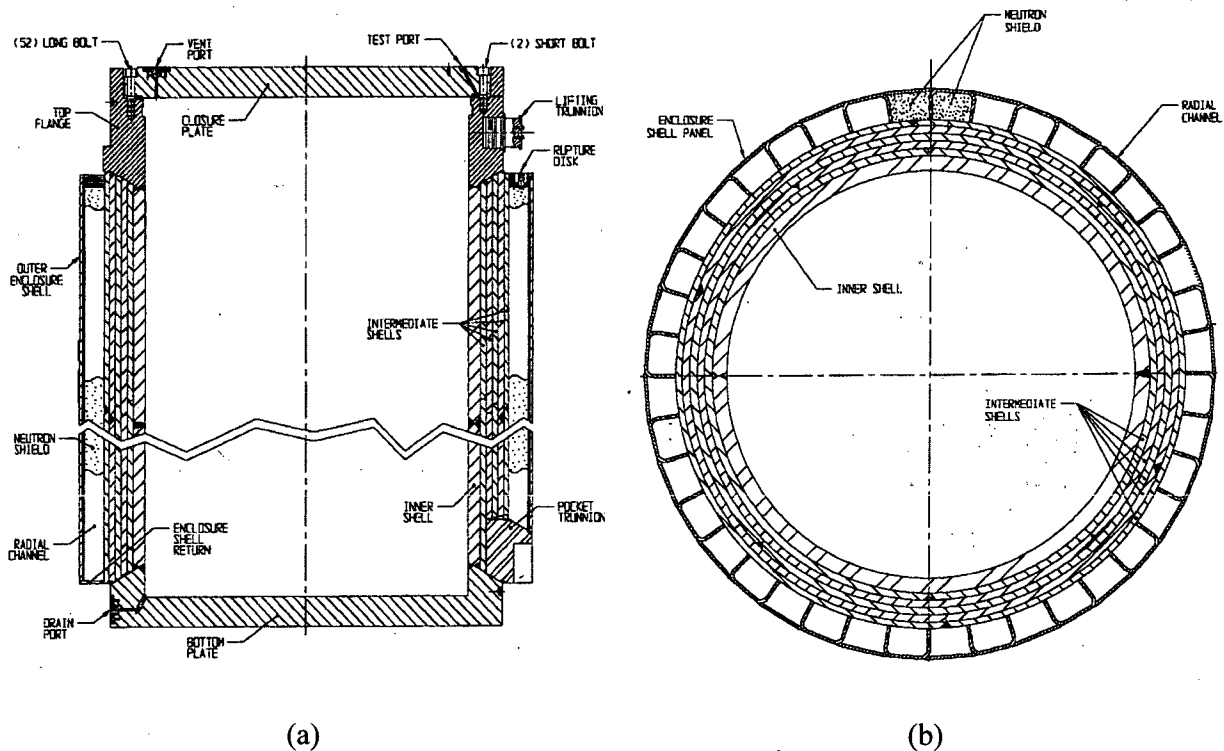


Figure IV-4. Rail-Steel cask overpack: (a) cross-sectional view through the center of the cask, (b) cross-sectional view through the mid-plane of the overpack (Holtec 2004).

The overpack shells, metal base cup, flange, closure plate, and neutron shield region are the major components of the overpack and together comprise most of its volume. The overpack shells, metal base cup, flange, and closure plate are represented explicitly in the thermal model with minor alterations to simplify the solid modeling and meshing process. The most significant change is extending the length of the inner layers of the overpack shells to the length of the outer layer. Note these length changes are expected to have a minor effect on the overall thermal response of the overpack, and only in the radial direction since the materials used for the metal plate cup and flange have similar properties (carbon steel) to the overpack shells. The intermediate shells and the neutron shield region are each represented as a single volume also to minimize geometric complexity; however, their thermal properties are properly accounted for in the thermal model using the techniques described in Sections IV.2.3.3 and IV.2.3.4.

The overpack contains additional components used to service the overpack during normal operations or designed to function only during abnormal ambient conditions such as fires. These features include seals, gas ports, rupture disks, and lifting and pocket trunnions as observed in Figure IV-4. These components are not included in the model because their effects are assumed: (1) negligible due to their small volume and mass relative to the other components in the overpack, (2) highly localized with no effect to the overall thermal performance of the cask at locations of interest, or (3) both.

IV.2.1.2 Multipurpose Canister

The MPC is a cylindrical vessel approximately 1.73m (68.3in) in diameter (outside) and 4.83m (190.3in) in length. The MPC is made from a cylindrical shell 1.2cm (0.5in) thick and 4.76m (187.4in) in length, a circular baseplate 6.35cm (2.5in) thick, and a circular plate lid 24.1cm (9.5in) thick (see Figure IV-5a). The baseplate is welded to the bottom of the MPC shell, and this shell is intern welded to the exterior surface of the lid. At the top, the MPC shell is flushed against a large groove on the end perimeter of the circular plate lid. An annular closure ring welded on the groove and to the top of the shell seals the contents of the MPC. In the horizontal position, the shell and the base plate rest on the inner shell of the overpack. Drain and vent ports on the MPC lid are used to evacuate and fill the MPC with a inert gas (generally helium). With the exception of the closure ring and drain ports, all these components are modeled explicitly. The closure ring is assumed to be part of the lid.

The SNF (or SNF assemblies) is stored in a fuel basket inside the MPC (see Figure IV-5b). The fuel basket is made by welding a series of perpendicular and parallel plates to form an array of storage cells. Each storage cell contains a single fuel assembly. The Rail-Steel cask is designed to carry four general types MPCs: (1) the MPC-24/-24E/-24EF, which contains a maximum of 24 PWR fuel assemblies; (2) the MPC-32, which contains a maximum of 32 PWR fuel assemblies, (3) the MPC-68/-68F, which contains a maximum of 68 BWR assemblies and (4) the MPC-HB, which contains a maximum of 80 Humboldt Bay BWR assemblies. These MPC types are similar in design; however, the MPC-24 is designed to carry a greater specific heat load and the highest total heat load. For this reason, attention is focused on the MPC-24. In the MPC-24, the fuel cells are physically separated from one another by a gas pocket called the flux trap. The length of the fuel basket is approximately 4.48m (176.5in). The fuel assembly might not reach this length; in such cases, spacers are installed on the baseplate and on the MPC lid to hold the fuel assemblies in place (see Figure IV-5a).

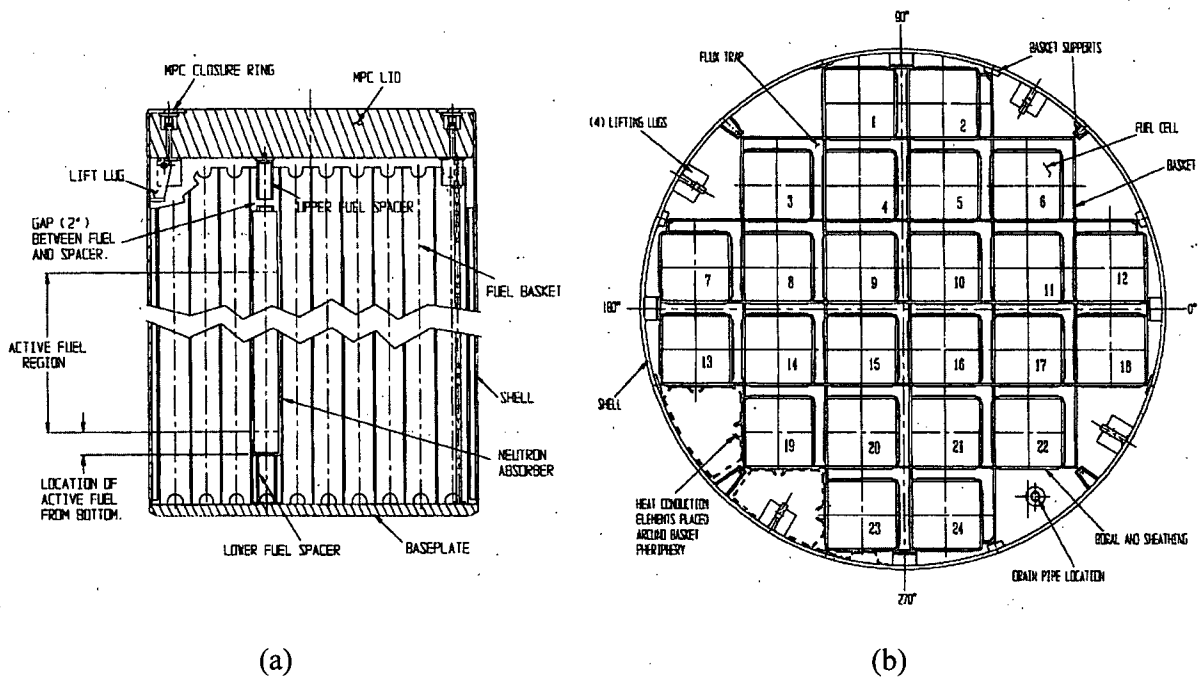


Figure IV-5. Rail-Steel cask MPC: (a) cross-sectional view through the axis of the cask, (b) cross-sectional through the midplane of the overpack (Holtec 2004).

A single fuel assembly consists of an array of fuel rods, each rod separated by a gas space (when the MPC is backfilled) as shown in Figure IV-6a. The total number of rods per assembly varies with fuel assembly design. Each fuel rod consists of a number of cylindrical fuel pellets fitted into a thin walled pipe, called the fuel cladding. The fuel cladding, inner diameter is slightly larger than the diameter of the pellets as shown in Figure IV-6b. The fuel pellets are held tightly against each other using the force of a spring. The radial dimensions of the rod components vary between fuel rod designs. In general, the length of the fuel column is only a fraction of the total length of the fuel rod and marks the active fuel region. The total length of the fuel rod is approximately the same as the length of the fuel assembly. Additional supports are added to the ends of the fuel assembly and at regular intervals along the length of the assembly for structural integrity, to maintain spacing between the rods, and for handling purposes.

The Rail-Steel cask system is designed to carry a number of PWR fuel rods; it's impractical to analyze the Rail-Steel cask system with all these fuel rod designs. Similarly, it's impractical to model the MPC contents with all the components described above because: (1) the wide range of component length scales creates additional meshing complexities, and (2) alternative methods have been employed in the SAR literature and in this study to obtain equivalent thermal properties for the MPC internal contents with good results (see Section 0). Hence, the fuel-basket region, which includes the fuel assembly, basket walls, and flux trap gaps, is not represented explicitly in the Rail-Steel cask model.

The MPC shell contains support structures that help keep the fuel basket laterally in place and lift logs which are used during loading and unloading operations. Some slots between the periphery

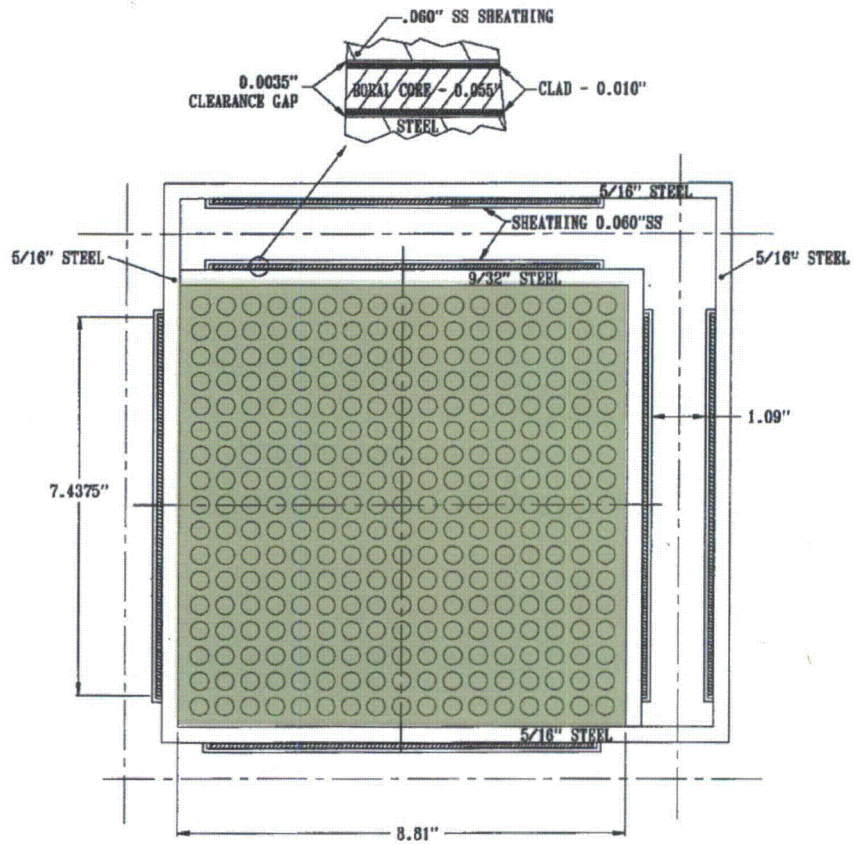
of the fuel basket and the MPC shell wall contain thin wall heat conduction elements. These conduction elements extend the full length of the basket and provide an effective heat conduction path between the MPC basket and MPC shell. With the exception of the heat conduction elements, all other structural elements in the fuel-basket periphery region are ignored for the same reason cited in Section IV.2.1.1. The fuel heat conduction elements are not represented explicitly, but their thermal effect is included through the use of a simplified analytical model explained in the Rail-Steel cask SAR.

To simplify the modeled geometry, the fuel-basket region and fuel-basket periphery region are modeled as two concentric cylindrical regions extending the length of the fuel assembly (see Figure IV-7). The diameter of the equivalent fuel-basket region (Zone 1) is calculated in Holtec International (1997) using the hydraulic diameter of the fuel-basket periphery region (Zone 2). The hydraulic diameter takes into account the perimeter of the fuel basket and MPC inner shell wall, and the average basket-to-shell gap length—indirectly obtained from total surface area between the perimeter of the fuel basket and MPC inner wall—through which heat transfer occurs. For the MPC-24 basket, the hydraulic diameter is approximately 12.7cm (5in) (Holtec International, 1997). The hydraulic diameter is also equal to the inner diameter of the MPC shell minus the inner diameter of the equivalent fuel-basket cylinder region; in this way the equivalent fuel-basket cylinder diameter and periphery annulus gap length may be obtained (Zone 2). The hydraulic diameter takes into account the perimeter of the fuel basket and MPC inner shell wall, and the average basket-to-shell gap length—indirectly obtained from total surface area between the perimeter of the fuel basket and MPC inner wall—through which heat transfer occurs. For the MPC-24 basket, the hydraulic diameter is approximately 12.7cm (5in) (Holtec International, 1997). The hydraulic diameter is also equal to the inner diameter of the MPC shell minus the inner diameter of the equivalent fuel-basket cylinder region; in this way the equivalent fuel-basket cylinder diameter and periphery annulus gap length may be obtained.

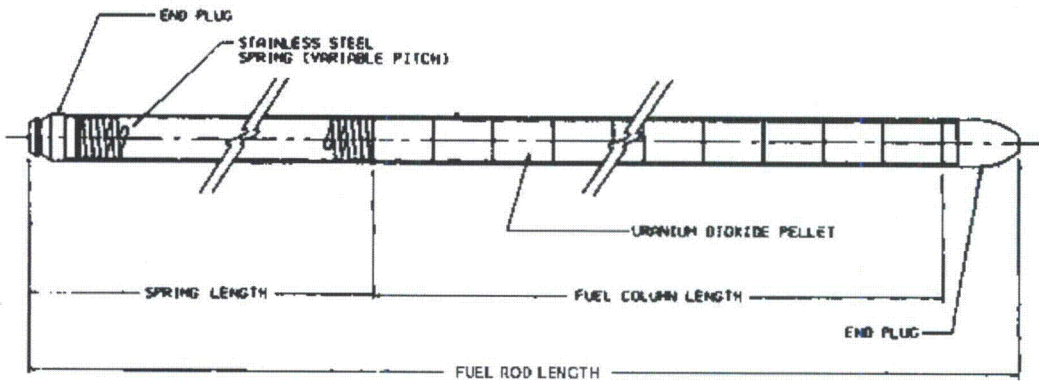
IV.2.1.3 Rail-Steel Cask Impact Limiters

The impact limiters are relatively low density cylindrical components that are not only designed to absorb energy during impact but also serve as insulators during fires in the uncrushed state. The main body of the impact limiter has a maximum diameter of 3.25m (128in) and a maximum length of 1.52m (60in) Figure IV-7.

Most of the impact limiter is honeycomb material enclosed in a thin shell metal wall. The honeycomb material and outer shell walls are supported in the interior of the limiter by a large-diameter circular plate welded (1) on one side to a small-diameter, thin-wall, cylinder and (2) on the perimeter to a large-diameter, thick wall, cylinder. The small- and large-diameter cylinders extend axially outward from the large-diameter plate into the interior of the limiter a distance of approximately 54.9cm (21.6in) and 34.6cm (13.5in), respectively. The small diameter cylinder forms the smallest diameter cavity in the impact limiter, on the side facing the external environment. This air-filled cavity is covered with a circular plate. In the upper limiter, the large diameter cylinder also extends in the opposite direction a distance of 36.8cm (14.5in) from the large-diameter plate, protruding beyond the surface of the limiter facing the overpack. In the lower limiter, the large-diameter cylinder only extends from the large-diameter plate to the surface of the limiter. Triangular channels are welded to the large-diameter plate and to the large-



(a)



(b)

Figure IV-6. Fuel assembly (Holtec 2004) (a) and fuel rod (b).

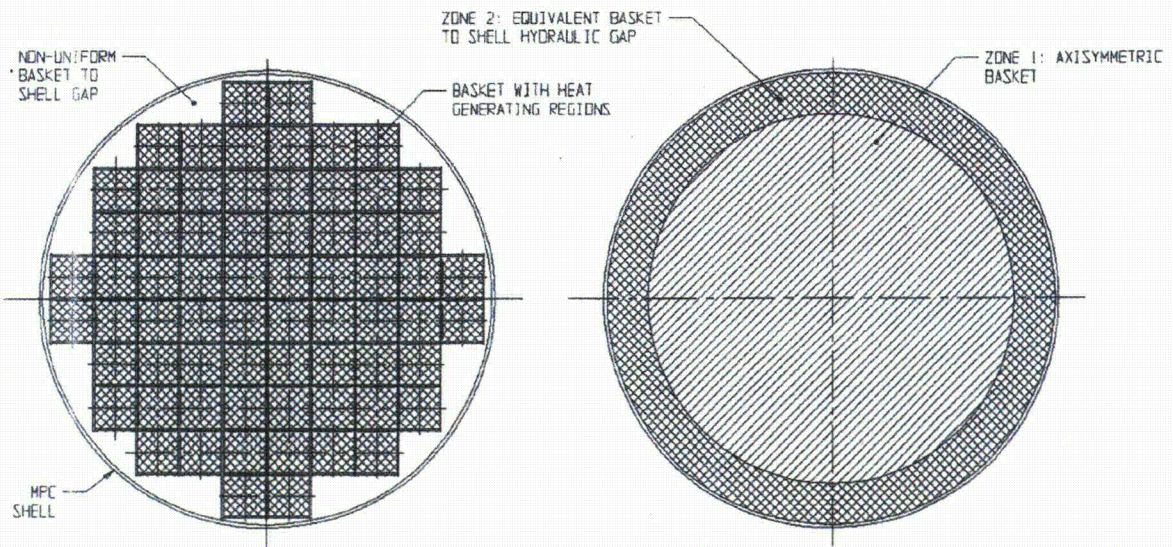


Figure IV-7. Fuel-basket region (left) and equivalent fuel-basket region (right). (Holtec 2004).

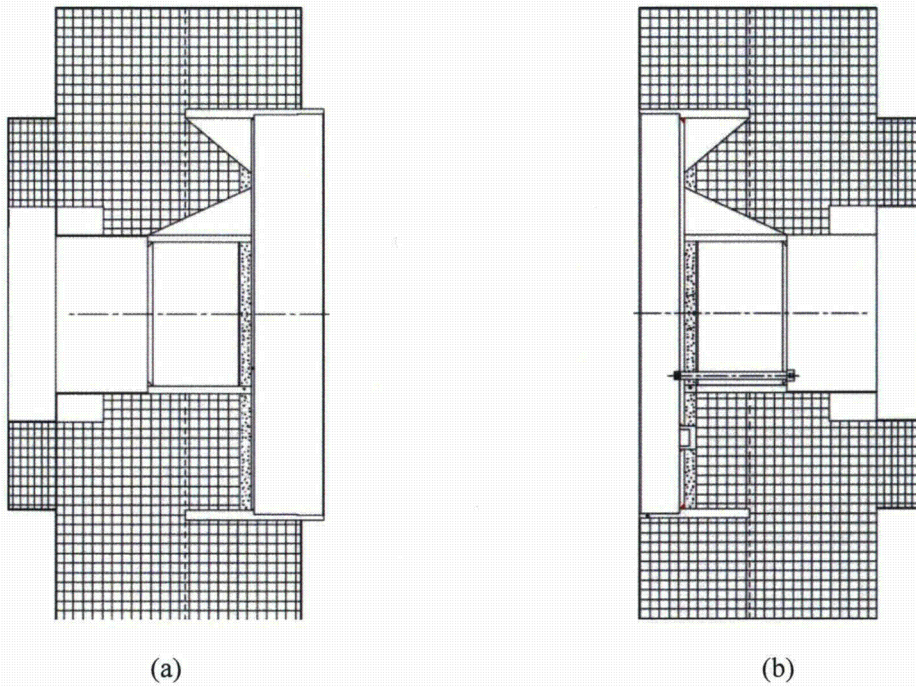


Figure IV-8. Rail-Steel cask upper (a) and lower (b) impact limiters (Holtec 2004)..

and small-diameter cylinders at regular angular intervals in the interior of the impact limiter. Each impact limiter contains a circular segment of neutron shielding, 6.35m (2.5in) thick, next to the large-diameter plate and between the triangular channels. This neutron shield provides axial neutron attenuation and serves as a heat barrier between the impact limiter body and the overpack ends. The neutron shield is covered at the other end by a thin shell wall.

The impact limiters are bolted to ends of the overpack. The upper limiter bolts to the sides of the flange and the lower limiter to the metal base cup.

The impact limiters are assumed to stay intact after the hypothetical accident scenarios described in Chapter 4. This assumption is reasonable since the height of the flatbed rail car is approximately that of the diameter of the overpack. This height precludes any significant damage to the impact limiter during an accident scenario involving, for example, the overturn of the rail car flatbed. Since the limiters are assumed to stay intact, they are modeled in their original shape. The impact limiter, shell walls are not considered. The neutron shield material in the limiters is retained since it serves as a heat barrier between the main body of the limiter and the overpack. Only the large-diameter, thick-wall, cylinder is explicitly modeled since it serves as a direct conduction path from the exterior to the interior of the limiter.

IV.2.2 Rail-Steel Cask Thermal Behavior and Model Assumptions

The MPC-24 is designed to carry a maximum heat load of 20kW (0.833kW per fuel assembly). This heat generation rate is non-uniform along the length of the active fuel region. Table IV-1 shows the normalized, axial heat generation rate distribution for a typical Rail-Steel cask, PWR assembly (Holtec International, 2004). This table is used in Holtec International (1997) to calculate the heat generation rate through the active length of the basket (i.e., in the axial direction). The Rail-Steel cask system is designed to reject heat passively to the environment under normal conditions of transport. Thus, heat is dissipated from the fuel rods to the exterior surfaces of the cask only by a combination of conduction, convection, and radiation heat transfer modes.

Table IV-1. Axial burn up profile in the active fuel region of the Rail-Steel cask.

Axial Distance from Bottom of Active Fuel(% of Active Fuel Length)	Normalized Value
0% to 4-1/6%	0.548
4-1/6% to 8-1/3%	0.847
8-1/3% to 16-2/3%	1.077
16-2/3% to 33-1/3%	1.105
33-1/3% to 50%	1.098
50% to 66-2/3%	1.079
66-2/3% to 83-1/3%	1.050
83-1/3% to 91-2/3%	0.960
91-2/3% to 95-5/6%	0.734
95-5/6% to 100%	0.467

For normal transportation conditions, the external temperature is higher than the internal temperature of the cask; therefore, heat will be dissipated outwardly starting from the fuel rods. Inside the fuel rods, heat is dissipated outward by (1) conduction through the gas space between rods; and (2) by radiation exchange between the fuel rods, and between the fuel rods and the walls of the basket. Convection is assumed negligible in this region since radiation effects dominate at high temperatures. Heat is then dissipated by conduction through the gas space in the flux traps, and by radiation between the basket walls. Convection is also assumed negligible in flux trap region. In the fuel-basket periphery, heat is dissipated to the MPC shell (1) by conduction through the heat conduction elements and the gas; and (2) by radiation between the walls of the fuel basket and the MPC, and between the inner walls of the heat conduction elements. In this region, convection enhances heat transfer between the inner walls of the heat conduction elements through the Rayleigh effect; this effect is taken into account through the results provided in the Rail-Steel cask SAR. A two-dimensional, finite element model is used to determine the heat convection coefficient for this region of the basket.

Heat transfer from the MPC shell to the overpack inner shell occurs through a MPC-overpack non-concentric gap. In the horizontal position the MPC makes contact with the overpack at the bottom. This contact gap is approximately 0.5 mm (0.02in) across. In this region, heat is also dissipated by conduction through the variable gas-filled gap, and by radiation between the outer and inner walls of the MPC and overpack, respectively. A two-dimensional, analytical model is used in the Rail-Steel cask SAR to obtain an effective conductivity through the variable length gap and is discussed in Section IV.2.3.2. Heat transfer through the inner and intermediate shells occurs by conduction through the shell material and through the contact gaps between the shells. These contact gaps are assumed to be five microns (2000 μ -in) across as in the Rail-Steel cask SAR. Conduction in the neutron shield region occurs in parallel through the radial connectors and the neutron shield material. A simple thermal resistor network is used to calculate the effective thermal conductivity through intermediate shells and through neutron shield region (see Sections IV.2.3.3 and IV.2.3.4).

The Rail-Steel cask system is designed to maintain the temperature of components below their operational temperature limits¹ for normal conditions of transport, and for a 30-minute, fully-engulfing, regulatory fire and subsequent cool down period (10CFR71.73). For longer fully-engulfing fires, such as the ones depicted in this study, a significant amount of heat may be transferred to the interior of the Rail-Steel cask, raising the temperature of some of its components above their operational temperature limits. This is expected to occur in the neutron shield region. The operational temperature limit of the neutron shield insulation is 149°C (300°F). In our model, the neutron shield material is assumed to decompose completely shortly after it reaches this temperature limit, immediately triggering thermal radiation exchange between the overpack enclosure shell and the outermost intermediate shell. The assumption used here is a significant departure from what is assumed in the SAR, but is conservative in that heat from the fire is transferred more efficiently to the interior layers of the overpack. More will be said in Section IV.2.3 regarding this topic. As with the neutron shield, the aluminum honeycomb is expected to reach temperatures beyond the operational temperature limits. However, the honeycomb material is not expected to completely melt. Given the results in Pierce et. al. (2003),

¹ The term operational temperature limit does not necessarily mean melting point. Operational temperature limits are given in the Rail-Steel SAR.

the regression rate of the honeycomb material is expected to be minimal over a three hour period and have only a local effect.

Heat dissipation through the cross section (i.e., in the axial direction) of the MPC and overpack, and through the limiters is assumed to occur mostly by conduction. Heat conduction occurs in parallel through each of the materials that comprise this cross section. Thermal radiation in the axial direction is possible; however, since view factors tend to diminish with the distance square and angle of view, and the temperature gradients are weak along the axis compared to the radial direction, as observed in contour results presented in Chapter 4, these effects are neglected in the basket region. Thus, radiation effects are assumed to be mostly in the radial direction except near the lateral ends of the MPC. Thermal radiation exchange occurs between the MPC outer surface and the overpack inner lid and between the MPC outer surface and the overpack bottom plate. In the limiters, the thin metal shell covering the neutron shield radiates to the small diameter plate located directly across the air-gap that fills the small diameter cylinder (see Figure IV-8 and the description in Section IV.2.1.3).

With the exception of the contact gaps already mentioned (e.g., between intermediate shell layers and between MPC and overpack), all contact gaps in the Rail-Steel cask are assumed perfect. This assumption is conservative in that heat is allowed to penetrate the Rail-Steel cask with reduced thermal resistance.

IV.2.3 Rail-Steel Cask Materials and Thermal Properties

The Rail-Steel cask system is made from a variety of steel and aluminum alloys. The overpack inner shell is made from SA203-E cryogenic steel, and the metal base cup, flange, and closure plate are made from SA350-LF3 cryogenic steel. The intermediate shells are made from SA516-70 carbon steel, and the radial channels and enclosure plates from SA515-70 carbon steel. The neutron shield material is Holtite-A, a synthetic neutron-absorbing polymer with one percent boron carbide sold commercially under the trade name NS-4-FR (Holtec International, 2004). The variable-length gap between the MPC and overpack is filled with helium.

The MPC shell, lid, and baseplate, and the basket, fuel-cell walls are made from alloy X, a generic term used in various SARs that usually stands for one of the following stainless steel metals: SA304, SA304LN, SA316, or SA316LN (Holtec International, 2004). The thermal properties of SA304 are assumed for these components. Very little difference in thermal properties is found between SA304 and the other stainless steel materials already mentioned. On one side of each fuel cell wall is a thin layer of Boral sandwiched between the fuel cell wall and thin stainless steel sheathing. Boral is a neutron absorber made of boron carbide and aluminum alloy 1100 (Holtec International, 2004). The Boral layer and stainless steel sheathing extend the length of the active fuel region. The MPC-24 is designed to carry intact zircaloy and stainless steel clad fuel assemblies. In this study, the fuel rods are assumed to be made from zircaloy cladding as done in the Rail-Steel cask for conservative results. The fuel pellets are uranium dioxide (UO₂). The MPC heat conduction elements are made from aluminum alloy 1100. All void spaces inside the MPC are filled with helium (Holtec International, 2004).

The honeycomb in the impact limiter is made from aluminum 5052, and the large-diameter, cylinder from carbon steel (SA516). The neutron shield segments are also made from Holtite-A.

Table IV-2 provides the thermal conductivity for materials used in the Rail-Steel cask at several temperatures. For aluminum 1100 and the various carbon steels, data from Rail-Steel cask SAR is available only over a limited temperature range since the analysis in that report showed cask temperatures within a limited range due to the limited 30 minute fire exposure and subsequent cool down. For these materials, the data trend is decreasing; therefore, the thermal conductivity value at the highest temperature is used at higher temperatures, a conservative assumption since the thermal conductivity values used are higher than what they should be. Note also that Holtite-A is replaced with air once the temperature of the neutron shield region reached the operational temperature limit of that material. In reality, only a fraction of the Holtite-A decomposes. Some of the gases generated in the shield region outgas through the neutron shield rupture disks at high pressures. Up to 90% of these gases come from moisture in the Holtite-A (Federal Register, 2000). Experiments show that up to fifty percent (by weight) of the NS-4-FR eventually degrades by the time temperature of the material reaches 800°C, leaving behind charred remains (Soo-Haeng et. al., 1996), and these are not expected to combust (Soo-Haeng et. al., 1996; Federal Register, 2000). The thermal conductivity of helium varies with pressure in addition to temperature; however, the pressure dependency is much weaker over the range of 101 to 689kPa (14 to 100lb/in²) (Petersen, 1970).

Table IV-2. Thermal conductivities for the Rail-Steel cask materials.

Material	Thermal Conductivity W/m-°C (Btu/ft-hr-°F)				
	92°C (200°F)	226°C (450°F)	377°C (700°F)	477°C (900°F)	726°C (1340°F)
Air [§]	0.026 (0.015)	0.040 (0.023)	0.050 (0.028)	0.055 (0.031)	0.067 (0.038)
Stainless Steel [§]	14.5 (8.3)	18.3 (10.5)	20.4 (11.8)	21.9 (12.6)	25.4 (14.6)
Aluminum Alloy 1100*	228 (131)	212 (122)	—	—	—
Aluminum-Honeycomb [‡]	3.5 (2.0)	4.1 (2.4)	4.8 (2.8)	5.2 (3.0)	—
Boral (B ₄ C)*	83.3 (48.2)	83.1 (48.0)	81.3 (47.0)	80.5 (46.5)	—
Carbon Steel- Int. Shells*	42.3 (24.5)	41.7 (24.1)	38.8 (22.4)	—	—
Carbon Steel-N. Shield*	50.7 (29.3)	49.1 (28.4)	42.6 (24.6)	—	—
Cryogenic Steel*	41.1 (23.8)	41.0 (23.7)	38.5 (22.3)	—	—
Helium [§]	0.17	0.22 (0.12)	0.26 (0.15)	0.29 (0.16)	0.35 (0.20)
Holtite-A*	0.65 (0.37)	—	—	—	—
UO ₂ *	6.0 (3.4)	6.0 (3.4)	5.1 (2.9)	—	—
Zircaloy*	13.5 (1.78)	14.6 (8.4)	16.2 (9.3)	17.8 (10.2)	—

[§]Incropera and Dewitt, 1996

*Holtec International, 2004

[‡]Thermophysical Properties Research Laboratory Inc., 2001

Table IV-3 provides the specific heat for these same materials at several temperatures. Temperature dependent values are given only for those materials which exhibited large variation in temperature. With the exception of stainless steel, aluminum 5052, and carbon steel, the specific heat of most materials used in the Rail-Steel cask is fairly constant. Of interest are the properties of carbon steel, the specific heat increases abruptly above 800°C and reaches a peak at around 1010°C (1850°F), the Curie temperature. This behavior is associated with changes in the magnetic state of these materials and has been observed for a great number of carbon steel materials (Yafei, 2009). For Holtite-A, limited data is available above its operational temperature limit. Air properties are used beyond this limit. In addition, radiation exchange between the inner and outer surface of the neutron shield region is also allowed above this operational temperature limit to maximize heat input.

Table IV-3. Specific heat for the Rail-Steel cask materials.

Material	Specific Heat J/kg-°C (Btu/lbm-°F)				
	92°C (200°F)	226°C (450°F)	377°C (700°F)	477°C (900°F)	726°C (1340°F)
Air [§]	1010 (0.24)	—	—	—	—
Stainless Steel [§]	482 (0.11)	535 (0.12)	563 (0.13)	575 (0.13)	611 (0.14)
Aluminum [§]	903 (0.21)	—	—	—	—
Aluminum-Honeycomb [‡]	890 (0.21)	976 (0.23)	1057 (0.25)	1100 (0.26)	—
Carbon Steel [§]	434 (0.10)	505 (0.12)	590 (0.14)	653 (0.15)	1169 (0.27)
Boral (B ₄ C) [*]	2478 (0.59)	—	—	—	—
Helium [§]	5193 (1.2)	—	—	—	—
Holtite-A [*]	1632 (0.39)	—	—	—	—
UO ₂ [*]	234 (0.056)	—	—	—	—
Zircaloy [*]	304 (0.073)	—	—	—	—

Table IV-4 provides densities for stainless steel, carbon steel, zircaloy, and UO₂ at 92°C (200°F), and for air and helium at various temperatures. Since the density of most metals changes very little with temperature, only the values at 92°C (200°F) are used. The density of Holtite-A is assumed not to vary significantly from 92°C to its operational temperature limit. Recall that air properties are used above this limit to replace Holtite-A.

Table IV-5 shows the emissivity values obtained from Rail-Steel cask SAR. The exterior surface of the Rail-Steel cask is coated with Carboline 890 paint and the overpack inner surfaces with Thermaline 450 paints, but these coatings are only good up to 216°C (422°F) and 262°C (505°F), respectively (Holtec International, 2004). Note also the internal surfaces of the heat conduction elements are sandblasted to increase radiation between opposite sides of the heat conduction elements.

Table IV-4. Densities for the Rail-Steel cask materials.

Material	Density kg/m ³ (lbm/ft ³)				
	92°C (200°F)	226°C (450°F)	377°C (700°F)	477°C (900°F)	726°C (1340°F)
Air [§]	0.98 (0.061)	0.69 (0.043)	0.54 (0.034)	0.46 (0.029)	0.35 (0.022)
Stainless Steel [§]	7900 (493)	—	—	—	—
Aluminum [§]	2702 (168)	—	—	—	—
Aluminum-Honeycomb [‡]	526 (32)	—	—	—	—
Carbon Steel [§]	7854 (490)	—	—	—	—
Boral (B ₄ C)*	544 (34)	—	—	—	—
Helium [§]	0.14 (0.008)	0.10 (0.006)	0.077 (0.0048)	0.065 (0.0041)	0.048 (0.003)
Holtite-A*	1681 (105)	—	—	—	—
UO ₂ *	10956 (684)	—	—	—	—
Zircaloy*	6551 (409)	—	—	—	—

Table IV-5. Emissivity for some of the Rail-Steel cask materials and paints.

Material	Emissivity
Zircaloy	0.8
Painted Surface	.85
Rolled Carbon Steel	.66
Stainless Steel	.36
Sandblasted Aluminum	.40

IV.2.3.1 Effective Thermal Properties of Fuel Basket and Fuel-basket Periphery

Thermal properties for the fuel-basket region and fuel-basket periphery are obtained from the Rail-Steel cask SAR. In that report, the fuel basket and the fuel-basket periphery cross sections were replaced with two concentric cylinders each with equivalent effective thermal properties as described in Section IV.2.1.2. The procedure used to obtain the in-plane thermal conductivities of the fuel basket and fuel-basket periphery as a function of temperature is described in this Rail-Steel cask SAR but is summarized here for completeness.

First, the cross section of the fuel assembly is modeled using a detailed two-dimensional, finite element model of the cross-section of a 17x17OAF fuel assembly rod arrangement (see Figure

IV-6a), a uniform heat generation rate over each fuel rod, and a uniform temperature applied to the periphery of the fuel assembly. The 17x17OAF assembly used was determined to be the most resistive assembly design (Holtec International, 2004). The finite element model takes into account radiation between the rods and conduction across the helium gap. The effective thermal conductivity is obtained from the following equation:

where q_g is the heat generation rate per fuel cell per unit length, a is half the length of one side of the fuel cell, and ΔT is the maximum temperature difference in the fuel assembly (Sanders et. al., 1992). Since radiation is not linearly dependent on temperature, the model is run several times, each time with increasing uniform temperature near on the edge of the fuel assembly, to obtain effective properties at various temperatures. The detail fuel assembly is thus replaced with a homogenized fuel cell region (see Figure IV-7)

Second, the in-plane thermal conductivity of the basket storage wall, Boral, and stainless steel sheathing are replaced with an equivalent thermal conductivity using the thermal resistor network described in Rail-Steel cask SAR. The representative network takes into account the thermal resistances perpendicular to the wall and along the wall.

Third, the cross section of the MPC is modeled using a two-dimensional, finite element representation of the homogenized, fuel-basket walls, with a uniform heat generation rate applied over each homogenized fuel assembly, and a uniform temperature applied over the perimeter of the MPC shell. The model in the Rail-Steel cask SAR took into account: (1) conduction through the homogenized fuel assemblies, the helium gas in the flux traps, and the basket periphery, (2) radiation between homogenized basket walls, and (3) convection due to Rayleigh effects in the basket periphery. The effective conductivities of the basket region (k_b) and periphery region (k_p) are given by (Holtec International, 1999):

where

Here ΔT_{bm} is the maximum temperature difference in the basket, ΔT_{pm} is maximum temperature difference in the MPC cross section, A_s is the surface area per unit length, W is basket periphery annular gap length. The equivalent fuel-basket thermal conductivities are given in Table IV-6. The effective axial thermal conductivities of the fuel basket are obtained in the Rail-Steel cask SAR using the resistor method which reduces to an area weighted average since the basket length (L) in the resistance (L/kA) is equal across all materials. The specific heat and density are obtained using a mass and volume weighted average, respectively. Near the ends of the basket, the fuel rods are filled with gas, decreasing the in-plane and axial thermal conductivity of the

basket slightly, since the thermal conductivity of helium is smaller than the UO₂ pellets. Note that the temperature conductivities vary very little in temperature.

The properties in Table IV-6 are used over the length of the basket. For consistency, temperature varying properties are implemented in the thermal model.

Fuel spacers separate the ends of the fuel assembly from the MPC lid and MPC bottom plate. In these regions, conduction is predominately through the helium gas and through the fuel spacer and fuel basket walls. Thermal radiation also occurs between the walls of the basket and the fuel spacers.

The homogenized material properties used in the fuel spacer region are estimated by taking into account the properties of the fuel region, fuel spacer, the helium, the fuel basket ends, and thermal radiation. A sensitivity study using theoretical bounds indicated the temperatures obtained in the regions of interest were barely influenced by the properties used.

Table IV-6. Effective thermal conductivity for the fuel-basket region.

Effective Thermal Properties	92°C (200°F)	226°C (450°F)	377°C (700°F)	477°C (900°F)	726°C (1340°F)
In-Plane Thermal Conductivity W/m-°C (Btu/ft-hr-°F)	1.9 (1.1)	2.6 (1.5)	3.4 (1.9)	—	—
Axial Thermal Conductivity W/m-°C (Btu/ft-hr-°F)	3.4 (1.9)	3.8 (2.2)	4.3 (2.5)	4.6 (2.6)	—
Specific Heat J/kg-°C (Btu/lbm-°F)	305 (0.073)				
Density kg/m ³ (lbm/ft ³)	2688 (168)				

Fourth, the thermal conductivity in the basket periphery is further enhanced to account for heat dissipation through heat conduction elements. The equivalent resistor network through the heat conduction elements is obtained using a two-dimensional, analytical model explained in the Rail-Steel cask SAR. This resistance is added in parallel with the resistance obtained from the two-dimensional, finite element model for the basket periphery region. The fuel-basket periphery, in-plane conductivity is given in Table IV-7.

The axial thermal conductivity is obtained from an area weighted average using aluminum 1100 and helium properties. The area of the periphery region is given in Holtec International (1997). The area of the heat conduction elements is estimated at 3.5 times the fuel-basket, cell pitch (27.3cm [10.7in]), multiplied by the thickness of the elements (3.175mm [0.125in]) and the total number of aluminum inserts (8) (Holtec International, 1999). The specific heat and density of the fuel-basket periphery is obtained from an area and mass weighted average, respectively, again considering only aluminum 1100 and helium.

Heat transfer through the periphery region is further enhanced by radiation between the inner walls of the heat conduction elements and the walls of the MPC and fuel basket. The emissivity of stainless steel and sandblasted aluminum are not very different as observed in Table IV-6.

Table IV-7. Effective thermal conductivity of the aluminum heat conduction elements.

Effective Thermal Properties	92°C (200°F)	226°C (450°F)	377°C (700°F)	477°C (900°F)	726°C (1340°F)
In-Plane Thermal Conductivity W/m-°C (Btu/ft-hr-°F)	0.43 (0.25)				
Axial Thermal Conductivity W/m-°C (Btu/ft-hr-°F)	10 (5.8)				
Specific Heat J/kg-°C (Btu/lbm-°F)	964 (0.23)				
Density kg/m ³ (lbm/ft ³)	132 (8.25)				

IV.2.3.2 Effective Thermal Properties of MPC-Overpack Helium Gap

In the horizontal position, the MPC rests on the overpack forming a non-concentric, variable-length, helium gap. This gap is not modeled explicitly. Instead, a two-dimensional, analytical model derived in Holtec International (1997) is used to obtain an effective conductivity through the variable-length gap. This model included the effects of the contact region as explained below.

To account for radial heat dissipation through the variable-length, helium gap and through the metal-to-metal contact area, equations for the overall heat conducted through these regions are summed and then equated to the overall heat conducted through a concentric gap to obtain an effective thermal conductivity for a constant-length helium gap (i.e., concentric gap). The following equation taken from the Rail-Steel cask SAR is used to obtain the effective thermal conductivity across the gap (k_{gap}):

$$k_{gap} = \frac{k_{gas} t + \epsilon}{t + \epsilon}$$

where k_{gas} is the conductivity of the gas, t is the thickness of the concentric gap and ϵ (0.5mm [0.02in]) is the metal-to-metal, contact area width. Results reported in the SAR show the effective conductivity through the equivalent concentric gap is twice the conductivity of helium.

IV.2.3.3 Effective Thermal Properties of Overpack Intermediate Shells

The Rail-Steel cask consists of a series of shell-gas layers between the inner shell wall and the outermost intermediate shell of the overpack. The contact gaps are assumed to be 0.05 mm (0.002in) across (Holtec International, 2004). No radiation is assumed through these gaps since radiation accounts for less than five percent of the effective conductivity for gaps of this size. The in-plane thermal conductivity is obtained by adding the resistances across each shell and gap in series. The axial and circumferential conductivities are assumed to be that of the shell layer material since the thermal conductivity of air and the gap area of air contribute very little.

Similarly, the specific heat and density of the intermediate shell layers are assumed to be equal to the intermediate shell material.

Table IV-8. Effective thermal conductivity of the intermediate shells in the in-plane directions.

Effective Thermal Properties	92°C (200°F)	226°C (450°F)	377°C (700°F)	477°C (900°F)	726°C (1340°F)
In-Plane Thermal Conductivity W/m-°C (Btu/ft-hr-°F)	13.2 (7.6)	15.6 (9.0)	17.0 (9.8)	18.6 (10.7)	22.1 (12.7)

IV.2.3.4 Effective Thermal Properties of Neutron Shield Region

The neutron shield region consists of the Holtite-A inside the cavities formed between the outermost intermediate shell and the outer enclosure shell, and between the radial channels. Note the outer enclosure shell is not included here since it is modeled explicitly. The neutron shield region includes the Holtite-A material and the radial sections of the channel (2 per channel for a total of 40). This region is also modeled as a single volume with homogenized thermal properties.

Table IV-9 shows the effective properties in the neutron shield region. The effective thermal conductivity in the in-plane and axial direction are obtained by summing the resistance through the radial channels and through the neutron shield material in parallel. Since both the Holtite-A and radial channels extend the same length in the axial direction, the resistance equation in the axial direction reduces to an area weighted average of the individual material conductivities.

Table IV-9. Effective conductivity of the neutron shield region.

Effective Thermal Properties	92°C (200°F)	226°C (450°F)	377°C (700°F)	477°C (900°F)	726°C (1340°F)
In-Plane Thermal Conductivity W/m-°C (Btu/ft-hr-°F)	4.3 (2.4)	3.5 (2.0)	3.2 (1.8)	3.1 (1.8)	2.7 (1.5)
Axial Thermal Conductivity W/m-°C (Btu/ft-hr-°F)	3.6 (2.0)	3.3 (1.9)	3.0 (1.7)	3.0 (1.7)	2.6 (1.5)
Specific Heat J/kg-°C (Btu/lbm-°F)	1315 (0.31)	505 (0.12)	590 (0.14)	653 (0.15)	1170 (0.28)
Density kg/m ³ (lbm/ft ³)	2113	552 (34)			

The thermal conductivity in the circumferential direction is assumed to be that of Holtite-A since the total thickness of the radial channels in this direction is small compared to the total circumferential length of the Holtite-A. Note that this is a conservative assumption in the sense

that heat dissipated through the neutron shield region is preferentially in the in-plane and axial directions as a result of the latter assumption. This assumption does not have an impact in the uniform heating run, but it does have impact on the CAFE-fire runs, where heat input around the circumference of the cask varies. In this case, heat will be dissipated more readily through the in-plane direction; thus giving higher temperatures in the interior of the cask.

The specific heat and density of the neutron shield region are obtained using a mass and area weighted average, respectively. Holtite-A is expected to reach its temperature limit during the early transient period of a fire. When this happens, Holtite-A partially decomposes leaving char residue behind. Most of the excess gas generated in Holtite-A outgases through the rupture disks when the pressure inside the neutron shield region reaches the disks design limits. In the thermal model, when Holtite-A temperature limit is reached, Holtite-A is replaced with air, and radiation is activated by setting the emissivity to an appropriate value. Note that air effectively lowers the specific heat and density of the neutron shield region. The effective specific heat of the neutron shield region is greatly influenced by the specific heat values of carbon steel since the density of air in the mass weighted average is very small compared to carbon steel.

IV.2.4 Rail-Steel Cask, Finite Element Model and Boundary Conditions

A steady-state case is run to obtain the initial conditions of the Rail-Steel cask and to compare results against those provided in the Rail-Steel SAR and in Adkins et. al. (2006). The steady-state model consisted of the Rail-Steel cask being exposed to a 37.8°C (100°F) ambient temperature, radiation boundary condition. This boundary condition is applied over the entire outer surface of the cask using an emissivity of 0.85. In addition, insolation is applied over the outer curved surfaces of the cask (193.8W/m² [34.1 Btu/ft²-hr-°F]) and over the flat ends of the cask (96.9W/m² [17.0 Btu/ft²-hr-°F]) as specified in the American Society of Testing Materials E 2230 (ASTM 2008). A convection boundary condition is also applied to the outer surface of the cask using a heat transfer coefficient of 3W/m² (5 Btu/ft²-hr-°F). This value is obtained from a set of correlations described in the Rail-Steel cask SAR—assuming turbulent flow—and is within the same order of magnitude as values obtained from correlations in (Incropera and Dewitt, 1996).

In general steady-state results are slightly higher than those presented in the Rail-Steel cask SAR, but lower than those reported in Adkins et. al. (2006). For example, the current study found a maximum fuel cladding temperature of 376°C (710°F), compared to 372°C (701°F) in the Rail-Steel cask SAR and 392°C (738°F) in Adkins et. al. (2006). The largest differences are observed in the extreme ends of the overpack, where temperatures in the Rail-Steel cask are lower (by ~25°C) than reported here and significantly lower (~50°C) than what is reported in Adkins et. al. (2006). These differences are attributed to dissimilarities in modeling assumptions and approaches, and boundary conditions. For example, in Adkins et. al. (2006) a gap is assumed between the overpack and the limiters. Overall, however, the temperatures obtained from these three studies showed similar spatial trends and good agreement given the differences cited above.

The steady-state case is used to assess the suitability of the mesh. The mesh is initially 169,600 elements; this corresponded to a nominal element size of 10.2cm (4in). This value is decreased to 5.1cm (2in) and then increased to 15.2cm (6in) to study the effects of element size on temperatures at locations of interest (as shown in the results of Chapter 4 and later in this Appendix). Results of the 15.2cm, element-size mesh showed some difference in the

temperatures in the interior of the cask when compared to those of the 10.2cm, element-size mesh. This is expected since large cells are created in the interior of the cask. Near the exterior of the overpack, small geometric features resulted in small size elements. Results of the 5.1cm, element-size mesh showed very little difference when compared to the 10.2cm element mesh. The 5.1cm, element-size mesh had smaller elements in the interior and about the same near the exterior of the overpack. Therefore a third case is run, this time using the 10.2cm mesh, with a refined mesh in the near the exterior of the overpack. Results from this mesh showed some difference (less than 5 degrees in the neutron shield region), but not enough to justify the extra computational time needed to run this mesh. Figure IV-9 shows the final mesh used to run the five scenarios described in Chapter 4.

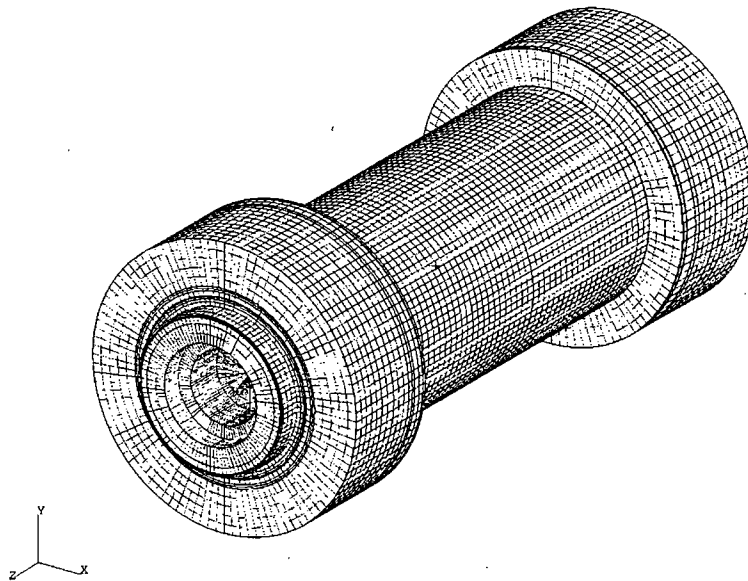


Figure IV-9. Rail-Steel cask finite element mesh (model is symmetric, only half shown).

The uniform heating case described in Chapter 4 is run initially to verify the Rail-Steel cask FE model. This exercise gave an additional measure of confidence in the Rail-Steel cask model. The boundary conditions for this case consisted of the Rail-Steel cask being exposed to an 800°C (1472°F) ambient-temperature, radiation boundary condition. This boundary condition is applied over the entire outer surface of the cask using an emissivity of 0.9. A convection boundary condition is also applied to the outer surface of the cask using a heat transfer coefficient of 85W/m² (15.2 Btu/ft²-hr-°F). This value is obtained in the Rail-Steel cask SAR from a set of correlations described there and assuming a 15m/s (49ft/s) vertical flame speed, a value significantly higher than what is specified in Nakos (2005) but nevertheless conservative in that it will result in a higher heat input to the cask. Convection accounts for about 10-20% of the total heat input for large objects inside a fire, the rest is through thermal radiation (Nicolette and Larson, 1989).

The uniform heating case is run for 30 minutes, followed by an 11.5 hour transient cool down. During the cool down period, the boundary conditions are set back to their steady-state case

values, except for the emissivity of the outer cask which remained the same to simulate what happens in actual fires—a blanket of soot covers the cask. Also, the neutron shield region is assumed to contain air with radiation interaction between the outer enclosure shell and the outermost intermediate shell.

Overall, maximum temperatures obtained using the model developed here and in the Rail-Steel cask SAR are similar. The difference in purpose of the two analyses leads to some different assumptions, which in turn leads to slightly different results.

For the remaining cases, the external boundary conditions are obtained from CAFE, the computational fluid dynamics code coupled to P-Thermal. As is mentioned in Section IV.2, a boundary condition is setup in PATRAN that allowed CAFE results to be communicated to P-Thermal and vice-versa. The cool down period for these cases also used the steady-state case boundary conditions (from 10 CFR 71.71).

IV.2.5 Rail-Steel Cask Thermal Analysis Results

Pages 394 through 402 show results for the five scenarios already described in Chapter 4. These results are not discussed here, but are presented to supplement results discussed in Chapter 4. Figure IV-10 shows results for the regulatory uniform heating case cited in the previous section. This is the P-Thermal only run. Figure IV-11 shows results for the regulatory CAFE fire and together with Figure IV-10 may be useful in determining the differences between uniform and non-uniform fire conditions. The effect that large objects have on fires and their implications to modeling large casks in fires has been discussed in Nicolette and Larson (1989). Figure IV-12 shows results for the fully engulfing CAFE fire with the cask on the ground, and Figure IV-13 and Figure IV-14 show results for the cask on ground but outside the fire. The last three cases are for a three hour fire and subsequent cool down period.

IV.3 Rail Cask with Lead Shielding

The Rail-Lead cask (NAC International, 2004) is also certified to transport spent nuclear fuel material on rail cars. This cask is chosen because it presents quite a different design philosophy from the Rail-Steel cask. The Rail-Lead cask uses lead for the gamma shield. Moreover, the Rail-Lead cask is certified to carry SNF without a separate MPC. As in the Rail-Steel cask analysis, the Rail-Lead cask is assumed to be in the horizontal configuration, as it would be during transportation, and most likely after an accident scenario. Only the thermally relevant components of the Rail-Lead cask are considered to estimate the thermal response of this cask.

The Rail-Lead cask uses a single lead gamma shield as opposed to a multilayer carbon steel gamma shield like the one used in the Rail-Steel cask. This lead shield melts at relatively low temperatures, but remains in the overpack in molten form until the temperature is low enough to change back to the solid state. This process has an impact of the cask ability to attenuate gamma rays as described in Chapter 5 and Appendix V. One unique feature of the Rail-Lead cask is that it can transport the spent nuclear fuel in a directly loaded fuel basket in addition to inside an MPC as is seen in the Rail-Steel cask. The directly loaded configuration is a significant design departure from the MPC configuration since there is no barrier between the fuel assemblies and

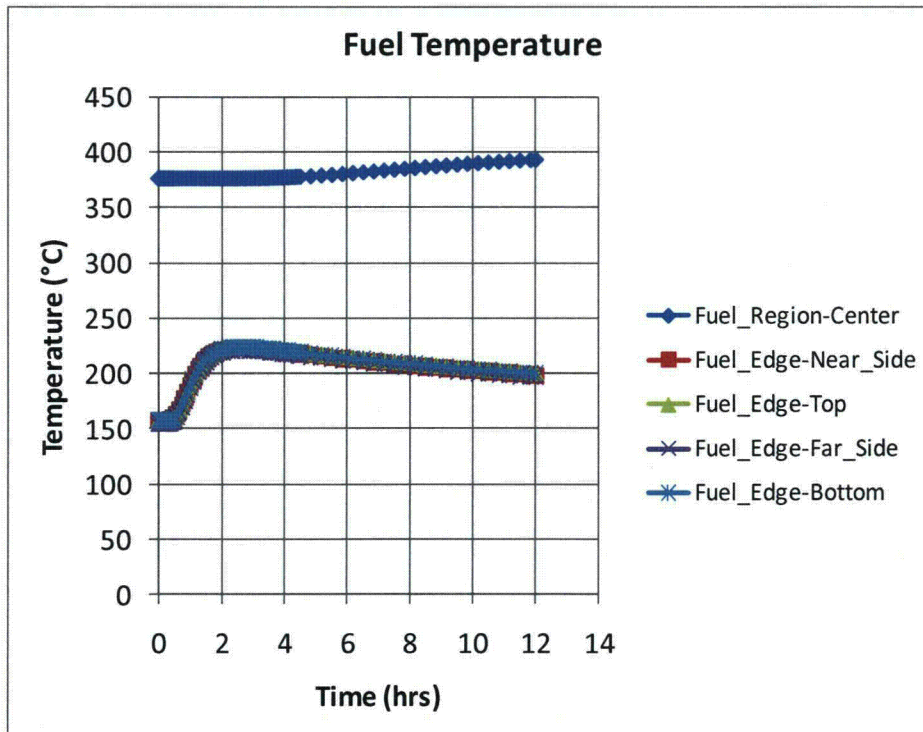
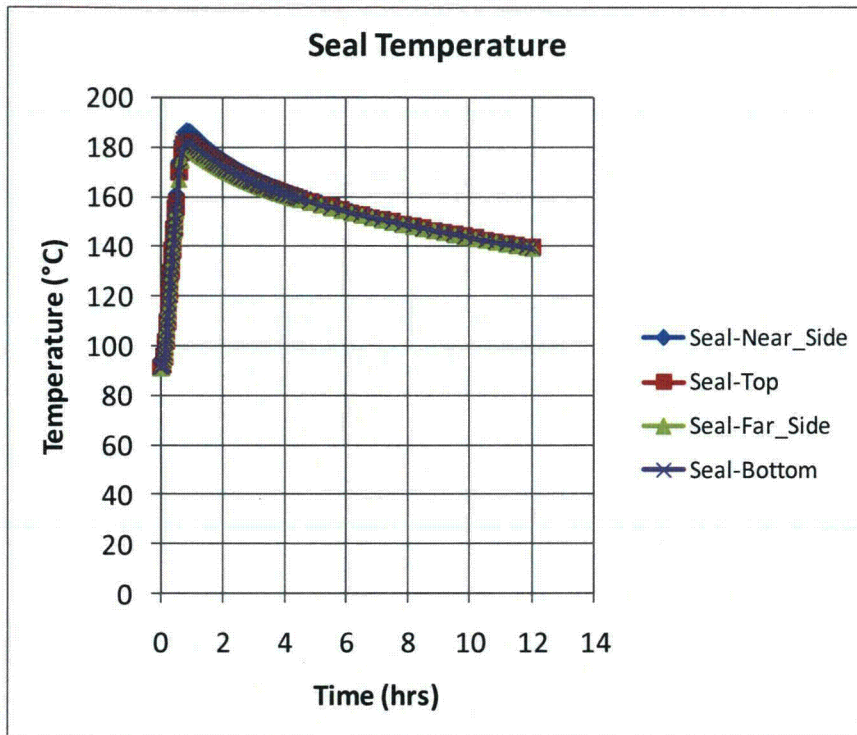
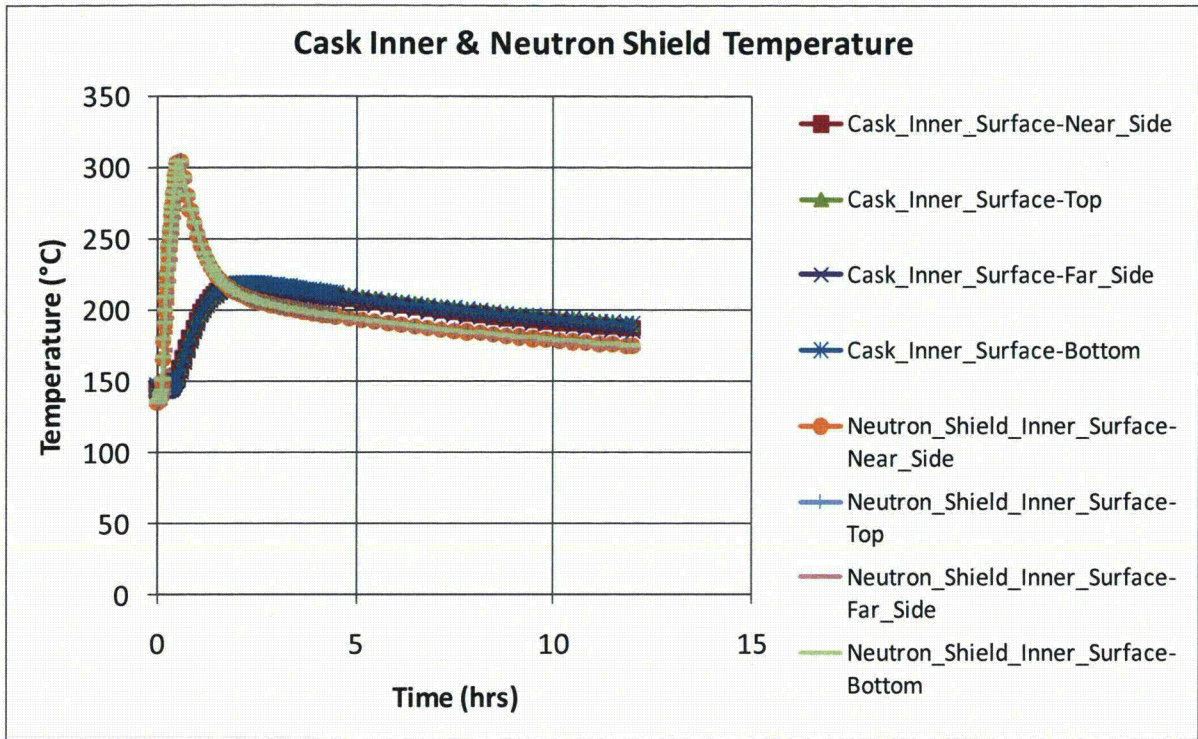


Figure IV-10. Rail-Steel Cask Regulatory Uniform Heating Results (P-Thermal)



S

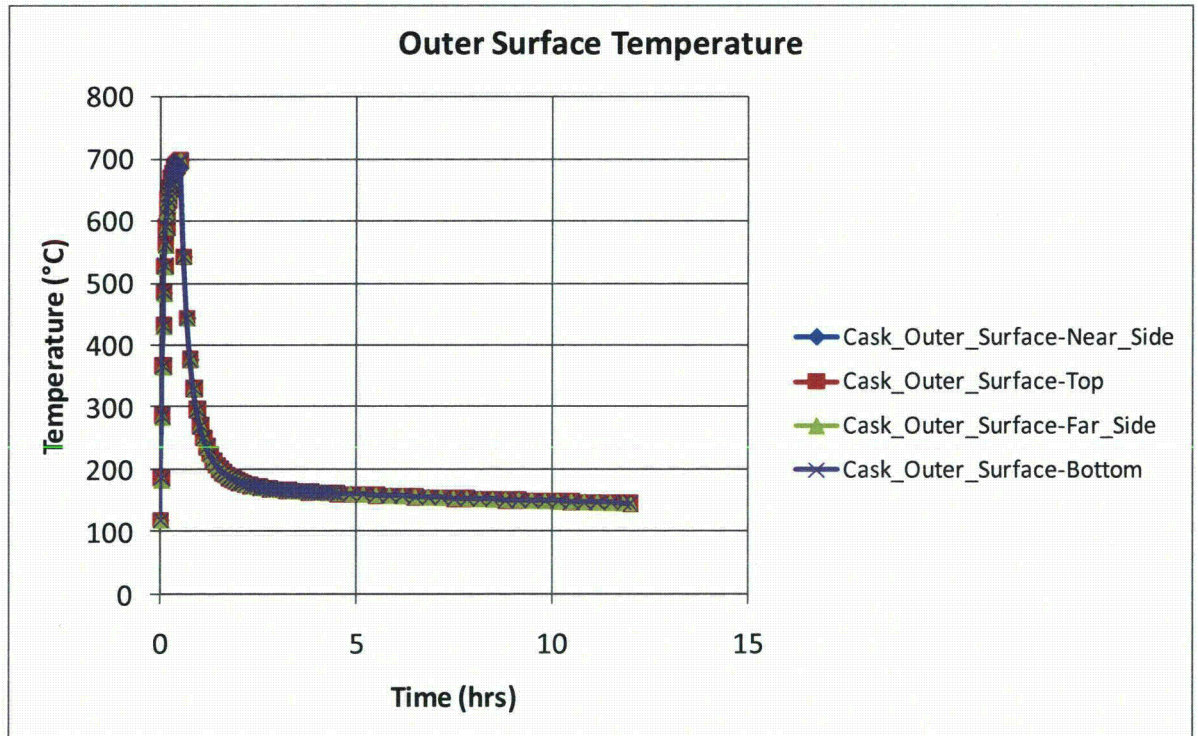


Figure IV-10. Rail-Steel Cask Regulatory Uniform Heating Results (P-Thermal) – Continue

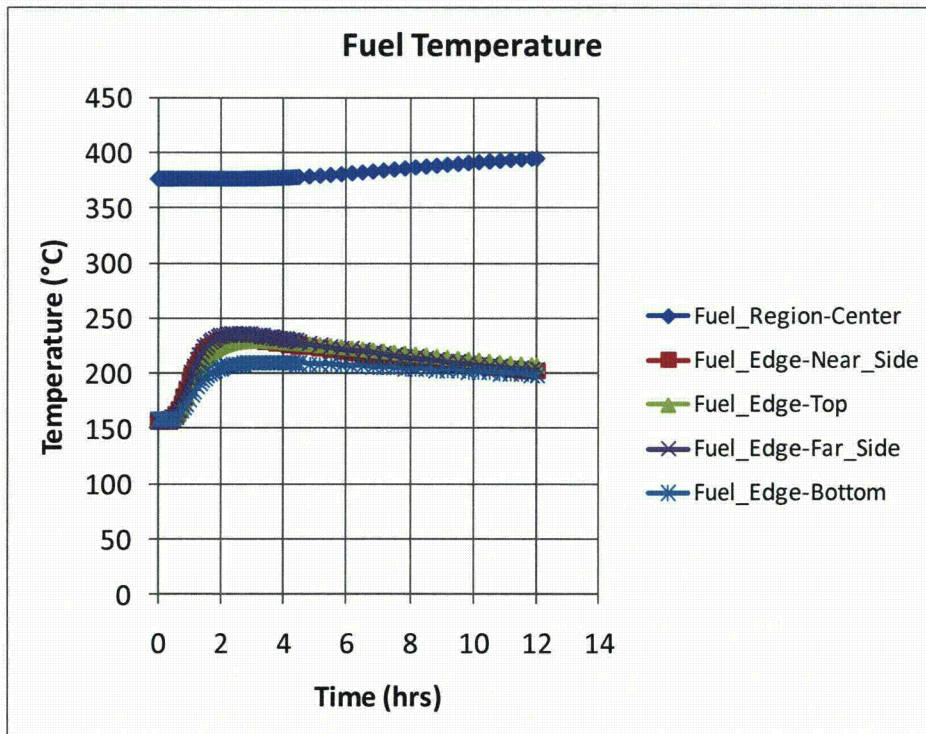
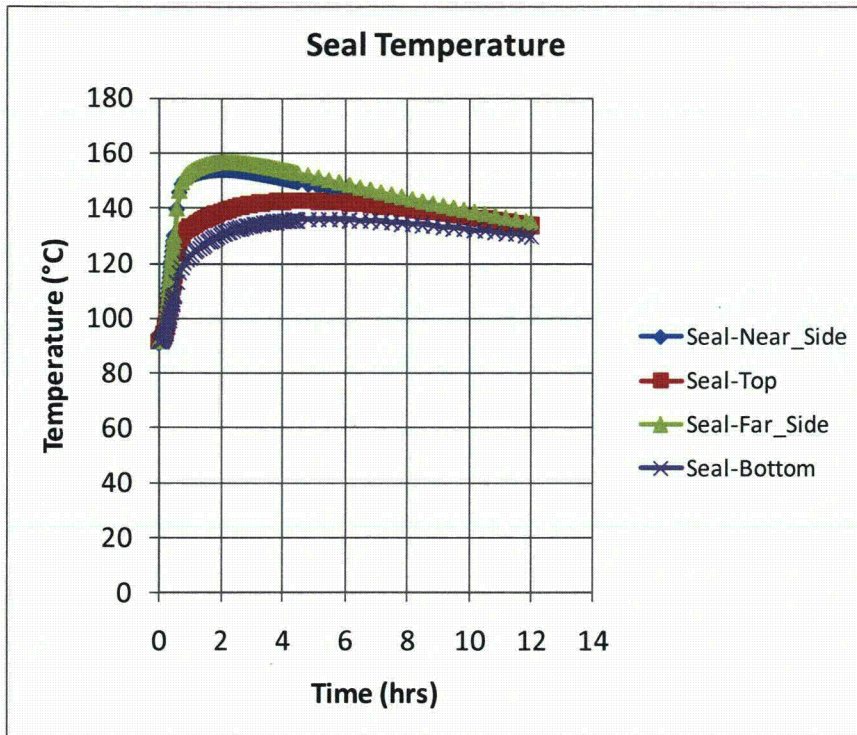


Figure IV-11. Rail-Steel Cask CAFE regulatory fire.

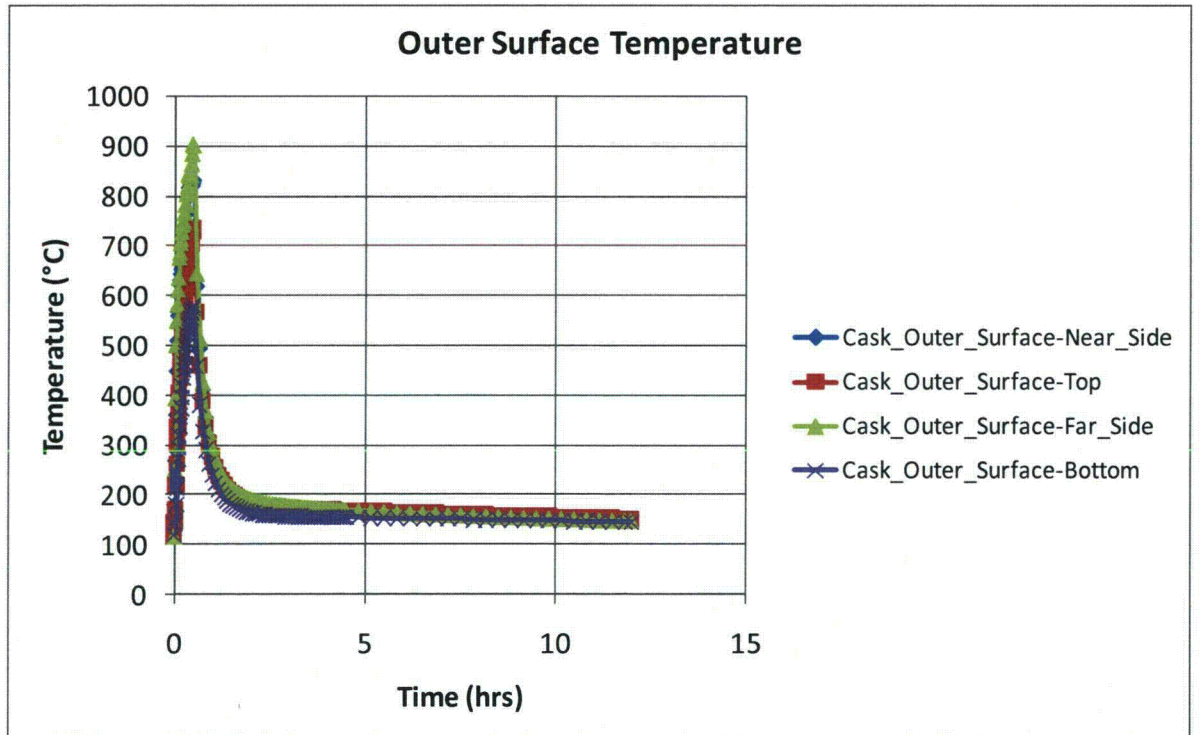
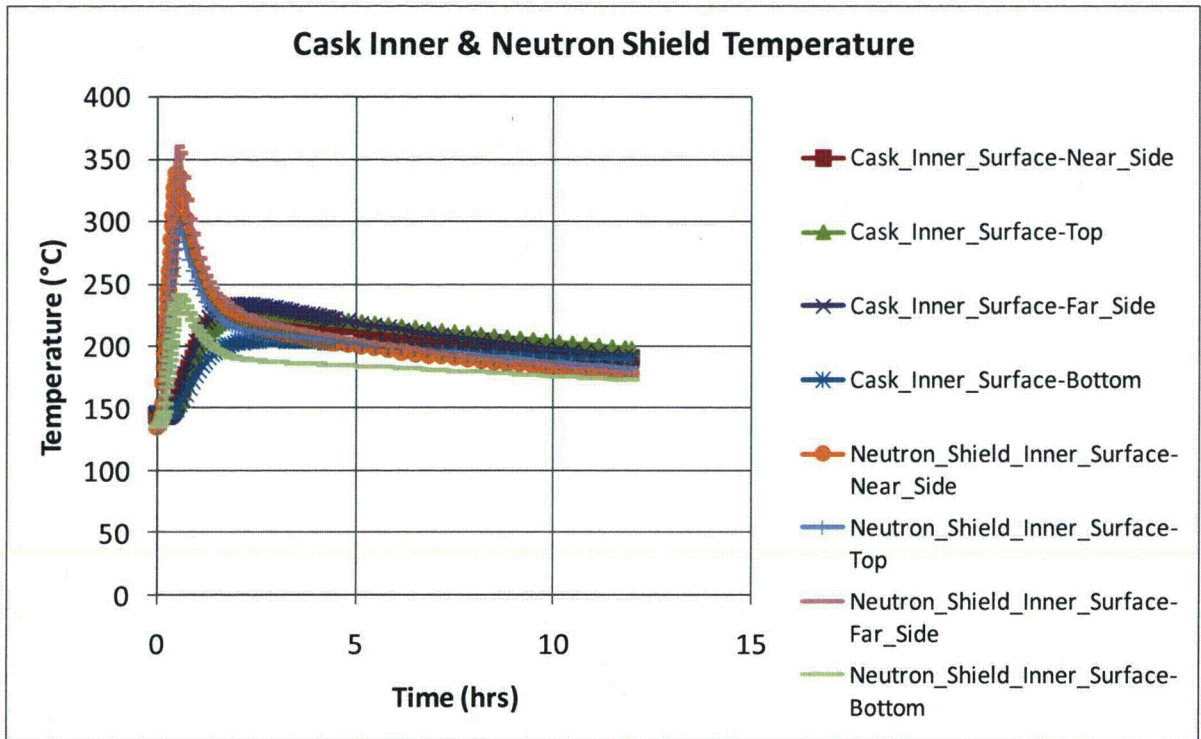


Figure IV-11. Rail-Steel Cask CAFE regulatory fire. – Continue

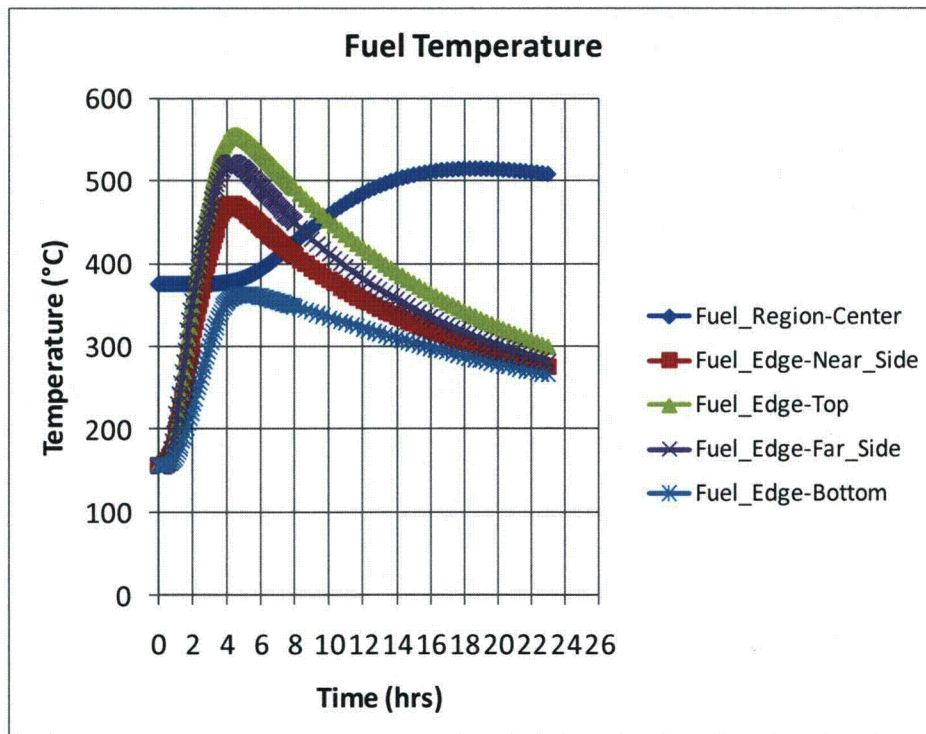
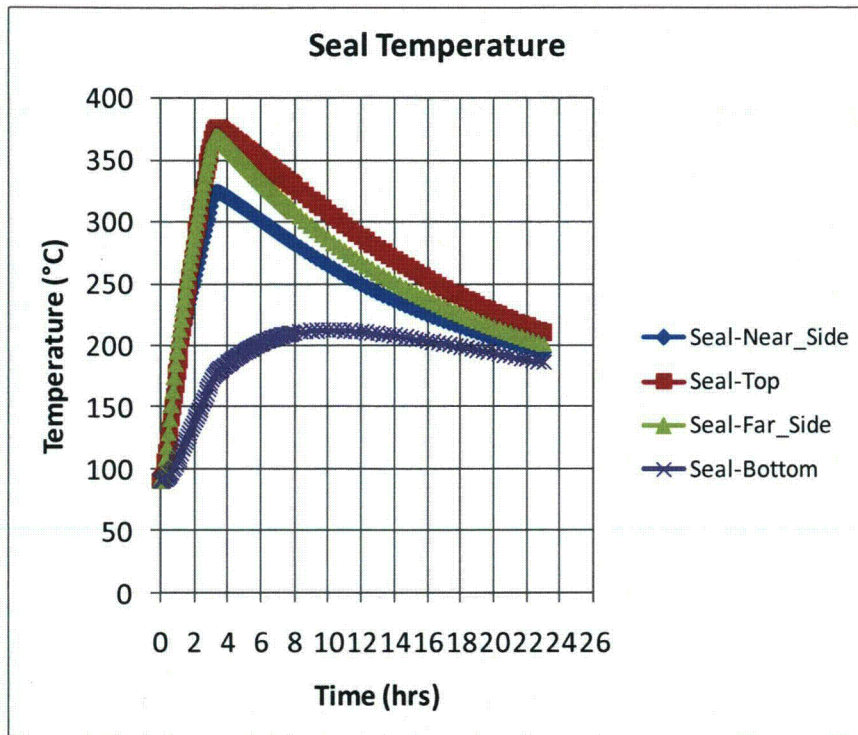


Figure IV-12. Rail-Steel Cask CAFE fire with cask on ground and at the pool center.

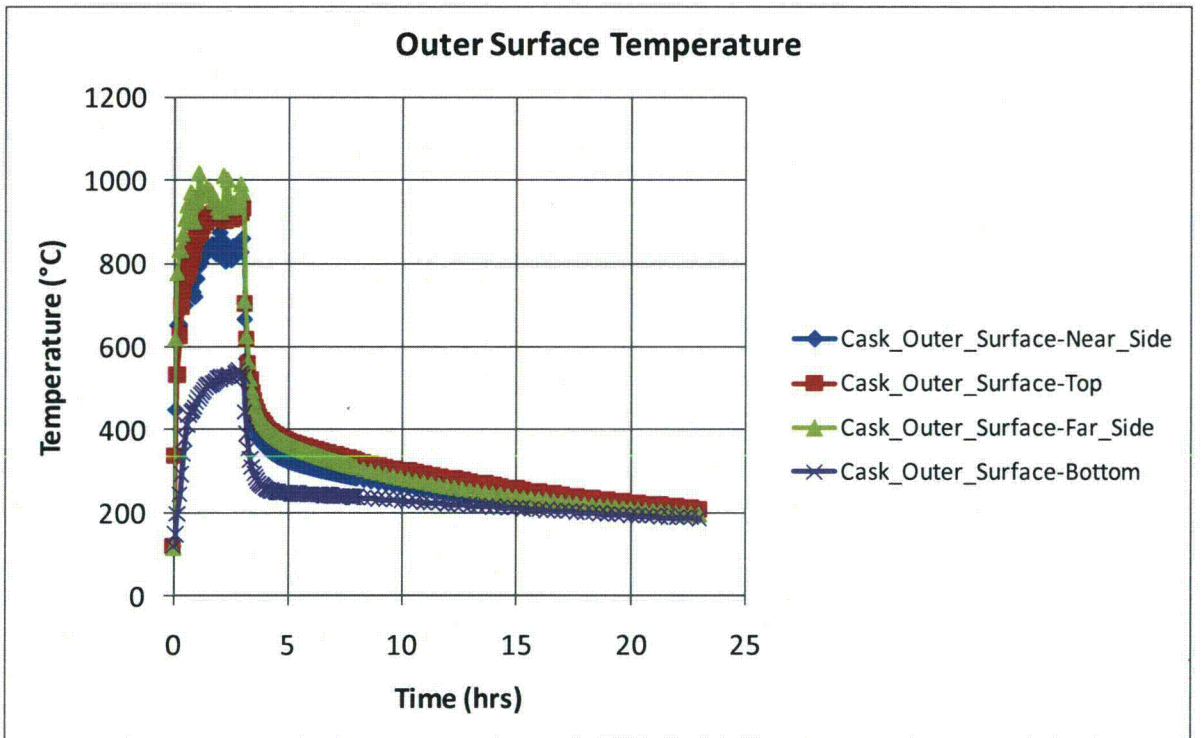
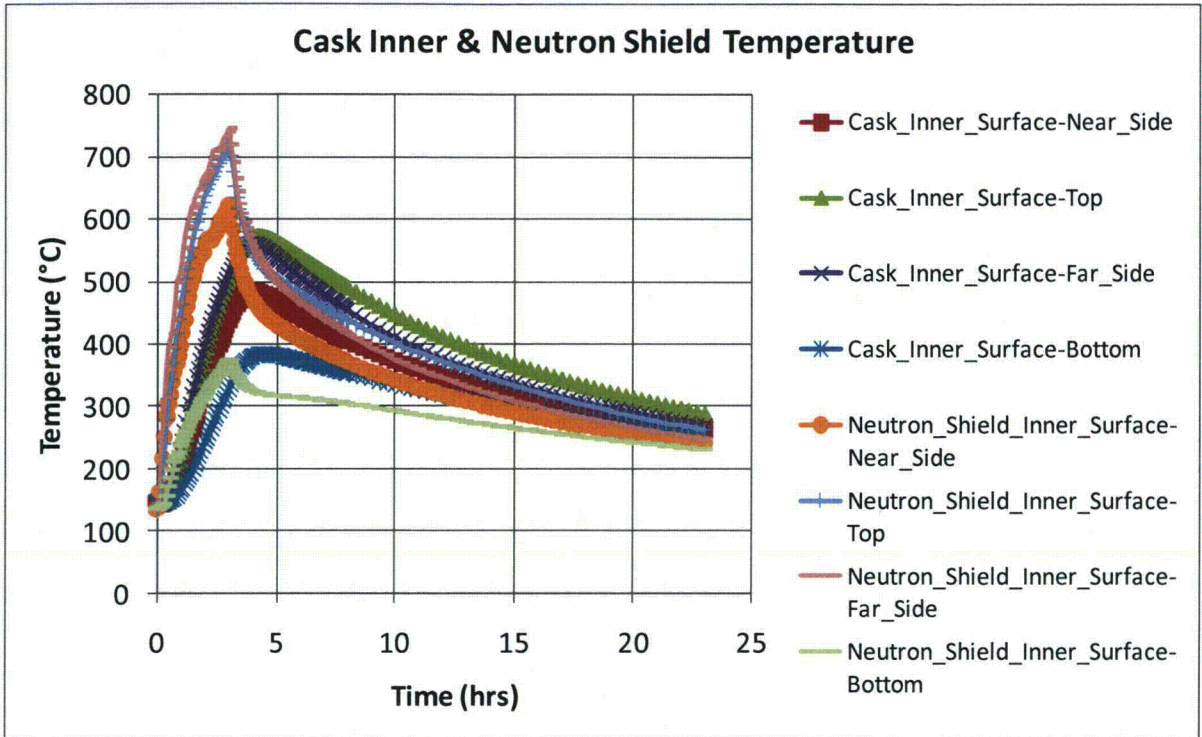


Figure IV-12. Rail-Steel Cask CAFE fire with cask on ground and at the pool center. – Continue

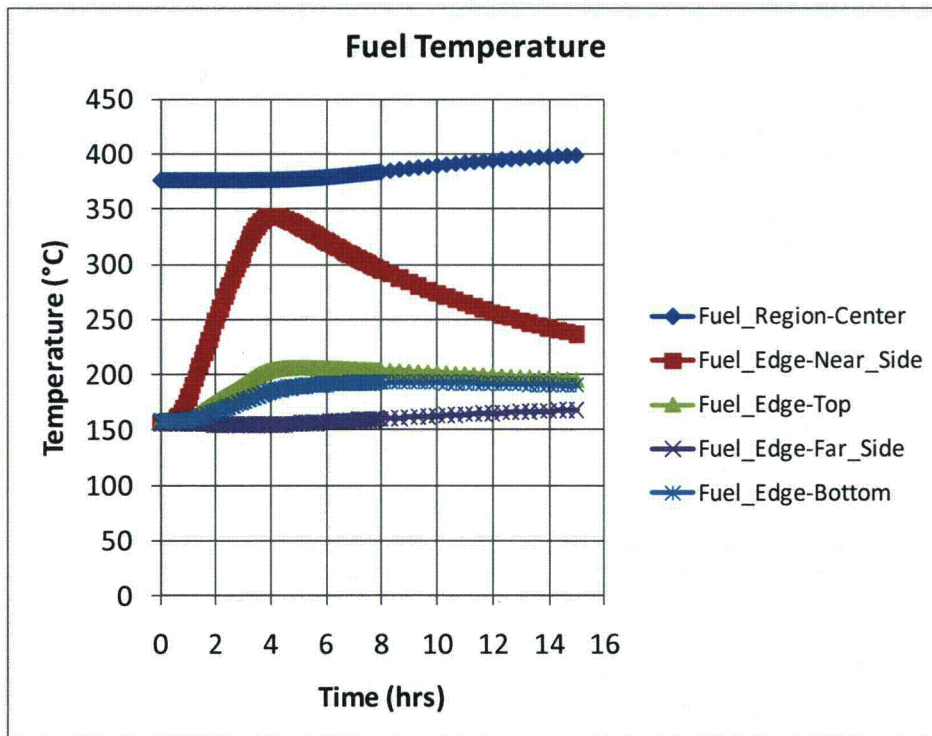
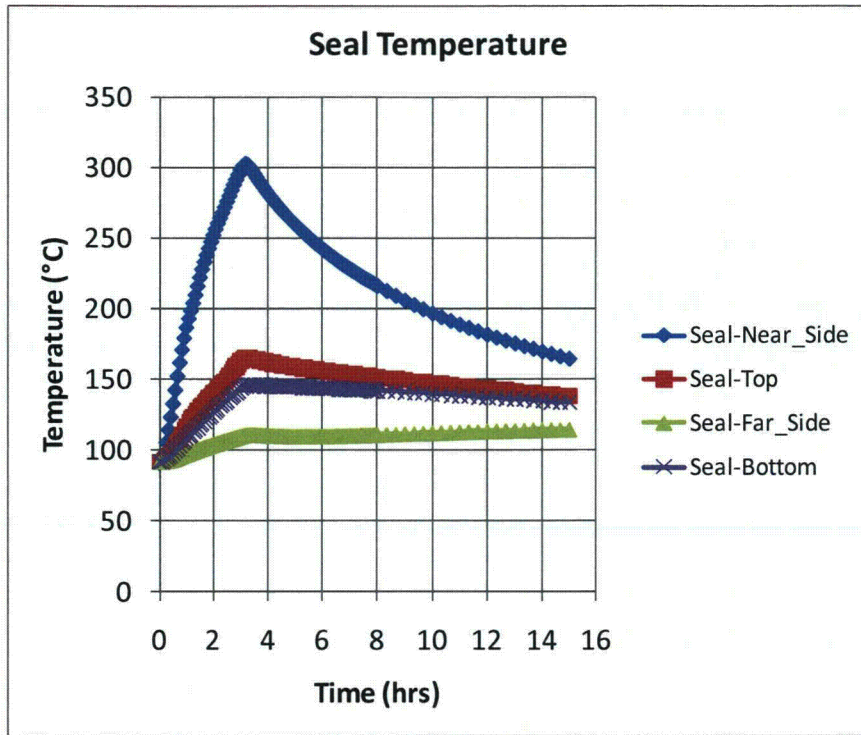


Figure IV-13. Rail-Steel Cask CAFE fire with cask on ground 3.0m (10ft) from the edge of the pool.

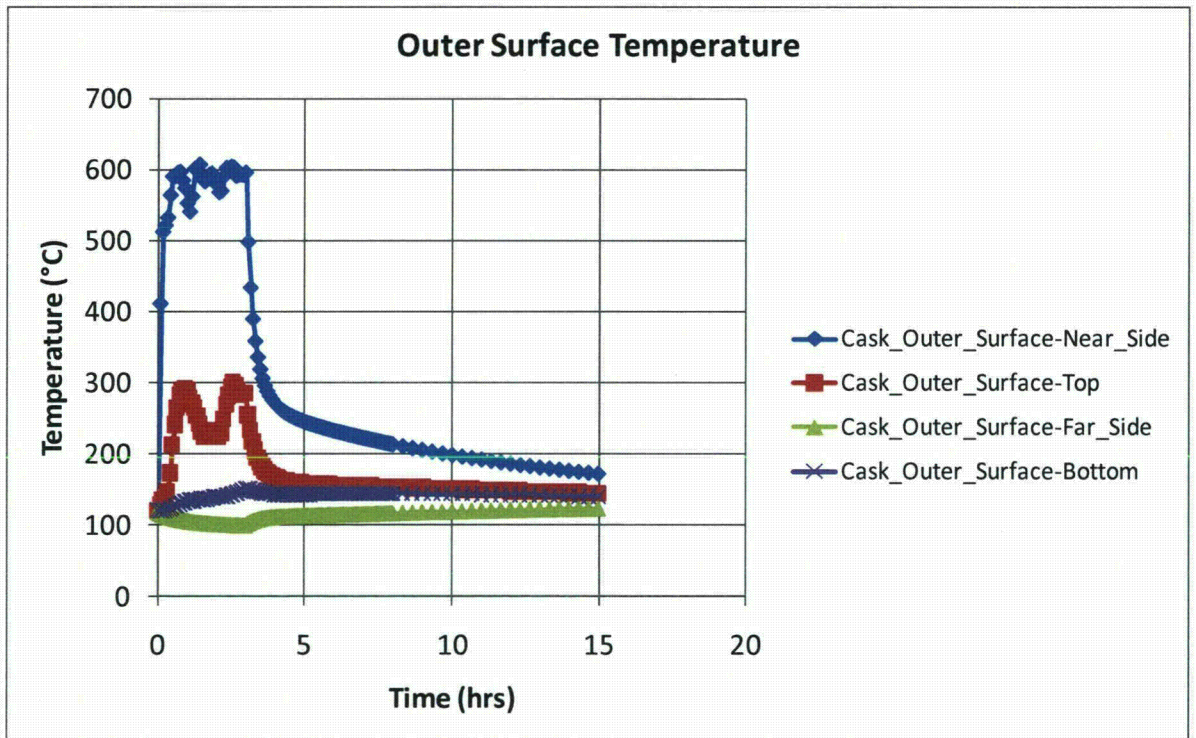
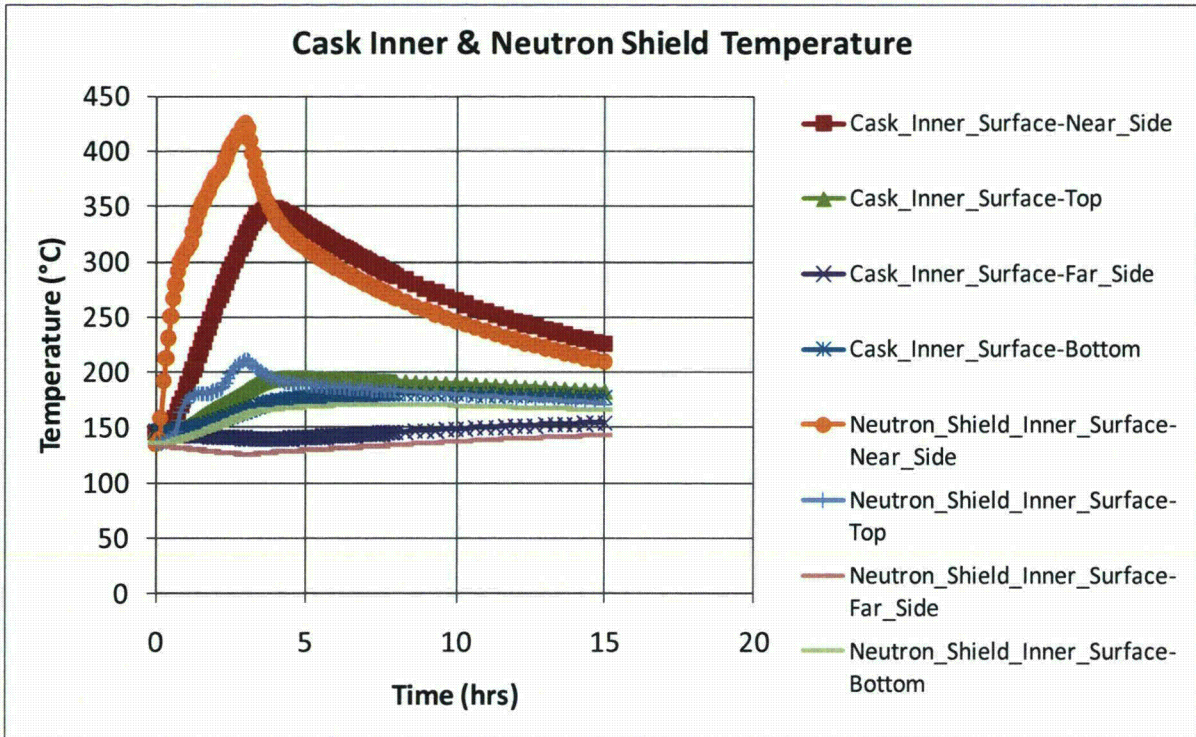


Figure IV-13. Rail-Steel Cask CAFE fire with cask on ground 3.0m (10ft) from the edge of the pool. - Continue

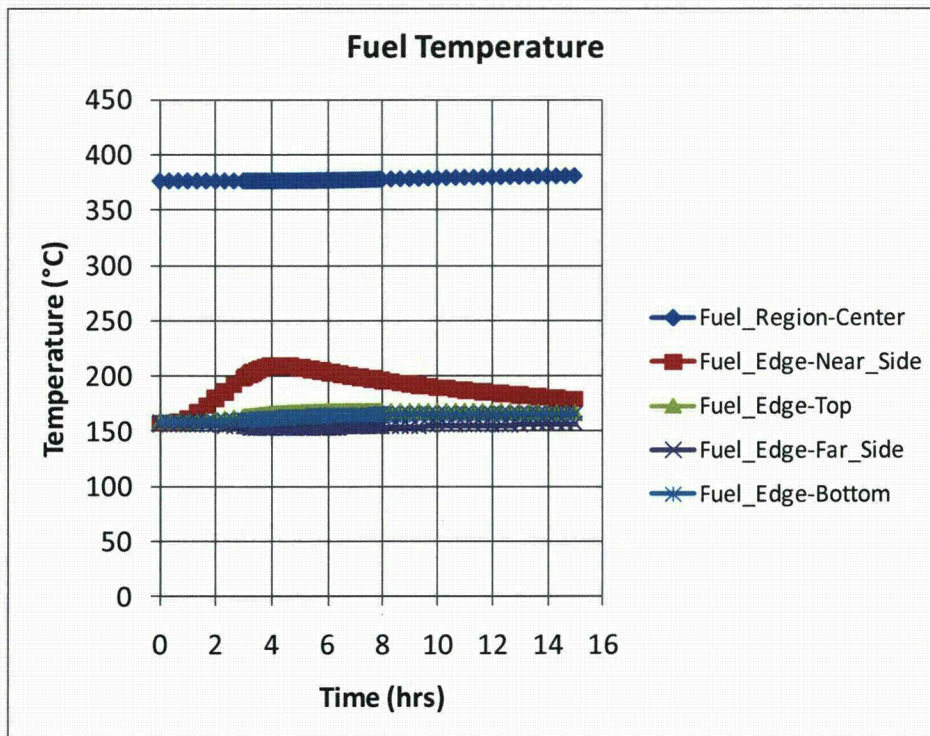
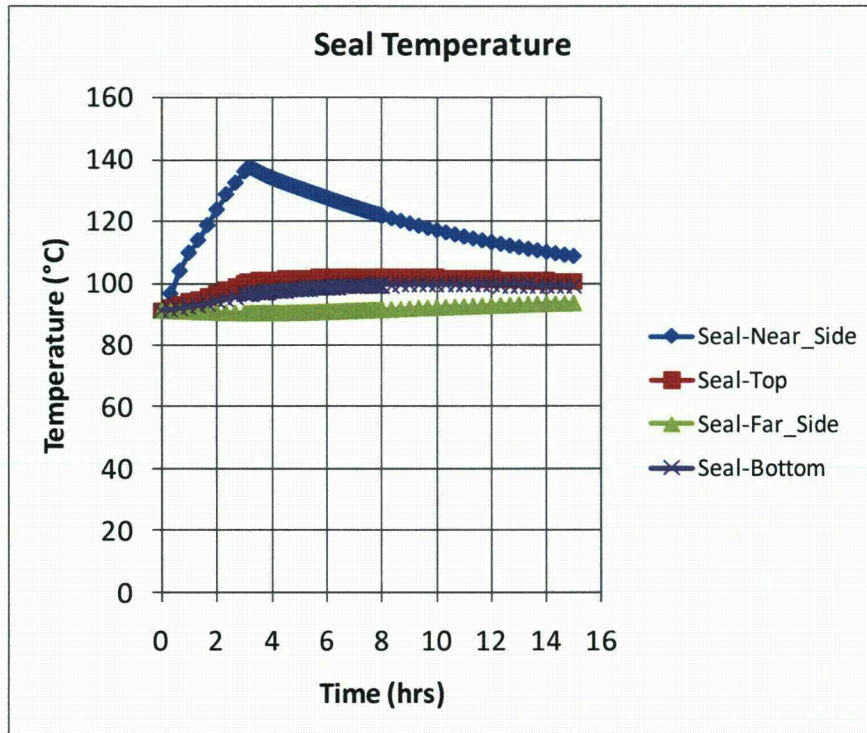


Figure IV-14. Rail-Steel Cask CAFE fire with cask on ground 18.3m (60ft) from the edge of

the pool.

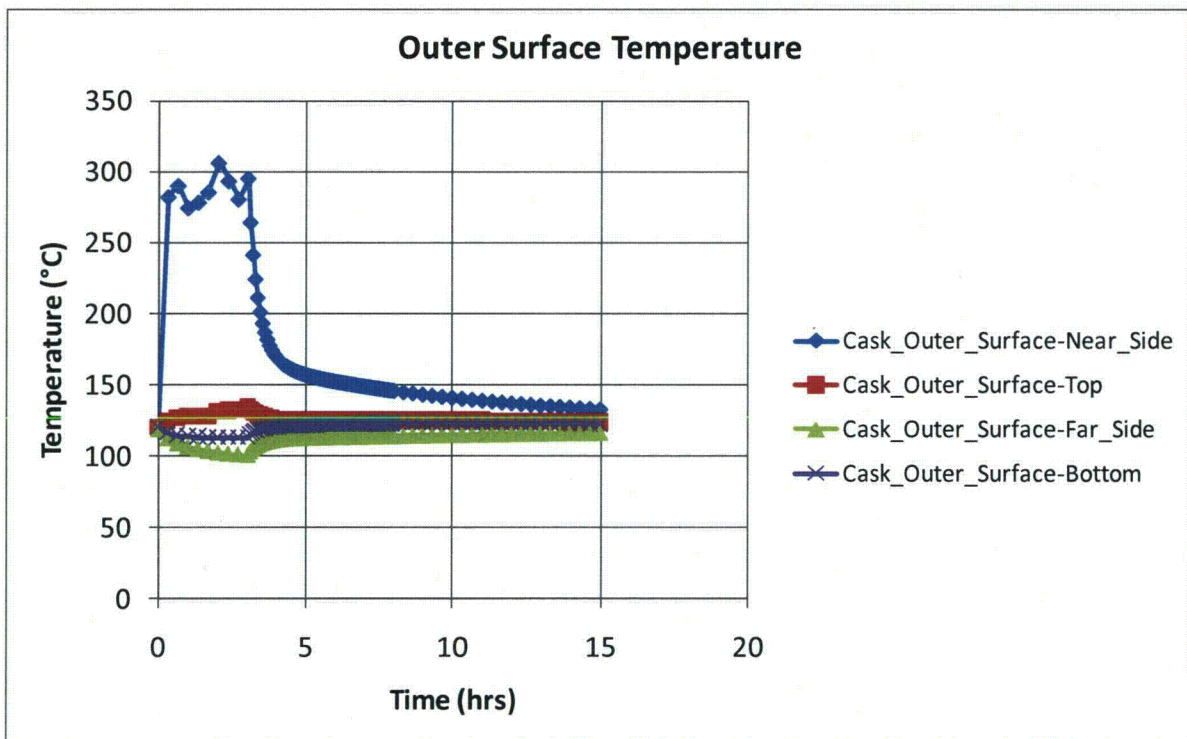
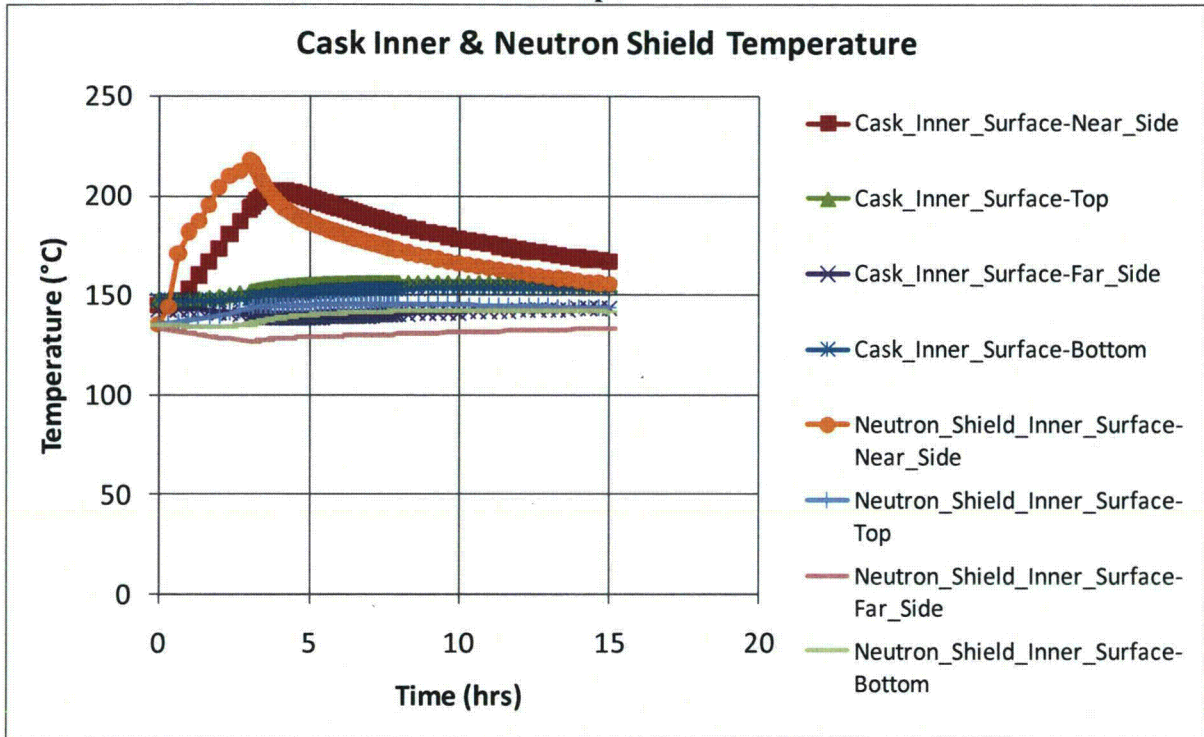


Figure IV-14. Rail-Steel Cask CAFE fire with cask on ground 18.3m (60ft) from the edge of the pool. – Continue

the inner walls of the overpack. For this reason, this analysis focuses on the directly loaded configuration. Finally, the Rail-Lead cask uses wood filled impact limiters as opposed to an aluminum honeycomb, a minor difference from the thermal analysis point of view, but nevertheless important to point out.

In most cases, results reported in the Rail-Lead cask SAR (NAC International, 2004) are used but modified where necessary as is done with the Rail-Steel cask analysis. The only significant departure is how the interior of the overpack is treated in the Rail-Lead cask SAR as explained in the introduction of this Appendix. Unlike the method used in that SAR, the directly loaded basket is replaced with a cylinder having equivalent effective thermal properties using a simple, three-dimensional, finite element model and the thermal resistor network method. As is done in the Rail-Steel cask analysis, the neutron shield region is replaced with an equivalent thermal region using the thermal resistor network method. The impact limiters are also modeled in the uncrushed state for the same reasons cited in Section IV.2.1.3.

IV.3.1 Geometry Considerations

The directly loaded Rail-Lead cask consists of an overpack, a fuel basket, and limiters at each end of the basket as shown in Figure IV-15. The directly loaded fuel basket is an open fuel container designed to fit snug within the overpack interior cavity. The overpack is designed to attenuate both the heat, and the neutron and gamma rays generated inside the fuel basket. The overpack contains two lids, each fitted with seals that completely seal the contents inside the overpack from the outside environment. The total length of the Rail-Lead cask, including the limiters, is approximately 6.5m (256 in).

IV.3.1.1 Overpack

The Rail-Lead cask overpack is also a multilayer cylindrical vessel approximately 2.20m (86.7in) in diameter and 4.90m (193in) in length (see Figure IV-15). The inner cavity of the overpack is approximately 1.80m (71in) in diameter and 4.19m (165in) in length. The cross section of the overpack vessel is made of three shells layers arranged in following order starting from the center of the overpack: an inner shell, a lead shell, and an outer shell (see Figure IV-16). As in the Rail-Steel cask, these shells are tightly coupled to each other and are welded to the overpack bottom plate and top flange. The lead shell acts as the gamma shield in this design. The thickness of the inner shell wall is not constant throughout, but tapers in slightly through most of the overpack side wall. That allows the thickness of the lead shell to increase slightly through the same section of the overpack, where the gamma shielding is most needed. Radial channels are also welded to the outer shell to enhance heat transfer through the neutron shield region. The outer enclosure shell is formed the same way as in the Rail-Steel cask. Similarly, the cavities formed by the outer enclosure shell, the radial channels, and the outer enclosure shell are filled with a neutron shield material. The neutron shield region increases the diameter of the overpack an additional 29.2cm (11.5in). Unlike the Rail-Steel cask, the overpack contains inner and outer lids that fit into the flange and complete the double containment barrier. Both the inner lid and bottom plate contain 5cm (2in) thick cylindrical layer of neutron shield within them.

The inner, outer, and lead shells, the flange, the inner and outer lids, and the bottom plate are represented explicitly in the thermal model with minor alterations to simplify the model. The most significant change is making the thickness of the inner shell and lead shell constant throughout. Their thickness is kept equal to the corresponding thicknesses in the middle section

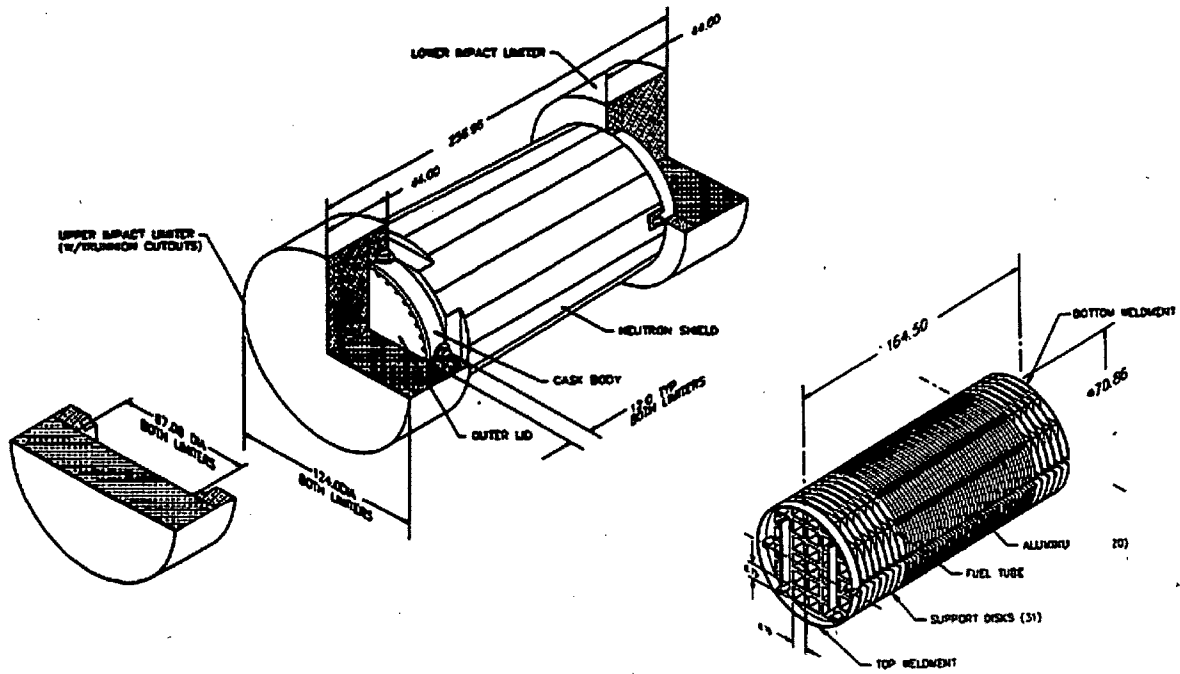


Figure IV-15. Rail-Lead cask components with the direct loaded fuel basket shown to the right (NAC International, 2004).

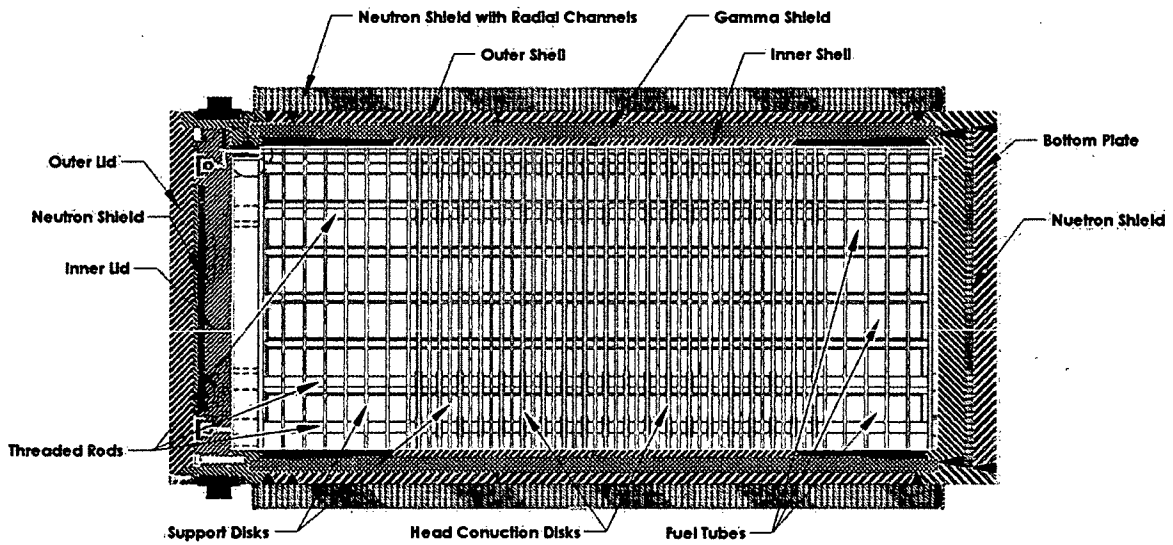


Figure IV-16. Cross-section view of the Rail-Lead cask with the directly loaded fuel basket.

of the overpack. As in the Rail-Steel cask model, the neutron shield region is represented as a single volume to minimize geometric complexity. As with the Rail-Steel cask, the Rail-Lead cask overpack contains a number of features that serve a special purpose. These features are omitted from the model as is done in the Rail-Steel cask model and for the same reasons: (1) negligible due to their small volume and mass relative to the other components in the overpack, (2) highly localized with no effect to the overall thermal performance of the cask at locations of interest, or both.

IV.3.1.2 Directly Loaded Fuel Basket

In the Rail-Lead cask, the nuclear spent fuel is stored in a directly loaded basket (see Figure IV-15). In this configuration, the fuel basket can store up to 26 PWR fuel assemblies. The total length of the fuel basket is 4.18m (164.5in) and the diameter is a little less than the inner diameter of the overpack. The fuel basket consists of thirty-one support disks and twenty heat transfer disks, aligned parallel to each other, and each precisely separated using six threaded rods and spacer nuts. The heat transfer disks are placed between the support disks in the region where the heat decay rate is at a maximum. Except for the end support disks, all support disks are the same thickness; the end support disks are twice as thick. Except for the end support disks, all heat transfer disks are slightly thicker. Both disk types contain twenty-six square holes spaced at regular intervals, and aligned between disks. Each square hole fits a thin walled, square, fuel tube which extends almost the length of the basket. These tubes are welded to the disks and accommodate the fuel assemblies. The fuel assemblies extend almost the entire length of the fuel basket. The basket active fuel region is assumed to be 3.66m (144in) in length as suggested in the Rail-Lead cask SAR. Additional plates and a short length cylinder are welded to the end support disks for extra support and complete the fuel-basket design. The fuel basket fits within the inner cavity of the overpack, but there are a small gap between the basket disks and the inner wall of the overpack, and between the ends of the basket, and the lid and bottom plate walls.

As in the Rail-Steel cask, each fuel assembly consists of an array of fuel rods, each separated by a helium gas space. The total number of rods in the fuel assembly, the dimensions of each rod, and the type of fuel cladding vary between assembly designs. A more complete description of the fuel assembly and fuel rods is given in Section IV.2.1.2.

The fuel basket and fuel assemblies are not explicitly included in the model. Instead, a separate three-dimensional model is generated to obtain the effective properties of the basket in the in-plane and axial directions. Since the basket support disks, gas regions, and heat transfer disks repeat at regular intervals in the active fuel region, a three-dimensional, quarter solid model of a section comprising two support disk, heat transfer disk, and the gas and fuel tubes between them is generated to obtain the effective properties of the basket in the in-plane and axial directions. The diameter of the support and heat transfer disks is assumed the same to simplify the solid modeling and mesh process. The same model is used for the portion of the fuel basket without the heat transfer disk. In this case, the material properties and boundary conditions for the heat transfer disk are replaced with those of the gas region.

IV.3.1.3 Impact Limiters

The impact limiters in the Rail-Lead cask are cylindrical wood-filled structures also encased in a thin metal shell. Each impact limiter is 3.15m (124in) in diameter and 1.12m (44in) in length (see Figure IV-15). The depth of the cap where the overpack fits is 30.5cm (12in.). These limiters serve the same purpose as the impact limiters in the Rail-Steel cask (see Section

IV.2.1.3). Since the impact limiters are mostly wood and have very little metal structures, they are modeled as two coupled solid wood structures, retaining their volume and shape.

IV.3.2 Rail-Lead Cask Thermal Behavior and Model Assumptions

The Rail-Lead cask is also designed to release heat passively under normal conditions of transport. In the direct loaded configuration, the basket is designed to accommodate a maximum heat load of 22.1kW (0.85kW per fuel assembly). Figure IV-17 shows the normalized, axial heat generation rate distribution for a 0.85 kW PWR assembly. As with the Rail-Steel cask, heat is dissipated from the fuel rods to the exterior surfaces of the Rail-Lead cask by a combination of conduction, convection, and radiation heat transfer.

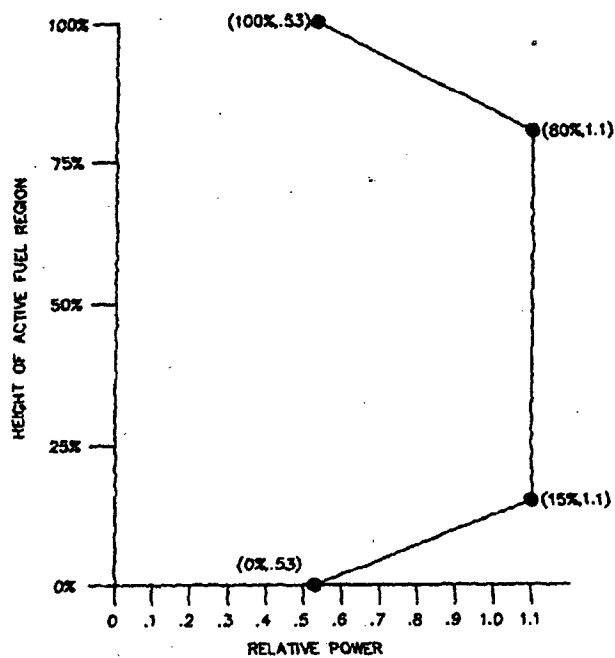


Figure IV-17. Axial burn up profile for the directly loaded fuel basket (NAC International, 2004).

The fuel assembly design in the Rail-Lead cask is conceptually the same as in the Rail-Steel cask model; therefore, the same heat transfer mechanisms are present as described in Section IV.2.2. The approach described in Section IV.2.3.1 is also used in the Rail-Lead cask SAR to obtain the effective thermal conductivity of the fuel assembly in the radial direction. Values presented in the Rail-Lead cask SAR are used in this study and are not much different from what is used in the Rail-Steel cask SAR, as expected. Heat generated in the assembly is dissipated by conduction through the fuel tube walls. From the tubes, heat is then radially dissipated by conduction through the support and heat transfer disks, and through the gas in the void formed between the tubes and the inner wall of the overpack; and by radiation to the adjacent tubes and disks, and to

the inner wall of the overpack. As in the Rail-Steel cask fuel basket, convection is limited to a few regions around the basket perimeter. However, unlike the HI-STAR configuration, the convective cells in the Rail-Lead cask fuel basket are confined to the gas void between adjacent disks. Moreover, heat dissipated from the adjacent disks through this void tends to decrease the temperature gradient across this void region, reducing temperature gradient induced flow. In the Rail-Lead cask model, convection is neglected in this region since it is not expected to be significant given the Nusselt values presented in the Rail-Steel cask SAR for a similar void configuration.

Heat is dissipated radially by conduction and radiation through the gap between the disks and the overpack inner wall. This gap is assumed to be 1.65mm (0.065in) across as stated in the Rail-Lead cask SAR. As mentioned before, a three-dimensional, quarter section of the fuel basket is generated to obtain effective thermal conductivities in the in-plane and axial directions (see Figure IV-18). The small gap between the disks and the inner wall of the overpack is included (not clearly visible in Figure IV-18). Except for convection, all modes of heat transfer are accounted for in this model, and included radiation between the tubes, between the tubes and the disks, between the tubes and the inner shell (also not shown), between the disks, and between the disks and the inner shell. In the horizontal position, the disks make contact with the inner shell wall. To account for conduction through the contact area between the disks and the inner shell wall, the same model derived in Holtec International (1997) is employed to enhance conductivity through the equivalent concentric gap (see Section IV.2.3.2). Note that both the support and heat transfer disk diameters are assumed to be the same after thermal expansion.

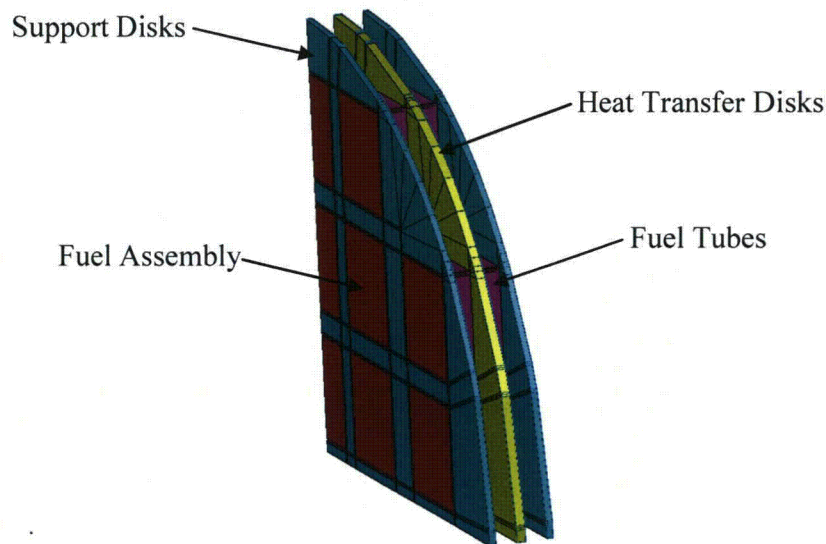


Figure IV-18. Three-dimension, quarter section of the directly loaded basket. The helium material is not shown.

Heat transfer through the inner shell, lead, and outer shell of the overpack occurs by conduction through the shell materials. These are modeled explicitly. As in the Rail-Steel cask, conduction in the neutron shield region occurs in parallel through the radial connectors and the neutron shield material.

Heat transfer from the cross section of the direct loaded basket and overpack to the axial ends of the overpack is assumed to occur by conduction and radiation. Heat conduction occurs in parallel through each of the connecting materials that comprise the basket and overpack. The effective thermal properties are obtained in the same manner as in the Rail-Steel cask model. Radiation is assumed to occur between the end disks of the basket to the interior wall of the inner lid and bottom plate of the overpack.

The Rail-Lead cask system is also designed to maintain the temperature of critical components below their design limits during and after a 30 minute, fully engulfing, hypothetical accident condition (HAC) scenario. For fire accident scenarios lasting longer than the HAC fire described in 10 CFR 71.73, a significant amount of heat may be transferred to the interior of the cask. As in the Rail-Steel cask, the temperature of the neutron shield is expected to reach temperatures beyond the temperature limits. Heat then is dissipated by conduction through the gas layer in the neutron shield and by radiation between the outer wall of the intermediate shell layer and the outer enclosure shell. Similarly, the lead shell is expected to melt since its melting point is around 321°C (611°F). The impact limiters are made of wood encased in a thin metal layer and are sealed to prevent moisture from deteriorating the wood over long periods of time. Since the impact limiters are assumed to stay intact (i.e., with the content sealed) after the initial accident event (e.g., derailment), the wood is not expected to char significantly. Charring is therefore not taken into account in this model.

IV.3.3 Rail-Lead Cask Materials and Thermal Properties

The Rail-Lead cask is made of stainless steel, lead, copper, aluminum, NS-4-FR, Boral neutron absorber and helium. The inner and outer shell, the outer enclosure shell, the bottom plate, the top flange, and the inner lid of the overpack are made from stainless steel, type 304. The gamma shield is made from copper-lead, and the outer lid from stainless steel, type 630. The radial channels are made from a combination of stainless steel, type 304, copper, and a small section of carbon steel. The stainless steel in the channel serves as the main support component while the copper enhances conduction through the channels. The overpack neutron shield is made from NS-4-FR. The impact limiters are redwood and balsa layers encased in a thin stainless steel shell.

In the fuel basket, the support disks, threaded rods, and spacer nuts are made from stainless steel, type 630, and the top and bottom support plates, short length cylinder, and fuel tubes from stainless steel, type 304. The heat transfer support disks are made from aluminum alloy 6061. As with the Rail-Steel cask, adjacent to each fuel tube wall is a layer of Boral sandwiched between the tube wall and a thin layer of stainless steel sheathing. The fuel rods are made from zircaloy or stainless steel cladding, but are assumed to be zircaloy as in the Rail-Steel cask analysis. The pellets are made from UO₂. The empty gas space, which encompasses most of the volume inside the overpack cavity, is filled with helium.

Table IV-10 through Table IV-13 provide the thermal conductivity, specific heat, density, and emissivity for those materials used in the Rail-Lead cask which are different from the Rail-Steel cask, or for which the properties are significantly different (see Table IV-2 through Table IV-5

for additional properties). The properties of NS-4-FR reported in the Rail-Lead cask SAR are marginally different from those reported for Holtite-A, as expected. The thermal conductivity of redwood and balsa vary depending on the direction of the grain. For balsa, values from MSC Patran material database are used and compared well with values in Incropera and Dewitt (1996). The MSC Patran database references are given in Table IV-10. NUREG-0361 (NRC 1978) gives

Table IV-10. Thermal conductivities for the Rail-Lead cask materials.

Material	Thermal Conductivity W/m ² ·°C (Btu/ft·hr·°F)				
	92°C (200°F)	226°C (450°F)	377°C (700°F)	477°C (900°F)	726°C (1340°F)
Aluminum 6061*	171 (98.8)	176 (101.7)	176 (101.7)		
Copper [§]	402 (232.4)	386 (223.1)	376 (217.3)	369 (213.3)	352 (203.5)
Balsa [¥]	0.050 (0.029)	—	—	—	—
Lead [‡]	33.9 (19.6)	29.3 (16.9)	16.7 (9.7)	15.3 (8.8)	14.7 (8.5)
Redwood [€]	3.6 (2.0)	5.5 (3.1)	—	—	—
Stainless Steel Type	17.5 (9.9)	18.3 (10.6)	20.7 (12.0)	24.6 (14.2)	—

*Nuclear Acceptance Corporation International, 2004

[§]Incropera and Dewitt, 1996

[¥]McAdams, 1954; Perry, 1963; Weast, 1966

[‡]Kelley, 1960; Schorsch, 1966; Weast, 1966

[€]NUREG-0361, 1978

Table IV-11. Specific heat for the Rail-Lead cask materials.

Material	Specific Heat J/kg·K (Btu/lbm·F)				
	92°C (200°F)	226°C (450°F)	377°C (700°F)	477°C (900°F)	726°C (1340°F)
Copper [§]	390 (0.093)	406 (0.097)	422 (0.101)	431 (0.103)	451 (0.108)
Balsa [¥]	2302 (0.55)	—	—	—	—
Lead [‡]	131 (0.031)	—	—	—	—
Redwood [€]	2386 (0.57)	3898 (0.93)	—	—	—

Table IV-12. Densities for the Rail-Lead cask materials.

Material	Density kg/m ³ (lbm/ft ³)				
	92°C (200°F)	226°C (450°F)	377°C (700°F)	477°C (900°F)	726°C (1340°F)
Aluminum	2823 (176)	—	—	—	—
Copper ^s	8933 (558)	—	—	—	—
Balsa [‡]	130 (8.1)	—	—	—	—
Lead [‡]	11350 (709)	—	—	—	—
Redwood ^c	352 (22)	—	—	—	—

Table IV-13. Emissivity for some of the Rail-Lead cask materials.

Material	Emissivity
Aluminum 6061	0.22
Stainless Steel Type 630	0.58

values through and along the grain for redwood; however, since the Rail-Lead cask SAR does not specifically describe the arrangement of the wood layers in the limiters, average properties (along and through the grain) are assumed. The specific heat and density of copper-lead provided in the Rail-Lead cask SAR are slightly lower and higher, respectively, than for plain lead (Incropera and Dewitt, 1996); properties from MSC Patran database are used instead since data is readily available above the melting temperature and included the specific latent heat of fusion (23.9kJ/kg [10.3Btu/lbm]). The specific heat of lead increases up to the melting point (by a factor of 1.07), but then remains approximately the same. Since these changes are small, the value at 92°C is used throughout the rest of the temperature range.

With the exception of the basket and neutron region, all components are modeled explicitly. The impact limiters are modeled in their intact state, with properties of redwood and balsa since the outer shell volume is significantly smaller than the total wood volume. Contact gap effects are assumed negligible. As in the Rail-Steel cask model, NS-4-FR is replaced with air when the former reached its temperature limit, but only in the neutron shield region of the overpack. Radiation is activated in this region by setting the emissivity to the appropriate value.

IV.3.3.1 Directly Fuel Loaded Basket

In the Rail-Lead cask SAR, fuel rods are evaluated to determine a representative fuel rod configuration. The fuel assembly is then modeled explicitly to obtain an equivalent in-plane thermal conductivity for the homogenized fuel assembly, as described in Section IV.2.3.1. The fuel assembly axial conductivity is next obtained with an area weighted average using the thermal conductivities of the individual components of the fuel rods and helium. The rest of the directly loaded basket with the homogenized fuel assembly is then included explicitly in the normal condition run, but is not included in the subsequent regulatory fire accident run. Instead, the maximum temperature difference between the fuel basket and the inner wall of the overpack

calculated in the normal condition run is added to the inner wall temperature of the overpack calculated in the regulatory fire run to obtain an estimate of the temperature of the center of the fuel basket for the regulatory run. Since homogenized properties for the fuel basket region were not provided in the Rail-Lead cask SAR, a different approach is used in this study to obtain these properties. This alternate approach (1) reduces geometric modeling complexities while maintaining the overall response of the cask and (2) is consistent with the approach employed to model the Rail-Steel cask.

The directly loaded fuel basket is replaced with a homogenized cylinder having equivalent effective thermal conductivities in the in-plane and axial directions. As described in Section IV.3.2, two variations of the same three-dimensional, quarter section, finite element model are generated. The first model included a support disk, a heat transfer disk, and the fuel tubes and helium space between the disks (see Figure IV-18). The second model did not include the heat transfer disk; instead, it is replaced with helium and the boundary conditions are modified to reflect this change.

Since the effective in-plane and axial conductivities for the fuel basket are not explicitly given in the Rail-Lead cask SAR (i.e., the fuel basket was modeled explicitly in that SAR), these effective conductivities are obtained using the following four step procedure.

First, the detail cross section of the fuel assembly is replaced with a homogenized fuel region having equivalent thermal properties. This analysis is done in the Rail-Lead cask SAR, as explained above, and the analysis results are included in this study. As expected, the thermal conductivities reported in the Rail-Lead cask SAR are close to those reported in Rail-Steel cask SAR for similar fuel assemblies, which serves as a check. Second, the fuel tube, Boral, and stainless steel sheathing are replaced with a homogenized wall having an equivalent thermal conductivity as described in the Rail-Lead cask SAR.

Third, both three-dimensional, quarter section models described above (and shown in Figure IV-18) are used to obtain the in-plane and axial effective thermal conductivities. Each model is evaluated with two sets of boundary conditions:

- (1) a uniform temperature applied over the outer circumference of the inner shell; adiabatic conditions over the in-plane ends; and uniform heat generation in the homogenized fuel assemblies; and
- (2) adiabatic conditions applied over the outer circumference of the inner shell; a uniform temperature over one of the in-plane ends, and a uniform heat flux over the other in-plane end; and no uniform heat generation in the homogenized fuel assemblies.

In the first case, the in-plane thermal conductivity is obtained using the same procedure described in Section IV.2.3.1. In the second case, the axial thermal conductivity is obtained using the standard relationship:

Here A is the cross sectional area of the basket; L is the thickness across the modeled section; q is the uniform heat flux applied over one of the cross sectional area, axial ends; and T_1 is the

uniform temperature applied over the other cross sectional area, axial end. T_q is the average temperature where uniform heat flux is applied and is calculated using the simulation results. A second option is to apply constant temperatures at both axial ends of the basket, then calculate the total heat flow (qA) through the basket using the simulation results, and lastly calculate the effective axial conductivity using the above equation. To obtain temperature dependent thermal conductivities, this third step is repeated a number of times using a wide range of uniform circumferential temperatures and applied heat fluxes.

Fourth, the thermal conductivities obtained in the previous step are added using an equivalent thermal resistor network model to obtain in-plane and axial thermal conductivities, respectively, over the entire fuel basket.

Table IV-14 shows the thermal properties used for the basket. These properties are applied to the homogenized fuel-basket cylinder. The equivalent specific heat and density are obtained using a mass and volume weighted average, respectively, over the individual component properties. The volume of each component in the fuel basket (i.e., support disks, heat transfer disks, fuel tubes, etc.) is given in the Rail-Lead cask SAR.

Table IV-14. Effective thermal properties of the directly loaded fuel basket.

Effective Thermal Properties	92°C (200°F)	226°C (450°F)	377°C (700°F)	477°C (900°F)	726°C (1340°F)
Radial Thermal	3.2 (1.8)	3.8 (2.1)	4.3 (2.4)	5.0 (2.8)	5.9 (3.4)
Axial Thermal Conductivity	2.4 (1.4)	3.2 (1.8)	3.8 (2.1)	4.5 (2.6)	5.8 (3.3)
Specific Heat	332 (0.079)				
Density	2450 (153)				

IV.3.3.2 Neutron Shield Region

The neutron shield region is modeled using the same approach used in the SARs (NAC International, 2004, Holtec International, 2004). Both reports used the thermal resistor network method to obtain the in-plane and axial effective thermal conductivities (see Section IV.2.3.4). In the case of the Rail-Lead cask, there are fewer radial channels than in the Rail-Steel cask; however, as will be demonstrated shortly, this shortcoming is compensated for by adding copper in the neutron shield region. Table IV-15 shows the thermal properties used for the neutron shield region in the Rail-Lead cask. The circumferential thermal conductivity is assumed to be that of NS-4-FR. As before, the specific heat and density are obtained from a mass and area weighted average. Note the thermal conductivity is slightly higher than in the Rail-Steel cask even though the Rail-Lead cask contains fewer channels. This is expected since the neutron shield in the Rail-Lead cask contains copper which has a much higher thermal conductivity than carbon steel.

IV.3.4 Rail-Lead Cask Finite Element Model

The following description is short since most of the details are similar to the Rail-Steel cask analysis described in Section IV.2.4. In the Rail-Lead cask runs, the cask model had 109,662

Table IV-15. Effective thermal conductivities for the neutron shield region of the Rail-Lead cask.

Effective Thermal Properties	92°C (200°F)	226°C (450°F)	377°C (700°F)	477°C (900°F)	726°C (1340°F)
In-Plane Thermal Conductivity W/m-°C (Btu/ft-hr-°F)	8.1 (4.6)	7.9 (4.5)	7.7 (4.4)	7.7 (4.4)	7.4 (4.2)
Axial Thermal Conductivity W/m-°C (Btu/ft-hr-°F)	7.6 (4.3)	7.3 (4.2)	7.3 (4.2)	7.2 (4.1)	6.9 (3.9)
Specific Heat J/kg-°C (Btu/lbm-°F)	1406 (0.33)	535 (0.12)	563 (0.13)	575 (0.13)	611 (0.14)
Density kg/m ³ (lbm/ft ³)	1983 (123)	380 (23)			

elements (see Figure IV-19); this corresponds to a nominal element size of 10.2cm (4in). The element count is less than in the Rail-Steel cask since the Rail-Lead cask is smaller and has fewer features which add to the element count. A mesh refinement study is also conducted with the Rail-Lead cask model with a similar outcome. The boundary conditions for the normal condition, steady-state run, the regulatory uniform heating run, and the CAFE fire runs are the same as discussed in Sections IV.2 and IV.2.4. They are not repeated here.

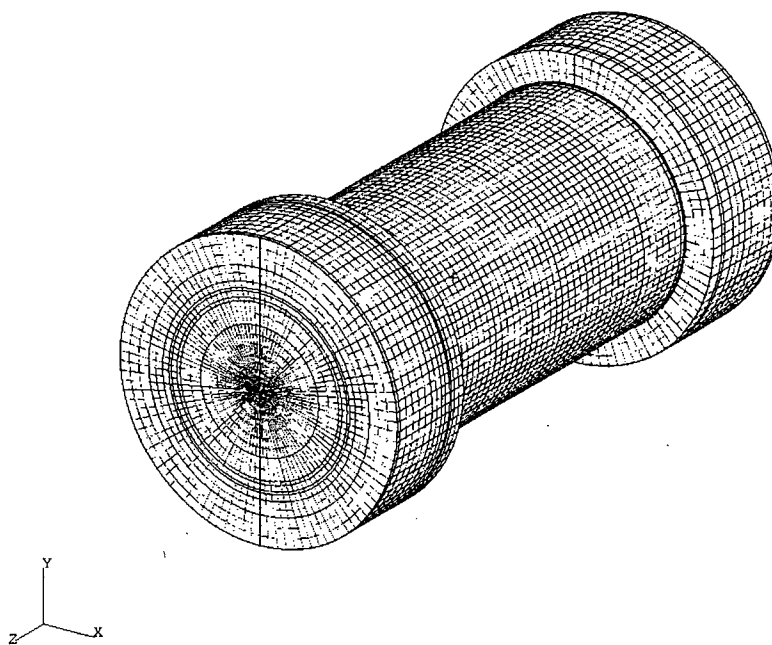


Figure IV-19. The Rail-Lead cask mesh (mesh is symmetric, only half shown).

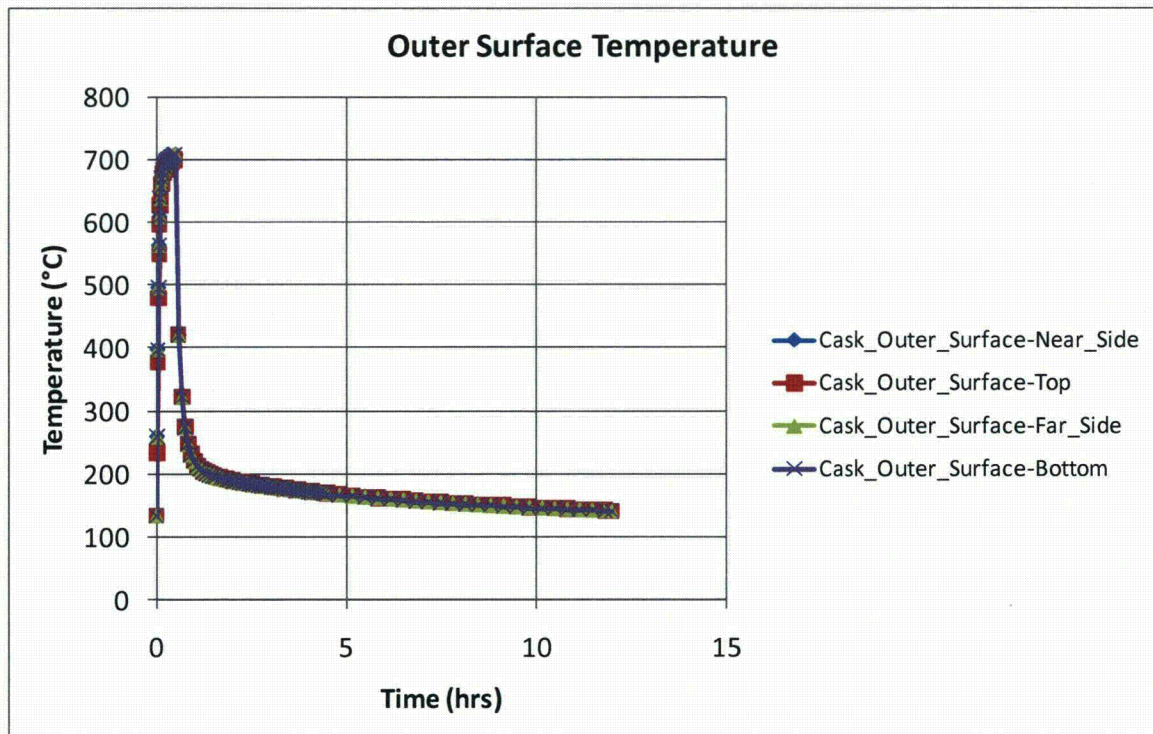
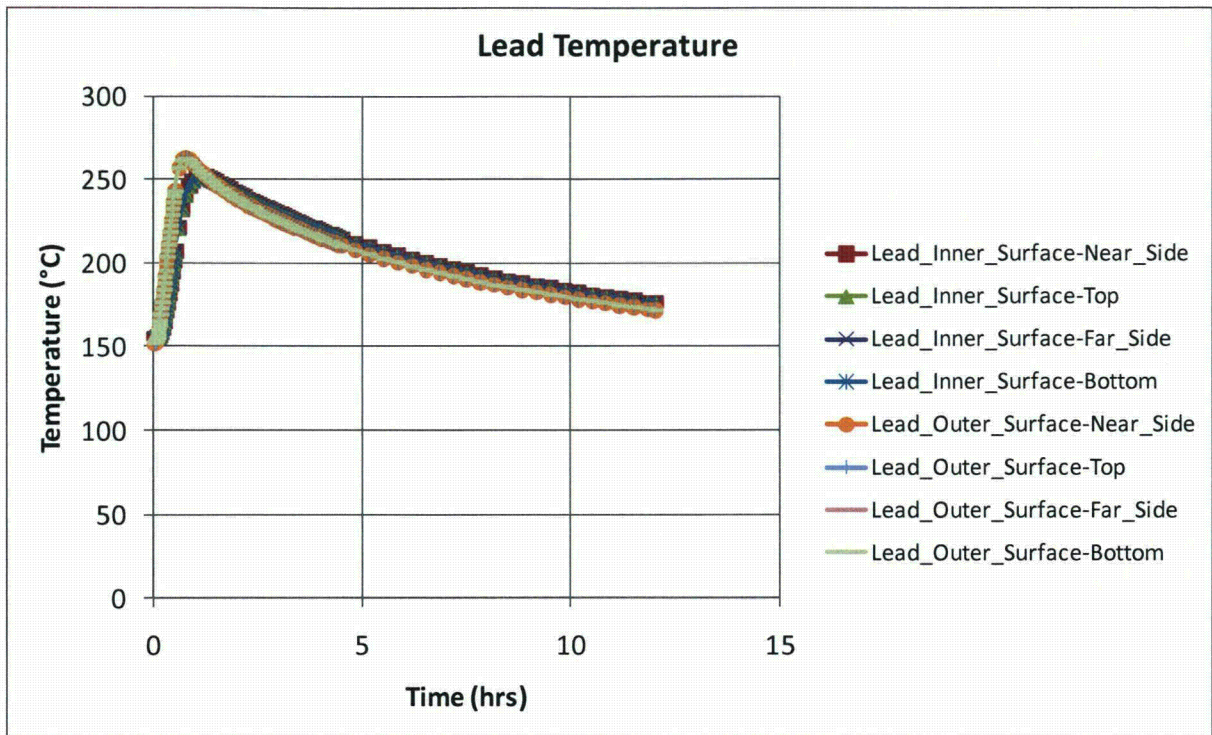


Figure IV-20. Rail-Lead cask Regulatory Uniform Heating Results - Continue

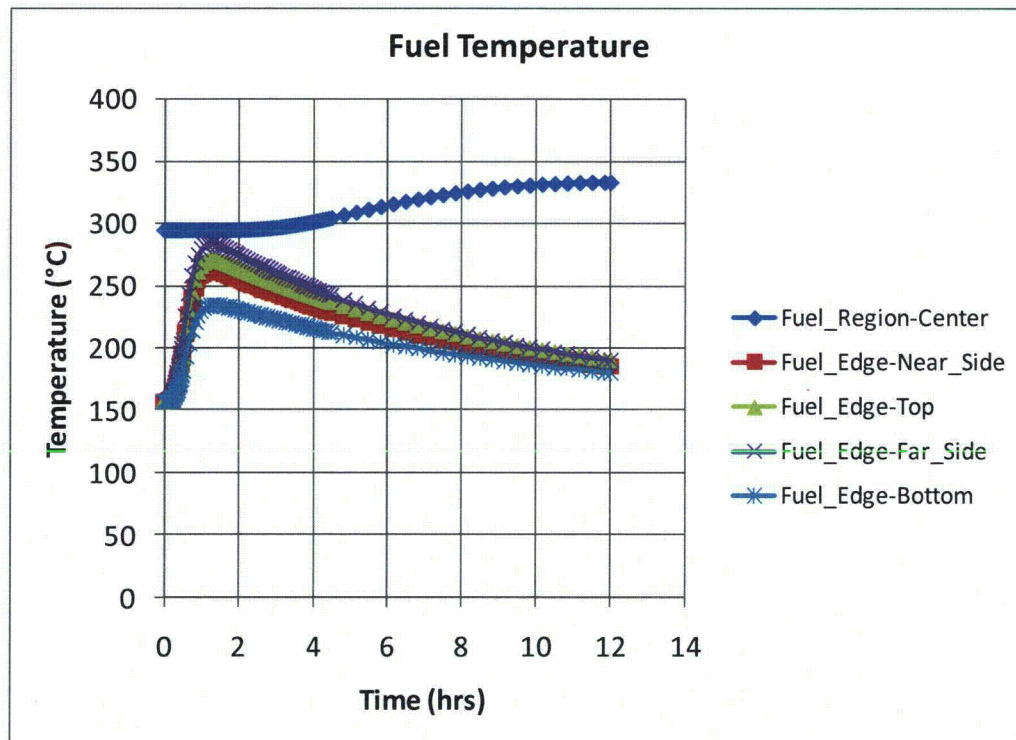
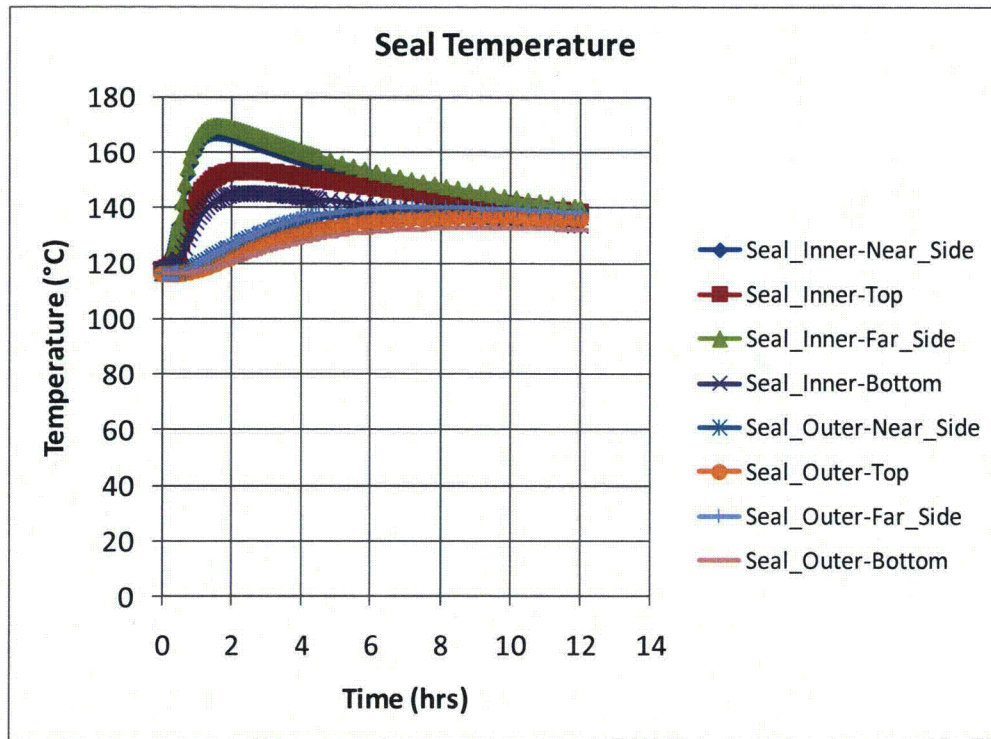


Figure IV-21. Rail-Lead Cask CAFE Regulatory Fire

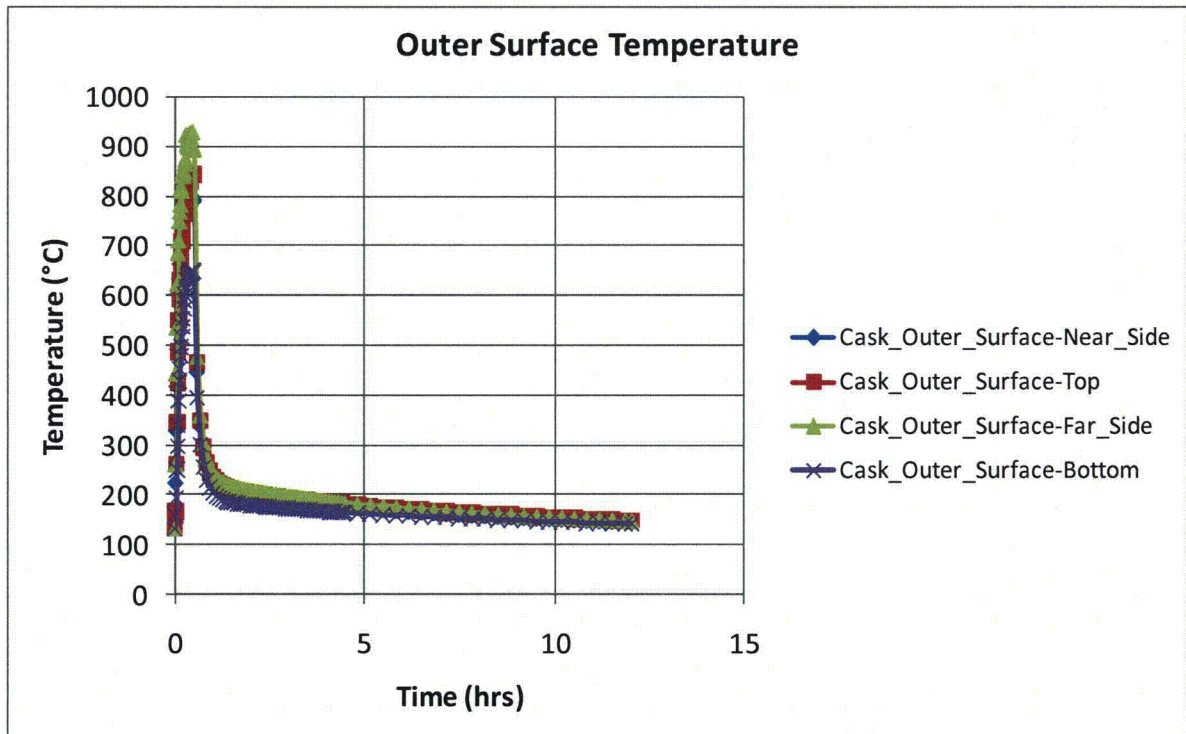
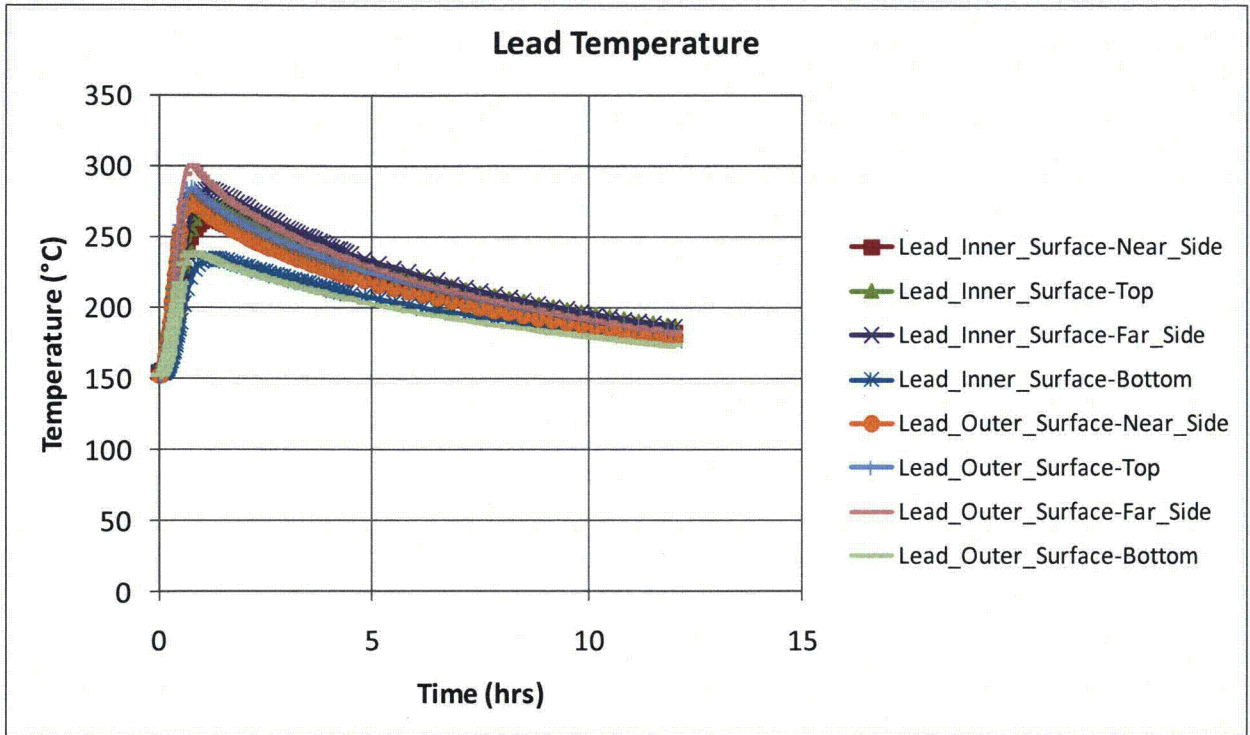


Figure IV-21. Rail-Lead Cask CAFE Regulatory Fire - Continue

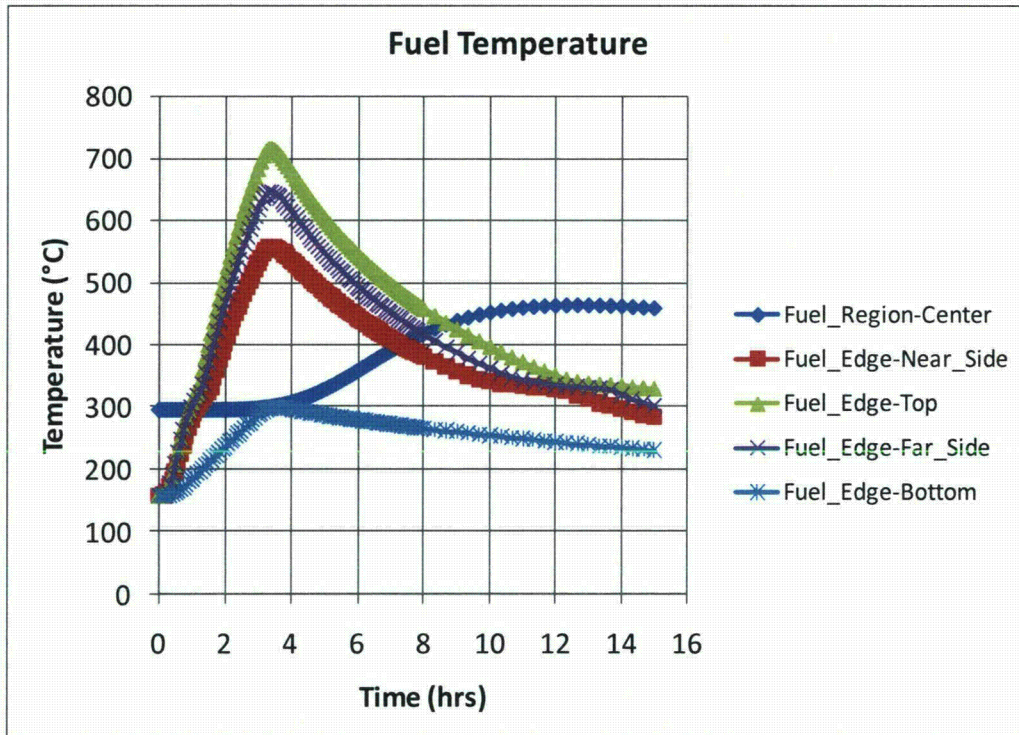
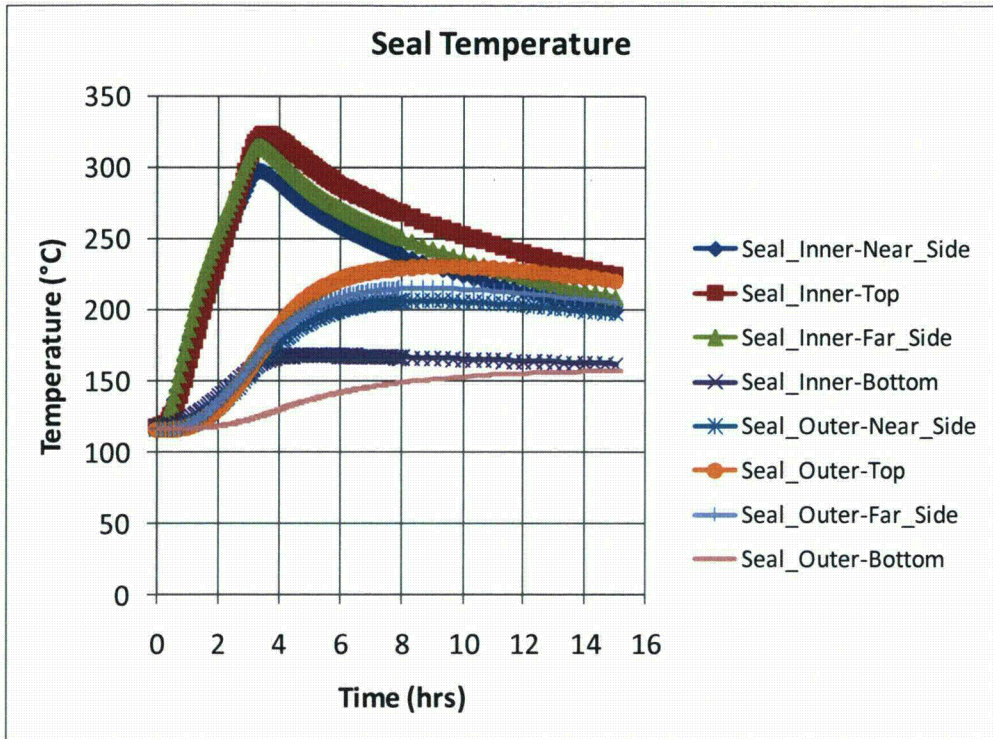


Figure IV-22. Rail-Lead cask on ground at the pool center.

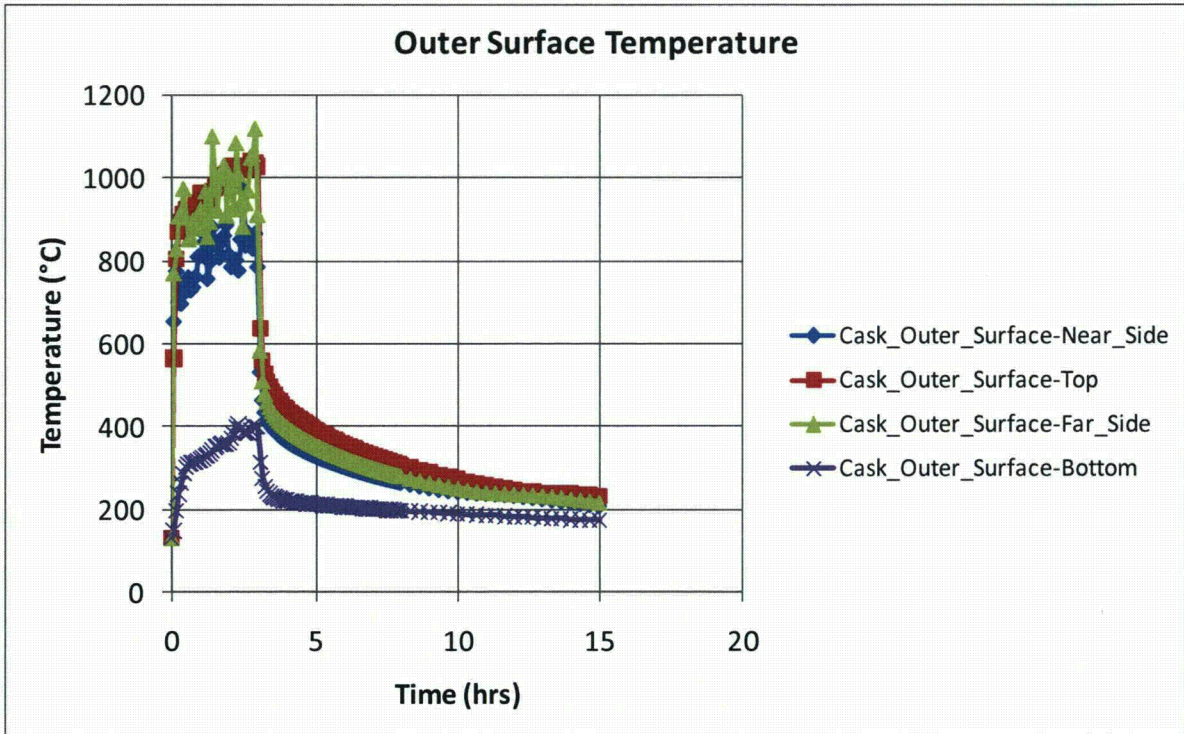
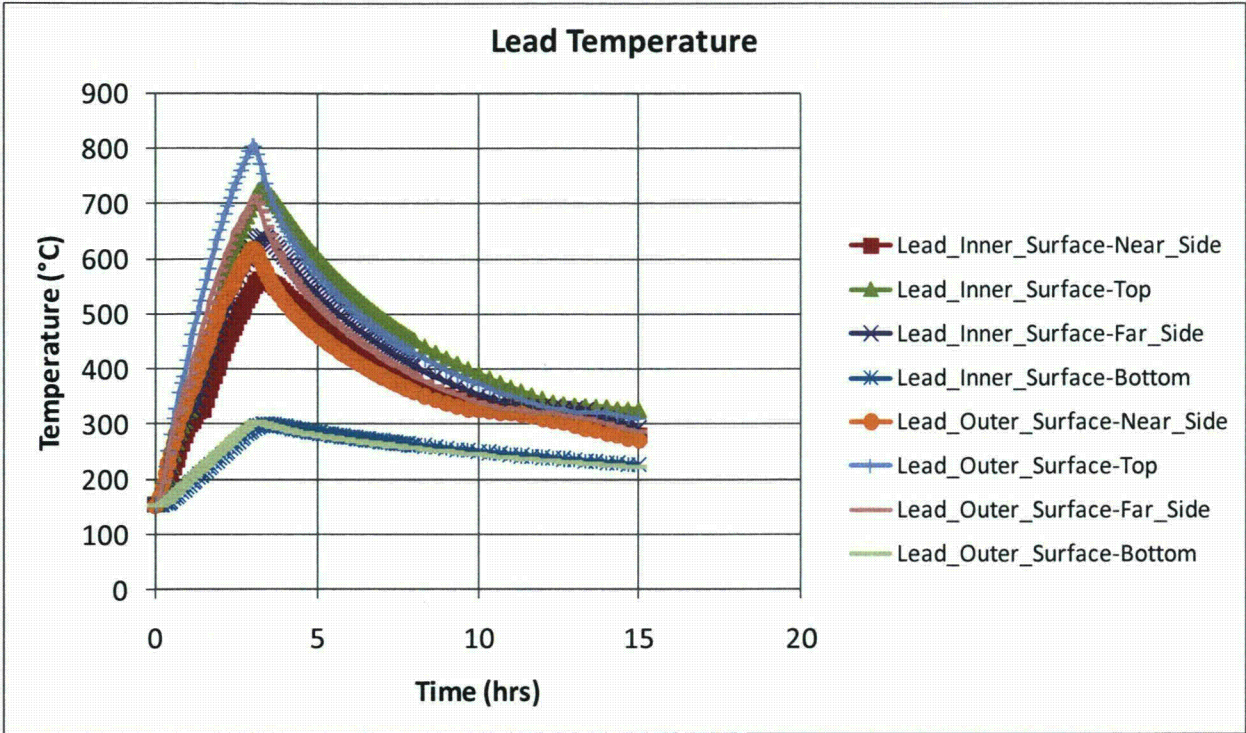


Figure IV-22. Rail-Lead cask on ground at the pool center. - Continue

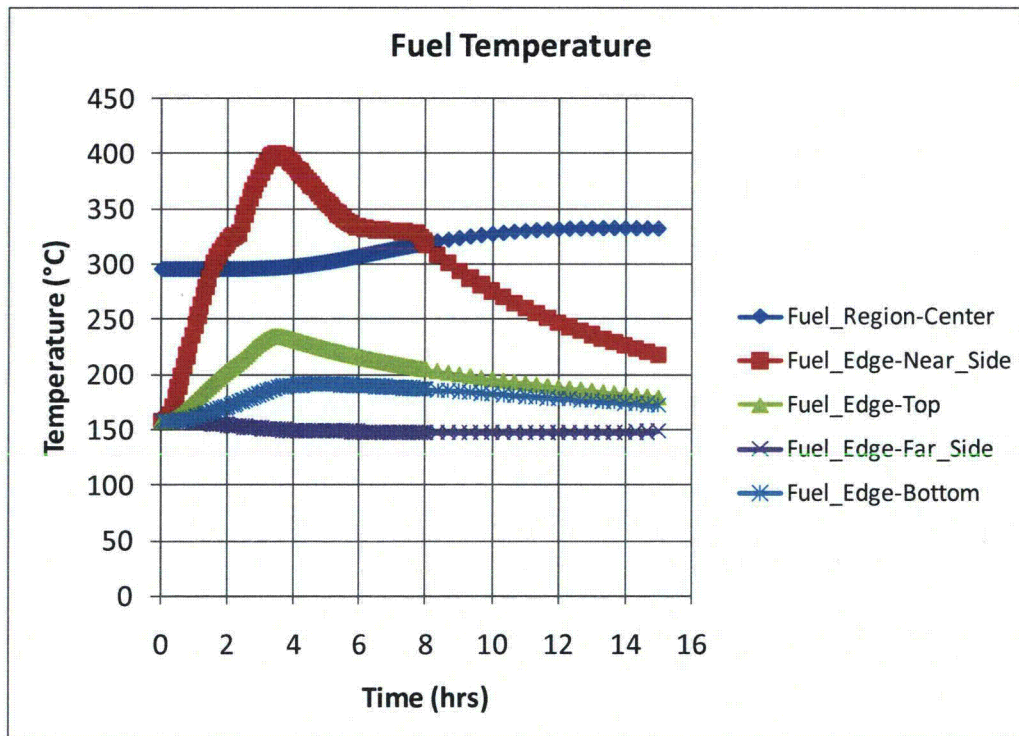
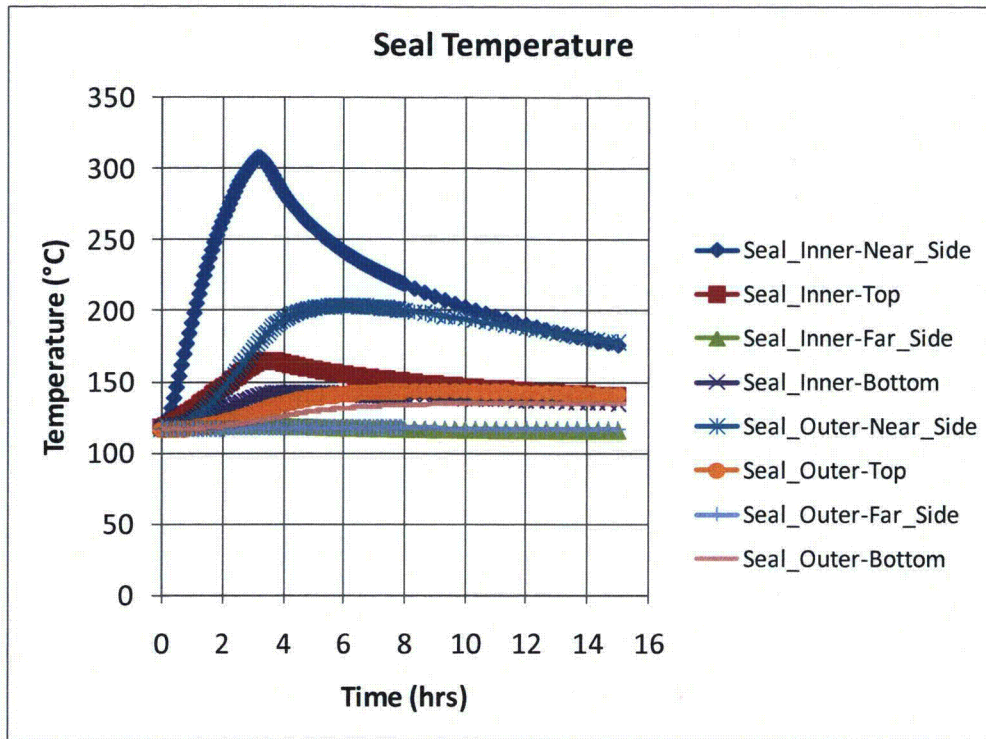


Figure IV-23. Rail-Lead cask on ground 3.0m (10ft) from the edge of the pool.

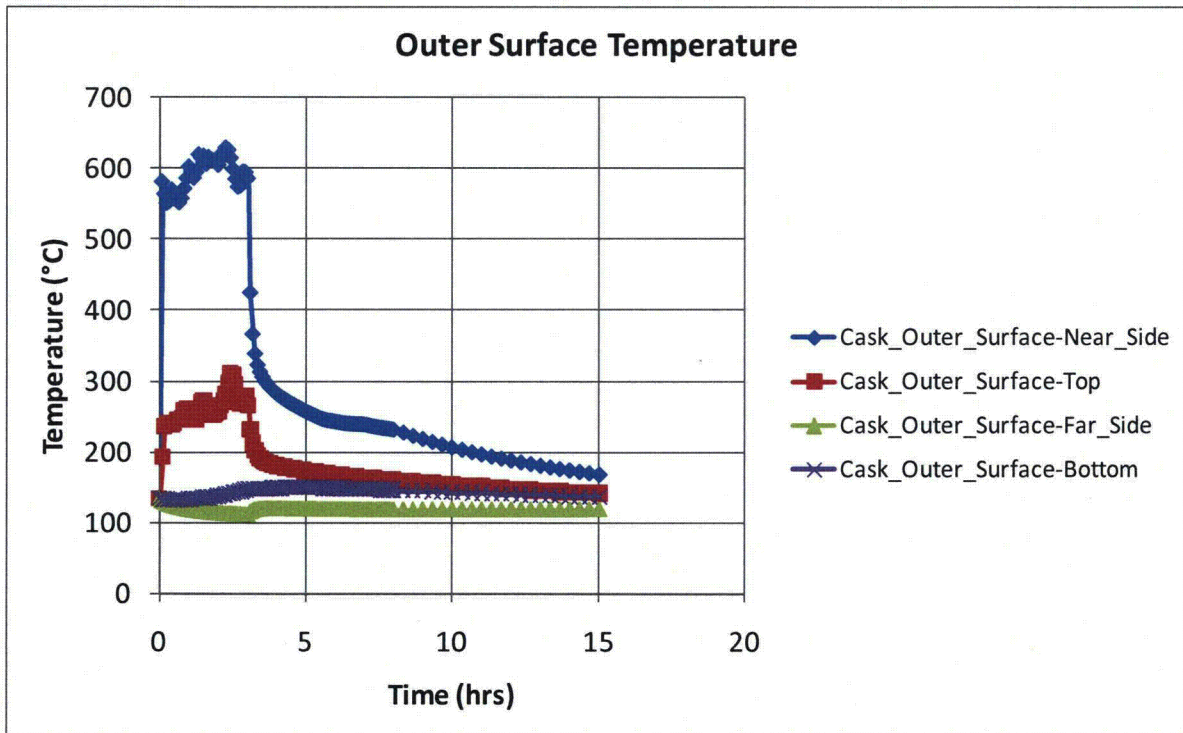
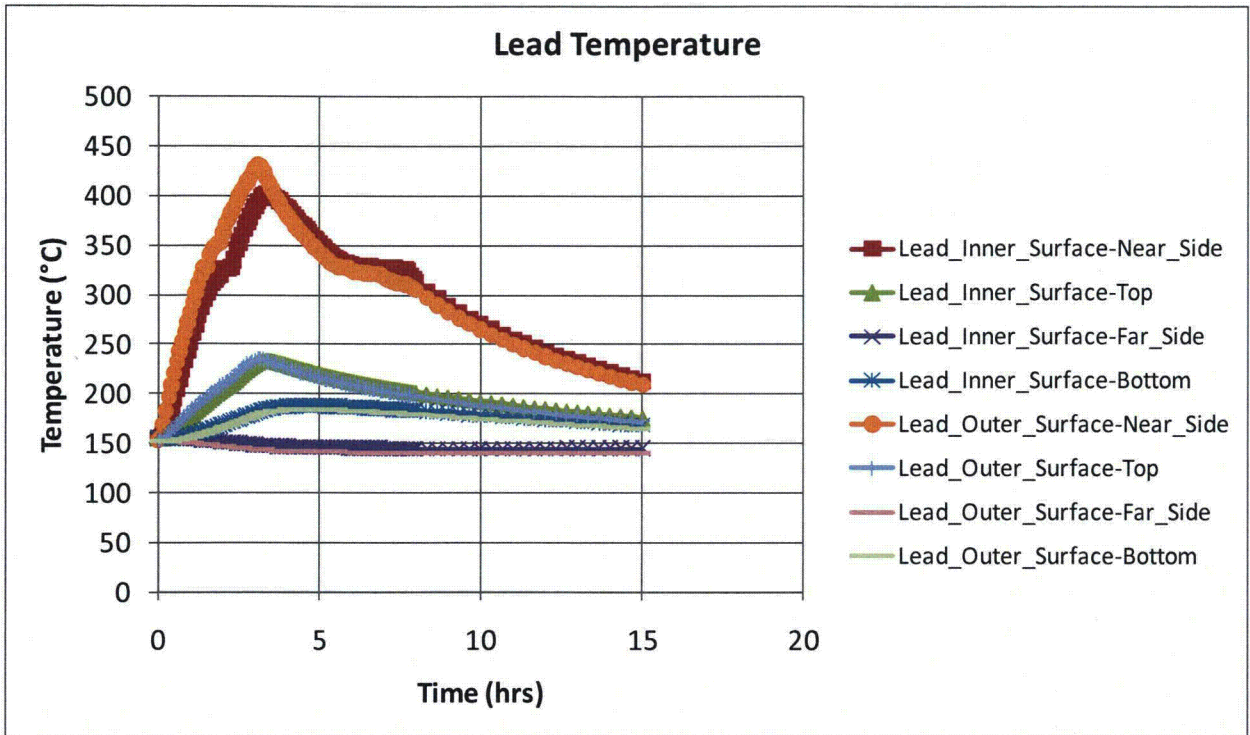


Figure IV-23. Rail-Lead cask on ground 3.0m (10ft) from the edge of the pool. - Continue

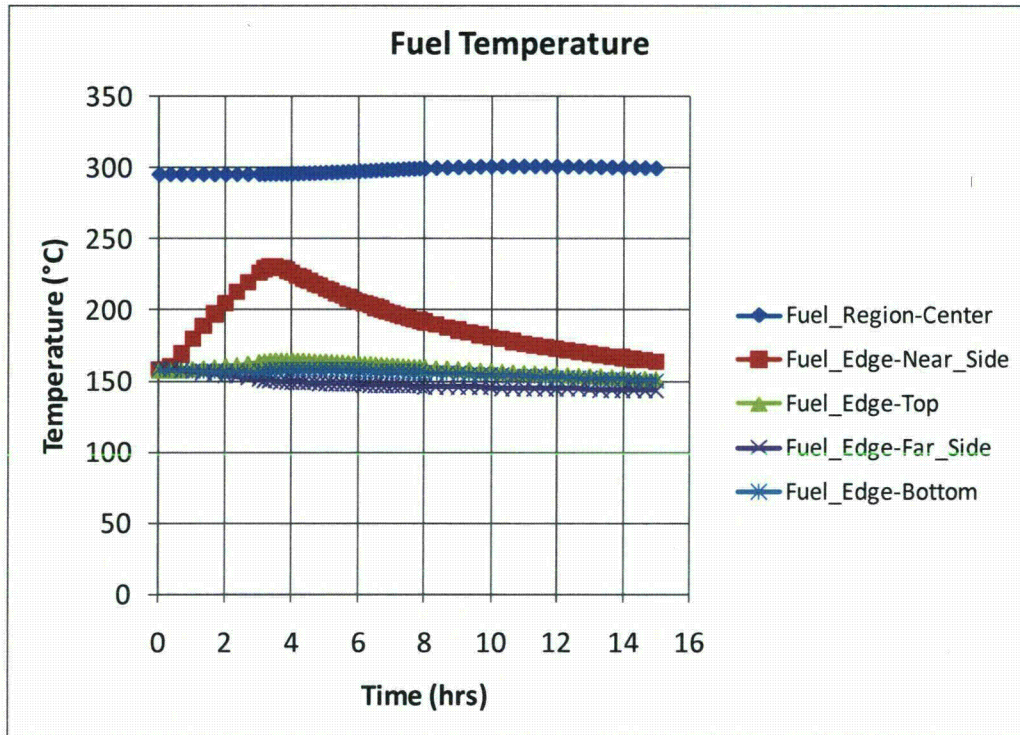
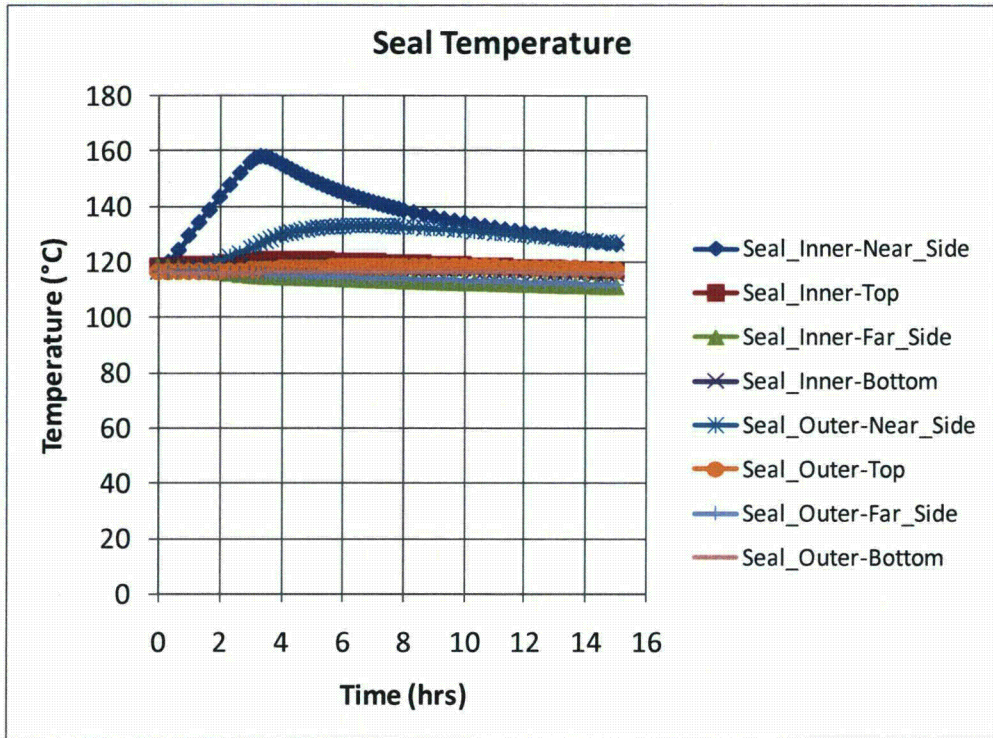


Figure IV-24. Rail-Lead cask on ground 18.3m (60ft) from the edge of the pool.

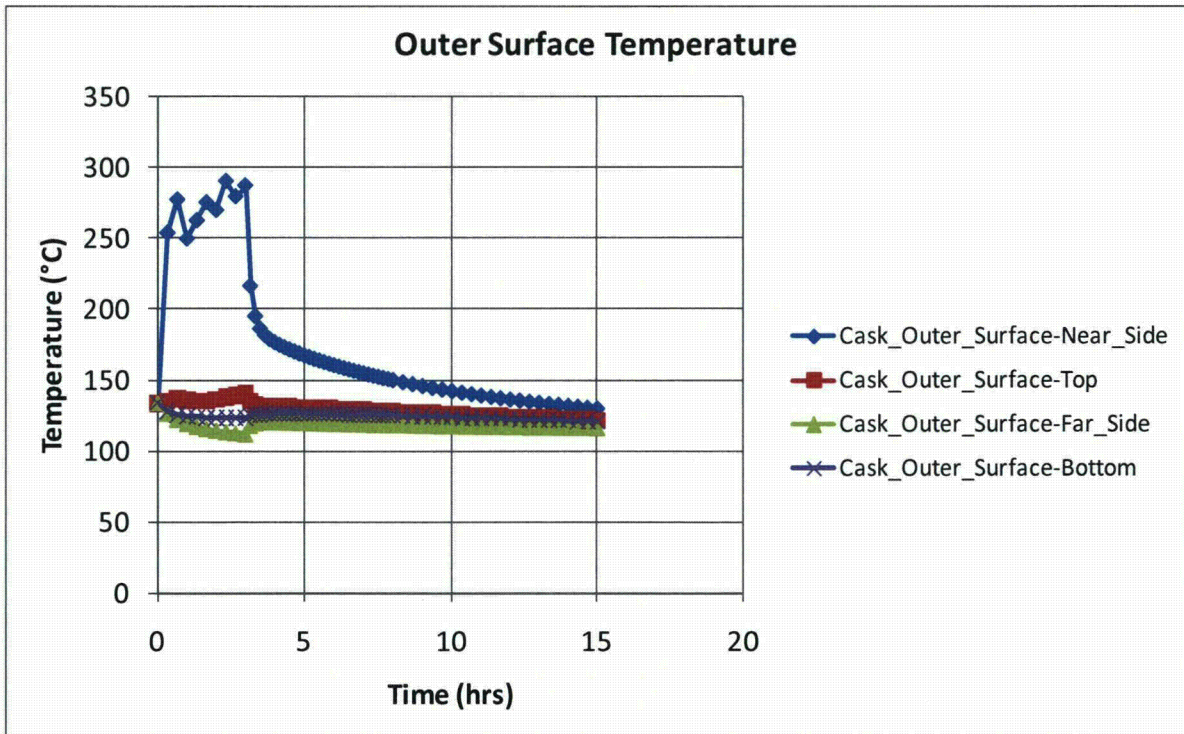
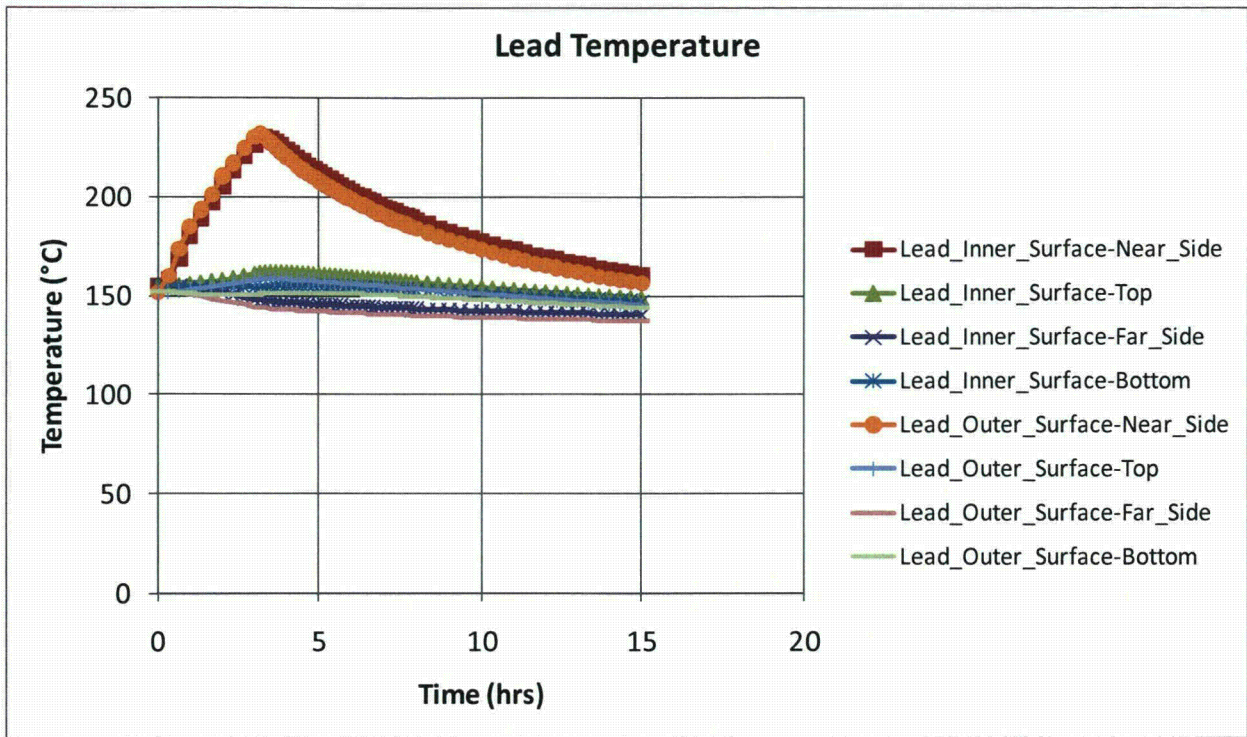


Figure IV-24. Rail-Lead cask on ground 18.3m (60ft) from the edge of the pool. – Continue

Overall, maximum temperatures obtained using the model developed here and in the Rail-Lead cask SAR are also similar. Again, the difference in purpose of the two analyses leads to some different assumptions, which in turn leads to slightly different results.

IV.3.5 Rail-Lead Cask Thermal Analysis Results

The following figures (see pages 415 through 423) show additional results for the Rail-Lead cask not provided in Chapter 4. Figure IV-20 shows results for the regulatory uniform heating case. Recall this is a P-Thermal only run. Figure IV-21 shows results for the regulatory CAFE fire; Figure IV-22 shows results for the fully engulfing CAFE fire run with the cask on the ground; and Figure IV-23 and Figure IV-24 show results for the CAFE fire runs with the cask on the ground and outside the pool area. As with the Rail-Steel cask, the last three cases are run for a total of three hours. A discussion of these results and their implications is provided in Chapter 4.

IV.4 Truck Cask with Depleted Uranium

The Truck-DU cask is slightly different from the two previously analyzed casks. This cask is certified to transport up to four PWR spent fuel assemblies on a truck flat bed and uses depleted uranium for the gamma shield. In this analysis, the cask is assumed to be in the horizontal configuration, as it would most likely be after an accident scenario. For the Truck-DU cask, results reported in the Truck-DU FDR (General Atomics, 1993) are used, but modified where necessary to reflect the current study.

IV.4.1 Geometric Considerations

The Truck-DU consists of an overpack, a fuel basket, and limiters at each end. Like the Rail-Lead cask, the Truck-DU is a single containment cask with no MPC. Compared to the Rail-Steel and Rail-Lead casks, however, this cask is smaller in size [1.00m (39.8in) in diameter at the center, 2.3m (90in) in diameter at the impact limiters, and 5.94m (234in) in length] since it only carries four spent fuel assemblies. Figure IV-25 shows the layout of the Truck-DU cask.

IV.5 Truck Cask with Depleted Uranium

The Truck-DU cask is slightly different from the two previously analyzed casks. This cask is certified to transport up to four PWR spent fuel assemblies on a truck flat bed and uses depleted uranium for the gamma shield. In this analysis, the cask is assumed to be in the horizontal configuration, as it would most likely be after an accident scenario. For the Truck-DU cask, results reported in the Truck-DU FDR (General Atomics, 1993) are used, but modified where necessary to reflect the current study.

IV.5.1 Geometric Considerations

The Truck-DU consists of an overpack, a fuel basket, and limiters at each end. Like the Rail-Lead cask, the Truck-DU is a single containment cask with no MPC. Compared to the Rail-Steel and Rail-Lead casks, however, this cask is smaller in size [1.00m (39.8in) in diameter at the center, 2.3m (90in) in diameter at the impact limiters, and 5.94m (234in) in length] since it only carries four spent fuel assemblies. Figure IV-25 shows the layout of the Truck-DU cask.

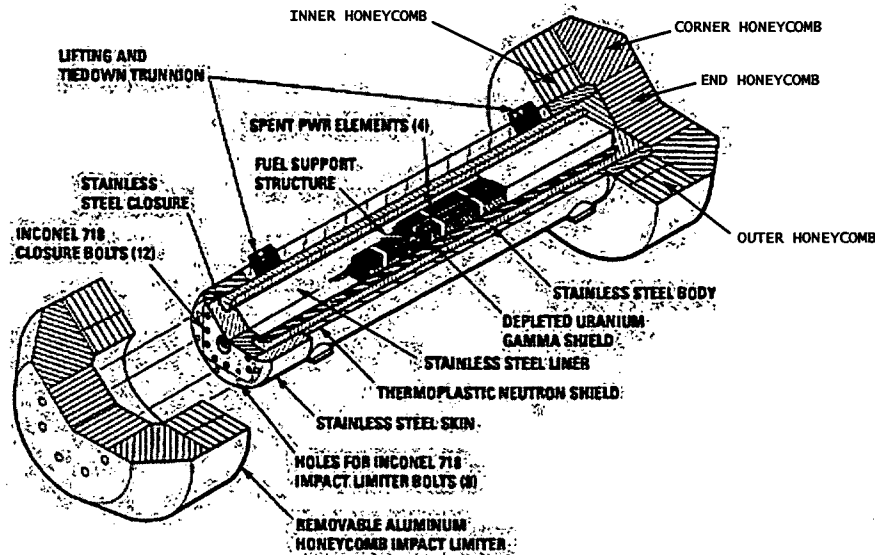


Figure IV-25. Components of Truck-DU cask (General Atomics 1993).

IV.5.1.1 Fuel Assembly and Interior Cavity of the Overpack

The inner cavity of the Truck-DU is a rectangular box 0.46x0.46m (18x18in) in the cross section and 4.25m (167in) long. Inside this cavity, the fuel assemblies are stored within four slots formed by a steel, fuel support structure (FSS). The details of the fuel assembly are discussed in Section IV.2.1.2. The FSS is made from four panels [0.016m (0.61in) thick] arranged in a perpendicular cross pattern. The fuel assembly and FSS together are referred to as the fuel basket in this section. Fuel spacers and other support structures complete the remaining space at the ends of the fuel basket. These regions are referred to in this section as the fuel basket ends.

In this analysis, the fuel basket and the fuel basket end regions are each represented as single volumes to minimize geometric complexity, but their thermal response is accounted for using effective properties.

IV.5.1.2 Overpack

The overpack center cross section is made from a five layer cross section. The first three inner layers are square with rounded corners. The first layer, the cavity liner, is a thin steel wall [9.5mm (0.376in) thick] that separates the contents of the cask from the gamma shield. The second layer is a thick wall [6.7cm (2.6in) at the center of the cask] of depleted uranium which serves as the gamma shield. The third, and last square layer, is a thick wall [7.6cm (3in)] of steel. In the axial direction, the depleted uranium layer tapers off and extends just past the ends of the inner cavity of the overpack. The cavity liner and the thick steel wall extend almost to the axial ends of the gamma shield. The cavity liner and the thick steel wall mate with a square shaped, steel flange at the top of the overpack and a square shaped, metal base cup at the bottom. The inner cavity of the overpack is sealed off from the environment using a steel lid [0.28m (11in)

thick at the center] which fits on the flange as shown in Figure IV-25. The metal base cup is 0.24m (9.5in) thick.

The last two layers, the neutron shield and the thin steel outer skin wall [1cm (0.4in) thick], form the rest of the center cross section of the overpack. The outer surface of the neutron shield layer and the outer skin wall are circular in shape. In the axial direction, the neutron shield and the outer skin wall extend the interior plane wall of the impact limiters. Both layers mate with an impact limiter support structure (ILSS) at these extreme ends. The ILSS is design to support the impact limiters using a series of ribs, 1.9cm (0.75in) thick, that extend radially outward from the exterior surface of the thick steel wall to the interior surface of the outer shell wall of the of the ILSS. The space between these ribs and between the exterior surface of the thick steel wall and the interior surface of the outer shell wall of the ILSS is filled with a neutron shield material. In the axial direction, the ILSS extends to the end of the lid at the top, and to the metal base cup at the bottom.

The cavity liner, gamma shield, thick steel wall, flange, base metal cup, lid, neutron shield region, and outer skin wall are represented explicitly in the thermal model with minor alterations to simplify the model. The ILSS are represented as single volumes to minimize geometric complexity, but their thermal response is accounted for appropriately using effective properties. As with the Rail casks, the Truck-DU cask overpack contains a number of features that serve a special purpose (e.g., valves, seals, trunnions, etc.) These features are omitted from the model as is done in the previous Rail cask models and for the same reasons: (1) negligible due to their small volume and mass relative to the other components in the overpack, (2) highly localized with no effect to the overall thermal performance of the cask at locations of interest, or both.

IV.5.1.3 Impact Limiters

The Truck-DU cask, impact limiters bolt to the top and bottom of the overpack. These impact limiters are similar to the Rail-Steel limiters in that they are made of aluminum honeycomb material encased in a thin steel shell. The honeycomb material is arranged as shown in Figure IV-25.

In this model, the impact limiters were assumed undamaged; hence, they are modeled using the geometry shown in Figure IV-25. The encasing steel shell is neglected since the total volume of the shell is small compared to the rest of the honeycomb material.

IV.5.2 Truck-DU Thermal Behavior and Model Assumptions

Like the Rail casks, the Truck-DU cask is designed to release heat passively under normal conditions of transport. The Truck-DU fuel basket is designed to accommodate a maximum heat load of 2468W (a maximum of four fuel assemblies at 617W per assembly). Table IV-16 shows the normalized, axial heat generation rate distribution for a 617W PWR assembly. This axial heat generation profile is applied over the active fuel region which encompasses only about 3.66m (144 in) of the total fuel assembly length.

As with the Rail casks, heat is dissipated from the fuel rods to the exterior surfaces of the Truck-DU cask by a combination of conduction, convection, and radiation heat transfer. Heat transfer from the fuel assemblies to the outer surface of the overpack and the limiters is similar to the

Table IV-16. Axial burn up profile in the active fuel region of the Truck-DU cask

Axial Distance from Bottom of Active Fuel(% of Active Fuel Length)	Normalized Value
0-1.4	0.432
1.4-4.2	0.630
4.2-7.6	0.847
7.6-11.1	0.964
11.1-15.3	1.09
15.3-24.3	1.22
24.3-38.9	1.22
38.9-66.0	1.09
66.0-77.9	0.964
77.9-84.7	0.847
84.7-91.7	0.630
91.7-96.3	0.432
96.3-100	0.252

other rail casks. The only exception is there are fewer large voids through the cross section of this cask. Heat dissipation from the center cross section of the cask is predominately by conduction and radiation through the fuel assembly and the FSS. Conduction dominates through the overpack cross-section. In the axial direction, radiation occurs between the ends of the fuel assembly and inner cavity wall. Conduction through the honeycomb material is complex; however, effective properties found in the Truck-DU cask FDR are used to obtain the thermal response of the impact limiters.

The Truck-DU cask is also designed to maintain the temperature of critical components below their design limits during and after a 30 minute, fully engulfing, hypothetical accident condition (HAC) scenario. For fire accident scenarios lasting longer than the HAC fire described in 10 CFR 71.73, a significant amount of heat may be transferred to the interior of the cask. As in the Rail casks, the temperature of the neutron shield material is expected to reach temperatures beyond its temperature limit. Heat then is assumed to be dissipated by conduction through a gas layer in the neutron shield region and by radiation between the outer surface of the thick steel wall layer and the inner surface of the outer skin wall.

IV.5.3 Truck Lead Materials and Thermal Properties

The Truck-DU cask is made of stainless steel, depleted uranium, copper, aluminum, polypropylene, Boral neutron absorber (B₄C) and helium. With the exception of spacers, bolts, and the lifting trunnions, which are all ignored in this analysis, all major components of the overpack are made from stainless steel, type XM-19. The outer skin wall of the overpack is made from a combination of XM-19 and copper. The stainless steel serves as the main support component while the copper enhances conduction in the axial direction. The neutron shield material is made from polypropylene which has a melting point above 149°C (300°F). The

impact limiters are made from various density, aluminum alloy materials. The stainless steel shell (XM-11 and XM-19) encasing the honeycomb material is ignored in this study. As with previous fuel basket wall materials, the FSS is made from stainless steel and B₄C.

With the exception of XM-19 and the honeycomb material, all material properties can be found in Sections IV.2.3 and IV.3.3. Table IV-17 and Table IV-18 show the material properties used for XM-19 and the honeycomb material. The honeycomb material is classified by location in the limiter (see Figure IV-25).

IV.5.3.1 Effective Thermal Properties

Effective properties were used for the active fuel basket region, the ends of the fuel basket, the neutron shield region, the ILSS region, and the outer skin wall (see Table IV-19 and Table IV-20). These properties were obtained from the Truck-DU cask FDR (General Atomics, 1993). For the HAC scenarios, the polypropylene material was replaced with air above 149°C (300°F) since polypropylene melts at relatively low temperatures. Recall that radiation heat transfer was added between the outer surface of the thick steel wall layer and the inner surface of the outer skin wall to increase heat transfer to the interior of the cask during the fire as was done in previous Rail cask analysis.

IV.5.4 Truck-DU P-Thermal Finite Element Model

In the Truck-DU runs, the cask model had 241,700 elements (see Figure IV-26). The element count is higher than in the Rail cask analysis since the Truck-DU has a number of smaller features which add to the element count. The boundary conditions for the normal condition, steady-state run; the regulatory uniform heating run; and the CAFE fire run are the same as discussed in Sections IV.2 and IV.2.4. In this analysis, the fire is run for only one hour. This time frame corresponds to the total fuel burning time for the maximum capacity, fully loaded, fuel tanker truck.

Table IV-17. Thermal conductivities for the Truck-DU cask materials.

Material	Thermal Conductivity W/m ² °C (Btu/hr-ft ² °F)				
	92°C (200°F)	226°C (450°F)	377°C (700°F)	477°C (900°F)	726°C (1340°F)
XM-19	12.3 (7.1)	15.2 (8.8)	17.0 (9.8)	18.7 (10.7)	22.8 (13.2)
Inner Honeycomb k _r /k _z	8.7/2.6 (5.0/1.5)				
Outer Honeycomb k _r /k _z	6.5/2.0 (3.8/1.2)				
Corner Honeycomb k _r /k _z	1.7/2.9 (0.98/1.8)				
End Honeycomb k _r /k _z	2.6/8.6 (1.5/5.0)				

Table IV-18. Volumetric Specific heat for the Truck-DU cask materials.

Material	Volumetric Specific Heat (ρC_p) J/m ³ -°C (Btu/ft ³ -°F)
XM-19	4287264 (37242)
Inner Honeycomb	1553000 (41.7)
Outer Honeycomb	117000 (3.1)
Corner Honeycomb	39290 (1.05)
End Honeycomb	1553000 (41.7)

Table IV-19. Effective thermal conductivities for the Truck-DU cask materials.

Material	Thermal Conductivity W/m-°C (Btu/hr-ft-°F)				
	92°C (200°F)	226°C (450°F)	377°C (700°F)	477°C (900°F)	726°C (1340°F)
Active Fuel Region k_r/k_z	1.2/4.5 (1.0/3.8)	1.8/4.9 (1.5/4.2)	2.3/5.2 (2.0/4.4)	2.8/5.7 (2.4/4.9)	4.9/7.3 (4.2/6.2)
Fuel Region Ends k_r/k_z	0.28/3.3 (0.24/2.8)	0.31/3.8 (0.26/3.2)	0.33/4.1 (0.28/3.5)	0.35/4.6 (0.30/3.9)	0.40/6.3 (0.34/5.3)
Neutron Shield Region k_r/k_z	1.7/0.15 (1.5/0.12)				
ILSS $k_{r_bottom}/k_{r_top}/k_z$	2.2/3.9/0.85 (1.8/3.3/0.72)	2.8/4.9/1.0 (2.3/4.1/0.85)	3.2/5.6/1.2 (2.7/4.8/1.0)	3.5/6.1/1.3 (3.0/5.2/1.1)	4.2/7.5/1.5 (3.6/6.4/1.3)
Outer Skin Wall k_r/k_z	12.2/41.5 (10.4/35.4)	15.2/44.0 (13.0/37.5)	17.0/45.5 (14.5/38.8)	18.6/47.0 (15.9/40.0)	22.8/50.3 (19.4/42.9)

Table IV-20. Effective volumetric specific heat for the Truck-DU cask materials.

Material	Volumetric Specific Heat (ρC_p) J/m ³ -°C (Btu/ft ³ -°F)
Active Fuel Region	938700 (25.2)
Fuel Region Ends	1263000 (33.9)
Neutron Region	1715000 (46.0)
ILSS	1225000 (32.8)
Outer Skin Wall	3882000 (104.2)

Overall, maximum temperatures obtained in the normal condition, steady state run and in the regulatory uniform heating case using the model developed here are similar the results presented in the Truck-DU cask FDR. Again, the difference in purpose of the two analyses leads to some different assumptions, which in turn leads to slightly different results.

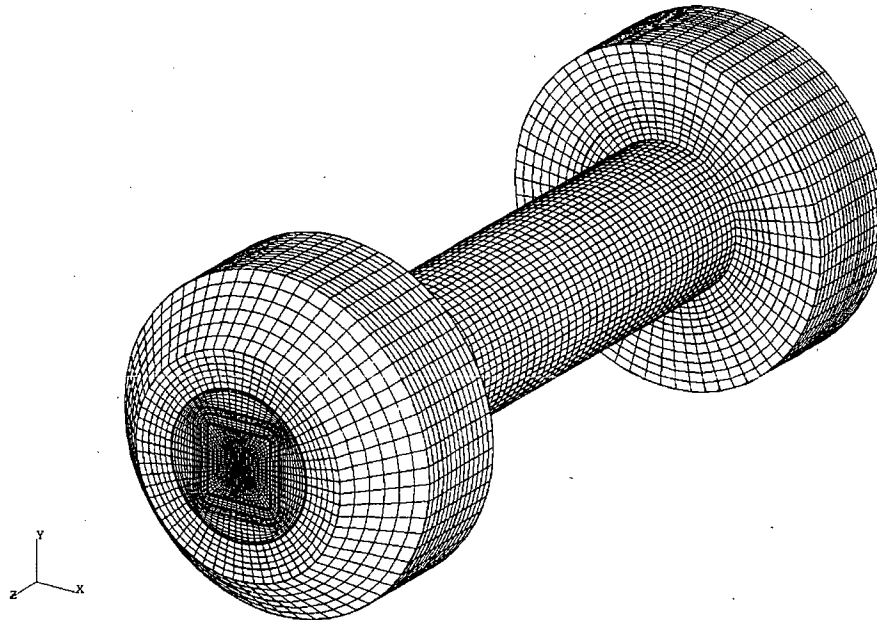


Figure IV-26. Truck-DU cask mesh

IV.5.5 Truck-DU Cask Thermal Analysis Results

Recall that for the Truck-DU cask, only one CAFE non-regulatory fire is run: the cask on ground and at the center of the pool (see Figure IV-27). This is the most severe case as demonstrated in the Rail-Steel and Rail-Lead cask analysis. Figure IV-28 shows additional results for this case not provided in Chapter 4. A discussion of these results and their implications is provided in Chapter 4.

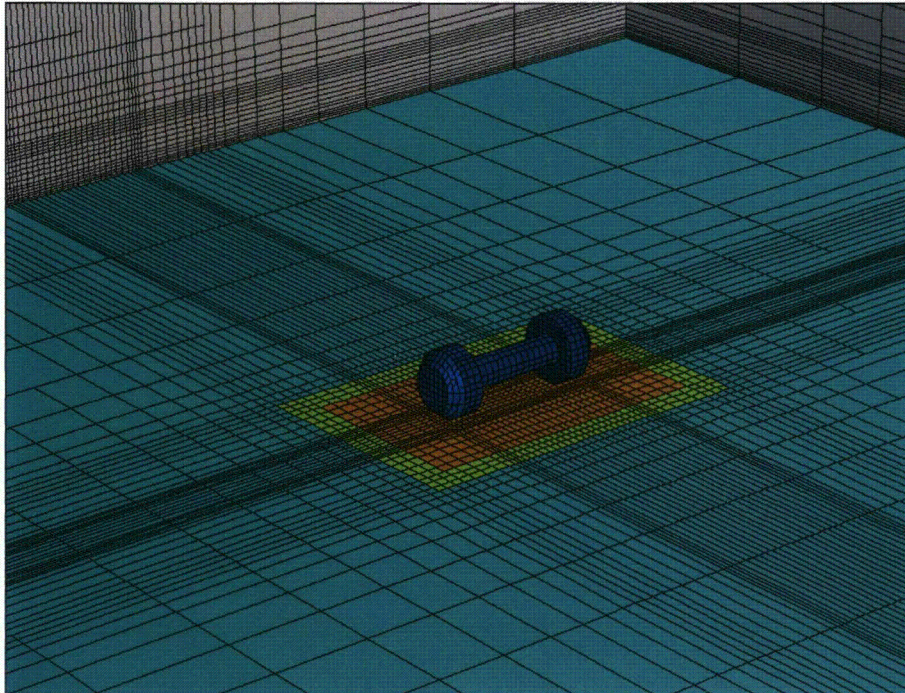


Figure IV-27. CAFE three-dimensional domain with Truck-DU cask on ground.

IV.6 CAFE Benchmark

Large, fully-engulfed objects have a great impact on the surrounding fire environment. To adequately predict incident heat flux to casks, computational fluid dynamics models must be employed with appropriate boundary conditions. Also, because of the impact that massive objects have on fires, computational fluid dynamics models must be validated against experimental data from tests that have similar size objects (Nicolette and Larson, 1989).

Since the development of the CAFE code (del Valle, et. al., 2009; del Valle, 2007; Are et.al., 2005; Lopez et. al., 2003), there has been a continuing effort to benchmark and fine-tune this fire model by making use of relevant empirical data from experiments. Continuing with this effort, prior to running the cases described in Chapter 4, CAFE is benchmarked against experimental data obtained from two fire test series conducted at Sandia National Laboratory Lurance Canyon Burn Site: (1) one using a large calorimeter in the center of the pool (Greiner, 2009; Kramer,

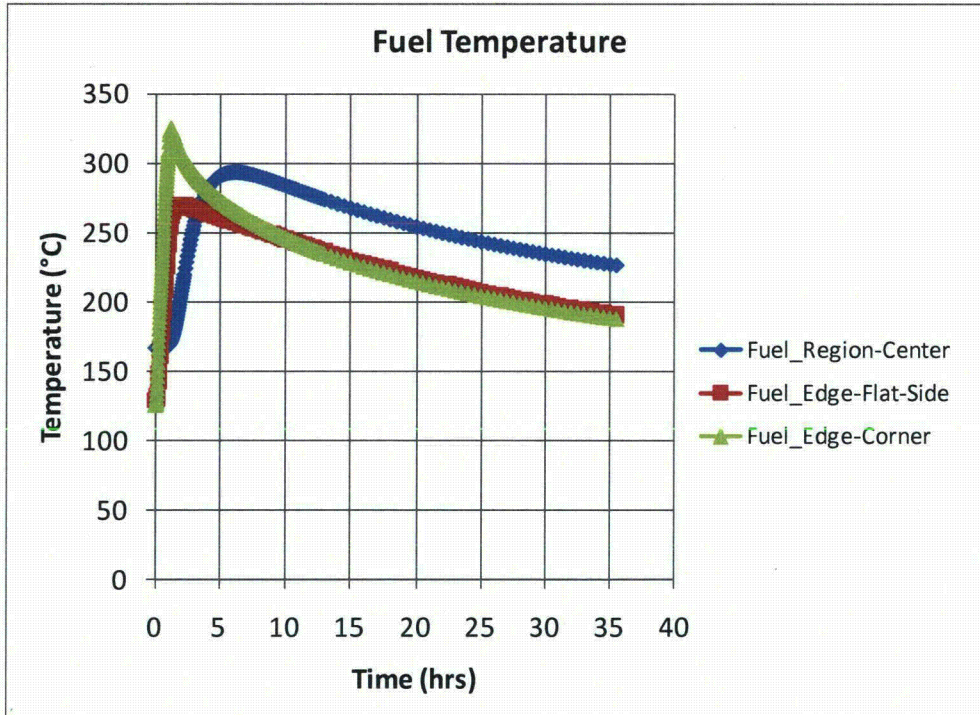
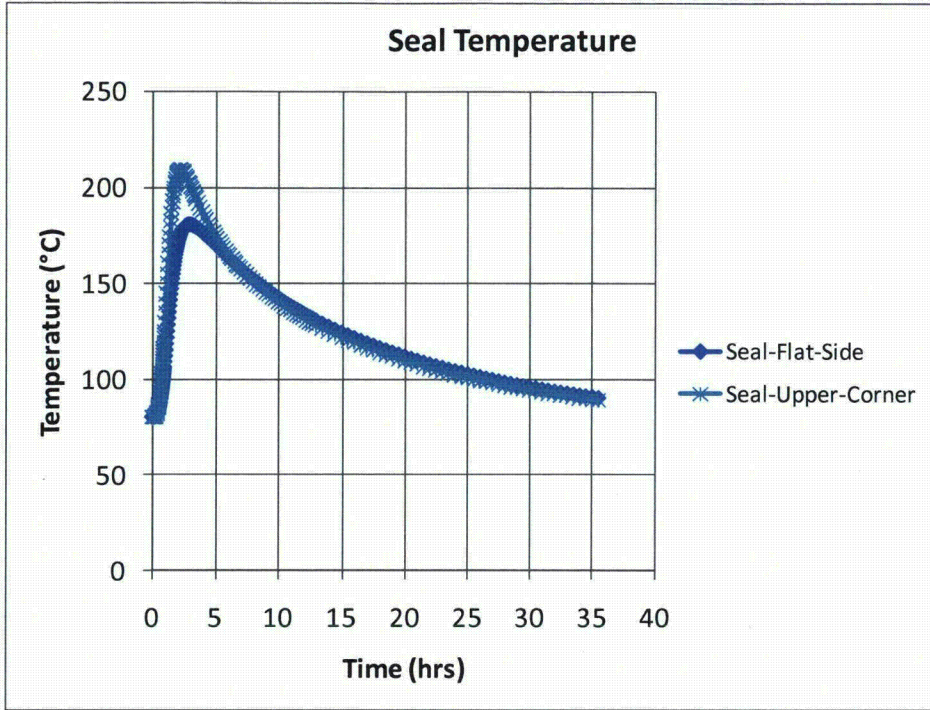


Figure IV-28. Truck-DU cask on ground at the pool center.

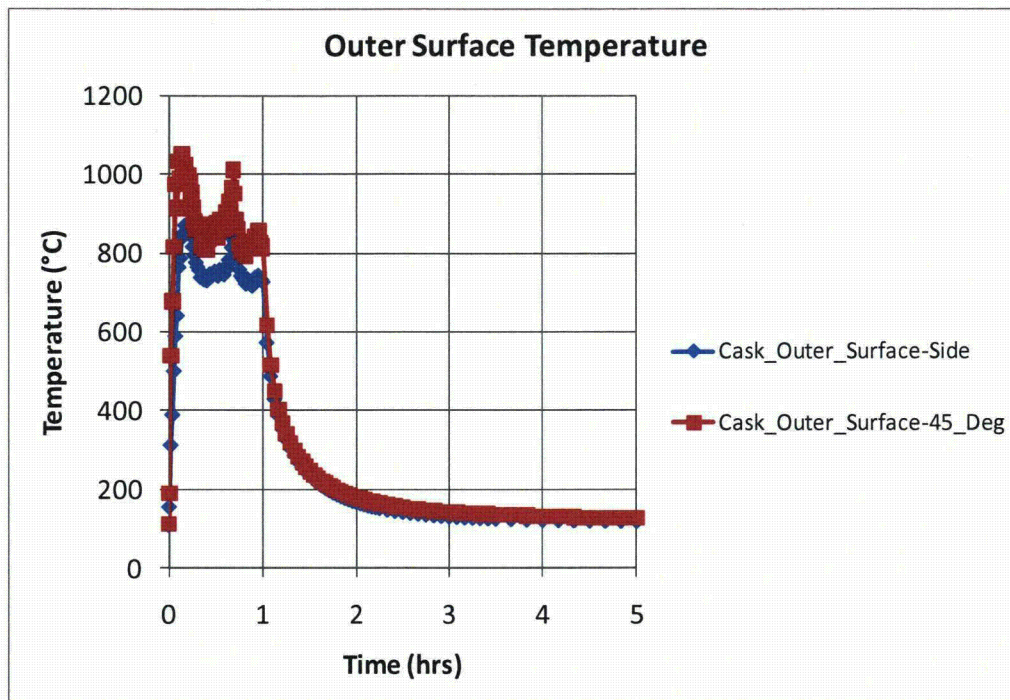


Figure IV-28. Truck-DU cask on ground at the pool center. - Continue

2008), and (2) the other using a smaller diameter calorimeter adjacent to the fire (Lopez et. al., 2003). The large calorimeter is close to the size of the casks analyzed in this study, and had a test setup and conditions that closely matched the regulatory hypothetical fire accident scenario outlined in 10CFR71.73 for certification of SNF transportation casks. The smaller diameter calorimeter test is used to benchmark CAFE's ability to predict heat flux to objects outside the fire plume. This section briefly describes these experiments, and shows benchmark results.

IV.6.1 Large Calorimeter Test and Benchmark Results

The large calorimeter is a carbon steel cylindrical pipe approximately 2.43m (96in) in diameter and 4.6m (180in) in length, with nominal 2.54cm (1in) thick walls, and had bolted lids on each end [see Figure IV-29(a)]. The calorimeter is placed on two stands at the center of a 7.93m (26ft) diameter fuel pool. The stands maintained the calorimeter 1m (39.4in) above the fuel surface. Approximately 2000 gallons of JP8 are used per test. Total burn time vary with tests, but is at least 25 minutes. All tests are conducted in relatively low wind conditions (<5m/s) to assure the calorimeter is fully or partially engulfed [see Figure IV-29(b)].

Thermocouples are installed on the interior walls of the calorimeter to measure interior surface temperatures. All TCs are installed in a ring configuration as shown in Figure IV-30. Heat flux gages are placed just outside the round walls of the calorimeter in a ring configuration and outside the lids to measure incident heat fluxes close to the outer walls of the calorimeter. Fuel burn rates are measured using a TC rake—a linear array of TCs traversing the depth of the fuel layer at known distance intervals. Directional flow probes are installed just outside of the calorimeter walls to measure the flow speed of hot gases near the calorimeter walls. Finally,

ultrasonic sensors placed on four towers—two sensor towers aligned with the calorimeter lids and two sensor towers perpendicular to the cylindrical section of the calorimeter, but on opposite sides—are used to measure wind speed and wind direction. Each tower is approximately 24.4m (80ft) from the center of the pool and had three ultrasonic sensors 2, 8 and 10m (6.5, 26.2, and 32.8ft) from the ground.

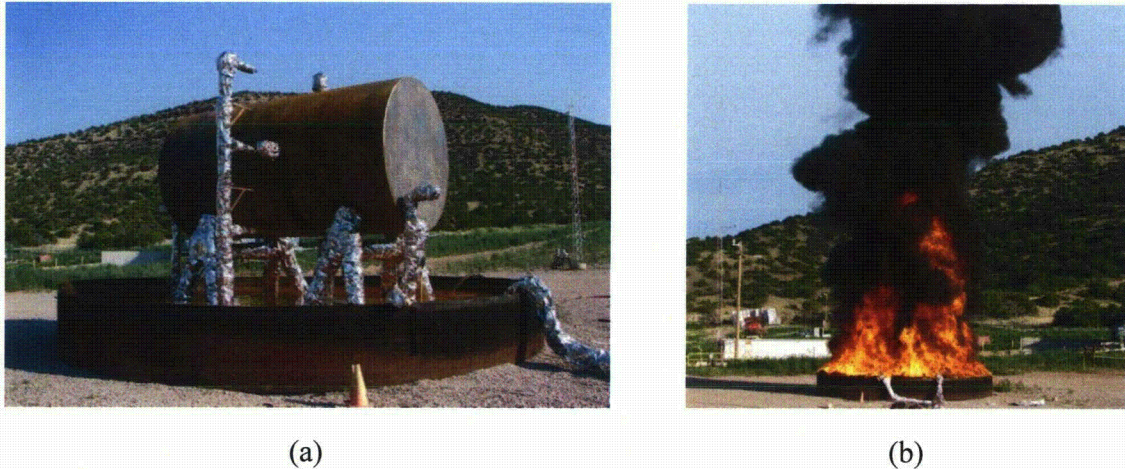


Figure IV-29. Large calorimeter fire test: (a) test setup and (b) fire fully engulfing the calorimeter.

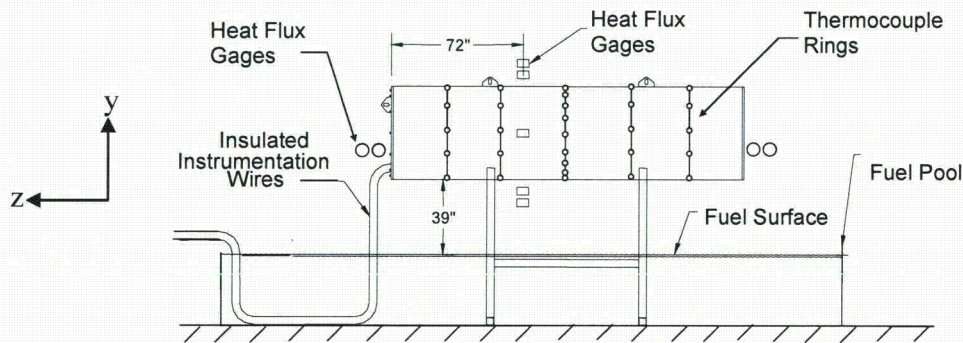


Figure IV-30. Side view (looking from the north) of calorimeter and test setup. Note: the calorimeter is centered with the pool. This drawing is not to scale.

Figure IV-31a shows average temperatures along the four circumferential sides of the calorimeter obtained from Test 1 and from the CAFE benchmark run. Data from Test 1 is chosen because the wind conditions and fire characteristics of this test best matched the regulatory conditions specified in 10CFR71.73 and the fire scenarios analyzed in this study. The test readings are taken from thermocouples located at 0 (north side, i.e., pointing out of the page), 90

(top side), 180 (south side, i.e., pointing into the page) and 270 (underneath) degrees. This plot illustrates that average temperature predictions obtained from CAFE envelope the average temperatures readings from the test.

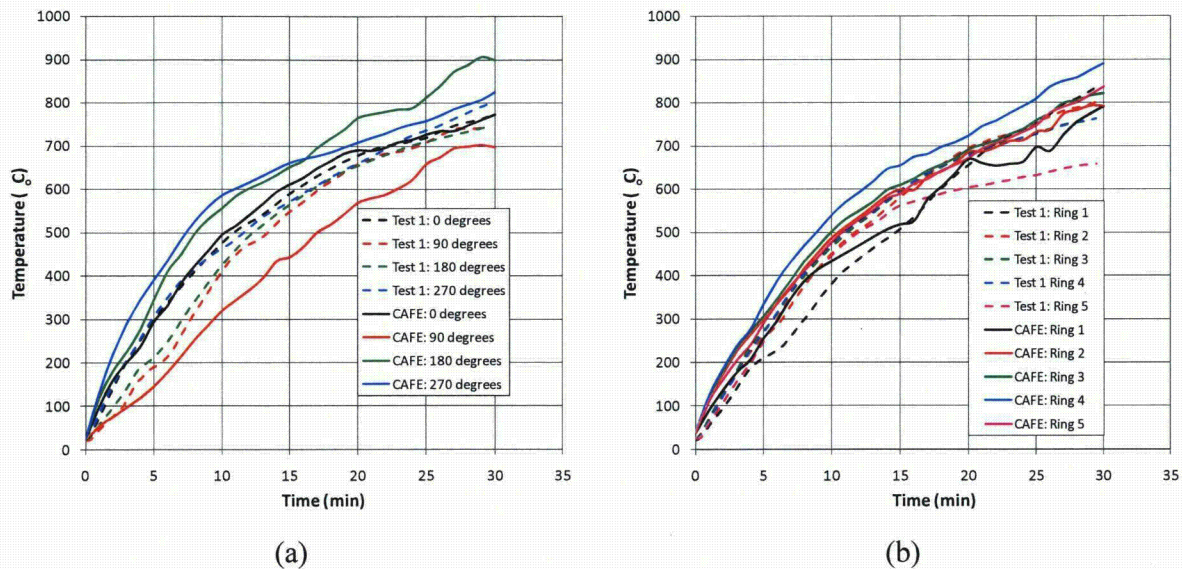


Figure IV-31. CAFE benchmark results using fully engulfed large calorimeter: (a) temperatures average along the 0, 90, 180, and 270 degree side looking at the calorimeter from the negative z-direction, and (b) temperatures averaged over each ring starting from Ring 1 located on the positive side of the z-axis.

From this perspective, CAFE over predicts temperatures underneath and on the south side of the calorimeter, and under predicts temperatures on the top of the calorimeter. Figure IV-31b shows a plot of average temperatures over each thermocouple ring starting from the left side of the calorimeter and moving along the negative z-axis as shown in Figure IV-30. From this perspective CAFE predicts the average temperatures over the rings reasonably well.

Closer inspection of the temperatures histories obtained from CAFE at each of the nodes corresponding to thermocouple locations revealed excellent agreement with test data over most of the cask, except at locations where the wind effects are strongest, the last two rings to the right of Figure IV-30 at 90 (top side), 180 (south side) and 270 (underneath) degrees. Temperatures at 180 and 270 degrees are higher than expected, while temperatures at 180 degrees are under predicted. Differences rapidly diminished going from the rings on the right side of the calorimeter to the rings on the left side as shown in Figure IV-30. Part of the reason for these discrepancies is the way in which the wind boundary conditions are applied in the computational fluid dynamics model. In the large calorimeter test series, wind speeds are obtained only at four locations around the pool, and at three heights. These height dependent data are applied uniformly over the corresponding cross sections of the domain, which does not necessarily reflect the actual conditions in the test. This leads to wind speeds being higher than expected in

some locations around the casks such as the south side of the cask near the ring 5 (rightmost ring in Figure IV-30).

IV.6.2 Small Calorimeter Test and Benchmark Results

Experimental data from a smaller pipe calorimeter is used to benchmark the view factor method used in CAFE (Lopez et al., 2003). The CAFE model for thermal radiation transport within and near large hydrocarbon fires is divided into two types, diffusive radiation inside the flame zone and clear air or view factor radiation outside the flame zone. Outside the flame zone, thermal radiation transport is modeled by the clear air or view factor method. The calculation of the view factor between the fire and an adjacent object is complicated due to the fact that the outer surface of a fire (or smoky region) is dynamically changing due to the puffing and turbulent nature of flames (Lopez et. al., 2003).

In the experiments, a calorimeter is positioned such that its axis is 1.5m (4.9ft) away from the center of the fuel pool. The wind blew the fire away from the calorimeter leaving a significantly larger gap between the pipe calorimeter and the plume. Results from tests and CAFE are presented in Figure IV-32. The temperatures shown are at the center ring of this calorimeter. The blue lines are obtained from experimental data and the black lines are obtained from CAFE. By looking at the temperature distribution of this very long pipe, it can be clearly seen how the external radiation algorithm worked on the far field object.

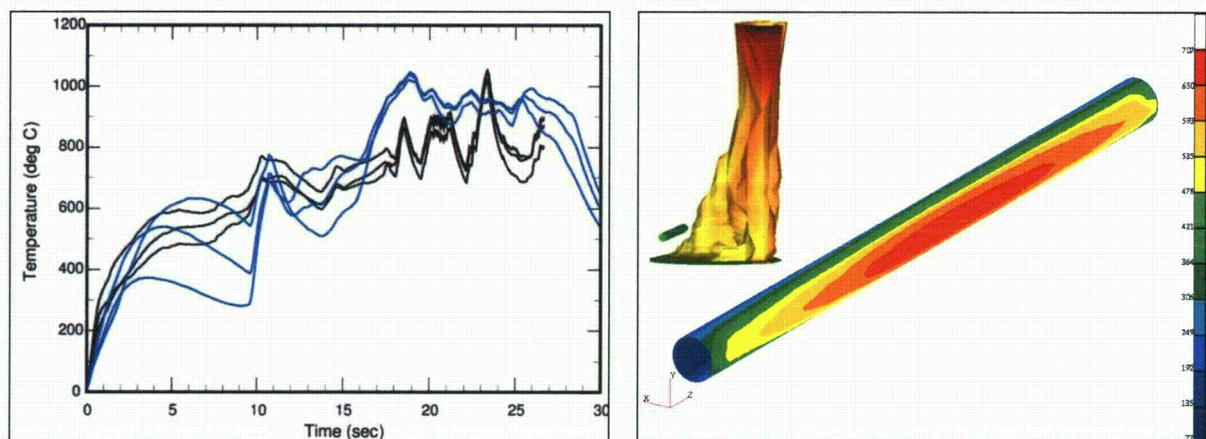


Figure IV-32. CAFE benchmark results using a small calorimeter 1.5m (4.9ft) from the edge of the fire.

IV.6.3 Summary of Benchmark Results

The fully engulfing benchmark results show that CAFE bounds the experimental calorimeter temperatures. Inside the fire, CAFE under estimates temperatures near the top of the calorimeter, while it over estimates temperatures on all other sides of the calorimeter. Taken as a whole, these results show that CAFE slightly over predicts the average temperature of the surface of the calorimeter. Therefore, it is expected that for the fully engulfing cases examined in this study, the cask surface temperatures predicted by CAFE will be close to or slightly higher than expected.

Outside the fire zone, CAFE is expected to predict reasonably accurate temperatures for objects near the fire. For objects further from the pool, results are expected to be less accurate given the method employed by the code. This is not a concern since the heat flux to objects outside the plume decreases with the distance squared, suggesting that the fire threat is also less severe with distance from the fuel pool as observed in the results for the 18.3m (60ft) standoff case.

IV.7 Summary

This appendix described the method employed to obtain the thermal response of the Rail-Steel, Rail-Lead, and Truck-DU casks to several hypothetical fires lasting longer than the hypothetical fire described in 10 CFR 71.73.

The approach used to model internals of these casks is similar to that presented in respective Risk cask SARs and in the Truck-DU cask FDR. Some mathematical models and results reported in these documents and used in this study are described in this appendix. In addition, modifications made to the cask models to simplify the complexities inherent in the cask design are noted. In general, boundary conditions and material properties are slightly different from those used in SARs. For consistency, the same properties are used in these casks where the same or similar type materials are used. Since realistic boundary conditions are sometimes difficult to implement using available data and/or current analysis tools, some simplifications also had to be made.

MSC PATRAN is the front end code employed to generate the material database, the finite element discretization, and the boundary conditions for the internals of the casks. P-Thermal is the finite element heat transfer code used to solve the internal thermal response of the casks. CAFE is the computational fluid dynamics (CFD) code used to generate the fire environment for the hypothetical fires lasting longer than the hypothetical fire described in 10 CFR 71.73. For these scenarios, CAFE and P-Thermal are coupled together to obtain the thermal response of the casks. P-Thermal is also used to generate the regulatory fire environments used for model verification. Results from these P-Thermal regulatory fires were compared against results presented in the SARs for the same regulatory environments. This served as a check to the current models.

Four hypothetical fire accident scenarios are analyzed for the rail casks and one hypothetical fire accident scenarios, the worst case in the rail cask analysis, is analyzed for the truck cask. These are the regulatory fire described in 10 CFR 71.73, a cask on the ground concentric with a fuel pool sufficiently large to engulf the cask, a cask on the ground with a pool fire offset by the width of a rail car (3 meters), and a cask on the ground with a pool fire offset by the length of a rail car (18 meters). These non-regulatory scenarios represent the hypothetical case in which the fuel pool and the cask are separated by one rail car width or one rail car length. Results of these analyses are shown in this section. These results show that the Rail-Steel, Rail-Lead, and Truck-DU casks maintain containment for the cases analyzed in this study.

APPENDIX V
DETAILS OF TRANSPORTATION ACCIDENTS

TABLE OF CONTENTS

V.1 Types of Accidents and Incidents.....	443
V.2 Accident probabilities.....	444
V.2.1 Historic accident frequencies	444
V.2.2 Development of Conditional Accident Probabilities.....	444
V.3. Accident Risks and Consequences	448
V.3.1 Loss of lead gamma shielding	448
V.3.1.2 Loss of lead shielding with fire	458
V.4 Release of Radioactive Materials in Accidents	462
V.4.1 Spent Fuel Inventory	462

List of Figures

Figure V-1 Event tree for highway accidents (from Mills, et al, 2006)445
Figure V-2 . Rail accident event tree (after Volpe, 2006) 447
Figure V-3. The RADTRAN Loss-of Shielding 2-D Model (O'Donnell, et al, 2005) 448
Figure V-6. Event tree branch for a rail fire accident (from Volpe, 2006, Figure 16) 459

List of Tables

Table V-1. Truck and railcar accidents per km, 1991 through 2007.....	444
Table V-2 Parameters of lead shield slumping from impact. Opposite sides of the cask are labeled "side 1" and "side 2" only to distinguish one side from the other.....	449
Table V-3 Radiation dose (Sv) to the MEI at various distances for the cask for 10 hours. The numbers in bold italics exceed the external dose rate of 10 CFR 71.51.	452
Table V-4. The "conditional dose risk," the product of dose and conditional probability, in Sv to the maximally exposed individual at distances from the cask from one to five meters for 10 hours.	453
Table V-5. The "conditional dose risk," the product of dose and conditional probability, in Sv to the maximally exposed individual at distances 10 to 100 meters from the cask for 10 hours.	454
Table V-6. Collective conditional dose risks due to loss of lead shielding in person-Sv in a semicircular area of radius 800 meters around the cask.	455
Table V-7. Average railcar accident frequencies on the routes studied.	456
Table V-8. Conditional collective dose risks per shipment (person-Sv) from loss of lead shielding, including conditional probabilities	457
Table V-9. Radiation dose (Sv) to the maximally exposed individual at various distances from a cask that has been in a fire.	458
Table V-10. Events leading to a train fire that could involve a spent fuel cask.....	460
Table V-11. Some parameters used in calculating loss of neutron shielding.....	461
Table V-12. Doses to an emergency responder five meters from the cask.	461
Table V-13. Collective doses (consequences) to an emergency responder in person-Sv from loss of neutron shielding.....	461
Table V-15. TBq inventory for the Rail-Lead cask.....	463
Table V-16. Unit conditional inhalation and external dose risks (Sv) for a hypothetical CRUD-only release.....	467
Table V-17. Average collective dose risks (person-Sv) for each route for a hypothetical CRUD-only release	467
Table V-18. Parameters for determining release functions for the accidents that would result in release of radioactive material.....	469
Table V-19. Sources of the parameter values in Table V-18.	470
Table V-20. Maximally exposed individual doses (consequences) in Sv from accidents that involve a release.	471
Table V-21 Maximally exposed individual conditional dose risks in Sv from accidents that involve a release.	471
Table V-22. Collective conditional inhalation and external dose risks for the end impact, 193 kph impact speed accident, for the 16 routes analyzed.	472
Table V-23. Total collective dose risks (person-Sv) for each route.....	472

APPENDIX V

DETAILS OF TRANSPORTATION ACCIDENTS

V.1 Types of Accidents and Incidents

The different types of accidents can interfere with routine transportation of spent nuclear fuel are:

- Accidents in which the spent fuel cask is not damaged or affected.
 - Minor traffic accidents (“fender-benders,” flat tires), resulting in minor damage to the vehicle. These are usually called “incidents.”¹
 - Accidents which damage the vehicle and or trailer enough that the vehicle cannot move from the scene of the accident under its own power, but do not result in damage to the spent fuel cask.
 - Accidents involving a death or injury, but no damage to the spent fuel cask.
- Accidents in which the spent fuel cask is affected.
 - Accidents resulting in loss of lead gamma shielding but no release of radioactive material.
 - Accidents in which there is a release of radioactive material.

In this analysis the first three types of accidents are considered together. Chapter 5, Section 5.3, discusses the radiation doses and risks from these types of accidents.

The Rail-Lead cask is the only cask studied that uses a lead gamma shield, and is therefore the only cask that could be involved in an accident causing a loss of lead gamma shielding. The shielding could thin or develop a gap in an accident. The Rail-All Steel rail cask is a monolithic steel cask and is loaded with canistered fuel, so that even in an accident there would be no release of radioactive material. Chapter 3 and Appendix III discuss the accident behavior of the Truck-DU cask, which uses a depleted uranium (DU) gamma shield, and conclude that the Truck-DU cask will not release radioactive material in any achievable accident. Accidents that involve the RAIL-All Steel and the Truck-DU are limited to the first two types described above, as discussed in Chapter 5. The NAC-STC could either lose lead shielding or release radioactive material in an accident, and is the only cask of the three whose behavior is discussed in this appendix.

¹ In Department of Transportation parlance, an “accident” is an event that results in a death, an injury, or enough damage to the vehicle that it cannot move under its own power. All other events that result in non-routine transportation are “incidents.” This document uses the term “accident” for both accidents and incidents.

V.2 Accident probabilities

V.2.1 Historic accident frequencies

The probability that a traffic accident happens is based on historic accident frequencies. These have been developed and the statistics validated by the Department of Transportation (DOT). Table V-1 shows truck and railcar accidents from 1991 through 1997 (DOT, 2008). Average accident frequencies for this period are:

- 1.87×10^{-6} /km for large trucks on interstates and primary highways.
- 1.08×10^{-7} /railcar km for freight rail

Accident frequencies decreased 33.5 percent for trucks and 53.8 percent for railcars between 1991 and 2007. The average is used in this document because there are annual fluctuations. The accident frequency trends are shown in Figure 5.2 in Chapter 5.

Table V-1. Truck and railcar accidents per km, 1991 through 2007.

YEAR	Truck ACCIDENTS/KM	RAILCAR ACCIDENTS PER RAILCAR KM
1991	2.39×10^{-6}	2.08×10^{-7}
1992	1.99×10^{-6}	1.91×10^{-7}
1993	2.19×10^{-6}	1.68×10^{-7}
1994	2.19×10^{-6}	1.64×10^{-7}
1995	2.39×10^{-6}	1.53×10^{-7}
1996	1.90×10^{-6}	1.39×10^{-7}
1997	1.89×10^{-6}	1.32×10^{-7}
1998	2.04×10^{-6}	1.19×10^{-7}
1999	1.84×10^{-6}	1.12×10^{-7}
2000	2.08×10^{-6}	1.12×10^{-7}
2001	1.99×10^{-6}	1.18×10^{-7}
2002	1.83×10^{-6}	1.12×10^{-7}
2003	1.85×10^{-6}	1.02×10^{-7}
2004	1.90×10^{-6}	1.00×10^{-7}
2005	1.73×10^{-6}	1.06×10^{-7}
2006	1.83×10^{-6}	1.04×10^{-7}
2007	1.59×10^{-6}	9.60×10^{-8}

V.2.2 Development of Conditional Accident Probabilities

Each specific accident scenario is described by a conditional probability (“conditional” on an accident happening). Conditional probabilities are derived from event trees, as described below.

V.2.2.1 Conditional probabilities of truck accidents

A transportation accident scenario can be disaggregated into a series of events. The conditional probability of a particular event in the scenario is best illustrated with an event tree: a diagram that includes all possible accident scenarios. Each branch of the tree is the series of events that comprise a particular accident scenario. The conditional probability is the product of the probabilities along a particular branch.

Figure V-1 is an event tree for truck accidents (Mills, et al, 2006). Calculation of the conditional probability of a truck in a collision with another vehicle on a bridge, then falling from the bridge onto a rocky embankment, is illustrative.

$$P_{\text{conditional}} = P_{\text{collision}} * P_{\text{bridge accident}} * P_{\text{fall off bridge}} * P_{\text{rocky soil}}$$

$$P_{\text{conditional}} = (0.054) * (0.064) * (0.02) * (0.046) = 3.18 \times 10^{-6}$$

The conditional probabilities are listed in the right-hand column of Figure V-1.

Truck Event Tree

ACCIDENT	TYPE	OBJECT STRUCK	SPEED DISTRIBUTION	SURFACE STRUCK	PROBABILITY		
Large truck accident on interstate highway	Collision with non-fixed object	Train	Train grade crossing		0.00082		
		0.001	Gasoline tanker truck	accident speeds	0.00246		
		0.003	Other vehicles (motorcycles, cars, other Trucks)		0.76916		
		0.938	Other smaller non-fixed objects (cones, animals, pedestrians)		0.04756		
		0.058					
		Bridge accident	Fall off bridge			Hard rock	3.45E-06
				0.02		Soft rock, rocky soil	3.18E-06
						Other soils, clay, silt	5.65E-05
						Railbed, roadbed	5.39E-06
						Water	6.22E-07
	Strike bridge structure		Large column	Initial accident speeds	0.00010		
			0.03	Small columns, abutments, other	Initial accident speeds	0.00329	
			0.97				
	Collision with fixed object	Building, wall	Initial accident speeds	0.00054			
		0.010	Other fixed objects (trees, signs, barriers, posts, guard rails)	0.03434			
		0.636	Slide on / into ground, culvert, ditch	0.01318			
		0.244					
		Into slope, embankment		Initial accident speeds	Hard rock	0.00014	
					Soft rock, rocky soil	0.00012	
					Other soils, clay, silt	0.00222	
		Non-collision	Fire / explosion		0.00630		
0.050	Other non-collision (jack-knife, rollover, mechanical problems)		0.11970				
0.950							

Figure V-1 Event tree for highway accidents (from Mills, et al, 2006)

The construction of the event tree of Figure V-1 is described in detail in Mills, et al. (2006). Details of collision accidents are discussed in Appendix III and of fire accidents, in Appendix IV.

V.2.2.2 Conditional probabilities of rail accidents

Figure V-2 is an event tree for rail.

Rail Event Tree



Figure V-2 . Rail accident event tree (after Volpe, 2006)

V.3. Accident Risks and Consequences

V.3.1 Loss of lead gamma shielding

The cask studied that uses lead as gamma shield is the Rail-Lead cask, so loss would occur only in rail accidents. The Rail-Lead gamma shield is a lead cylinder about 0.127 m. thick. The lead shell can slump in a sufficiently severe impact, leaving a gap in the lead shield which results in increased external gamma radiation. RADTRAN models a gap in the shield from an impact and translates this to an increase in the dose from the virtual radiation source (O'Donnell, et al., 2005; Dennis, et al., 2009) that is the basis for the incident-free transportation model (Figure II-1, Appendix II). Figure V-3 is a diagram of the loss-of-shielding model, which recognizes the two-dimensional symmetry of the lead-shielded cask. Only one side of the model is shown in the figure because the model is symmetric, with the axis of symmetry along the center of the cask. The structural analysis identified different gaps on opposite sides of the cask, and identified "side 1" and "side 2" only to distinguish the two sides from each other. The model of Figure V-3 is generic and applies equally to either side of the cask.

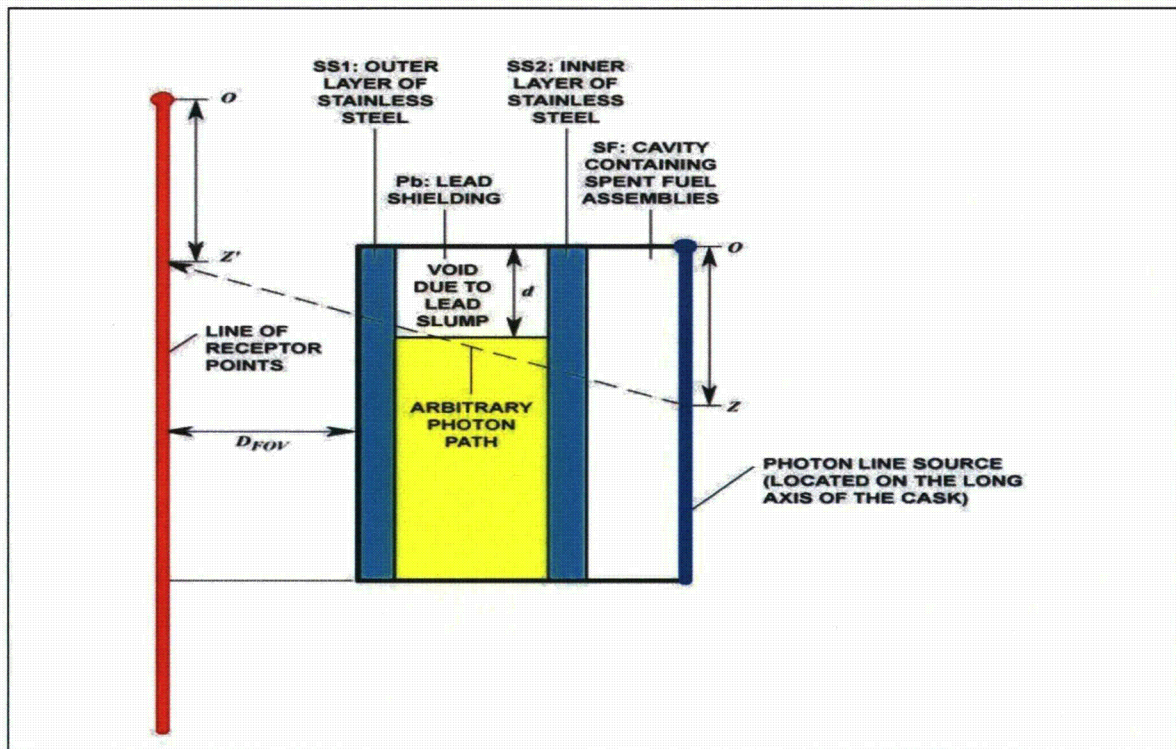


Figure V-3. The RADTRAN Loss-of Shielding 2-D Model (O'Donnell, et al, 2005)

V.3.1.1 Loss of lead shielding from impact

Appendix III (Section 3.2.2) described the various amounts of lead slump resulting from impact speed and aspect. Table V-2 shows the conditional probabilities of each combination of impact speed and orientation. The conditional probabilities shown in Table V-2 are those of a

fall from the bridge into a tunnel, a collision on the bridge, and a fall from a bridge onto hard rock (Mills et al, 2006, Table 9), the accident scenarios in which an impact could result in a lead slump. Table V-3 shows the slump as fractions of the longest dimension of the lead shield and combines the conditional probabilities in Table V-2 for each applicable accident scenario in the rail event tree (Figure V-2). Of the two rail casks studied, only the lead-shielded Rail-Lead cask might lose shielding in an accident.

As Table V-2 shows, the lead slump on one side of the cask may be different from the lead slump on the opposite side following an impact. This is particularly noticeable with the side impact. A radiation dose to any exposed person or population would therefore differ depending on the side of the cask to which the receptor was exposed. Table V-3 shows doses to the maximally exposed individual (MEI) at various distances from the cask. Table V-6 shows the population that could be exposed for each of the sixteen routes modeled.

Table V-2 Parameters of lead shield slumping from impact. Opposite sides of the cask are labeled “side 1” and “side 2” only to distinguish one side from the other.

Orientation	Impact Speed kph	Event Tree Impact Speed	Location (Side 1 or Side 2)	Maximum Slump (mm)	Slumped fraction	Conditional Probability from Rail Event Tree	Conditional Probability including Orientation	
End (Probability = 0.1)	193	>113	1	355.40	7.25E-02	1.34E-07	1.34E-08	
			2	355.48	7.25E-02			
	145	>113	1	83.20	1.70E-02	2.54E-06	2.54E-07	
			2	82.68	1.69E-03			
	97	80 to 113	1	18.28	3.73E-03	8.27E-04	8.27E-05	
			2	18.21	3.72E-03			
	48	48 to 80	1	6.43	1.31E-03	2.35E-03	2.35E-04	
			2	6.42	1.31E-03			
	Corner (Probability= 0.6)	193	>113	1	310.48	6.34E-02	1.34E-07	8.03E-08
				2	254.56	5.20E-02		
145		>113	1	114.52	2.34E-02	2.54E-06	1.53E-06	
			2	80.35	1.64E-02			
97		80 to 113	1	25.11	5.12E-03	8.27E-04	4.96E-04	
			2	20.55	4.26E-03			
48		48 to 80	1	1.28	2.61E-04	2.35E-03	1.41E-03	
			2	1.65	3.37E-04			
Side (Probability= 0.3)		193	>113	1	0.53	1.05E-04	1.34E-07	4.01E-08
				2	15.47	3.16E-03		
	145	>113	1	0.43	8.73E-05	2.54E-06	7.63E-07	
			2	20.88	4.26E-03			
	97	80 to 113	1			8.27E-04	2.48E-04	
			2	1.37	2.79E-04			
	48	48 to 80	1	0.06	1.31E-05	2.35E-03	7.05E-04	
			2	0.09	1.94E-05			

Figures V-4 and V-5 show doses to the MEI as a function of the fraction of shielding lost and as a function of distance from the cask.

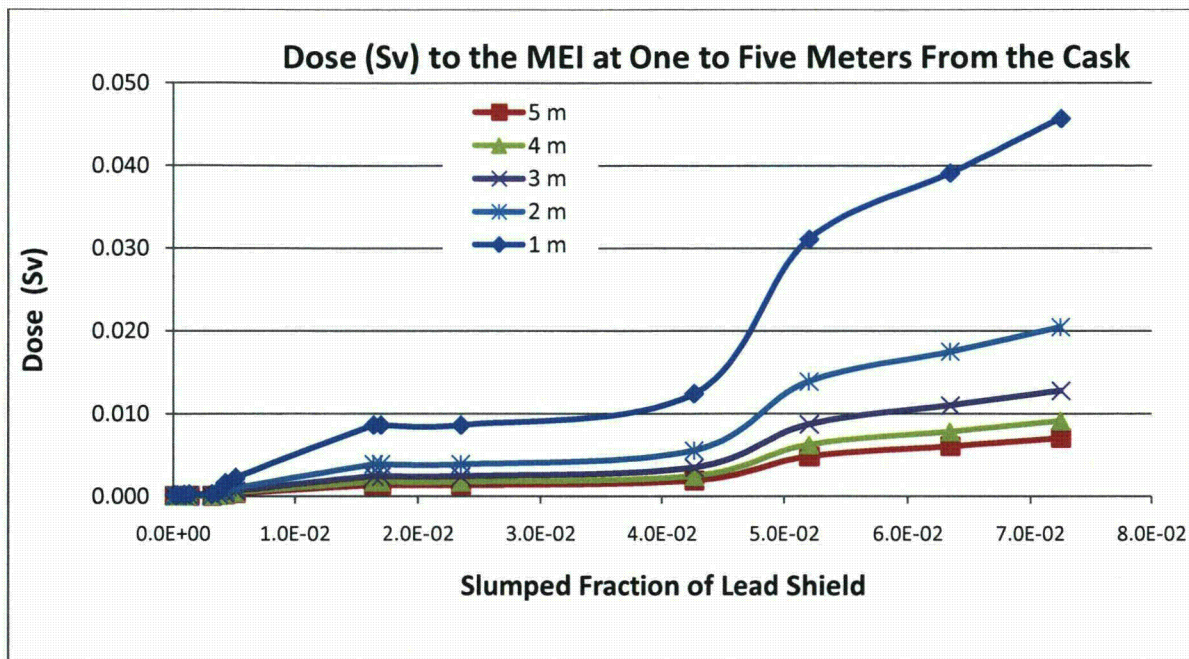


Figure V-4. Radiation dose for one hour to the maximally exposed individual (MEI) from loss of lead gamma shielding at distances from one to five meters from the cask carrying spent fuel.

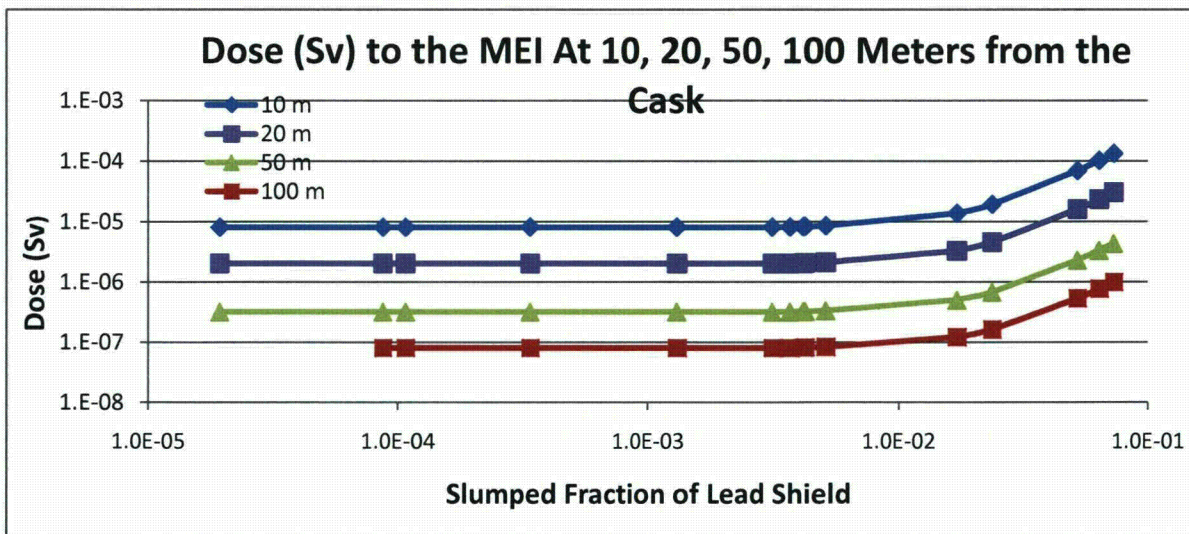


Figure V-5. Radiation dose to the maximally exposed individual from loss of lead gamma shielding at distances from 20 to 100 meters from the cask carrying spent fuel. The vertical axis is logarithmic, so that all of the doses can be shown on the same graph.

Table V-3 shows how the dose to the maximally exposed individual (MEI) depends on the fraction of the lead shield lost and distance from the cask, for a ten-hour exposure. The left-hand column of Table V-3 shows lead slump on "side 1" and "side 2" of the cask separately and does not identify the side, since there is an equal probability of exposure to each side. The doses shown in the table are computed by RADTRAN using the model discussed in V.3.1.

The large doses that occur at near the cask (one to five meters from the cask) would be sustained by emergency responders, none of whom would spend all ten hours that close to the cask. The one- to five-meter doses can be considered occupational rather than public doses. If a loss-of-shielding accident occurred on a public right of way – a railroad track in this case – no member of the public would be closer than ten meters. The public MEI dose (from the largest gap in the lead shield) would be 1.33 mSv.

The "dose risk" combines the probability of a particular accident with the consequence (the dose). It is a risk, not a dose, and is much smaller than the dose. Tables V-5 a and b show the conditional dose risk, the combination of the conditional probability with the consequence, for each fractional loss of lead shielding. This is the risk of a particular accident scenario if there is an accident, and does not include the probability of an accident. The columns in Tables V-6 are in order of descending risk.

Table V-3 Radiation dose (Sv) to the MEI at various distances for the cask for 10 hours. The numbers in bold italics exceed the external dose rate of 10 CFR 71.51.

Fraction of slumped lead	1 m	2 m	3 m	4 m	5 m	10 m	20 m	50 m
7.25E-02	4.6E-02	2.1E-02	1.3E-02	9.2E-03	7.1E-03	1.3E-04	3.1E-05	4.4E-06
6.34E-02	3.9E-02	1.8E-02	1.1E-02	7.9E-03	6.1E-03	1.0E-04	2.3E-05	3.4E-06
5.20E-02	3.1E-02	1.4E-02	8.7E-03	6.2E-03	4.8E-03	7.0E-05	1.6E-05	2.3E-06
2.34E-02	1.2E-02	5.6E-03	3.5E-03	2.5E-03	1.9E-03	1.9E-05	4.6E-06	6.9E-07
1.70E-02	8.6E-03	3.9E-03	2.4E-03	1.7E-03	1.3E-03	1.4E-05	3.3E-06	5.1E-07
5.12E-03	2.3E-03	1.0E-03	6.4E-04	4.6E-04	3.5E-04	8.5E-06	2.1E-06	3.4E-07
3.73E-03	1.6E-03	7.2E-04	4.5E-04	3.3E-04	2.5E-04	8.3E-06	2.1E-06	3.3E-07
3.16E-03	1.3E-03	6.1E-04	3.8E-04	2.8E-04	2.1E-04	8.2E-06	2.1E-06	3.3E-07
1.31E-03	5.7E-04	2.6E-04	1.7E-04	1.2E-04	9.5E-05	8.1E-06	2.0E-06	3.2E-07
4.26E-04	2.6E-04	1.2E-04	8.0E-05	5.9E-05	4.6E-05	8.1E-06	2.0E-06	3.2E-07
4.19E-04	2.6E-04	1.2E-04	7.9E-05	5.8E-05	4.6E-05	8.1E-06	2.0E-06	3.2E-07
3.34E-04	2.3E-04	1.1E-04	7.2E-05	5.3E-05	4.2E-05	8.1E-06	2.0E-06	3.2E-07
1.08E-04	1.6E-04	8.1E-05	5.3E-05	4.0E-05	3.2E-05	8.1E-06	2.0E-06	3.2E-07
8.73E-05	1.6E-04	7.8E-05	5.2E-05	3.9E-05	3.1E-05	8.1E-06	2.0E-06	3.2E-07
1.94E-05	1.4E-04	7.2E-05	4.8E-05	3.6E-05	2.9E-05	8.1E-06	2.0E-06	3.2E-07

Table V-4. The “conditional dose risk,” the product of dose and conditional probability, in Sv to the maximally exposed individual at distances from the cask from one to five meters for 10 hours.

Conditional Probability	Distance from the cask (m)				
	1	2	3	4	5
8.03E-08	3.7E-09	1.6E-09	1.0E-09	7.4E-10	5.7E-10
2.41E-07	9.4E-09	4.2E-09	2.6E-09	1.9E-09	1.5E-09
2.41E-07	7.5E-09	3.3E-09	2.1E-09	1.5E-09	1.2E-09
7.63E-07	9.5E-09	4.2E-09	2.7E-09	1.9E-09	1.5E-09
1.49E-03	1.3E-05	5.7E-06	3.6E-06	2.6E-06	2.0E-06
4.58E-06	3.9E-08	1.8E-08	1.1E-08	7.9E-09	6.1E-09
2.29E-06	5.1E-09	2.3E-09	1.5E-09	1.0E-09	8.1E-10
1.94E-05	3.1E-08	1.4E-08	8.8E-09	6.3E-09	4.9E-09
8.73E-05	1.2E-07	5.3E-08	3.3E-08	2.4E-08	1.9E-08
1.08E-04	6.2E-08	2.8E-08	1.8E-08	1.3E-08	1.0E-08
1.49E-03	3.8E-07	1.8E-07	1.2E-07	8.7E-08	6.9E-08
4.96E-04	1.3E-07	6.1E-08	3.9E-08	2.9E-08	2.3E-08
3.37E-04	7.7E-08	3.7E-08	2.4E-08	1.8E-08	1.4E-08
1.31E-03	2.2E-07	1.1E-07	7.0E-08	5.2E-08	4.2E-08

Table V-5. The “conditional dose risk,” the product of dose and conditional probability, in Sv to the maximally exposed individual at distances 10 to 100 meters from the cask for 10 hours.

Conditional Probability	Distance from the cask (m)			
	10	20	50	100
8.03E-08	1.1E-11	2.4E-12	3.5E-13	8.0E-14
2.41E-07	2.5E-11	5.6E-12	8.1E-13	1.9E-13
2.41E-07	1.7E-11	3.9E-12	5.6E-13	1.3E-13
7.63E-07	1.5E-11	3.5E-12	5.2E-13	1.3E-13
1.49E-03	2.0E-08	4.9E-09	7.5E-10	1.8E-10
4.58E-06	6.3E-11	1.5E-11	2.3E-12	5.6E-13
2.29E-06	1.9E-11	4.9E-12	7.7E-13	1.9E-13
1.94E-05	1.6E-10	4.0E-11	6.4E-12	1.6E-12
8.73E-05	7.2E-10	1.8E-10	2.9E-11	7.1E-12
1.08E-04	8.7E-10	2.2E-10	3.5E-11	8.7E-12
1.49E-03	1.2E-08	3.0E-09	4.8E-10	1.2E-10
4.96E-04	4.0E-09	1.0E-09	1.6E-10	4.0E-11
3.37E-04	2.7E-09	6.8E-10	1.1E-10	2.7E-11
1.31E-03	1.1E-08	2.7E-09	4.2E-10	1.1E-10
3.16E-03	2.5E-08	6.4E-09	1.0E-09	2.5E-10
3.73E-03	3.0E-08	7.5E-09	1.2E-09	3.0E-10

The collective dose risk to an exposed population within a radius r of the cask may be calculated by equation (V-1)

(V-1)

where A is the accident frequency on the route segment under consideration

r is the distance from the cask: 20, 50, 100 and 800 meters

$0.5\pi r^2$ is the area of the semicircle of people around the cask

PD is the population density per km^2 in the semicircle

D_{avi} is the average individual dose from the i^{th} fractional loss of shielding

P_{ci} is the conditional probability of the i^{th} fractional loss of shielding.

The index i indicates a particular fractional shielding loss; these are summarized above in Table V-3. The population at the shielding loss accident is exposed to only one side of the cask. Thus this analysis assumed that half of this population would be exposed to each side of the cask, so that dose risks were calculated separately for exposure to each side of the cask. The summation in equation (V-1) is the conditional dose risk of all of the accidents considered: the “universe” of accidents. Table V-6 shows collective conditional dose risks for the sixteen routes analyzed.

Table V-6. Collective conditional dose risks due to loss of lead shielding in person-Sv in a semicircular area of radius 800 meters around the cask.²

		Side 1				Side 2			
		ORNL	DEAF SMITH	HANFORD	SKULL VALLEY	ORNL	DEAF SMITH	HANFOR D	SKULL VALLEY
MAINE YANKEE	Rural	9.37E-10	6.91E-10	1.10E-09	8.57E-10	5.09E-09	3.75E-09	5.99E-09	4.66E-09
	Suburb	1.78E-08	1.91E-08	1.77E-08	1.72E-08	9.58E-08	1.03E-07	9.49E-08	9.22E-08
	Urban	1.93E-09	1.99E-09	1.86E-09	1.55E-09	1.03E-08	1.07E-08	1.00E-08	8.34E-09
KEWAUNEE	Rural	9.37E-10	4.61E-10	4.62E-10	5.91E-10	5.09E-09	2.50E-09	2.51E-09	3.21E-09
	Suburb	1.92E-08	2.03E-08	1.78E-08	2.08E-08	1.03E-07	1.09E-07	9.54E-08	1.12E-07
	Urban	2.10E-09	2.10E-09	1.94E-09	1.74E-09	1.13E-08	1.13E-08	1.04E-08	9.36E-09
INDIAN POINT	Rural	7.96E-10	5.72E-10	5.66E-10	6.63E-10	4.32E-09	3.11E-09	3.07E-09	3.60E-09
	Suburb	2.40E-08	1.98E-08	1.89E-08	2.02E-08	1.29E-07	1.06E-07	1.01E-07	1.08E-07
	Urban	2.56E-09	2.19E-09	2.12E-09	1.94E-09	1.37E-08	1.18E-08	1.14E-08	1.04E-08
IDAHO NATIONAL LAB	Rural	5.80E-10	2.40E-10	3.01E-10	5.99E-10	3.15E-09	1.30E-09	1.63E-09	3.26E-09
	Suburb	2.02E-08	2.01E-08	2.02E-08	1.97E-08	1.09E-07	1.08E-07	1.08E-07	1.06E-07
	Urban	1.70E-09	1.56E-09	1.97E-09	2.08E-09	9.13E-09	8.37E-09	1.06E-08	1.11E-08

Population dose risk ultimately depends on the accident frequency as well as on the population along the route where the accident happens. The accident frequency, accidents per km, is equated to the accident probability. The rail accident frequencies used in this analysis are from DOT, 2008. Average railcar accident frequencies for each of the 16 routes are shown in Table V-7. These accident frequencies are combined with the average dose risk integrated over the potentially exposed population.

Table V-8 shows the collective dose risks to populations on each side of the rail cask that has lost lead shielding on impact. These estimates include both the conditional probabilities and the accident frequencies on each route, as in Equation (V-1). Thus the differences in Table V-9 are due to differences in traffic accident frequencies.

² For a particular population density, the collective dose is the same for a semicircle (or any segment of a circle) of 20 m radius, 100 m. radius, or 800 m. radius, because the population in a semicircle is proportional to r^2 and the average dose is proportional to $1/r^2$. The average dose decreases as the total population increases.

Table V-7. Average railcar accident frequencies on the routes studied.

ORIGIN	DESTINATION	AVERAGE ACCIDENTS PER KM
MAINE YANKEE	ORNL	6.5×10^{-7}
	DEAF SMITH	5.8×10^{-7}
	HANFORD	4.2×10^{-7}
	SKULL VALLEY	5.1×10^{-7}
KEWAUNEE	ORNL	4.3×10^{-7}
	DEAF SMITH	3.3×10^{-7}
	HANFORD	2.4×10^{-7}
	DEAF SMITH	6.2×10^{-7}
	HANFORD	5.1×10^{-7}
	SKULL VALLEY	5.5×10^{-7}
INL	ORNL	3.6×10^{-7}
	DEAF SMITH	3.5×10^{-7}
	HANFORD	3.2×10^{-7}
	SKULL VALLEY	2.8×10^{-7}

Table V-8. Conditional collective dose risks per shipment (person-Sv) from loss of lead shielding, including conditional probabilities

ORIGIN	TYPE	Side 1				Side 2			
		ORNL	DEAF SMITH	HANFORD	SKULL VALLEY	ORNL	DEAF SMITH	HANFORD	SKULL VALLEY
MAINE YANKEE	Rural	3.09E-12	1.35E-12	1.97E-12	9.31E-13	1.70E-11	7.44E-12	1.09E-11	5.13E-12
	Suburban	5.87E-11	3.74E-11	3.16E-11	1.87E-11	3.19E-10	2.03E-10	1.72E-10	1.02E-10
	Urban	6.34E-12	3.89E-12	3.33E-12	1.69E-12	3.45E-11	2.12E-11	1.81E-11	9.18E-12
KEWAUNEE	Rural	1.22E-12	2.87E-13	3.06E-13	3.06E-13	6.74E-12	1.58E-12	1.69E-12	1.69E-12
	Suburban	2.51E-11	1.26E-11	1.18E-11	1.07E-11	1.36E-10	6.86E-11	6.40E-11	5.85E-11
	Urban	2.74E-12	1.31E-12	1.28E-12	9.01E-13	1.49E-11	7.11E-12	6.98E-12	4.90E-12
INDIAN POINT	Rural	3.36E-11	1.09E-12	1.15E-12	4.62E-13	1.85E-10	6.02E-12	6.34E-12	2.55E-12
	Suburban	1.01E-09	3.78E-11	3.83E-11	1.40E-11	5.49E-09	2.06E-10	2.08E-10	7.64E-11
	Urban	1.08E-10	4.18E-12	4.30E-12	1.35E-12	5.86E-10	2.27E-11	2.34E-11	7.36E-12
IDAHO NATIONAL LAB	Rural	2.22E-13	1.61E-13	4.38E-14	5.56E-13	1.23E-12	8.87E-13	2.41E-13	3.07E-12
	Suburban	7.75E-12	1.35E-11	2.94E-12	1.82E-11	4.22E-11	7.35E-11	1.60E-11	9.93E-11
	Urban	6.52E-13	1.05E-12	2.87E-13	1.92E-12	3.55E-12	5.69E-12	1.56E-12	1.05E-11

V.3.1.2 Loss of lead shielding with fire

Lead melts at 330 °C, so that a prolonged high-temperature fire could result in lead slump, leaving a gap in the gamma shield which results in increased external radiation emission. In calculating doses from a loss of lead shielding, RADTRAN models a gap in the shield as an increase in the dose from a virtual radiation source (O'Donnell et al., 2005; Dennis, et al., 2009). This virtual source is the same as the basis for the incident-free transportation model (Figure II.1, Appendix II).

The loss of lead shielding does not occur during a fire. Lead expands as it melts and can buckle the innermost cask shell. When the melted lead cools and solidifies, it occupies the same volume as before expansion but the volume available between the steel cask shells is larger because of the buckling of the inner shell, leaving a gap. Melting of lead and the formation of a gap in the lead are described fully in Appendix IV. Briefly, if the cask is offset from the fire, the gap would be in the section of lead shield facing the fire. In an engulfing fire, the gap would be at the upper surface of the cask. However, if the cask is turned after the melted lead has solidified; the gap in the lead would be on the side of the cask rather than at the top. Thus, in both cases, anyone facing the side of the cask with the shielding gap could sustain an increased radiation dose.

Two accidental fire scenarios can result in a loss of lead shielding:

- Fire Scenario 1: a sufficiently hot pool fire engulfing a cask on the ground can melt enough lead in three hours to create an 8.14 percent fractional shield loss.
- Fire Scenario 2: a sufficiently hot pool fire offset from the cask, burning for more than three hours, can create a 2.01 percent fractional shield loss.

These scenarios are described fully in Appendix IV. The doses sustained by the maximally exposed individual at various distances from the cask, exposed for an hour, are shown in Table V-9.

Table V-9. Radiation dose (Sv) to the maximally exposed individual at various distances from a cask that has been in a fire.

Fraction of lead lost	1 m	2 m	5 m	10 m	20 m	50 m	100 m
0.0201	7.0E-03	3.1E-03	1.1E-03	1.1E-05	2.6E-06	3.9E-07	9.4E-08
0.0814	3.5E-02	1.6E-02	5.4E-03	1.1E-04	2.6E-05	3.7E-06	8.5E-07

No lead shielding would be lost until after the fire was out and the cask had cooled enough for the lead to solidify, since only then would there be a gap in the lead shield. Thus no one would be exposed for many hours after the accident, and with a fire this severe, nearby residents and the public would probably have been evacuated. The maximally exposed individual in this case would be an emergency responder. Under these circumstances, measures could be taken to mitigate emergency responder exposures.

Volpe (2006, Figure 16) postulates a chain of events leading to a fire, from which the probability of these scenarios can be calculated. The relevant portion of the Volpe figure is shown in Figure V-6.

Fire Event Tree

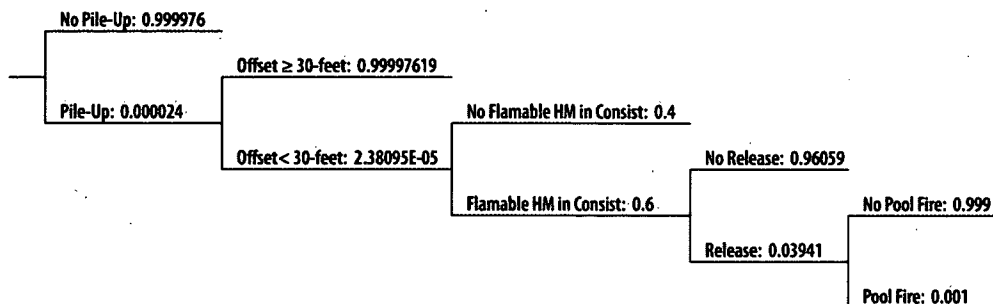


Figure V-4. Event tree branch for a rail fire accident (from Volpe, 2006, Figure 16)

The first of these events is a major derailment, as shown in Table V-11. Volpe estimates that the speed at the time of the accident for such a derailment is at least 80 km/hr. If a pileup could occur in any kind of derailment other than in a tunnel, from Figure V-2, the probability of such a major derailment is

$$(0.7355) \cdot (0.0155) \cdot (0.06614 + 0.00061) \cdot (0.0011 + 0.0004 + 0.0077 + 0.0113) = 1.56 \times 10^{-5}$$

Table V-10 lists the other events in the scenario, together with the probability of each event. These events are a pileup, a flammable hazardous cargo within 10 meters (about half a rail-car length), leaking of that hazardous substance, and ignition of a pool fire. The net probability of the sequence of events shown in Table V-10 following a major pileup is 1.35×10^{-14} . The net probability depends on the very small pileup probability of 2.4×10^{-5} . Thus it is instructive to estimate the probability without the assumption of a pileup. Using the “no pileup” branch, the net probability for the events of Table V-10 is 5.6×10^{-10} , still an exceedingly small number.

Thus the conditional probability of Fire Scenario 1, a major derailment that does not involve a pile-up but leads to a three-hour pool fire that surrounds the cask, is

$$(1.56 \times 10^{-5}) \cdot (5.6 \times 10^{-10}) = 8.8 \times 10^{-15}$$

The conditional probability of Fire Scenario 2, a major derailment that does not involve a pile-up but leads to a three-hour fire offset from the cask by more than 10 meters, is then

$$(1.56 \times 10^{-5}) \cdot (2.36 \times 10^{-5}) = 3.7 \times 10^{-10}$$

Table V-10. Events leading to a train fire that could involve a spent fuel cask

EVENT	PROBABILITY	ALTERNATIVE EVENT	PROBABILITY
		No major derailment	0.99999
Pileup	2.4×10^{-5}	No pileup	0.99998
Offset < 10 m	2.38×10^{-5}	Offset > 10 m	0.99998
Flammable hazardous material in another railcar	0.6	No flammable material available	0.4
Release of flammable material	0.0394	No release of flammable material	0.9606
Pool fire	0.001	No pool fire	0.999

The average accident frequency for the 16 rail routes studied is 3.9×10^{-3} (the range is from 1.5×10^{-4} to 4.2×10^{-2}). Thus, the average probability of an accidental fire that could cause loss of lead shielding in a rail cask is 3.4×10^{-19} if the cask is concentric with the fire and 1.4×10^{-14} if the cask and fire are offset by 10 meters or more. The largest dose risk would be 4.9×10^{-17} Sv.

V.3.2 Loss of Neutron Shielding

The neutron shield is usually a hydrocarbon or carbohydrate polymer, sometimes borated, since boron and organic polymers are good neutron absorbers. Neutron shielding burns, and could be destroyed in a fire. The neutron dose from loss of shielding in a fire is estimated using the parameters listed in Table V-11. The conditional probability of a truck fire is from Figure V-1. The conditional probability of a rail fire is a combination of the fire probability in Figure V-2 and the following steps from Figure V-5.

- A pileup
- Flammable cargo on the train
- Release of the flammable cargo

The neutron TI for the Truck-DU cask is from General Atomics, 1998; the TI for the Rail-Lead cask, from NAC International, 2002; and the TI for the Rail-All Steel cask, from Holtec International, 2004. The RADTRAN external dose rate is modeled as entirely neutron emission. The other parameters are the same as those used in calculating doses from an accident in which there is no release of radioactive material and no loss of lead shielding (Chapter 5, Section 5.4).

Table V-11. Some parameters used in calculating loss of neutron shielding.

Parameter	Truck-DU	Rail-Lead	Rail-All Steel
Conditional probability of a fire	0.0063	8.9×10^{-8}	8.9×10^{-8}
Dose rate at one meter from the cask in mSv/hour (mrem/hour)	1.78 (178)	1.81 (181)	1.82 (182)
Shielding of residents.	none	none	none
Time until the cask is removed (hours)	10	10	10

The neutron doses to emergency responders (five meters from the cask) are shown in Table V-12, the collective doses on the 16 routes are shown in Table V-13, and the total collective dose risks, including accident frequency, are shown in Table V-14. For the Rail=Lead cask, the neutron doses would add to the gamma dose from the loss of lead shielding.

Table V-12. Doses to an emergency responder five meters from the cask.

Cask	Dose in Sv	Ten-hour 10 CFR 71.51 dose in Sv
Truck-DU	0.00729	0.1
Rail-Lead	0.00761	0.1
Rail-All Steel	0.00763	0.1

Table V-13. Collective doses (consequences) to an emergency responder in person-Sv from loss of neutron shielding.

FROM	TO	Truck-DU	Rail-Lead	Rail-All Steel
MAINE YANKEE	ORNL	7.49E-04	7.17E-04	7.40E-04
	DEAF SMITH	7.01E-04	6.71E-04	6.93E-04
	HANFORD	6.23E-04	5.96E-04	6.15E-04
	SKULL	6.38E-04	6.11E-04	6.31E-04
KEWAUNEE	ORNL	6.87E-04	6.57E-04	6.78E-04
	DEAF SMITH	6.41E-04	6.13E-04	6.33E-04
	HANFORD	5.98E-04	5.72E-04	5.91E-04
	SKULL	6.17E-04	5.91E-04	6.10E-04
INDIAN POINT	ORNL	7.28E-04	6.97E-04	7.20E-04
	DEAF SMITH	6.95E-04	6.65E-04	6.87E-04
	HANFORD	6.38E-04	6.11E-04	6.31E-04
	SKULL	6.63E-04	6.34E-04	6.55E-04
INL	ORNL	5.78E-04	5.53E-04	5.71E-04
	DEAF SMITH	6.16E-04	5.89E-04	6.08E-04
	HANFORD	3.78E-04	3.62E-04	3.73E-04
	SKULL VALLEY	6.41E-04	6.13E-04	6.33E-04

Table V-14. Collective dose risks in person-Sv from loss of neutron shielding.

FROM	TO	Truck-DU	Rail-Lead	Rail-AllSteel
MAINE YANKEE	ORNL	4.7E-06	6.4E-11	6.6E-11
	DEAF SMITH	4.4E-06	6.0E-11	6.2E-11
	HANFORD	3.9E-06	5.3E-11	5.5E-11
	SKULL	4.0E-06	5.4E-11	5.6E-11
KEWAUNEE	ORNL	4.3E-06	5.8E-11	6.0E-11
	DEAF SMITH	4.0E-06	5.5E-11	5.6E-11
	HANFORD	3.8E-06	5.1E-11	5.3E-11
	SKULL	3.9E-06	5.3E-11	5.4E-11
INDIAN POINT	ORNL	4.6E-06	6.2E-11	6.4E-11
	DEAF SMITH	4.4E-06	5.9E-11	6.1E-11
	HANFORD	4.0E-06	5.4E-11	5.6E-11
	SKULL	4.2E-06	5.6E-11	5.8E-11
INL	ORNL	3.6E-06	4.9E-11	5.1E-11
	DEAF SMITH	3.9E-06	5.2E-11	5.4E-11
	HANFORD	2.4E-06	3.2E-11	3.3E-11
	SKULL	4.0E-06	5.5E-11	5.6E-11

V.4 Release of Radioactive Materials in Accidents

V.4.1 Spent Fuel Inventory

A Rail Lead -cask is the only cask studied that would release any radioactive material in an accident. Since there is no traffic accident that would result in a release from the Truck-DU or Rail-All Steel cask, the inventory of those casks is not relevant to this analysis. The fuel used in this analysis is PWR fuel, 45,000 MWD/MTU burnup, the maximum burnup that a Rail-Lead cask would transport, and has cooled for nine years before transport. The radionuclide inventory of this fuel was determined using ORIGEN (Croff, 1980). The radionuclide activities in the inventory were “normalized” by dividing each activity by the A_2 value for that radionuclide. The A_2 value, the amount of the radionuclide that could be transported in a Type A container, is an indication of the radiotoxicity; the larger the A_2 value, the smaller the radiotoxicity of that nuclide. The normalized radioactivities were then sorted and added until 99.99 percent of the total normalized radioactivity was reached.³ The radionuclides selected this way are listed in Table V-15, together with their actual radioactivities (not the normalized radioactivities). Normalized radioactivities are used only to identify 99.9 percent of the radiotoxicity. The actual activity is the basis for the release fraction of each radionuclide.

³ The “total normalized activity” referred to here is not the total A_2 value as calculated by the formula in 10 CFR Part 71 Appendix A.

Table V-15. TBq inventory for the Rail-Lead cask.

Radionuclide	TBq
	26 Assemblies
²⁴⁰ Pu	7.82E+03
²³⁹ Pu	1.84E+02
¹³⁷ Cs	4.38E+04
²³⁸ Pu	7.18E+01
²⁴³ Cm	2.50E+01
¹⁵⁴ Eu	9.01E+02
¹³⁴ Cs	4.03E+02
⁸⁵ Kr	2.26E+03
²⁴¹ Am	1.58E-01
²⁴² Cm	1.00E+00
¹⁵⁵ Eu	2.63E+02
²³¹ Pa	3.12E-02
¹⁰⁶ Ru	7.50E+00
²³⁶ U	1.92E-01
⁶³ Ni	8.99E+02
²³³ U	5.75E-01
²⁴¹ Pu	6.13E-01
^{113m} Cd	5.24E+00

V.5.3 Dispersion of Released Radionuclides

If a spent fuel cask transportation accident did result in the release of radioactive material, the public could be exposed if the material was dispersed through the air. Experimental work reviewed by Sprung et al (2000, pp.7-30 et seq) indicates that only very small particles with analytic mean aerodynamic diameter (AMAD)⁴ ten microns or less would be released from a cask in an accident, because the only release path is through the seals at the ends of the cask. In addition, particles larger than this are filtered by larger particles inside the cask. Ten microns is generally considered the upper limit of respirability. Thus particles accidentally released from a cask will be released as a respirable aerosol.

The discussion below is an abbreviated discussion of air dispersion, a subject that is treated extensively and in detail in textbooks like Wark and Warner (1981).

The basic equation for atmospheric dispersion of an aerosol is the Gaussian dispersion equation: Equation (V-2) (Turner, 1994, Chapter 2).

$$(V-2) \quad \frac{CHI}{Q} = \frac{1}{2\pi u \sigma_y \sigma_z} \exp\left[\frac{-y^2}{2\sigma_y^2}\right] \exp\left[\frac{-z^2}{2\sigma_z^2}\right]$$

⁴ The AMAD is the diameter of a sphere of density 1 gm/cm³ that has the same inertial properties as the actual particle.

where CHI^5 = the concentration of particles in the air
 Q = the radioactivity or mass of airborne particles
 u = the wind speed
 σ_y, σ_z are meteorological constants and are functions of the downwind distance x .

The wind direction is traditionally along the x axis of a Cartesian coordinate system, the crosswind direction is y , and z represents the altitude above ground. When the plume of released material rises buoyantly to a height H , the Gaussian equation becomes

$$(V-3) \quad \frac{CHI}{Q} = \frac{1}{2\pi u \sigma_y \sigma_z}$$

where H is the height to which the plume rises before being blown downwind. For a ground-level release along the plume centerline, Equations (V-2) and (V-3) reduce to

$$(V-4) \quad \frac{CHI}{Q} = \frac{1}{2\pi u \sigma_y \sigma_z} \exp\left[\frac{-y^2}{2\sigma_y^2}\right] \exp\left[\frac{-H^2}{2\sigma_z^2}\right]$$

Radioactive gases released in accident will disperse in the air according to Equations (V-1) and (V-3). Particles, however, have mass and will settle on the ground. The settling velocity V_t —the terminal velocity of a particle in the indicated size range—is given by Equation (V-5)

(V-5)

where g = gravitational acceleration
 d = particle aerodynamic diameter
 ρ = particle density
 μ = air viscosity at ambient temperature

Ground deposition rate is then described by Equation (V-6) (Wark and Warner, 1981, Chapter 5)⁵

$$(V-6) \quad \frac{w_p}{Q} = \frac{V_t}{2\pi u \sigma_y \sigma_z} \exp\left[\frac{-y^2}{2\sigma_y^2}\right] \exp\left[\frac{-\left(H - \frac{xV_t}{u}\right)^2}{2\sigma_z^2}\right]$$

⁵ The Greek letter χ is traditionally used to represent air concentration, but is so easily confused in typescript with the 24th letter of the alphabet that it is often written phonetically (“chi”).

where w_p is the particle deposition rate. These equations are programmed in RADTRAN.

Both wind and air temperature profiles affect the dispersion of airborne material. The predominant motion of airborne material is downwind, while crosswind motion is diffusive. Light winds, stable air, and temperature inversions result in less dispersion and higher airborne and ground concentrations of radionuclides. Strong winds and turbulent air are good conditions for dispersion and result in lower airborne and deposited radionuclides concentration and consequently result in lower radiation doses to the public, even though the plume of radioactive material may spread over a large area.

RADTRAN calculates external doses from deposited material (“groundshine”) and from material that remains suspended in the air (“cloudshine”). The code also calculates internal committed doses from airborne material that is inhaled, and from material that becomes resuspended in the air. The doses reported are the sums of the groundshine, cloudshine, inhaled, and resuspended inhaled doses, unless otherwise indicated. Adding these doses to sum to a “total effective dose equivalent” is NRC practice in determining public exposure, as discussed in 10 CFR 20.1301. RADTRAN accommodates a number of atmospheric dispersion conditions.

V.5.4 Release fractions

Release of radionuclides into the environment from a cask depends on releases from the fuel rods into the cask and from the cask to the environment. If the cask contains canistered fuel, the cask structural analysis in Chapter 4 shows that the canister does not rupture even under the most severe accidents analyzed, so no radioactive material can exit the cask. In the present study, therefore, only the Rail-Lead transporting uncanistered could release any radioactive material or CRUD as a consequence of a traffic accident. Only PWR spent fuel is considered in this section.

V.5.4.1 CRUD

Radioactive material available for release comes from both spent fuel and Chalk River Unidentified Deposits (CRUD). CRUD is a corrosion product that forms on the outside of the fuel rods; its source is not the fuel rod inventory but other metallic structures in the reactor. In a PWR reactor its radioactive constituents are ^{60}Co , ^{58}Co , ^{54}Mn , ^{51}Cr , ^{59}Fe , ^{95}Zr , ^{125}Sb , and ^{65}Zn . ^{60}Co is the only CRUD constituent sufficiently long-lived to be part of any accidental release. Although CRUD deposits on the outside of fuel rods, cask seals would have to be breached for CRUD to be released. Sprung, et al (2000, Page 7-49) and Hanson et al (2010) estimate the amount of CRUD per fuel rod for PWR and BWR spent fuel. The estimates include the following assumptions:

- CRUD forms on the outside rods of the assemblies
- Thirteen percent of the rod area is covered with a CRUD layer. The layer is between 33 and 100 microns thick. The total amount of CRUD was thus assumed to be 8.5 microns thick over the entire surface of the outside rods. The density of the CRUD layer was assumed to be one gram per cm^3 for the CRUD that could be airborne in the cask (Einziger and Beyer, 2007)
- CRUD was assumed to be entirely ^{60}Co , and the activity was calculated using Equation (V-7).

(V-7)

Einzigler and Beyer (2007) estimate that, with certain conservative assumptions, about 15 percent of the CRUD formed could remain airborne in the cask and available to be swept from the cask in the event of cask depressurization. Using these estimates, the CRUD activity in the Rail-Lead would be:

- 268 TBq (7075 Ci) in a cask carrying twenty-six 17x17 PWR assemblies

And the airborne fraction in the cask would be 40.2 TBq (1061 Ci).

The fraction of airborne particles that could be swept from the cask depends on the pressure differential between the cask and the environment:

$$F_{CE} = (1 - f_{\text{deposited}})(p_{\text{atm}}/p_{\text{inp}}) \quad (\text{V-6})$$

Where F_{CE} is the fraction released from the cask to the environment, $f_{\text{deposited}}$ is the fraction of airborne material in the cask deposited on its inner surface, p_{atm} is the atmospheric pressure and p_{inp} is the cask internal pressure. The only release path that would be available is through the seals at the end of the cask. If the accident involves a collision that fails the seals but there is no fire and no damage to the fuel rods, the cask temperature would probably be close enough to ambient that the pressure differential between the cask and the environment would be insufficient to sweep CRUD from the cask.

If there is a fire but no thermal failure of the seals, there can be no CRUD-only release. The cask seals modeled in this study would not fail thermally, as shown in Chapter 4 and Appendix IV, so these casks would not have a CRUD-only release. For the modeled casks, if the cask seals fail, the fuel rods fail as well, as happens in a severe impact accident (Section V.5.4.3). Thus, an accident in which the seals in this study are breached but the fuel remains undamaged, is a hypothetical situation. This hypothetical situation is considered in the following paragraphs of this section. Assuming that the ambient temperature is 300 K and that elastomeric seals fail at 450 K, then from the Ideal Gas Law,

$$p_{\text{atm}}/p_{\text{inp}} = T_{\text{atm}}/T_{\text{inp}} = 300/450 = 0.667^6 \quad (\text{V-7})$$

From Figure 7.5 of Sprung et al (2000), about one percent of the 15 percent of the CRUD that has spalled from the rods, or about 0.15 percent, would be respirable (10 microns or less aerodynamic diameter). From Equation (V-6) the fraction of CRUD that would be released is 0.001.

This scenario was modeled using RADTRAN, assuming release at ground level, the same dispersion formulation as described in Section V.5.3, and deposition velocity calculated using Equation (V-4). Unit conditional inhalation and external dose risks are shown in Table V-16. These conditional dose risks do not include populations along the route or accident probabilities (frequencies).

⁶ The metal seal failure temperature is 477 deg. K, so that in the case of a metal seal $p_{\text{atm}}/p_{\text{inp}} = 0.628$

Table V-16. Unit conditional inhalation and external dose risks (Sv) for a hypothetical CRUD-only release.

ROUTE SEGMENT TYPE	INHALED	RESUSPENDED	CLOUDSHINE	GROUNDSHINE	TOTAL
Rural	1.43E-10	3.85E-12	5.45E-10	1.93E-08	2.00E-08
Suburban	1.43E-10	3.85E-12	5.45E-10	1.93E-08	2.00E-08
Urban	4.15E-10	1.12E-11	1.58E-09	5.62E-08	5.82E-08

Internal doses include doses from direct inhalation and from material resuspended in air. External doses include cloudshine and groundshine. The NRC cites the total effective dose equivalent (TEDE) which includes both internal and external doses.

The average collective dose risks shown in Table V-17 are the averages of the products of the dose risks as shown in Table V-16, and the population and accident frequency along each route. Average accident frequencies for each route are in Table V-8.

Table V-17. Average collective dose risks (person-Sv) for each route for a hypothetical CRUD-only release

	ORNL	DEAF SMITH	HANFORD	SKULL VALLEY
MAINE	2.07E-04	1.57E-06	2.13E-04	2.15E-04
KEWAUNEE	8.59E-05	1.66E-06	8.56E-05	8.63E-05
INDIAN	1.05E-04	1.72E-06	8.84E-05	8.91E-05
INL	7.23E-05	1.25E-06	6.66E-05	6.71E-05

The average collective dose risks reported in Table V-17, while very small, are several orders of magnitude larger than the dose risks from an accident involving release as reported in Table V-23, below. However, the values in Table V-17 result from analyzing a purely hypothetical accident, while those in Table V-23 are from a realistic accident.

V.5.4.2 Spent Fuel Radionuclides

When fuel rods are fractured in an impact, they depressurize, and the consequent overpressure sweeps fuel particles out of the cask if there is a breach in the seal. The depressurization and release of material from the rod is described very clearly in Hanson, et al., 2008,

When commercial spent nuclear fuel (CSNF) is handled in a dry environment, whether as fuel assemblies, canned, or within a container, one possible mechanism for radionuclide release is a drop accident scenario, [in which] it is possible that the cladding could fracture, and cans or containers could breach..., (Sprung et al. 2000)⁷. Upon clad breach, it is expected that the rod would rapidly depressurize, releasing its fill gas (e.g., He) and fission gases (e.g., Kr, Xe) that have been released from the fuel matrix, depending on the size of the cladding defect and fuel burnup characteristics

⁷ This citation is made by Hanson, et al.

(Einziger and Beyer 2007⁸)..... It is also possible for fuel fines to be ejected as the high-pressure fill and fission gases rapidly escape through the defect.... (Hanson, et al, 2008, Section 1)

These authors examined the behavior of relatively high burnup fuel. The release fractions from the rods to the cask, under the described conditions, are developed from the data of Hanson, et al for 45 GWD/MTU spent fuel. Einziger (2007) describes the formation of a rim on the fuel pellet that has a higher porosity than the body of the pellet. This porosity results in reduced hardness of the pellet (Hanson et al, Figures 1.6 and 1.7)). However, the pellet rim is toughened by grain refinement, suggesting that release of fine particles from the fuel rods could be smaller than releases from lower burnup fuel. Figure V-6 shows the difference between a rim and the pellet interior.

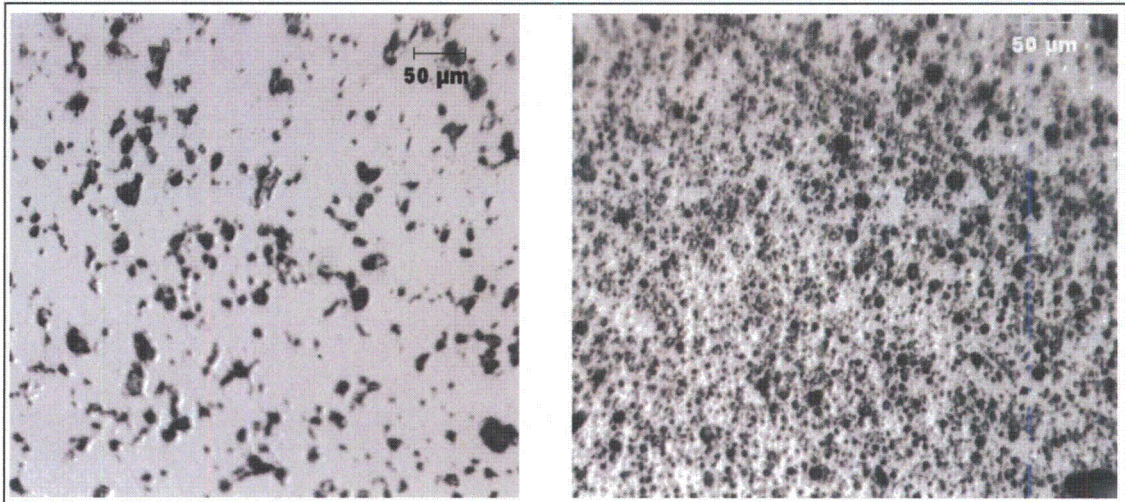


Figure V-6. Electron micrographs of the fuel pellet interior (left-hand picture) and the fuel pellet rim (right-hand picture). (Courtesy of Dr. R. E. Einziger, NRC)

Figure 1.10 of Hanson et al. suggests a release fraction for fission gases (⁸⁵Kr in the fuel in this analysis) of 0.5 percent. These authors suggest that volatile fission products like the cesium isotopes exhibit release behavior like fission gases. However, any cesium isotope would be released as the oxide or chloride, and would therefore behave more like volatile compounds than like gases. Because the volatile compounds tend to migrate to the fuel rim and Einziger (2007) recommends 3×10^{-5} as an appropriate release fraction for rim material, this release fraction is used for volatiles, including ruthenium, in the present analysis.

Hanson et al. describe a number of mechanical tests performed on unoxidized fuel of varying burnup. Page 4.12 of Hanson et al. summarizes release fractions from these tests for the fuel that appears to be the most appropriate. A release fraction of 4.8×10^{-6} , based on the information in Hansen, et al, 2008, is used in this analysis for release of fine particles from the rod to the cask.

⁸ See Footnote 7.

Figure 7.11 of Sprung et al (2000) presents release fractions of several compounds as functions of the available leak area. The compounds studied represent the physical/chemical groups present in spent nuclear fuel: gas, volatiles, and particulate matter. This figure served as the basis for estimating the cask-to-environment release fractions of the physical/chemical groups studied.

Table V-18 summarizes the parameters from which release fractions were developed.

Table V-18. Parameters for determining release functions for the accidents that would result in release of radioactive material.

	Cask Orientation	End	Corner	Side	Side	Side	Side	Corner
	Impact Speed (kph)	193	193	193	193	145	145	145
	Seal	metal	metal	elastomer	metal	elastomer	metal	metal
Cask to Environment Release Fraction	Gas	0.800	0.800	0.800	0.800	0.800	0.800	0.800
	Particles	0.70	0.70	0.70	0.70	0.70	0.70	0.64
	Volatiles	0.50	0.50	0.50	0.50	0.50	0.50	0.45
	Crud	0.001	0.001	0.001	0.001	0.001	0.001	0.001
Rod to Cask Release Fraction	Gas	0.005	0.005	0.005	0.005	0.005	0.005	0.005
	Particles	4.80E-06	4.80E-06	4.80E-06	4.80E-06	4.80E-06	4.80E-06	2.40E-06
	Volatiles	3.00E-05	3.00E-05	3.00E-05	3.00E-05	3.00E-05	3.00E-05	1.50E-05
	Crud	1.00	1.00	1.00	1.00	1.00	1.00	1.00
Conditional Probability for combined rod-cask-environment release		2.68E-08	1.61E-07	8.02E-08	8.02E-08	1.52E-06	1.52 e-06	5.81e-05

Table V-19 shows sources of the parameter values in Table V-18. The parameter values are consistent with Sanders, et al, (1992).

Table V-19. Sources of the parameter values in Table V-18.

		Release fraction	Comment
Cask to Environment Release Fraction	Gas	0.800	The basis of each release fraction is the size of the gap in the seal – the leak area --, provided for each combination of impact speed and orientation by Table III-1 of Appendix III. Release fractions were obtained from the graph of Figure 7.11 (p. 7-53) of Sprung, et al (2000).
	Particles	0.70	
	Particles – Corner Impact	0.64	
	Volatiles	0.50	
	Volatiles - Corner Impact	0.45	
	CRUD	0.001	This release fraction is based on Einziger and Beyer (2007) and discussed in Section V.5.4.1.
Rod to Cask Release Fraction	Gas	0.005	From Hanson, et al, 2008, Figure 1.10 (page 1.10) for 45 GWD/MTU burnup
	Particles	4.80E-06	From the release fraction in Hanson, et al, 2008, Table 4.10.
	Particles – Corner Impact	2.4E-06	
	Volatiles	3.00E-05	Average of values in Hanson, et al (2008), Section 4.3, p. 4.12.
	Volatiles - Corner Impact	1.5E-05	
	CRUD	1.00	

The release from these potential accidents is not at ground level but at about two meters above ground, taking into account the height of the flatcar and the diameter of the horizontally mounted cask. The factor H in Equation (V-4) is the release height, two meters in this case. The gas flowing from the cask is warmer than ambient and the heat rate is about 660 watts per assembly⁹, so that the plume of material will be lofted slightly. Using Equation (V-4), RADTRAN models the maximum air concentration and ground deposition at about 21 meters downwind from the cask. The maximally exposed individual would be located at this point. A graph the plume is presented in Figures 5-4a and 5-4b in Chapter 5. Results of the RADTRAN calculation, the radiation dose (consequence) that could result if radioactive material was released in a spent fuel cask accident, are shown in Table V-20.

⁹ For nine-year-cooled PWR fuel from the ORIGEN analysis. 660 watts per assembly = 17160 watts per cask = 4.1 Kcal/sec.

Table V-20. Maximally exposed individual doses (consequences) in Sv from accidents that involve a release.

Cask Orientation	Impact Speed (kph)	Seal	Inhalation	Resuspension	Cloudshine	Groundshine	Total
End	193	metal	1.6	1.4E-02	8.8E-05	9.4E-04	1.6E+00
Corner	193	metal	1.6	1.4E-02	8.8E-05	9.4E-04	1.6E+00
Side	193	elastomer	1.6	1.4E-02	8.8E-05	9.4E-04	1.6E+00
Side	193	metal	1.6	1.4E-02	8.8E-05	9.4E-04	1.6E+00
Side	145	elastomer	1.6	1.4E-02	4.5E-06	3.6E-05	1.6E+00
Side	145	metal	1.6	1.4E-02	8.8E-05	9.4E-04	1.6E+00
Corner	145	metal	0.73	0.0063	0.0001	0.0009	0.73

When the doses in Table V-20 are multiplied by the probabilities in Table V-18, the “conditional dose risks” of Table V-21 result.

Table V-21 Maximally exposed individual conditional dose risks in Sv from accidents that involve a release.

Cask Orientation	Impact Speed (kph)	Seal	Inhalation	Resuspension	Cloudshine	Groundshine	Total
End	193	metal	4.3E-08	3.7E-10	2.4E-12	2.5E-11	4.3E-08
Corner	193	metal	2.6E-07	2.2E-09	1.4E-11	1.5E-10	2.6E-07
Side	193	elastomer	1.3E-07	1.1E-09	7.0E-12	7.6E-11	1.3E-07
Side	193	metal	1.3E-07	1.1E-09	7.0E-12	7.6E-11	1.3E-07
Side	145	elastomer	2.41E-06	2.09E-08	6.90E-12	5.50E-11	2.42E-06
Side	145	metal	2.42E-06	2.09E-08	1.34E-10	1.44E-09	2.44E-06
Corner	145	metal	4.23E-05	3.66E-07	2.98E-09	5.37E-08	4.27E-05

Population doses are calculated by integrating the rural, suburban, and urban population densities, respectively, over the largest plume footprint in the dispersion calculation: 1420 km² for neutral meteorological stability. Collective dose risks are calculated by multiplying each population dose by the appropriate conditional probability. Collective doses are presented in Table V-22 for the end impact, 193 kph impact speed accident, as an example.

Table V-22. Collective conditional inhalation and external dose risks for the end impact, 193 kph impact speed accident, for the 16 routes analyzed.

	Collective Internal Dose Risk (person-Sy)				Collective External Dose Risk (person-Sy)			
	ORNL	DEAF SMITH	HANFORD	SKULL VALLEY	ORNL	DEAF SMITH	HANFORD	SKULL VALLEY
MAINE YANKEE								
RURAL	2.6E-14	1.1E-	1.6E-14	7.7E-15	2.3E-	1.0E-17	1.5E-17	7.0E-18
SUBURBAN	5.1E-13	3.2E-	2.7E-13	1.6E-13	4.6E-	2.9E-16	2.5E-16	1.5E-16
URBAN	8.8E-12	5.4E-	4.6E-12	2.3E-12	8.0E-	4.9E-15	4.2E-15	2.1E-15
KEWAUNEE								
RURAL	1.0E-14	2.4E-	2.5E-15	2.5E-15	9.2E-	2.2E-18	2.3E-18	2.3E-18
SUBURBAN	2.2E-13	1.1E-	1.0E-13	9.3E-14	2.0E-	9.8E-17	9.2E-17	8.4E-17
URBAN	3.8E-12	1.8E-	1.8E-12	1.3E-12	3.4E-	1.6E-15	1.6E-15	1.1E-15
INDIAN POINT								
RURAL	2.8E-13	9.1E-	9.6E-15	3.8E-15	2.5E-	8.2E-18	8.7E-18	3.5E-18
SUBURBAN	8.7E-12	3.3E-	3.3E-13	1.2E-13	7.9E-	3.0E-16	3.0E-16	1.1E-16
URBAN	1.5E-10	5.8E-	6.0E-12	1.9E-12	1.4E-	5.3E-15	5.4E-15	1.7E-15
IDAHO NATIONAL LAB								
RURAL	1.1E-12	1.7E-	3.5E-13	2.1E-12	3.6E-	5.4E-15	1.1E-15	6.6E-15
SUBURBAN	1.5E-15	1.1E-	2.9E-16	3.7E-15	4.8E-	3.4E-18	9.4E-19	1.2E-17
URBAN	5.3E-14	9.3E-	2.0E-14	1.3E-13	1.7E-	3.0E-16	6.5E-17	4.0E-16

Internal doses include doses from direct inhalation and from material resuspended in air. External doses include cloudshine and groundshine. The NRC cites the total effective dose equivalent (TEDE) which includes both inhalation (internal) doses and external doses. The complete collective dose risk is the product of the collective dose risk as shown in Table V-23 and the accident frequency along the route. Average accident frequencies for each route are in Table V-7.

Table V-23 shows the total dose risk for each route.

Table V-23. Total collective dose risks (person-Sy) for each route

	ORNL	DEAF SMITH	HANFORD	SKULL VALLEY
MAINE YANKEE	3.6E-09	2.2E-09	1.9E-09	9.6E-10
KEWAUNEE	1.5E-09	7.4E-10	7.2E-10	5.1E-10
INDIAN POINT	6.1E-08	2.3E-09	2.4E-09	7.7E-10
INL	3.7E-10	6.0E-10	1.6E-10	1.1E-09

V.6. Summary

The more important technical observations for the analysis of accidents are:

- Event trees based on current accident statistics show that the probability of a severe accident for either truck or rail is one in 100,000 or less). The probability of a fire that would damage a cask on a railcar enough to cause loss of gamma shielding or release of radioactive material is negligible.
- The analyses in Appendices III and IV demonstrate that there would be no releases of radioactive material from a cask carrying canistered fuel, and the only cask that would suffer a loss of lead shielding or release of radioactive material is the Rail-Lead cask. Most accidents involving spent fuel casks – 99.991 percent – do not lead to either a release of radioactive material or a loss of lead gamma shielding.
- The external dose from loss of lead shielding is negligible unless more than two percent of the lead shield is lost and unless the receptor is within four meters of the cask, as shown in Table V-3.
- If the fuel rods are not breached in an accident, even if the seals are compromised, there would be no net flow of gas out of the cask, and nothing would be released.

BIBLIOGRAPHY

Code of Federal Regulations (CFR) 2009, Volume 10, Part 20 and Part 71

Code of Federal Regulations (CFR) 2009, Volume 49, Parts 173-179.

Are, N., M. Greiner, and A. Suo-Anttila. 2005. "Benchmark of a Fast-Running Computational Tool for Analysis of Massive Radioactive Material Packages in Fire Environments," *Journal of Pressure Vessel Technology*, Vol. 127, pp. 508-514, American Society of Mechanical Engineers (ASME).

Adkins, H.E., Cuta, J.M., Koepfel, B.J., Guzman, A.D., Bajwa, C.S. 2006. *Spent Fuel Transportation Package Response To The Baltimore Tunnel Fire Scenario*, NUREG/CR-6886, Rev. 1, PNNL-15313, Pacific Northwest National Laboratory, Richland, WA.

American Society for Testing Materials (ASTM). 2008. *E 2230, Standard Practice for Thermal Qualification of Type B Packages for Radioactive Material*, ASTM International.

ASTM E 2230, Standard Practice for Thermal Qualification of Type B Packages for Radioactive Material, ASTM International, 2008.

Ammerman, D.J. and Gwinn, K.W. 2004. *Collapse of the Cypress Street Viaduct – Effect on a Postulated Spent Fuel Truck Cask*, Proceedings of the 45th INMM Annual Meeting, Orlando, FL.

Ammerman, D.J., Stevens, D., and Barsotti, M. 2005 *Numerical Analyses of Locomotive Impacts on a Spent Fuel Truck Cask and Trailer*, Proceedings of the ASME PVP 2005, Denver, CO.

BEIR VII (National Research Council Committee on the Biological Effects of Ionizing Radiation Phase 2. 2006. *Health Effects From Exposure to Low Levels of Ionizing Radiation* National Academy Press, Washington, DC.

Bonzon, I.L. and Schaumann, J.T. 1976. *Container Damage Correlation with Impact Velocity and Target Hardness*, IAEA-SR-10/21, Transport Packaging for Radioactive Materials, IAEA, Vienna, Austria.

Croff, A.G. 1980. *ORIGEN2 - A Revised and Updated Version of the Oak Ridge Isotope Generation and Depletion Code*, ORNL-5621, Oak Ridge National Laboratory, Oak Ridge, TN.

Del Valle, M.A., Kramer, M.A., Lopez, C., Suo-Anttila, A., and Greiner, M. 2007 "Temperature Response of a Rail-Cask-Size Pipe Calorimeter in Large-Scale Pool Fires",

proceedings of the 15th International Symposium on the Packaging and Transportation of Radioactive Materials (PATRAM).

del Valle, M. 2009. Benchmark and sensitivity study of the Container Analysis Fire Environment (CAFE) computer code using a rail-cask-size pipe calorimeter in large-scale pool fires, M.S. Thesis, UNIVERSITY OF NEVADA, RENO, MAI 47/03.

Dennis, M.L., Osborn, D. O., Weiner, R. F., Heames, T.J. 2008. *Verification and Validation of RADTRAN 6.0* SAND2008-4556, Sandia National Laboratories, Albuquerque, NM.

Dennis, M.L., Weiner, R.F., Osborn, D.M., Heames, T.J. 2009. "Dose Estimates in a Loss-of-Lead-Shielding Truck Accident" SAND2009-5107, Sandia National Laboratories, Albuquerque, NM.

Einzigler, R.E.. 2007. "Source Terms for Spent fuel Transportation and Storage Cask Evaluation" Proceedings of the 15th International Symposium on the Packaging and Transportation of Radioactive Materials, PATRAM 2007, Miami, Florida.

Einzigler, R.E. and Beyer, C. 2007. "Effect of High-Burnup Fuel on Source Term In Cask Accidents," *Nuclear Technology* v. 199, pp 134-146.

Federal Register, Vol 46, page 21629, April 13, 1981.

Federal Register, Vol. 65, No. 203, Thursday, October 19, 2000, Rules and Regulations, page 62597

Figueroa, V.G. and C. Lopez. 2010. *8ft Diameter Calorimeter Fire Test Series*, SAND report under preparation, Sandia National Laboratories, Albuquerque, NM.

Fischer, L.E.; Chou, C.K.; Gerhard, M.A.; Kimura, C.Y.; Martin, R.W.; Mensing, R.W.; Mount, M.E.; Witte, M.C. 1987. *Shipping Container Response to Severe Highway and Railway Accident Conditions*, NUREG/CR-4829, Lawrence Livermore National Laboratory, Livermore, CA.

General Atomics. 1998. *Safety Analysis Report for Packaging*, General Atomics Project 4439, San Diego, CA

Gonzales, A. 1987. *Target Effects on Package Response: An Experimental and Analytical Evaluation*, SAND86-2275, Sandia National Laboratories, Albuquerque, NM

Greiner, M., del Valle, M., Lopez, C., Figueroa, V., and Abu-Irshaid, E., 2009, "Thermal Measurements of a Rail-Cask-Size Pipe-Calorimeter in Jet Fuel Fires," ASME 2009 Summer Heat Transfer Conference, HT2009-88520, San Francisco, California USA.

- Griego, N.R.; Smith, J.D.; Neuhauser, K.S. 1996. "Investigation of Radtran Stop Model Input Parameters for Truck Stops," SAND96-0714C. Sandia National Laboratories. Albuquerque, NM.
- Haire, M.J. and Swaney, P.M. 2005. "Cask Size and Weight Reduction Through the Use of DUO₂-Steel Cermet Material" *Waste Management '05*, Tucson, AZ.
- Hanson, B.D., Daniel, R.C., Casella, A.M., Wittman, R.S., Wu, W., MacFarlan, P.J., Shimskey, P.J. 2008. *Fuel-In-Air FY07 Summary Report Rev. 1* PNNL-17275, Pacific Northwest National Laboratory, Richland, WA.
- Hibbit, Karlsson and Sorensen. 1998. *ABAQUS/Standard User's Manual* (Hibbit, Karlsson and Sorensen, Inc., HKS, 1080 Main Street, Pawtucket, RI, 02860 4847) Version 5.8 edition (1998).
- Hoffman, E. L. and Attaway, S. W. 1991. *Structural Analysis Of The Source Term Transportation Cask*, SAND91-1543, Sandia National Laboratories, Albuquerque, NM,
- Holtec International. 1997. *HI-STAR 100 System Cask Thermal Design Package* Holtec Report HI-951325.
- Holtec International. 2004. *Safety Analysis Report for the HI-STAR* Holtec Report 951251.
- Husek, H.J. 1986. *Structural Alloys Handbook*, Battelle Memorial Institute, Columbus, OH
- Incropera, F.P. and Dewitt, D.P. 1996. *Fundamentals Of Heat And Mass Transfer*, John Wiley & Sons, New York.
- Interagency Steering Committee on Radiation Standards (ISCORS). 2002. *A Method for Estimating Radiation Risk from TEDE*, ISCORS Technical Report No. 1, USDOE Office of Environmental Policy and Guidance, Washington, DC.
- Johnson, P.E. and Michelhaugh, R.D. 2003. *Transportation Routing Analysis Geographic Information System (TRAGIS) User Manual*, ORNL/NTRC-006, Oak Ridge National Laboratory, TN.
- Kalan, R. J., C.J.R Clutz, and D.J. Ammerman. 2005. "Analysis of a 17 x 17 Pressurized Water Reactor (PWR) Fuel Assembly," letter report to DOE-RW, August 2005
- Kelley, K.K. 1960. Enthalpy plots DWG K38745 Bureau of Mines 584.
- Koski, J.A. 2000. "Measurement of Temperature Distributions in Large Pool Fires with the use of Directional Flame Thermometers," in Proceedings 2000 ASME Pressure Vessels and Piping Conference, Seattle WA.
- Kramer, M.A., M. del Valle, and M. Greiner. 2008. "Measurement and Uncertainty of Heat Flux to a Rail-Cask Sized Pipe Calorimeter in a Pool Fire," PVP2008-61600, proceedings

of the 2008 ASME Pressure Vessels and Piping Conference, PVP2008, Chicago, Illinois, Conference Paper.

- Livermore Software Technology Corporation, LS-DYNA User's Manual, 7374 Las Positas Road, Livermore, CA 94550 US
- Lopez, A.R., L.A. Gritz, and M.P. Sherman. 1998. *Risk Assessment Compatible Fire Models (RACFMs)*, Sandia National Laboratories Report SAND97-1562.
- Lopez, C., J. Koski, and A. Suo-Anttila. 2003. "Development and Use of the CAFE-3D Code for Analysis of Radioactive Material Packages in Fire Environments," INMM Conference, Orlando, FL.
- Lorenz, R.A. et al. 1980. *Fission Product Release from Highly Irradiated LWR Fuel*, NUREG/CR-0722, Oak Ridge National Laboratory, Oak Ridge, TN, February 1980.
- Lorenz, R.A., et al., 1978. *Fission Product Release from Simulated LWR Fuel*, NUREG/CR-0274, Oak Ridge National Laboratory, Oak Ridge, TN, July 1978.
- McAdams, W.H. 1954. *Heat Transmission*, 3rd. Ed.
- Mills, G.S., Sprung, J.L., Osborn, D.M. 2006. *Tractor/Trailer Accident Statistics* SAND2006-7723, Sandia National Laboratories, Albuquerque, NM.
- MSC Software Corporation. 2008 *MSC PATRAN/Thermal Version 2008r2*, MSC Software Corporation, Santa Ana, California, <http://www.mscsoftware.com>.
- Nakos, J.T. 2005. *Uncertainty Analysis of Steady State Incident Heat Flux Measurements in Hydrocarbon Fuel Fires*, SAND2005-7144 Sandia National Laboratories, Albuquerque, NM
- Nicolette, V.F. and Larsen, D.W. 1989. "Influence Of Large, Cold Objects On Engulfing Fire Environments", SAND89-2175C, Sandia National Laboratories, Albuquerque, NM.
- Nuclear Acceptance Corporation (NAC) International. 2002. *Safety Analysis Report for the NAC Universal Multi-Purpose Canister System*, NRC Docket 71-9235, Atlanta, GA.
- Neuhauser, K.S., Kanipe, F.L, Weiner, R.F. 2000. *RADTRAN 5, Technical Manual*, Sandia National Laboratories, Albuquerque, NM.
- Nuclear Acceptance Corporation (NAC) International. 2004. *Safety Analysis Report for the NAC Storage Transport Cask*, NRC Docket 71-9235, Atlanta, GA.
- O'Donnell, B., James, S., Weiner, R.F. 2005. "Calculations for Loss of Shielding Resulting From Transportation Accidents," Institute for Nuclear Materials Management, Annual Meeting, Fort Lauderdale, FL.

- Perry, J.H. 1963. *Chemical Engineering Handbook*, 4th Ed.
- Petersen, H. 1970. *The Properties of Helium*, Riso Report No. 224, Danish Atomic Energy Commission
- Pierce, J.D., P.J. Gronewald, J. Mould, R. Oneto. 2003. Radiant heat test of Perforated Metal Air Transportable Package (PMATP), SAND2003-2750, Sandia National Laboratories, Albuquerque, NM
- Pierron, O.N., Koss, D.A., Motta, A.T. 2003. Tensile Specimen Geometry and Constitutive Behavior of Zircaloy-4, *Journal of Nuclear Materials*, 312, 257-261
- Quintiere, J.G. 1998. *Principles of Fire Behavior*, Delmar Publishers, Albany, New York.
- Ross, S.S., Weiner, R.F., Best, R.E., Maheras, S., McSweeney, T. 2002. *Transportation Health and Safety Calculation/Analysis Documentation in Support of the Final EIS for the Yucca Mountain Repository CAL-HSS-ND-000003*, USDOE Office of Civilian Radioactive Waste Management, Las Vegas, NV.
- Sanders, T.L., Seager, K.D., Rashid, Y.R., Barrett, P.R., Malinauskas, A.P., Einziger, R.E., Jordan, H., Duffey, T.A., Sutherland, S.H., Reardon, P.C. 1992. *A Method for Determining the Spent-Fuel Contribution to Transport Cask Containment Requirements*, SAND90-2406, Sandia National Laboratories, Albuquerque, NM
- Sandoval, R.P., Einziger, R.E., Jordan, H., Malinauskas, A.P., Mings, W.J. 1988. *Estimate of CRUD Contribution to Shipping Cask Containment Requirements* SAND88-1358. Sandia National Laboratories, Albuquerque, NM.
- Schorsch, R.H. 1966. *Engineering properties of selected metals*.
- Shleien, B., Slaback, L.S., Birky, B.K. 1998. *Handbook of Health Physics and Radiological Health, Third Edition*. Williams and Wilkins, Baltimore, MD.
- SIERRA Solid Mechanics Team. 2009. *Presto 4.11 User's Guide*. SAND2009-3213, Sandia National Laboratories, Albuquerque, NM, November 2009 Sandia National Laboratories, Albuquerque, NM.
- SIERRA Solid Mechanics Team. 2009. *Presto 4.14 User's Guide*. SAND2009-7401, Sandia National Laboratories, Albuquerque, NM, November 2009 Sandia National Laboratories, Albuquerque, NM.
- Society of Fire Protection Engineers (SFPE). 2002. *The SFPE Handbook of Fire Protection Engineering*, 3rd edition, National Fire Protection Association, Quincy, MA,
- Soo-Haeng, C., D. Jae-Bum, R. Seung-Gy, D. Chun-Ho., 1996. "Fabrication and Characteristics of Resin-Type Neutron Shielding Materials for Spent Fuel Shipping Cask," *Journal of Industrial and Engineering Chemistry*, Vol. 7, No. 3, June 1996, 597-604

- Suo-Anttila, A., C. Lopez, C., and I. Khalil. 2005. *Users Manual for CAFE-3D: A Computational Fluid Dynamics Fire Code*, Sandia National Laboratories Report, SAND2005-1469.
- Stabin, M.G. 2009. "Doses from Medical Radiation Sources," Health Physics Society Topical Articles, <http://www.hps.org/hpspublications/articles/dosesfrommedicalradiation.html>
- Sprung, J.L., Ammerman, D. J., Breivik, N.L., Dukart, R.J., Kanipe, F.L., Koski, J. A., Mills, G.S., Neuhaiuser, K.S., Radloff, H.D., Weiner, R.F., Yoshimura, H.R.. 2000. *Re-Examination of Spent Fuel Risk Estimates* NUREG/CR-6672, Sandia National Laboratories, Albuquerque, NM.
- Steinman, R. L., Weiner, R.F., Kearfott, K. 2002. "Comparison of Transient Dose Model Predictions and Experimental Measurements." *Health Physics* v. 83 (2002), p.504 et seq
- Suo-Antilla, A., C. Lopez, and I. Khalil. 2005. *User Manual for CAFE-3D: A Computational Fluid Dynamics Fire Code*, SAND2005-1469, Sandia National Laboratories, Albuquerque, NM.
- Taylor, J.M. and Daniel, S.L. 1977. *RADTRAN: A Computer Code to Analyze Transportation of Radioactive Material*, SAND76-0243, Sandia National Laboratories, Albuquerque, NM.
- Thermophysical Properties Research Laboratory Inc. 2001. *Thermophysical Properties of Kaowool, Honeycomb, Foam and Cork*, Report No. 2649, August 2001
- Turner, D.B. 1994. *Workbook of Atmospheric Dispersion Estimates* Lewis Publishers, New York, NY
- Tubiana, M. and Aurengo, A. 2005. "Dose-effect relationship and estimation of the carcinogenic effects of low doses of ionizing radiation: the Joint Report of the Académie des Sciences (Paris) and the Académie Nationale de Médecine" *Int. J. Low Radiation*, V 2, pp. 1-19
- U.S. Bureau of the Census. 2008. <http://www.census.gov>
- U.S. Department of Energy (DOE). 1986. *Environmental Assessment Yucca Mountain Site, Nevada Research and Development Area, Nevada*. DOE/RW-0073. U.S. Department of Energy, Office of Civilian Radioactive Waste Management, Washington, D.C.
- U.S. Department of Energy (DOE). 2002. *Final Environmental Impact Statement for a Geologic Repository for the Disposal of Spent Nuclear Fuel and High-Level Radioactive Waste at Yucca Mountain, Nye County, Nevada*. DOE/EIS-0250F, Washington, DC, Chapter 6 and Appendix J.

- U.S. Department of Transportation (DOT). 2004a. "Maximum Posted Speed Limits by Type of Road," (Table 2-9) Bureau of Transportation Statistics Research and Innovative Technology Administration, Washington, DC
- U.S. Department of Transportation (DOT). 2004b. "Rail freight Average Speeds, Revenue Ton-Miles, and Terminal Dwell Times" (Table 2-9) Bureau of Transportation Statistics Research and Innovative Technology Administration, Washington, DC
- U.S. Department of Transportation (DOT). 2005. State Transportation Statistics 2004, Bureau of Transportation Statistics, Research and Innovative Technology Administration, Washington, DC
http://www.bts.gov/publications/state_transportation_statistics/state_transportation_statistics_2005/pdf/entire.pdf
- U.S. Department of Transportation (DOT). 2007. "Traffic Safety Facts 2007" (Tables 1-32, 2-03, 2-04, 2-09, 2-28, 2-37) Bureau of Transportation Statistics Research and Innovative Technology Administration, www.bts.gov, Washington, DC
- U.S. Department of Transportation (DOT). 2009. "Commodity Flow Survey: Shipment Characteristics by Mode of Transportation for the U.S., 2007" (Table 1) Bureau of Transportation Statistics Research and Innovative Technology Administration, Washington, DC
- U.S. Department of Transportation (DOT). 2008. National Transportation Statistics 2008, Bureau of Transportation Statistics, Research and Innovative Technology Administration, Washington, DC
http://www.bts.gov/publications/national_transportation_statistics/html/table_02_23.htm
- U.S. Nuclear Regulatory Commission (NRC). 1975. *Reactor Safety Study*, WASH-1400, Washington, DC.
- U. S. Nuclear Regulatory Commission (NRC). 1977. *Final Environmental Statement on the Transportation of Radioactive Material by Air and Other Modes*, NUREG-0170, U.S. Nuclear Regulatory Commission, Washington, DC.
- U. S. Nuclear Regulatory Commission (NRC). 1978. *Safety Analysis Report for the Plutonium Air Transportable Package, Model PAT-1*, NUREG-0361, U.S. Nuclear Regulatory Commission, Washington, DC.
- U. S. Nuclear Regulatory Commission (NRC). 2003. "Safety of Spent Fuel Transportation," NUREG/BR-0292, U.S. Nuclear Regulatory Commission, Washington, DC.
- U. S. Nuclear Regulatory Commission (NRC). 2003b. "United States Nuclear Regulatory Commission Package Performance Study Test Protocols," NUREG-1768, U.S. Nuclear Regulatory Commission, Washington, DC.
- U. S. Nuclear Regulatory Commission (NRC). 2008. "State of the Art Reactor Consequence Analysis – Reporting Offsite Health Consequences" SECY-08-0029, and Commission

Voting Record on SECY-08-2009, U.S. Nuclear Regulatory Commission, Washington, DC.

- Volpe Center. 2006. *Spent Nuclear Fuel Transportation Risk*, Draft Report, Volpe National Transportation Systems Center, Cambridge, MA (Document available from Sandia National Laboratories)
- Waddoups, I.G. 1975. *Air Drop Test of Shielded Radioactive Material Containers*, SAND75-0276, Sandia National Laboratories, Albuquerque, NM,
- Wark, K. and Warner, C.F. 1981. *Air Pollution: Its Origin and Control*, Harper and Row, New York, NY
- Weast, R.C. 1966. *Handbook of Chemistry and Physics*, 47th Ed.
- Weiner, R.F., LaPlante, P.A., Hageman, J.P. 1991. "Risks of Incident-Free Transportation of Radioactive Materials by Highway" *Risk Analysis* v. 11, pp.660-666.
- Weiner, R. F. and Tenn, H. F. 1999. *Transportation Accidents and Incidents Involving Radioactive Materials (1971-1998)*, Sandia National Laboratories, Albuquerque, NM
- Weiner, R.F., Dennis, M.L. Hinojosa, D., Heames, T.J., Penisten, J.J., Marincel, M.K., Osborn, D.M. 2009. *RadCat 3.0 User Guide*, SAND2009-5129P. Sandia National Laboratories, Albuquerque, NM
- Wellman, G. W., and Salzbrenner, R. 1992. *Quasistatic Modeling and Testing of Exclusion Region Barrier Mock-Ups*, SAND92-0024, Sandia National Laboratories, Albuquerque, NM.
- Wooden, D.G. , 1986. *Railroad Transportation of Spent Nuclear Fuel* SAND86-7083, Sandia National Laboratories, Albuquerque, NM
- Yafei, S., T. Yongjun, S. Jing, N. Dongjie. 2009. *Effect of Temperature and Composition of Thermal Properties of Carbon Steel*, Chinese Control and Decision Conference, Guilin, China

